РОССИЙСКАЯ АКАДЕМИЯ НАУК
ИНСТИТУТ ПРОБЛЕМ БЕЗОПАСНОГО
РАЗВИТИЯ АТОМНОЙ ЭНЕРГЕТИКИ

ТРУДЫ ИБРАЭ

Под общей редакцией члена-корреспондента РАН *Л.А. Большова*

Выпуск 1

МОДЕЛИ ВЗАИМОДЕЙСТВИЯ МАТЕРИАЛОВ ТОПЛИВНЫХ ЭЛЕМЕНТОВ В ПРОЦЕССАХ РАЗРУШЕНИЯ АКТИВНОЙ ЗОНЫ РЕАКТОРА ПРИ ТЯЖЕЛЫХ АВАРИЯХ НА АТОМНЫХ СТАНЦИЯХ

(на английском языке)

MODELS FOR THE FUEL ROD MATERIALS INTERACTIONS DURING REACTOR CORE DEGRADATION UNDER SEVER ACCIDENT CONDITIONS AT NPP

(in English)

Научный редактор доктор физико-математических наук *В.Ф.Стрижов*
Рецензенты: доктор физико-математических наук *О.И. Мелихов*
доктор технических наук *А.Е. Киселёв*

Издательство «Наука»
Москва, 2007

УДК 621.039
ББК 31.4
Т78

Т78 Модели взаимодействия материалов топливных элементов в процессах разрушения активной зоны реактора при тяжелых авариях на атомных станциях (на английском языке). Под научной редакцией д.ф.-м.н. В.Ф.Стрижова. — Труды ИБРАЭ РАН. Под общей редакцией чл.-кор. РАН Л.А. Большова. Выпуск 1. — М.: «Наука», 2007. — 127 с.: ил.

Разработанные в Институте проблем безопасного развития атомной энергетики Российской академии наук (ИБРАЭ РАН) модели основных явлений в процессах разрушения активной зоны реактора: окисление оболочек, поглощение водорода и механическая деформация, растворение UO_2 и ZrO_2 расплавом циркония, были объединены в пакете программ СВЕЧА. Для применения этих моделей при описании различных экспериментов с разрушением одиночного ТВЭЛ (включая тесты FZK QUENCH), они были внедрены в пакет программ SVECHA/QUENCH. Указанные модели также вошли в различные тяжелоаварийные коды: ICARE2 (IRSN, France), SCDAP/RELAP5 (NRC, USA), Российские тяжелоаварийные коды РАТЕГ/СВЕЧА, СОКРАТ. В настоящем выпуске представлены описания основных моделей пакетов программ СВЕЧА и SVECHA/QUENCH.

Models for the Fuel Rod Materials Interactions during Reactor Core Degradation under Sever Accident Conditions at NPP (in English). Edited by Professor V.F. Strizhov. — Proceedings of Nuclear Safety Institute RAS (IBRAE RAS). Edited by corresponding member of RAS L.A. Bolshov. Issue 1. — Moscow: Nauka, 2007. — 127 p.: illustrations.

A set of mechanistic models for the main degradation phenomena: cladding oxidation, hydrogen absorption and mechanical deformation, UO_2 and ZrO_2 dissolution by molten Zr, was developed in the Nuclear Safety Institute (IBRAE) RAS and combined in the code package SVECHA. In order to be applied to mechanistic modeling of various single-rod degradation experiments (including the FZK QUENCH tests), the models were tightly coupled in the advanced mechanistic code SVECHA/QUENCH. The models were also implemented in various system-level SA codes: ICARE2 (IRSN, France), SCDAP/RELAP5 (NRC, USA), the Russian SA codes RATEG/SVECHA and SOCRAT. The book presents the main models of the code package SVECHA and the single-rod code SVECHA/QUENCH.

ISBN 978-5-02-036139-3

CONTENTS

Foreword.
Models for the Fuel Rod Materials Interactions during Reactor Core Degradation under Severe Accident Conditions at NPP

M.S. Veshchunov

Severe accidents (SA) may result from the failure of systems designed to cope with accidents. For example, a small leak in the cooling system of the primary circuit along with a temporary failure of the emergency cooling system may lead to core uncovering. The continuous heat-up of the core by the decay heat of the fission products can cause substantial damage. During early-phase core degradation the fuel assemblies are oxydized by steam resulting in an uncontrollable temperature escalation owing to highly exothermic reaction of Zr oxidation, and can be disfigured by mechanical fracturing and/or by localised liquefaction, because of material interactions or by melting. During late-phase core degradation there is substantial melting of larger core regions and relocation of molten metallic and ceramic core materials to the lower reactor pressure vessel plenum.

A better understanding of in-vessel degraded core phenomena is important (a) for accident management, to understand the progression of the accident and the potential impact of any proposed strategies, (b) for risk assessments, and (c) for the design of next-generation reactors.

In spite of significant progress in understanding of the core degradation, there is still lack in mechanistic modeling of key processes of material interactions and relocations. Such a lack significantly reduces predictive power of severe accident codes in plant analysis and interpretation of empirical data, including TMI-2 accident.

A set of mechanistic models for the main degradation phenomena: cladding oxidation, hydrogen absorption and mechanical deformation, UO_2 and ZrO_2 dissolution by molten Zr, was developed in the Nuclear Safety Institute (IBRAE) of Russian Academy of Sciences and combined in the so-called code package SVECHA [1-3]. In order to be applied to mechanistic modeling of various single-rod degradation experiments (including the FZK QUENCH tests), the models were tightly coupled in the advanced mechanistic code SVECHA/QUENCH [4-5]. The models were also implemented in various system-level SA codes (ICARE2, SCDAP/RELAP5) including the Russian SA code RATEG/SVECHA (or SOCRAT), which will be described elsewhere.

In this book, the main models of the code package SVECHA and the single-rod code SVECHA/QUENCH are presented.

References

1. *M.S. Veshchunov, A.V. Palagin, A.M. Volchek, N.V. Yamshchikov, A.V. Boldyrev, R.R. Galimov, S.Yu. Kurchatov*, Code package SVECHA: Modeling of core degradation phenomena at severe accidents. Preprint IBRAE-18-94, Moscow, 1994.
2. *M.S. Veshchunov, A.V. Palagin, A.M. Voltchek, N.V. Yamshchikov, A.V. Boldyrev*, Code package SVECHA: Core degradation at severe accidents. Transactions of SMiRT-13 Conference, Vol.1, pp.159-163, 1995.
3. *M.S. Veshchunov, A.E. Kisselev, A.V. Palagin, A.M. Voltchek, N.V. Yamshchikov, A.V. Boldyrev*, Code package SVECHA: Modeling of core degradation phenomena at severe accidents. Proc. 7th Int. Meeting on Nuclear Reactor Thermal-Hydraulics NURETH-7, 1995, v.3, p.1914-1929.
4. *P. Hofmann, V. Noack, M.S. Veshchunov, A.V. Berdyshev, A.V. Boldyrev, L.V. Matweev, A.V. Palagin, V.E. Shestak*, Physico-Chemical Behavior of Zircaloy Fuel Rod Cladding Tubes During LWR Severe Accident Reflood. Report FZKA 5846, Karlsruhe, Germany, 1997.
5. *P. Hofmann, A. Miassoedov, L. Steinbock, M. Steinbrueck, A.V. Berdyshev, A.V. Boldyrev, A.V. Palagin, V.E. Shestak, M.S. Veshchunov*, Quench Behavior of Zircaloy Fuel Rod Cladding Tubes. Small-Scale Experiments and Modeling of the Quench Phenomena. Report FZKA 6208, INV-COBE(98)-D018, Karlsruhe, Germany, 1999.

Model for High-Temperature Oxidation of Zr Cladding in Steam under Fast Transient Conditions

A.V. Berdyshev, M.S. Veshchunov

1. Introduction

Oxidation of the cladding and other Zr components in the core by steam is a critical issue in light-water reactor accidents. This process leads to the embrittlement of the cladding, significant heat and hydrogen production. As a consequence of the exothermal reaction of Zr with steam, fast temperature escalation, cladding melting and disintegration of the core structure may occur.

Usually in the severe accident codes the Zircaloy-steam reaction is represented by parabolic rate equations developed from laboratory experiments. This approach fairly well describes oxidation kinetics observed under well defined conditions of the isothermal experiments conducted in unlimited steam environments with the metal specimens, which thickness is much greater than the characteristic oxygen diffusion length in the metal $L_D \approx \sqrt{D\Delta t}$ (D is the oxygen diffusion coefficient in β-Zry, Δt is the duration of the experiment). During a severe accident, however, these conditions may not be valid. Therefore, a more realistic approach to the description of the oxidation kinetics is required.

The Oxidation model of the SVECHA code developed for the description of the Zr cladding oxidation kinetics [1-3] is based on the system of the partial derivatives oxygen diffusion equations with non-equilibrium boundary conditions (corresponding to the high cooling or heating rates) at the phase boundaries. The displacement velocities of boundaries between different phases of the cladding are determined by the oxygen and zirconium flux match conditions at the moving boundaries. Equilibrium oxygen boundary concentrations are determined as functions of temperature in accordance with the equilibrium zirconium-oxygen binary phase diagram. However, under conditions of a fast temperature transient some relaxation time is necessary to attain equilibrium values of the oxygen concentration near the interfaces between various phases. This relaxation process at the interfaces is simulated by the first order rate equations for the boundary concentrations, on the basis of experimental investigations.

In the single-rod quench experiments [4] performed in the FZK (Karlsruhe, Germany) a characteristic time of quick temperature decrease was in the range from 5 to 10 seconds. On the other hand, a finite time is required for oxygen boundary concentrations to reach new equilibrium values. As follows from the experimental results [5], the oxygen boundary concentration relaxation time is of the same order as the above mentioned characteristic quenching time (5-10 s). In these experiments, oxygen concentrations adjacent to the β-Zr/α-Zr(O) boundary for samples heated at 100 K/s from 573 to 1673 K were measured. The boundary oxygen concentrations were determined after quenching at 1000 K/s from 1673 K following isothermal hold period 0; 2.5; 8 s. It was observed, that equilibrium boundary concentrations were attained between 2.5 and 8 s after the end of the ramp. Thus, from the comparison of the characteristic times it follows that under quenching conditions the oxygen boundary concentrations considerably differ from the equilibrium ones and should be taken as functions of time.

Another important feature of the fast temperature transients revealed in the quench experiments [4] is an essential radial temperature gradient across the oxide layer. It was estimated, that in the oxide scale for every 100 μm of the oxide layer temperature drop is about 100 K. The oxygen diffusion coefficients in the oxide are rather steep functions of the temperature, and ratio of the diffusion coefficients near the inner and outer oxide surfaces varies from 2 to 3 for every 100 μm of the oxide layer. Under

these conditions the assumption about a constant value of the diffusion coefficient across the oxide layer accepted in the simplified oxidation model [1-3] could be hardly justified.

In addition, from common consideration it follows that under conditions of fast temperature changes, when oxygen concentration distributions in the reaction zones are essentially nonlinear, the simplified oxidation model can result in significant errors in modeling of cladding oxidation.

The oxidation model which naturally overcomes all above mentioned simplified oxidation model deficiencies essential for high cooling rates is based on the accurate system of partial derivative diffusion equations.

2. Model description

2.1. Basic equations

Currently, it is established with confidence by numerous investigations that cladding oxidation by steam can be described with a good accuracy by the solution of the moving boundary diffusion problem.

Oxygen distributions in various reaction zones are governed by the first and second Fick's laws, which in the case of cylindrical-symmetry geometry have the following form, respectively

$$F_i = v_i c_i - D_i \frac{\partial c_i}{\partial r} \ , \qquad (1)$$

and

$$\frac{\partial c_i}{\partial t} = -\frac{1}{r}\frac{\partial}{\partial r}\left(rF_i\right) \ , \qquad (2)$$

where subscript i denotes various reaction layers; D_i is the diffusion coefficient, v_i is the convective velocity of the reaction layer, c_i is the oxygen molar density at time t and distance r from the cladding axis; F_i is the oxygen flux.

It is assumed in the model that convective movements of the reaction layers due to mutual transformations of the zirconium phases with different densities occur without density changes of the individual phases. This assumption can be mathematically expressed in the form

$$\frac{\partial}{\partial r}\left(rv_i\right) = 0 \ . \qquad (3)$$

Substituting Eq. (3) and Eq. (1) into Eq. (2) yields

$$\frac{\partial c_i}{\partial t} + v_i(r,t)\frac{\partial c_i}{\partial r} = \frac{1}{r}\frac{\partial}{\partial r}\left(rD_i(r,t)\frac{\partial c_i}{\partial r}\right). \qquad (4)$$

During fast transient regimes temperature is a function of spatial coordinate and time. Hence, the diffusion coefficients dependent on temperature should be taken as functions of the same variables.

The displacement velocities of boundaries between different phases of the cladding are determined by oxygen and zirconium flux match conditions at a moving boundary. For the reaction layers i and i-1, these conditions lead to the equations

$$(c_i^{(1)} - c_{i-1}^{(2)})\frac{dr_i}{dt} = D_{i-1}\left.\frac{\partial c_{i-1}}{\partial r}\right|_{r=r_i} - D_i\left.\frac{\partial c_i}{\partial r}\right|_{r=r_i} + c_i^{(1)}v_i^{(1)} - c_{i-1}^{(2)}v_{i-1}^{(2)}, \qquad (5)$$

$$(\rho_i - \rho_{i-1})\frac{dr_i}{dt} = \rho_i v_i^{(1)} - \rho_{i-1}v_{i-1}^{(2)}, \qquad (6)$$

where ρ_i is the zirconium molar density; r_i is the interface coordinate between the reaction layers i and i-1; superscripts (1) and (2) denote values at the left and right boundaries of a reaction layer, correspondingly, Fig. 1.

Eqs. (5) and (6) are easily reduced to the form

$$\frac{dr_i}{dt} = \frac{D_{i-1}\left.\frac{\partial c_{i-1}}{\partial r}\right|_{r=r_i} - D_i\left.\frac{\partial c_i}{\partial r}\right|_{r=r_i}}{(c_i^{(1)}\frac{\rho_{i-1}}{\rho_i} - c_{i-1}^{(2)})} + v_{i-1}^{(1)}\frac{r_{i-1}}{r_i}, \quad (7)$$

$$v_i^{(1)} = \frac{\rho_{i-1}}{\rho_i}v_{i-1}^{(1)}\frac{r_{i-1}}{r_i} + \frac{dr_i}{d}(1-\frac{\rho_{i-1}}{\rho_i}). \quad (8)$$

In order to describe by the above equations (4), (7) and (8) the oxygen diffusion and phase boundary motion occurring during cladding oxidation, initial and boundary conditions should be specified.

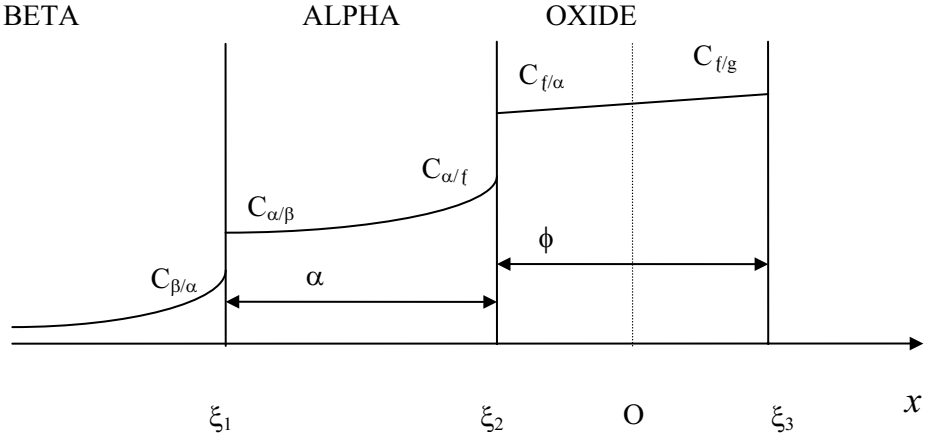

Fig. 1. Schematic representation of oxygen profiles in multi-layered structure of oxidized Zr cladding.

2.2. Boundary conditions

Equilibrium oxygen boundary concentrations are defined as functions of temperature by the zirconium-oxygen phase diagram. Under conditions of a fast temperature transient from value T_1 to T_2, oxygen concentrations near the interfaces change from one equilibrium state to another during certain time interval. This relaxation process at the interface between β-Zr and α-Zr(O) was experimentally investigated in [5]. In the same work [5], the first order rate equations for the description of the non-equilibrium boundary concentration behavior were suggested:

$$\frac{dc_i^{(1)}}{dt} = \frac{c_{i,e}^{(1)} - c_i^{(1)}}{\tau_i}, \quad (9)$$

$$\frac{dc_i^{(2)}}{dt} = \frac{c_{i,e}^{(2)} - c_i^{(2)}}{\tau_i}, \quad (10)$$

where τ_i is the characteristic relaxation time of non-equilibrium oxygen boundary concentration; $c_{i,e}^{(1)}$ and $c_{i,e}^{(2)}$ are the equilibrium oxygen boundary concentrations. The characteristic relaxation time τ_i is assumed in [5] to be inversely proportional to the corresponding diffusion coefficient D_i. However, such an assumption is not sufficiently substantiated. Indeed, according to this inference, oxygen concentrations in two phases in the vicinity of their interface will attain equilibrium values at different instants of time, this is in contradiction with the nature of the relaxation process at an interface between two phases. In addition, it is generally believed that activation energy of the interface kinetic process may significantly differ from that of atomic migrations in the bulk of the phases. This correlates with the results of our calculations, which show that measured in [5] oxygen concentrations adjacent to the alpha/beta boundary are satisfactory described by Eqs. (9), (10) with relaxation time independent on temperature and equal to 8 s. The comparison of the experimental and calculated data is presented in Fig. 2.

Since equilibrium oxygen boundary concentrations in tetragonal ZrO_2 and at the alpha/oxide interface are independent or weakly dependent

on temperature according to the phase diagram [6], the relaxation processes at relevant interfaces were not taken into consideration.

The boundary conditions for the convective-diffusion equations (4) at the interfaces between different zirconium phases are

$$c_i(r = r_{i-1}, t) = c_i^{(1)}(t), \qquad (11)$$

$$c_i(r = r_i, t) = c_i^{(2)}(t). \qquad (12)$$

As far as outer surfaces of the cladding are concerned, the boundary conditions may be of two types. If sufficient oxygen is available at the cladding surface, the oxygen concentrations must be specified at the boundary in the form of Eq. (11) or (12). In steam-starved surroundings, the boundary conditions must be imposed as follows:

$$D_i \left.\frac{\partial c_i}{\partial r}\right|_{r=r_i} = Q, \qquad (13)$$

where external oxygen flux Q should be found from the solution of a mass-transfer problem in the gas phase by a conjugated thermal-hydraulic model.

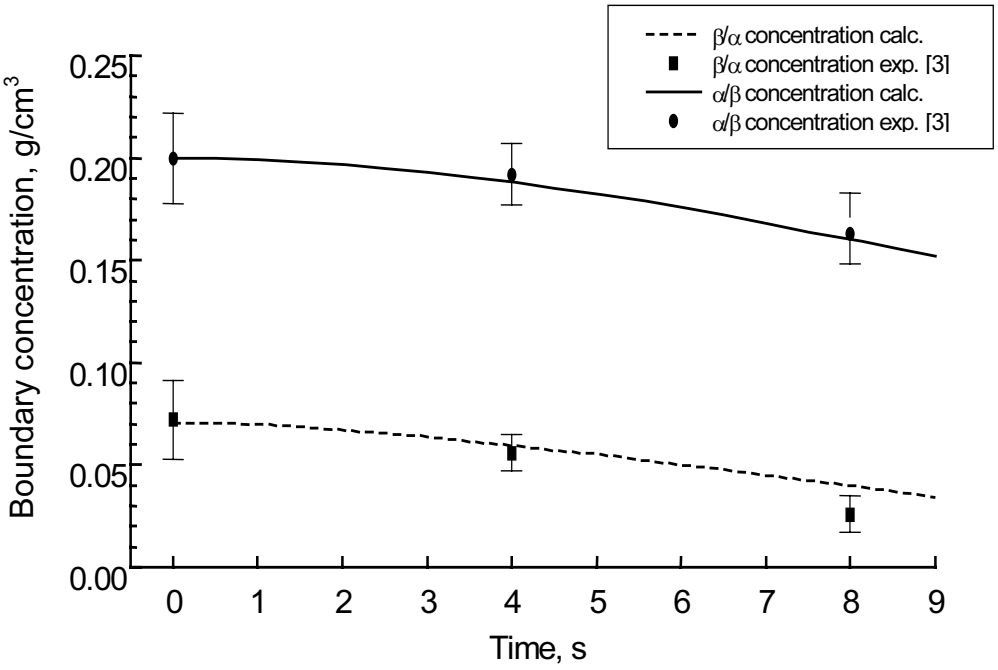

Fig. 2. Decrease in boundary oxygen concentration during cooling at 50 K/s from 1673 K. Experimental points [5] are shown for final temperatures of 1473 K and 1273 K, respectively.

2.3. Material properties

Material properties necessary for the modeling are the oxygen diffusion coefficients and boundary concentrations in the various phases. These parameters were chosen in accordance with recommendations of the work [7] (see also [2]). In [7, 2], final unique correlations for oxidation kinetics with determined confidential intervals were developed on the basis of the statistical analysis of the most reliable and mutually compatible data obtained by different methods and/or by different experimental groups in the isothermal tests. On this basis, oxygen diffusion coefficients in various phases of oxidized Zry: β-Zr, α-Zr(O), ZrO_2(tetr.), ZrO_2(cub.), were calculated, Figs. 3 and 4.

The model with the new data base obtained from the isothermal tests was thoroughly tested against various transient oxidation experiments [8, 9] and demonstrated a good agreement between experimental and calculated data, Fig. 5.

A similar procedure of diffusion coefficients determination was performed for Zr1%Nb alloy on the base of the test data from RIAR [10]. Results of these calculations are presented in the same graphs, Figs. 3 and 4, for direct comparison of the two materials.

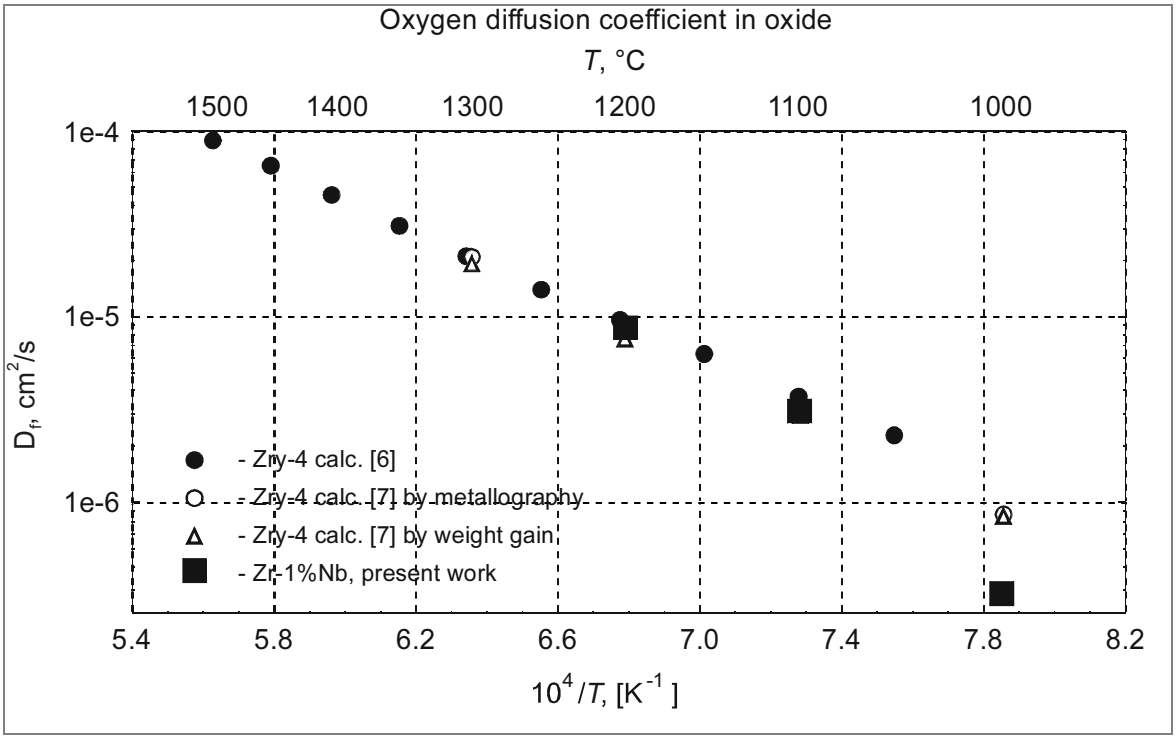

Fig. 3. Calculated oxygen diffusion coefficients in ZrO_2 for Zr1%Nb u Zircaloy-4.

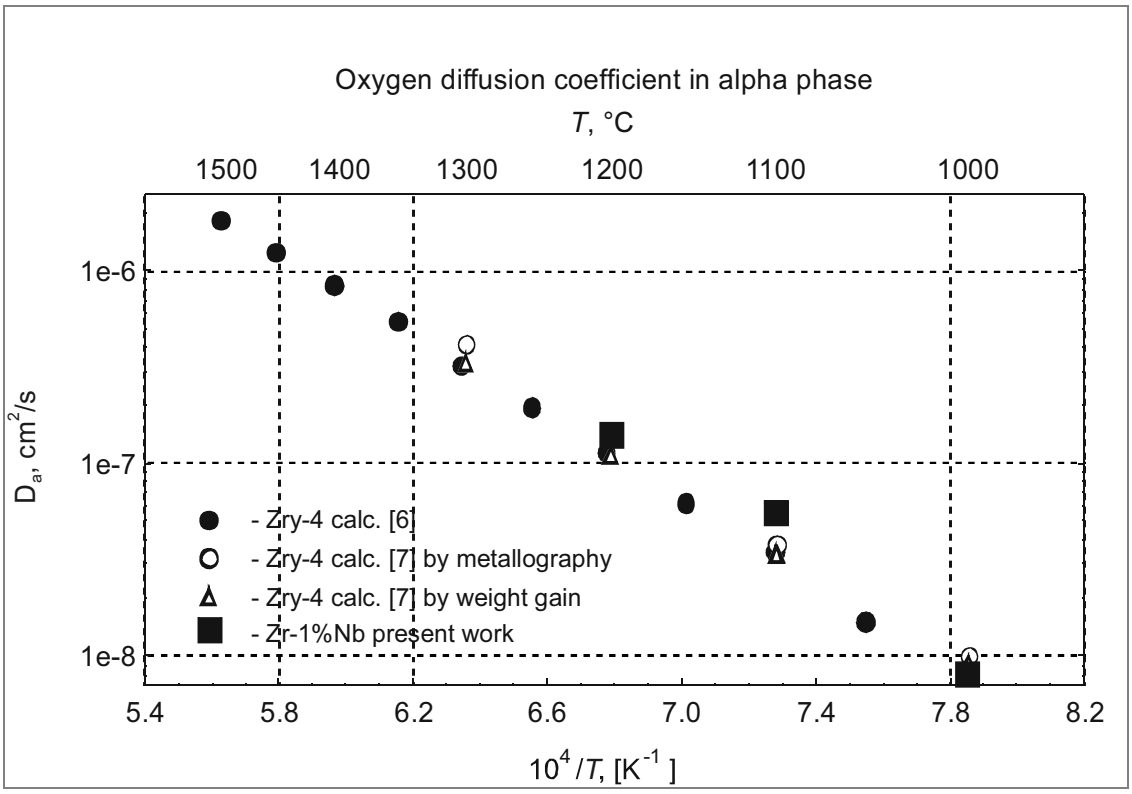

Fig. 4. Calculated oxygen diffusion coefficients in α-Zr for Zr1%Nb u Zircaloy-4.

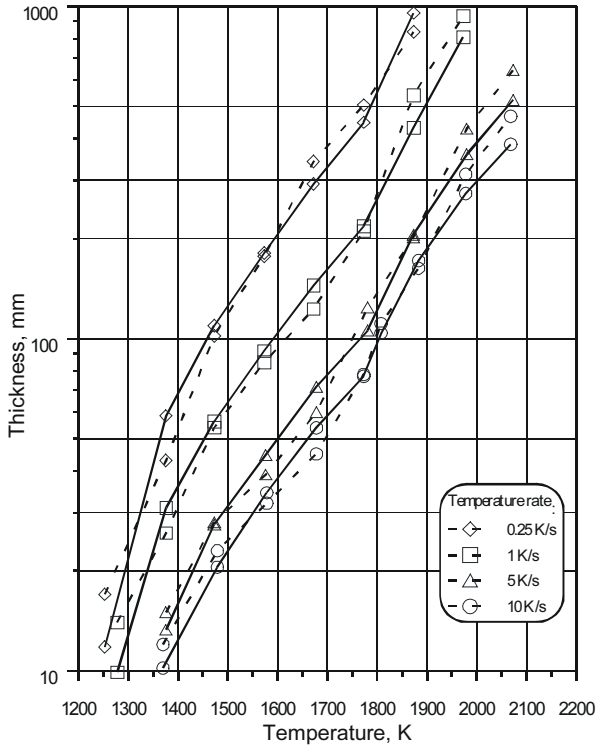

Fig. 5. Validation of the oxidation model against transient tests [9] with various heat-up rates: dependence of oxide scale thickness on maximum temperature.

2.4. Numerical methods

In order to simplify the numerical solution of the multi-layer diffusion problem with moving boundaries, this problem was reduced by the coordinate transformation to the convective-diffusion problem in a fixed region. The fully implicit finite-difference time discretisation along with the space discretisation was used. Since the largest concentration gradients are expected near the layer boundaries, the non-uniform space grid was applied. The obtained tridiagonal system of difference equations is solved by the efficient Thomas' algorithm. As a result, the developed numerical model is fast and compact and quite appropriate for implementation in a system code for the prediction of corrosion layer thickness and oxygen concentration profiles evolution.

3. Numerical calculations

The numerical calculations demonstrate that the consideration of the non-equilibrium boundary kinetics is most essential for the correct simulation of the oxygen stabilized alpha phase growth kinetics (Figs. 6 and 7).

This result is very important for the modeling of the cladding mechanical properties: crack propagation through the cladding, ballooning and burst of the cladding, etc., since the thickness of α-Zr(O) and β-Zr layers essentially determine cladding mechanical deformation behavior [2].

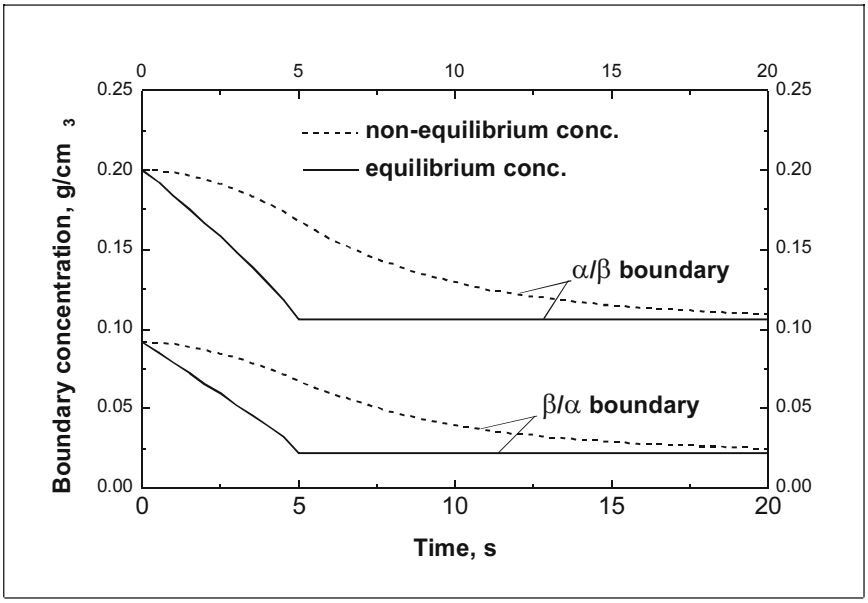

Fig.6. Boundary oxygen concentration variation during cooling from 1773 to 1273 K with 100 K/s.

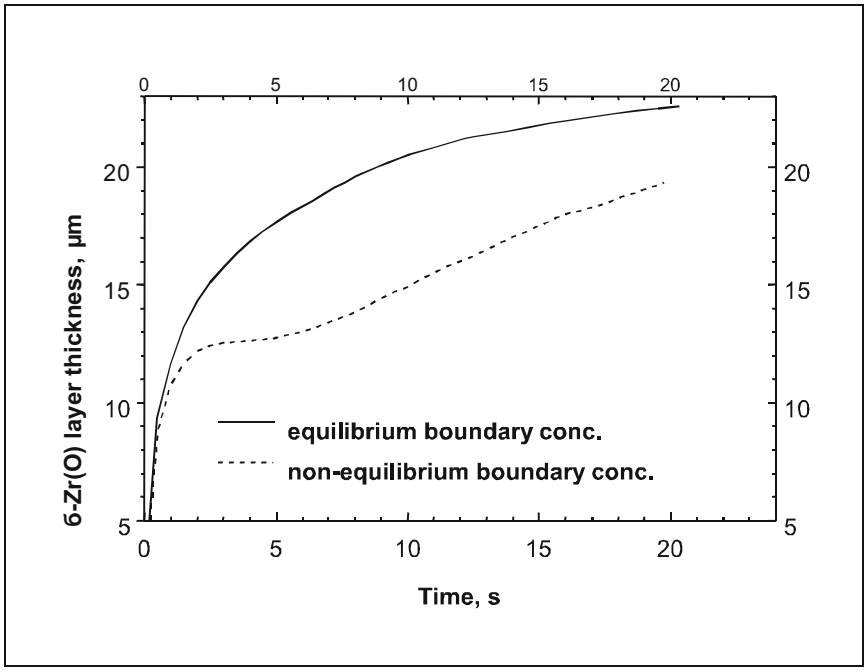

Fig. 7. α-Zr(O) layer growth kinetics during cooling from 1773 to 1273 K with 100 K/s.

In order to demonstrate an influence of a steep radial temperature gradient across the oxide layer ≈ 1 K/μm (such gradients are specific to the FZK quench tests [4], the comparison of the calculation results by the new advanced model and the simplified one [1-3] (using average temperatures in different cladding layers) was carried out.

It is seen that the simplified model can significantly overpredict the oxide layer thickness over a wide range of initial conditions and temperatures (Figs. 8 and 9).

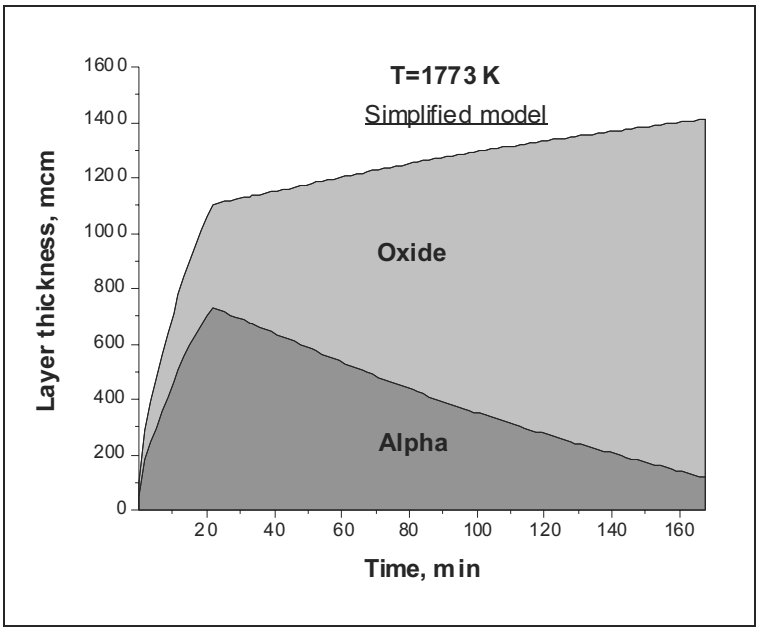

Fig. 8. Oxidation kinetics simulated by simplified model (diffusion coefficient is determined by the temperature averaged over the cladding layer $D = D(\bar{T})$ *).*

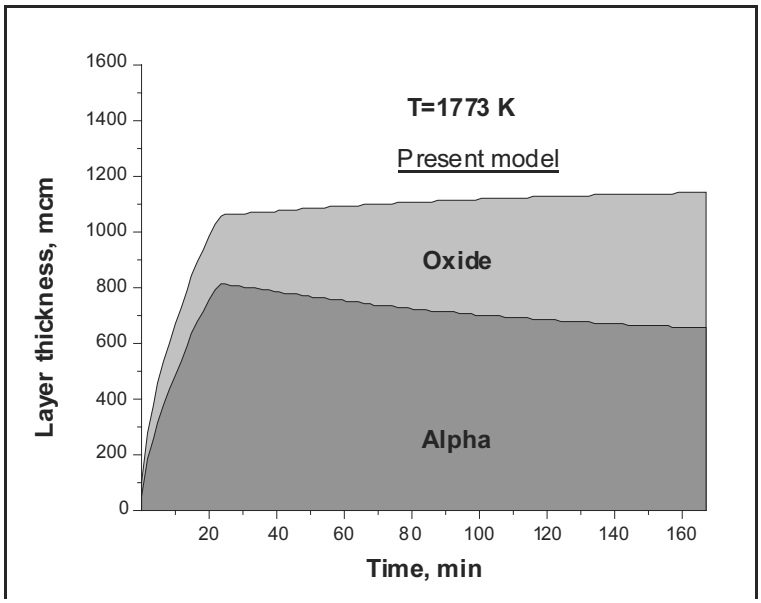

Fig. 9. Oxidation kinetics simulated by advanced model (diffusion coefficient depends on the temperature distribution inside the cladding layer $D = D\big(T(r)\big)$ *).*

4. Conclusions

Deficiencies of the simplified Zr oxidation model [1–3] which was developed for the description of oxidation kinetics under typical conditions of severe accidents, were revealed for extreme conditions of high-temperature quenching characterized by rather high cooling rates (>50 K/s) and steep radial temperature gradients across the cladding, on the basis of the theoretical estimations and experimental data obtained in the course of quench investigations [4]. For improvement of the oxidation kinetics calculations under conditions of fuel rod quenching by steam or water, the full range cladding oxidation model valid for arbitrary temperature transients is developed.

The model is based on the accurate system of partial derivative oxygen diffusion equations with non-equilibrium boundary conditions at the phase boundaries.

The moving boundary diffusion problem was reduced to the diffusion problem in a fixed region using a coordinate transformation. A fully implicit finite-difference method was employed to solve the diffusion equation for a one dimensional cylindrical geometry. Non-uniform space discretization and adaptive integration time step were incorporated in the numerical model. As a result, the obtained numerical model is fast and compact and quite appropriate for an implementation in the integral severe accident codes for the prediction of corrosion layer thickness and oxygen concentration profiles.

The numerical calculations demonstrated that a consideration of the non-equilibrium boundary kinetics is essential for the correct simulation of the oxygen stabilized alpha phase growth kinetics and, hence, for the accurate prediction of cladding mechanical properties: crack propagation through the cladding, ballooning and burst of the cladding, etc.

Comparison of the calculation results of the two oxidation models (full-range diffusion model presented in this report and simplified oxidation model [1-3]) under conditions of the radial temperature gradient across the oxide layer ≈1 K/μm observed in the quench tests [4] was made. It was demonstrated that predictions of the model can be significantly improved over a wide range of initial conditions if temperature of each layer is specified by an average value of temperature distribution in the relevant phase of the cladding. However, even if average temperatures of the reaction layers are used in the model, the cladding oxidation behavior predicted by the two models still remains quite different, especially at high cladding temperatures.

References

1. *M.S. Veshchunov, A.V. Palagin, A.M. Voltchek, N.V. Yamshchikov, A.V. Boldyrev*, Code package SVECHA: Core degradation at severe accidents, Transactions of SMiRT-13 Conference, Vol.1, pp.159-163, 1995.
2. *M.S. Veshchunov, A.V. Berdyshev, A.V. Boldyrev, L.V. Matweev, A.V. Palagin, V.E. Shestak*, Physico-Chemical Behavior of Zircaloy Fuel Rod Cladding Tubes During LWR Severe Accident Reflood. Part II: Modeling of quench phenomena, FZKA 5846, 1997.
3. *A.M. Voltchek, A.E .Kisselev, M.S. Veschunov*, Modelling of the Pellet/Cladding/Steam Interactions in the framework of the Oxygen Diffusion Theory (T<2273 K). NSI-SAAR-03-94, Moscow, 1994.
4. *P. Hofmann, V. Noack*, Physico-Chemical Behavior of Zircaloy Fuel Rod Cladding Tubes During LWR Severe Accident Reflood. Part I: Experimental Results of Single Rod Quench Experiments. FZKA 5846, 1997.
5. *F.C. Iglesias, S. Sagat, H.E. Sills*, Res. Mechanica, 17 (1986) 125.
6. *E. Gebhardt, G. Elssner*, Untersuchungen im System Zirconium-Sauerstoff, Teil 2. J. Nucl. Mater., 4 (1961) 255.
7. *A.V. Berdyshev, L.V. Matveev, M.S. Veshchunov*, Development of the Data Base for the Kinetic Model of the Zircaloy-4/Steam Oxidation at High Temperatures (1000 °C ≤T≤ 1825 ºC). Preprint IBRAE-97-05, Moscow, 1997.
8. *S. Leistikow, G. Schanz*, The Oxidation behavior of Zircaloy-4 in Steam between 600 and 1600 °C. Wekstoffe and Korrosion, 36 (1985) 105.
9. *P. Hofmann*, Chemical Interactions of Zircaloy-4 Tubing with UO_2 Fuel and Oxygen at temperatures between 900 and 2000 °C, Part1: Experimental results. KfK 4422, Kernforschungszentrum Karlsruhe, 1988.
10. *L. Yegorova, K. Lioutov, N. Jouravkova, A. Konobeev, V. Smirnov, V. Chesanov, A. Goryachev*, Experimental Study of Embrittlement of Zr-1%Nb VVER Cladding under LOCA-Relevant Conditions. NUREG/IA-0211, IRSN 2005-194, NSI RRC KI 3188. March 2005.

Models for Hydrogen Uptake and Release Kinetics by Zirconium Alloys at High Temperatures

M.S. Veshchunov, A.V. Berdyshev

1. Introduction

Hydrogen absorption by zirconium alloys in various atmospheres is studied in the last four decades since the primary concern of this process is the embrittlement which it might cause during pressurised water reactors normal operation (see, for example review [1]). There are two possible routes of hydrogen absorption by Zr cladding; first, direct reaction with molecular hydrogen (gaseous hydriding), and second, absorption of hydrogen liberated by the decomposition of water or steam during the oxidation process and absorbed as part of the oxidation mechanism. These two mechanisms are considered in Sections 2 and 3 of the present paper.

In many real cases, especially under conditions of fuel element quenching by water, both these mechanisms should be considered simultaneously and self-consistently, since in this case Zr cladding interacts with the steam/hydrogen containing gas mixture and the two mechanisms act competitively. For these reasons, a more detailed model considering the general situation and including both mechanisms as the limiting cases, is developed in Section 4.

2. Hydrogen uptake by zirconium alloys in hydrogen atmosphere

Kinetics of the hydrogen uptake and release by Zircaloy-4 (along with its solubility limits) at high temperatures has been recently specially studied by M. Steinbrueck in the FZK in separate-effect tests [2].

Specimens investigated in the tests [2] were Zry-4 cladding tube segments. The tests were performed in a small STA (Simultaneous Thermal Analysis) facility coupled with a mass spectrometer. The furnace of the STA facility was designed for temperatures up to 1600 °C. A sophisticated gas supply system provided various argon/hydrogen mixtures with hydrogen content between 0 and 100 %. The hydrogen solubility of Zry-4 in dependence on temperature (950-1450 °C) and hydrogen partial pressure (0-1 bar) was investigated along with kinetics of the uptake and release processes. It was found in the tests with hydrogen partial pressure increase from 0 to 0.5 bar and subsequent decrease from 0.5 to 0 bar, that the uptake and release of hydrogen by Zircaloy was a reversible process but non-symmetrical in time. The hydrogen uptake was rather a rapid process, thus, measured mass increase of a sample due to hydrogen uptake occurs practically simultaneously with growth of the hydrogen partial pressure in the gas mixture. The hydrogen release in these tests, however, was characterized by a comparatively large time delay after the hydrogen partial pressure drop.

A kinetic model describing experimental observations of hydrogen interactions with metal Zry in the FZK tests is presented in the following subsections.

2.1. Model description

Gas flow under experimental conditions is described by the model within an approximation of a constant and homogeneous pressure in the gas phase. This approximation is well grounded, since the process of the pressure homogenization is the most rapid transfer

process in the system and has the characteristic time $\tau_p \sim d/C_S \sim 10^{-4}$ s ($d \sim 1$ cm is a characteristic hydraulic diameter and $C_S \sim 10^4$ cm/s is the sound velocity in the gas mixture). In the experiments [2], considerable hydrogen absorption or release take place, hence, in order to afford constant total pressure in the gas, an additional convective flow across the gas hydraulic channel (Stefan flow) occurs. Therefore, mass fluxes of hydrogen and argon in the diffusion boundary layer of the gas phase near the metal surface take the form:

$$J^{(H_2)} = J_D^{(H_2)} + J_{St}^{(H_2)} = k_{H_2}(c_{H_2}(s) - c_{H_2}(b)) - v_{St} c_{H_2}(s), \quad (1)$$

$$J^{(Ar)} = J_D^{(Ar)} + J_{St}^{(Ar)} = k_{Ar}(c_{Ar}(s) - c_{Ar}(b)) - v_{St} c_{Ar}(s), \quad (2)$$

where $c_i = P_i/RT$ is the molar density of the i-th component in the gas mixture with corresponding partial pressure P_i; R is the gas constant and T is the gas temperature; indices s and b designate values near the oxide surface and in the bulk of the gas phase (outside the diffusion boundary layer), respectively, v_{St} is the velocity of the Stefan convection flow which affords constant total pressure in the gas, $P_{tot} = P_{H_2} + P_{Ar} = 1$ bar; k_{H_2} is the mass transfer coefficient of hydrogen in the gas phase.

Since the diffusion of Ar and H_2 takes place under conditions of the constant total pressure, the corresponding diffusion fluxes must locally compensate each other:

$$J_D^{(H_2)} = -J_D^{(Ar)}. \quad (3)$$

Flux matches for the two gas components at the metal surface take the form:

$$J_D^{(H_2)} + J_{St}^{(H_2)} = 0.5 J_{sol}^{(H)}, \quad (4)$$

$$J_D^{(Ar)} + J_{St}^{(Ar)} = 0, \quad (5)$$

where $J_{sol}^{(H)} = -D_H \left.\frac{\partial C_H}{\partial x}\right|_S$ is the hydrogen boundary diffusion flux in the solid phase, D_H is the diffusion coefficient of hydrogen atoms in the metal. From Eqs. (4) and (5) it follows:

$$2k_{H_2}\left(c_{H_2}(b) - c_{H_2}(s)\right) = D_H \left.\frac{\partial C_H}{\partial x}\right|_S \frac{\left(c_{tot} - c_{H_2}(s)\right)}{c_{tot}}, \quad (6)$$

where $c_{tot} = c_{H_2} + c_{Ar} = P_{tot}/RT$ is a constant value. Near the gas/solid interface, hydrogen concentration in the solid state and hydrogen partial pressure in the gas phase are related by the Sieverts law:

$$P_{H_2}^2(s) = K_S C_H(s), \quad (7)$$

where K_S is the Sieverts constant.

Substitution of Eq. (7) into Eq. (6) finally leads to:

$$D_H \left.\frac{\partial C_H}{\partial x}\right|_S = \frac{2k_{H_2}}{RT} \frac{P_{tot}}{\left(P_{tot} - P_{H_2}(s)\right)} \left(P_{H_2}(b) - \frac{C_H^2(s)}{k_s^2}\right). \quad (8)$$

Hydrogen concentration distribution in the solid phase is found from the diffusion equation

$$\frac{\partial C_H}{\partial t} = D_H \frac{\partial^2 C_H}{\partial x^2} \quad (9)$$

with the boundary condition Eq. (8) at the outer and at the inner surfaces of the tube.

Under real experimental conditions of the FZK tests, gas flows inside and outside of the Zircaloy tube might be significantly different and their accurate description becomes rather a complicated problem. In the present work, a simplified approach to this problem is used, in which an effective mass transfer coefficient of hydrogen in the gas phase is considered as an unknown fitting parameter.

2.2. Qualitative analysis of the model

For the qualitative analysis of the kinetics of hydrogen absorption/desorption by the metal zirconium, which can be performed on the basis of analytical consideration, a further simplification of Eqs. (8) and (9) can be attained using the following additional assumptions:

1. Zirconium layer is rather thin, so that the characteristic hydrogen diffusion time in the solid phase $\tau_D \approx L^2/D_{\rm H}$ (L is the thickness of the solid phase) is much smaller than the characteristic time of the mass transfer in the gas phase $\tau_g \approx \left(L/4k_{\rm H_2}\right)C_{Zr}/C_{\rm H_2}(b)$ ($C_{\rm Zr}$ is the zirconium molar density);
2. $P_{tot}/\left(P_{tot}-P_{H_2}(s)\right)\approx 1$, since this assumption does not strongly influence the final results of calculations by the complete numerical model (as will be seen further).

The first assumption allows consideration of hydrogen spatial distribution in the metal as a constant value depended only on time. In such a case, integration of Eq. (9) on the spatial coordinate across the metal phase and substitution of the boundary condition, Eq. (8), lead to the ordinary differential equation:

$$\frac{L}{2}\frac{dC_{\rm H}(s)}{dt}=\frac{2k_{\rm H_2}}{RT}\left[P_{\rm H_2}(b)-\frac{C_{\rm H}^2(s)}{k_s^2}\right] \qquad (10)$$

For the case of hydrogen absorption, when hydrogen partial pressure in the gas phase changes stepwise from zero to $P_{\rm H_2}(b)$ and metal zirconium is initially free of hydrogen, $C_{\rm H}(s,t{=}0){=}\,0$, solution of Eq. (10) has the form:

$$C_{\rm H}(s)=k_s^2P_{\rm H_2}(b)\frac{1-\exp(-2t\gamma)}{1+\exp(-2t\gamma)}, \quad (11)$$

where $\gamma=4\left(k_{\rm H_2}/L\right)\left(1/RTK_S^2\right)$.

The kinetics of hydrogen release is considered for a zirconium sample which is initially in equilibrium with the gas mixture with a finite hydrogen partial pressure and, hence, contains some hydrogen, $C_{\rm H}(t=0)=C_{\rm H,0}$, in accordance with the Sieverts law. Then, in accordance with experimental procedure the hydrogen partial pressure in the gas drops to zero and the system commences to relax to a new equilibrium state. This process is described by Eq. (10) with $P_{{\rm H}_2,g}(b)=0$:

$$\frac{dC_{\rm H}(s)}{dt}=-\frac{4k_{\rm H_2}}{LRT}\frac{C_{\rm H}^2(s)}{k_s^2}, \qquad (12)$$

which has the following solution:

$$C_{\rm H}(s)=\frac{C_{\rm H,0}}{1+\gamma t}. \qquad (13)$$

As one can see from the comparison of the solutions Eqs. (11) and (13), the hydrogen uptake and release occur in different ways. The hydrogen release is described by a slow hyperbolic function of time, whereas the hydrogen uptake obeys a rapid exponential time law.

It should be emphasized, that the hyperbolic time law, Eq. (13), of the hydrogen release from zirconium sample is valid only in one particular case, namely, when the hydrogen partial pressure $P_{\rm H_2}(b)$ in the gas flow drops exactly to zero; otherwise, the system during hydrogen desorption is described by Eq. (10) with non-zero value of $P_{\rm H_2}(b)$ and relaxes to the new equilibrium state exponentially. Hence, the model predicts that in possible tests with the gas hydrogen partial pressure drop to non-zero value, the kinetics of hydrogen absorption and release will be more similar and obey the same exponential time law.

2.3. Numerical calculations

The diffusion equation, Eq. (9), with the boundary conditions, Eq. (8), is numerically solved by the finite-differences method with the following set of the parameters:

$$D_{\rm H}=6.3\cdot10^{-3}\cdot\exp(-4250/T[{\rm K}])\ {\rm cm^2/s}\ [3],$$
$$K_{\rm S}=1.4\cdot10^{-3}\cdot\exp(8102.7/T[{\rm K}])\ {\rm atom\ ratio/atm^{1/2}}\ [2],$$
$$k_{\rm H_2}=4\ {\rm cm/s}\ \text{(fitting to the experimental data [2])}.$$

The calculated kinetics of hydrogen absorption and desorption by the Zircaloy tube segment is presented in Fig. 1. In this calculations the temperature decreased from 1150 to 1050 °C and the hydrogen partial pressure varied in the interval 0-0.5 bar, in accordance with the experimental conditions [2]. The calculated behavior of the system is fairly close to that observed in the experiments and corresponds to the qualitative consideration.

As was explained in the previous section, asymmetrical behavior of the system during absorption and release stages can be attained if the hydrogen partial pressure drops to non-zero value during the release stage. This analytical prediction was fairly confirmed by the subsequent FZK tests (specially designed to check this model prediction), as shown in Fig. 2, where calculation results are presented for the case when the hydrogen partial pressure is varied in the interval 0.2–0.5 bar.

3. Hydrogen uptake by zirconium alloys during high-temperature oxidation in steam

As shown in [1], in parallel with the oxide film formation process in water or steam, a fraction of the hydrogen generated by decomposition of the water entered the metal. The relationship between the amount of oxidation occurring and the amount of hydrogen absorbed is not a simple function, although it follows a characteristic pattern which seems to be general for all zirconium alloys, provided the analytical technique is sensitive enough to distinguish changes in the "uptake fraction" (that fraction of the hydrogen liberated by the corrosion process during any time period and which is absorbed by the metal).

The model of hydrogen absorption by Zr alloys during oxidation in steam was developed by the authors in [4]. It is essentially based on the experimental results of the KFKI (Hungary) tests [5] on the kinetics of hydrogen absorption by Zr1%Nb cladding during steam oxidation in the temperature range from 900 to 1200 ºC. The model corresponds to a particular case of a more general model presented in Section 5, for this reason, only main results will be presented in the current Section.

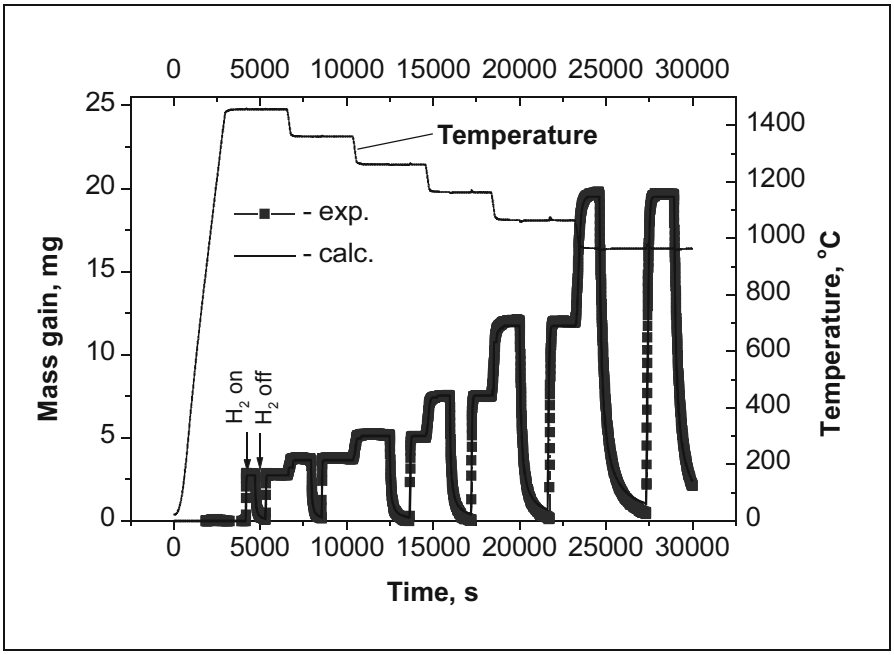

Fig. 1. Simulation of FZK tests [2] on H_2 uptake by Zry-4 tube segment: P_{H_2} = 0/0.5 bar.

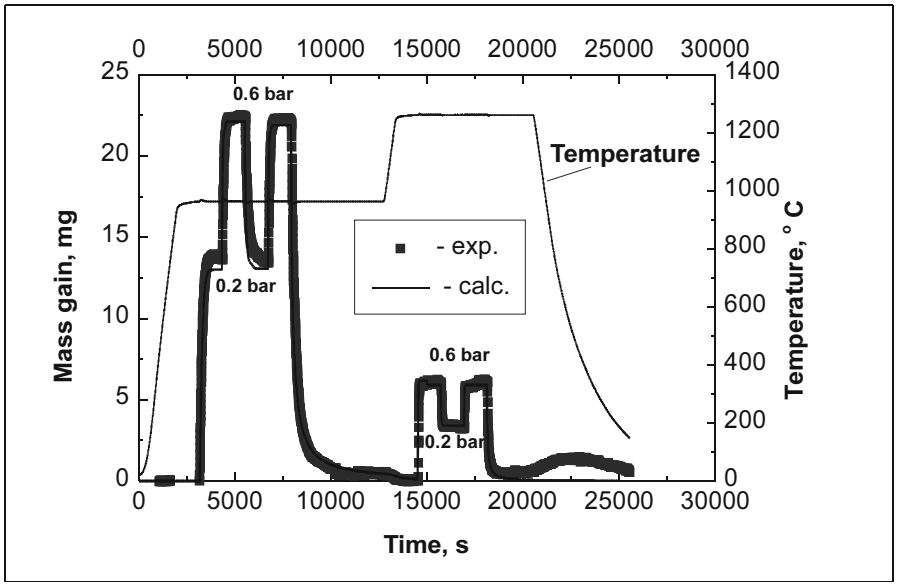

Fig. 2. Simulation of FZK tests [2] on H_2 uptake by Zry-4 tube segment: P_{H_2} = 0.2/0.6 bar.

The model takes into account that hydrogen may intrude into oxide in result of H_2O dissolution process in the form of positively charged protons. Discharge of protons by electrons occurs at the oxide/metal interface (rather than at the gas/oxide interface as considered in the standard approach) after diffusion transporting of highly mobile protons through the oxide scale.

For quantitative description of hydrogen behavior by this mechanism, mass transfer in the three layers: gas, oxide and metal, and at corresponding interfaces: gas/oxide and oxide/metal, is considered. The obtained system of equations explains the main features of the observed complicated kinetics of hydrogen uptake: (i) continuous increase of hydrogen concentration in the metal phase being roughly proportional to the oxidation mass gain, in the initial stage of the process; (ii) desorption of hydrogen to the gas phase accompanied by slow decrease of measured hydrogen concentration in the metal phase, in the late stage of the process; (iii) decrease of maximum hydrogen concentration in Zr attained at the absorption/desorption regime transformation, with temperature increase.

Numerical solution of the problem generally confirms the main conclusions of the simplified analytical treatment and furnishes a satisfactory fitting between measured kinetic curves [5] and calculations. Comparison of the experimental data and numerical calculations are presented in Figs. 3 and 4.

4. Hydrogen Uptake by Zirconium Alloys in Steam/Hydrogen Gas Mixtures

As explained in Section 2, there are two possible routes of hydrogen absorption by Zr cladding; first, direct reaction with molecular hydrogen, or gaseous hydriding (modeled in Section 3), and second, absorption of hydrogen liberated by the decomposition of water or steam during the oxidation process and absorbed as part of the oxidation mechanism (modeled in Section 4).

A more detailed model considering the general situation and including both mechanisms as the limiting cases, is developed in this Section. For this purpose the model [4] briefly presented in Section 4 is extended to the case of ternary gas mixtures ($H_2/H_2O/Ar$). The improved in such a way model is validated against experimental data [6]. In the experimental work [6] oxygen and hydrogen uptake by Zircaloy cladding segments in $H_2/H_2O/Ar$ gas flow was investigated.

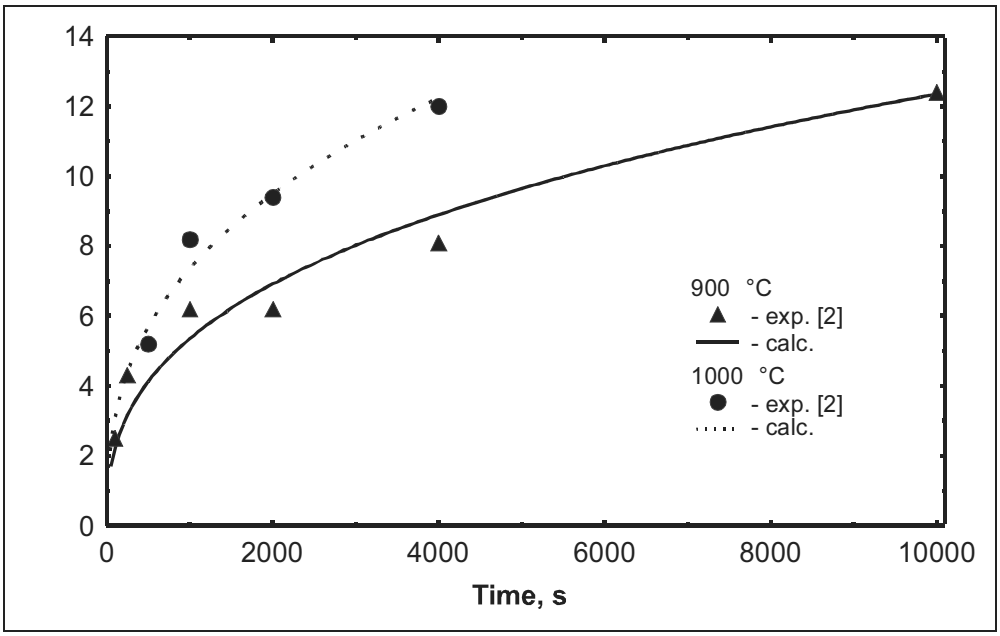

Fig. 3. Simulations of KFKI tests [5] on Zr/steam interactions at 900 and 1000 °C.

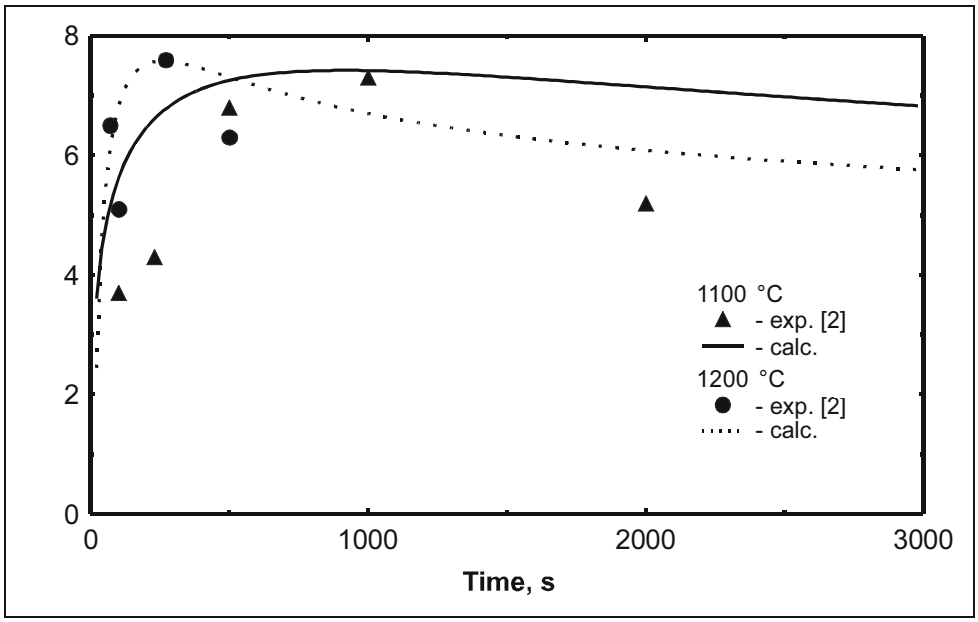

Fig. 4. Simulations of KFKI tests [5] on Zr/steam interactions at 1100 and 1200 °C.

4.1. Modeling of hydrogen uptake

As in the previous consideration [4], the mass transfer in the three layers: gas, oxide and metal, and at corresponding interfaces: gas/oxide and oxide/metal, are considered. In the present case the gas phase comprises the hydrogen/steam/argon mixture with some arbitrary molar ratio of the three components: H_2 :H_2O:Ar= X:Y:1.

4.1.1. Mass transfer in the gas phase

Under conditions of considerable hydrogen absorption, the convection (Stefan) flows in the gas should be taken into consideration. Correspondingly, mass fluxes of the four gas components (steam, hydrogen, oxygen and argon) take the form:

$$J_i^{(g)} = k_i(c_i(s) - c_i(b)) - vc_i(s), \quad (14)$$

where $i = 1, 2, 3, 4$ denote H_2, O_2, H_2O, and Ar, respectively; $c_i=P_i/RT$ is the molar density of the ith component in the gas mixture with corresponding partial pressure P_i ; indices s and b designate values near the oxide surface and in the bulk of the gas phase (outside the diffu-

sion boundary layer), respectively; v is the velocity of the convection flows which afford constant total pressure in the gas, $P_{\rm tot} = P_{\rm H_2O} + P_{\rm H_2} + P_{\rm O_2} + P_{\rm Ar} = 1$ bar.

In order to calculate these fluxes, one should determine boundary conditions for the partial pressures P_i of various components on the two faces of the diffusion boundary layer: at the gas/oxide interface and in the bulk of the gas phase. On the gas/oxide interface the boundary conditions can be represented in the form of the system of equations:

$$P_{\rm H_2O}(s) + P_{\rm H_2}(s) + P_{\rm O_2}(s) + P_{\rm Ar}(s) = P_{\rm tot}, \quad (15)$$

$$P_{\rm H_2O}(s) = kP_{\rm H_2}(s)P_{\rm O_2}^{1/2}(s), \quad (16)$$

$$P_{\rm O_2}(s) = P_{\rm O_2}(x) = \exp\left(-6\ln x + 2.58 - 136000/T\right), \quad (17)$$

where Eq. (16) corresponds to the mass action law for the reaction of the steam dissociation $H_2O = H + (1/2)O_2$, with $k = \exp(-6.61+29600/T)$; and Eq. (17) determines the dependence of the oxygen partial pressure of ZrO_{2-x} on stoichiometry deviation x, being in equilibrium with the gas phase at the interface (e.g. see [7]).

On the other boundary of the diffusion layer in the bulk of the gas phase the boundary conditions have the form:

$$P_{\rm H_2O}(b) + P_{\rm H_2}(b) + P_{\rm O_2}(b) + P_{\rm Ar}(b) = P_{\rm tot}, \quad (18)$$

$$P_{\rm H_2O}(b) = kP_{\rm H_2}(b)P_{\rm O_2}^{1/2}(b), \quad (19)$$

$$P_{\rm H_2}(b) = P_{\rm H_2}^{(0)}(b) + 2P_{\rm O_2}(b), \quad (20)$$

$$P_{\rm Ar}(b) = P_{\rm Ar}^{(0)}(b), \quad (21)$$

where superscript '0' denotes values at the entrance of the gas channel. For simplicity here it is assumed that the bulk gas volume is infinitely large; a more realistic approach is presented below in Section 4.5.

The system of Eqs. (18)-(21) determines the values of the partial pressures $P_i(b)$ in the bulk, whereas the system of Eqs. (15)-(19) is not sufficient for determination of the surface values $P_i(s)$. In order to calculate these values, the system of Eqs. (15)-(17) should be combined with the flux matching conditions for the components at the oxide surface:

$$k_1\left(c_1(s) - c_1(b)\right) - vc_1(s) = J_{\rm diss} - (1/2)J_{\rm H}^{(\rm ox)}, \quad (22)$$

$$k_2\left(c_2(s) - c_2(b)\right) - vc_2(s) = (1/2)J_{\rm diss} - (1/2)J_{\rm O}^{(\rm ox)}, \quad (23)$$

$$k_3\left(c_3(s) - c_3(b)\right) - vc_3(s) = -J_{\rm diss}, \quad (24)$$

$$k_4\left(c_4(s) - c_4(b)\right) - vc_4(s) = 0, \quad (25)$$

where $J_{\rm diss}$ specifies dissociation flux of the H_2O molecules on the oxide surface, $J_{\rm H}^{(\rm ox)}$ and $J_{\rm O}^{(\rm ox)}$ are diffusion fluxes of the two components (hydrogen and oxygen, respectively) in the oxide phase surface (see [4]).

Since only three amongst the four variables c_i are independent ($c_1+c_2+c_3+c_4 = P_{\rm tot}/RT$), the multicomponent Stefan-Maxwell equations for their interdiffusion fluxes result in a simple relationship:

$$k_4\left(c_4(s) - c_4(b)\right) = -\left[k_1\left(c_1(s) - c_1(b)\right) + k_2\left(c_2(s) - c_2(b)\right) + k_3\left(c_3(s) - c_3(b)\right)\right]. \quad (26)$$

Superposition of Eqs. (22)-(25) yields a relationship for the convection velocity in the gas:

$$v = \left(RT/2P_{tot}\right)\left(J_O^{(ox)} + J_H^{(ox)} - J_{diss}\right). \quad (27)$$

Taking into account that the oxygen flux in the gas phase can be generally neglected in comparison with the hydrogen and steam fluxes (owing to $\Delta P_{O_2} << \Delta P_{H_2}, \Delta P_{H_2O}$), the system of Eqs. (22)-(27) can be simplified and reduced to the final relationship:

$$k_1\left(c_1(s)-c_1(b)\right)+\left(1/2\right)J_{\mathrm{H}}^{(\mathrm{ox})}\left(P_{\mathrm{H_2O}}(s)+P_{\mathrm{Ar}}(s)\right)\Big/P_{\mathrm{tot}}=J_{\mathrm{O}}^{(\mathrm{ox})}. \quad (28)$$

4.1.2. Mass transfer through the oxide/gas interface

The derived Eq. (28) determines a relationship between the fluxes of various components in the gas and solid phases. In order to calculate these fluxes, it is necessary to determine relationships between concentrations of these components at the oxide/gas interface.

In accordance with [4], the following chemical reactions at the gas/oxide interface can be regarded as equilibrium:

- dissolution of water molecules at the oxide surface:
  $H_2O(g) + V_O^{2+} = 2H_{ab}^{+} + O_O(ox)$;
- oxygen transition from the oxide to the gas phase:
  $2O_O(ox) = O_2(g) + 2V_O^{2+} + 4e_\beta(ox/g)$;
- dissolution of hydrogen in the oxide in the form of positively charged protons:
  $H_{ab}^{+}(ox) + e_\beta(ox/g) = (1/2)H_2(g)$;
- dissolution of hydrogen in the oxide in the form of neutral atoms:
  $H_{ab}(ox) = (1/2)H_2(g)$.

Correspondingly, for each of these equilibrium reactions the mass action law can be applied:

$$P_{\mathrm{H_2O}}\left(s\right)C_v=\alpha C_{\mathrm{H+}}^2, \quad (29)$$

$$P_{\mathrm{O_2}}\left(s\right)C_v^2C_e^4=\beta, \quad (30)$$

$$C_{\mathrm{H+}}^2=\gamma\,P_{\mathrm{H_2}}\left(s\right)\Big/C_e^2, \quad (31)$$

$$C_{\mathrm{H}}=K_{\mathrm{S}}P_{\mathrm{H_2}}^{1/2}\left(s\right), \quad (32)$$

where α, β, γ, K_S are the equilibrium constants of the corresponding chemical reactions, C_v, C_e, C_{H+}, C_H are concentrations of anion vacancies V_O^{2+}, electrons, protons and neutral hydrogen atoms in the oxide near the interface, respectively.

Superposition of Eqs. (29)-(31) with Eq. (16) leads to an additional relationship amongst the equilibrium reaction constants:

$$k\beta^{1/2}/\alpha\gamma=1. \quad (33)$$

The charge neutrality condition at the interface completes the defect relations:

$$2C_v + C_{\mathrm{H+}} = C_e. \quad (34)$$

Equations (29)-(31) substituted into Eq. (34) yield:

$$\left(2\alpha C_{\mathrm{H+}}^3\Big/P_{\mathrm{H_2O}}\left(s\right)\right)+C_{\mathrm{H+}}^2-\left(k\beta^{1/2}/\alpha\right)^{1/2}P_{\mathrm{H_2}}^{1/2}\left(s\right)=0. \quad (35)$$

In the first limiting case, $P_{\mathrm{H_2}} << P_{\mathrm{H_2O}} \approx P_{\mathrm{tot}}$, solution of Eq. (35) yields $C_{\mathrm{H+}} \propto P_{\mathrm{H_2}}^{1/4}\left(s\right)$ (see [4]), therefore, since $C_{\mathrm{H}} \propto P_{\mathrm{H_2}}^{1/2}\left(s\right)$ (see Eq. (32)), one gets $C_H << C_{H+}$. For this reason, the input of the neutral hydrogen atoms in the hydrogen transport in the oxide phase can be neglected in this case. In the opposite limiting case, $P_{\mathrm{H_2O}} << P_{\mathrm{H_2}} \approx P_{\mathrm{tot}}$, from Eq. (35) one gets $C_{\mathrm{H+}} \propto P_{\mathrm{H_2}}^{1/6}\left(s\right)P_{\mathrm{H_2O}}^{1/3}\left(s\right)$, therefore, $C_H >> C_{H+} \to 0$, and the input of protons in the hydrogen transport in the oxide phase can be neglected, in accordance with observations [8]. In the general case both the inputs of the neutral and charged atoms should be considered.

4.1.3. Mass transfer in the oxide phase

Under an assumption that a relatively small amount of hydrogen dissolved in oxide practically does not influence the stoichiometric composition of its surface [4], the oxygen flux in the oxide phase can be presented in the standard form:

$$J_{\mathrm{O}}^{(\mathrm{ox})}=D_{\mathrm{O}}^{(\mathrm{ox})}\,\Delta C_{\mathrm{O}}/\delta(t), \quad (36)$$

where $D_{\mathrm{O}}^{(\mathrm{ox})}$ is the oxygen diffusivity in the oxide, ΔC_O is the oxygen concentration fall

across the oxide layer, $\delta(t)$ is the oxide layer thickness determined by the self-consistent solution of the oxygen diffusion problem in the multilayered system (gas/oxide/metal).

Analogously, the hydrogen flux in the oxide layer depends on the protons and neutral atoms concentration falls $\Delta C_{H+} = C_{H+}(s) - C_{H+}(b)$ and $\Delta C_H = C_H(s) - C_H(b)$ across this layer:

$$J_O^{(ox)} = D_{H+}^{(ox)} \Delta C_{H+} / \delta(t) + D_H^{(ox)} \Delta C_H / \delta(t), \quad (37)$$

where $D_{H+}^{(ox)}$ and $D_H^{(ox)}$ are the hydrogen ion (proton) and neutral atom diffusivities in the oxide, respectively; $C_{H+}(s)$ and $C_H(s)$) denote hereafter the protons and neutral atoms concentrations, respectively, at the gas/oxide interface (denoted above as C_{H+} and C_H), whereas $C_{H+}(b)$ and $C_H(b)$ denote the concentrations at the oxide/metal interface.

As noticed in [8], the value of $D_{H+}^{(ox)}$ has the same order of magnitude as $D_O^{(ox)}$ (estimated at 900 and 1000 °C as $\approx 8 \cdot 10^{-7}$ and $1.3 \cdot 10^{-6}$ cm^2/s, respectively). On the contrary, the value of $D_H^{(ox)}$ was evaluated in the bulk oxide slabs as negligibly small [8]. However, it is known from the literature (e.g. [1]) that very thin oxide layers (up to 1-2 μm) grown on the metal substrate are rather transparent for the hydrogen atoms (this might be associated with a different structure of initial layers loaded to high stresses at the metal/oxide interface). A similar conclusion can be derived from the observations [6, 9], that the mass gain of the Zr cladding in the steam/hydrogen mixtures starved with steam can be attributed to the hydrogen absorption in the initial period of cladding oxidation.

Therefore, in the present model an assumption (consistent with the above mentioned observations) is made that some critical thickness $\Delta \sim 1$ μm of the growing oxide layer exists, which separates two different regimes of the neutral hydrogen atom mobility in oxide. For layers thinner than this critical value, the diffusivity $D_H^{(ox)}$ will be considered as a finite value which can be evaluated from the analysis of the above mentioned tests [6, 9]. For thicker layers the mobility of neutral atoms will be neglected in comparison with that of protons.

An alternative assumption can be also made that some critical non-stoichiometry of oxide at the interface with the gas phase is responsible for the high values of the neutral hydrogen atom mobility in oxide. In the case of a growing oxide layer this assumption (on the critical substoichiometry) is equivalent to the first one (on the critical oxide thickness), however, in some important cases (e.g. "chemical thinning" of oxide under steam starved conditions) it extends an applicability range of the neutral atom diffusivity model to thicker oxide layers.

4.1.4. Mass transfer through the oxide/metal interface

For the quantitative description of the hydrogen uptake, additional equations determining hydrogen behavior at the oxide/metal interface were derived in [4], which resulted in a simple linear relations between the interface proton concentration in the oxide, $C_{H+}(b)$, and the hydrogen concentration in the α-layer of the metal phase, $C_H^{(\alpha)}$:

$$C_{H+}(b) = \lambda C_H^{(\alpha)}. \quad (38)$$

A similar equation for the neutral hydrogen concentration at the oxide/(α-layer) interface was derived:

$$C_H(b) = \lambda_1 C_H^{(\alpha)}, \quad (39)$$

where λ and λ_1 are the equilibrium constants.

Therefore, Eq. (38) and/or Eq. (39) determine the boundary conditions for the hydrogen diffusion problem in the metal α-phase which may be considered as a quasi-one dimensional problem due to a small thickness of the cladding wall in comparison with its radius:

$$\partial C_H^{(\alpha)} / \partial t = D_H^{(\alpha)} \partial^2 C_H^{(\alpha)} / \partial x^2, \quad (40)$$

where $D_H^{(\alpha)}$ is the hydrogen diffusivity in the metal α-phase. A similar to Eq. (40) equation can be written for the hydrogen diffusion in the β-phase of Zr cladding:

$$\partial C_H^{(\beta)} / \partial t = D_H^{(\beta)} \partial^2 C_H^{(\beta)} / \partial x^2, \quad (41)$$

where $D_H^{(\beta)}$ is the hydrogen diffusivity in the metal β-phase. The corresponding boundary condition at the interface between the two metal phases takes the form:

$$C_H^{(\beta)} = \lambda_2 C_H^{(\alpha)}, \quad (42)$$

where the equilibrium constant λ_2 determines the ratio of the two Sieverts constants for hydrogen in the β- and α-phase of the cladding, taken from, e.g. [2, 3]:

$$\lambda_2 = K_S^{(\beta)} / K_S^{(\alpha)}. \qquad (43)$$

The dependence of the Sieverts constant for the α-phase on the oxygen content observed in [3] will be neglected here for the sake of simplicity and, instead of this, the mean value will be used.

In the initial stage of the Zr cladding interactions with steam starved H_2/H_2O mixtures, one should consider the complete system of Eqs. (38)-(43). In other cases, one can simplify the problem and with a sufficient accuracy consider hydrogen distribution in each metal phase as homogeneous, taking into account that $D_H^{(\alpha)}$, $D_H^{(\beta)}$ are several orders of magnitude larger than the proton diffusivity in the oxide $D_{H+}^{(ox)}$ [3]:

$$C_H^{(\alpha,\beta)}(x,t) \approx C_H^{(\alpha,\beta)}(t). \qquad (44)$$

In this case the solution of the diffusion problem in the metal phase is reduced to the hydrogen balance equation (under one-side oxidation conditions):

$$\begin{aligned} &d\left(L_\alpha(t)C_H^{(\alpha)}\right)/dt + d\left(L_\beta(t)C_H^{(\beta)}\right)/dt = \\ &= -J_H^{(ox)} - d\left[\delta(t)\left(C_{H+}(s) + C_{H+}(b)\right)\right]/2dt, \end{aligned} \qquad (45)$$

where $L_{\alpha(\beta)}(t)$ is the α (β) — metal layer thickness (calculated by the oxidation model), $J_O^{(ox)}$ is determined by Eq. (37).

Under steam starved conditions in the case of the complete disappearance of the oxide layer, the Sieverts law for the outer α-layer of cladding provides the boundary condition for the diffusion problem:

$$C_H^{(\alpha)} = K_S^{(\alpha)} P_{H_2}^{1/2}(s), \qquad (46)$$

instead of Eq. (39). The consideration of such a problem generalises the analysis of the gaseous hydriding of pure β-Zr cladding, presented in [4].

4.2. Numerical realization of hydriding model

In the present model to simplify the problem solution the alpha and beta zirconium phases of the cladding were considered as one metal layer characterised by the average hydrogen content.

The final system of the numerically investigated equations has the following form:

$$d\left(L_m(t)C_{H+}(b)/\lambda\right)/dt = L_g J_H^{(ox)} - L_g\, d\left[\delta(t)\left(C_{H+}(s) + C_{H+}(b)\right)\right]/2dt, \qquad (47)$$

$$\left(2\alpha C_{H+}^3 / P_{H_2O}(s)\right) + C_{H+}^2 - A^2 (RT)^{-1/2} P_{H_2}^{1/2}(s) = 0, \qquad (48)$$

$$P_{tot} = P_{H_2O}(s) + P_{H_2}(s) + P_{O_2}(s) + P_{Ar}(s), \qquad (49)$$

$$k_4\left[P_{Ar}(s) - P_{Ar}(b)\right]/RT - \left(P_{Ar}(s)/2P_{tot}\right) J_H^{(ox)} = 0, \qquad (50)$$

$$k_1\left[P_{H_2}(s) - P_{H_2}(b)\right]/RT + \left[\left(P_{H_2O}(s) + P_{Ar}(s)\right)/2P_{tot}\right] J_H^{(ox)} = J_O^{(ox)}, \qquad (51)$$

where L_g = 1 or 2 for one-side or two-side cladding hydriding, respectively; the parameter A in Eq. (48) is determined by the relationship: $A^2 (RT)^{-1/2} = \left(k\beta^{1/2}/\alpha\right)^{1/2}$ and corresponds to that introduced in [4]; $L_m(t) = L_0 - L_g \delta(t)/1.5$ is the metal layer thickness (L_0 is the cladding thickness).

The system of equations (47)-(51) was reduced to the non-linear system of algebraic equations by usual implicit finite-difference time discretization. The obtained system of equations is solved by the Newton algorithm at each time step.

In order to demonstrate the influence of the gas composition on the hydrogen absorption, the same external conditions (temperature and gas pressure) as in the experiments [5] were considered. The results of the calculations of hydrogen absorption by the Zr1%Nb cladding in the gas mixtures with different H_2/H_2O ratio derived in [4] are presented in Fig. 5. As follows from these results, dilution of steam by hydrogen initially leads to the increase of the hydrogen absorption by the cladding. At some H_2/H_2O ratio the hy-

drogen absorption attains its maximum value and then decreases. For the steam content in the gas mixture lower than 1%, the hydrogen absorption by the cladding becomes comparable with that in the pure steam atmosphere, and continues to decrease with the further decrease of the steam content in the mixture.

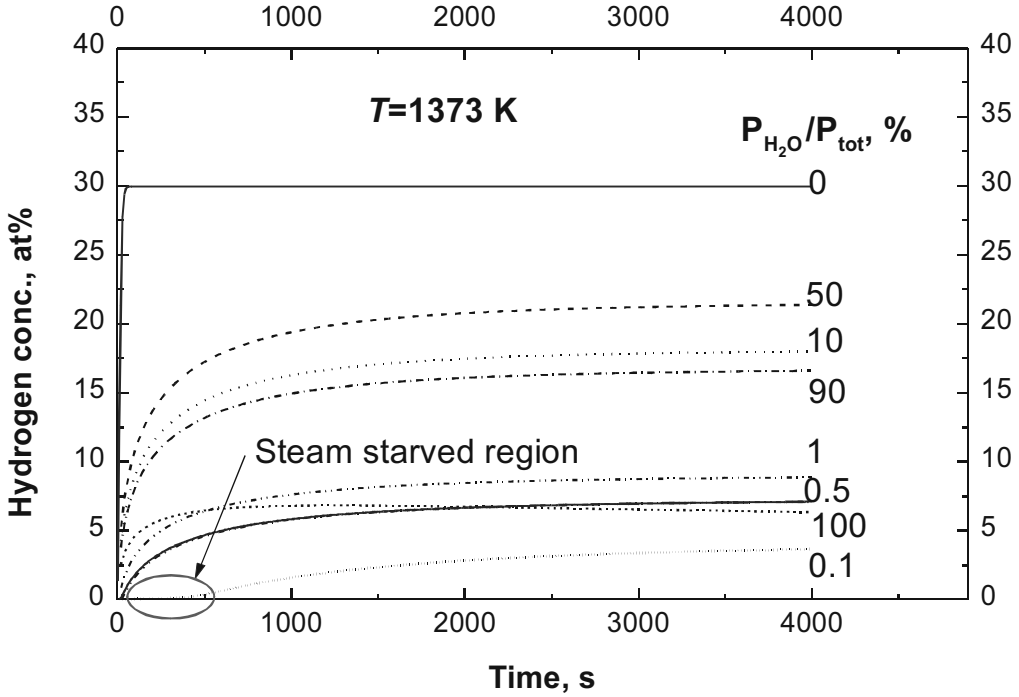

Fig. 5. Hydrogen absorption by Zr1%Nb cladding for various H_2/H_2O gas mixtures.

However, at low steam contents in the gas mixture (≤ 0.1 mol.%) steam starvation is sustained during a short initial time interval of oxidation. During this period while the oxide scale is rather small (≤ 1 μm), the direct gaseous hydriding from the H_2 reach atmosphere occurs leading to a noticeable increase of the integral value of the absorbed hydrogen [9]. This effect implemented in the model results in a noticeable increase of hydrogen uptake in steam starved regime, Fig. 6.

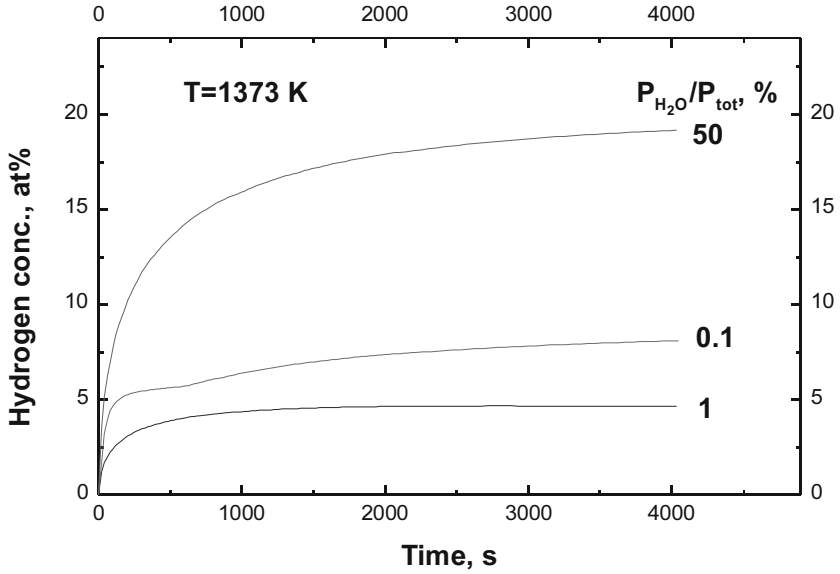

Fig. 6. Hydrogen absorption by Zr1%Nb cladding: effect of steam starvation at low H_2:H_2O ratios.

4.3. Coupling of hydriding and oxidation modules

The calculation results presented in the previous section were obtained by the stand-alone hydriding module in which oxidation kinetics is simulated by a parabolic correlation corresponding to the steam rich conditions (parabolic rate constants were taken according to the measurements [5]). However, when the steam content in the gas mixture becomes quite low so that the steam starvation conditions are valid, the parabolic time law for the oxide growth is not anymore valid and a more sophisticated approach to the oxidation kinetics description has to be applied. In this case a self-consistent solution of the oxidation and hydriding kinetics equations should be searched. To solve this problem, the coupling of the oxidation and hydriding modules was carried out.

The Zircaloy oxidation module (described in [10]) is based on the accurate system of the partial derivative equations for the oxygen diffusion in different Zry phases emerged as a result of the Zry-steam interaction. The displacement velocities of boundaries between different phases of the cladding are determined by the oxygen and zirconium flux matching conditions at a moving boundary. The usual implicit finite-difference time discretization followed by the space discretization at a non-uniform grid is used for the numerical approximation of the obtained system of equations. This procedure leads to the tridiagonal system of the finite difference equations which is solved by the Thomas algorithm.

The coupling between the oxidation and hydriding modules was accomplished in implicit way as follows.

The oxygen flux in Eq. (51) was approximated by the following relationship:

$$J_{\mathrm{O}}^{(\mathrm{O}x)} = D_{\mathrm{O}}^{(\mathrm{O}x)} \frac{\partial C_{\mathrm{O}}}{\partial r} = D_{\mathrm{O}}^{(\mathrm{O}x)} \frac{C_{\mathrm{O}}^{N} - C_{\mathrm{O}}^{N-1}}{r^{N} - r^{N-1}}, \qquad (52)$$

where C_O^N, C_O^{N-1} and r^N, r^{N-1} are the oxygen concentrations at the boundaries and coordinates of the first spatial mesh at the outer cladding surface.

The values of the oxygen concentration in oxide and of the hydrogen to steam ratio in the gas phase at the oxide surface are related by the formula [7]:

$$C_N = \frac{C_{O,eq}^{(Ox)}}{2}\left(2 - \exp\left(-1.77 - \frac{1.2810^4}{T}\right)\left(\frac{P_{H_2}(s)}{P_{H_2O}(s)}\right)^{\frac{1}{3}}\right), \qquad (53)$$

where $C_{\mathrm{O,eq}}^{(\mathrm{O}x)}$ is the stoichiometric oxygen concentration in oxide.

Besides, according to the Thomas algorithm the solid state oxygen concentrations are connected by the linear relationship:

$$C_{\mathrm{O}}^{N-1} = \alpha^N C_{\mathrm{O}}^{N} + \beta^N, \qquad (54)$$

where coefficients in the Thomas algorithm α^N and β^N are determined by the oxygen distribution in the cladding found at the previous time step and the boundary condition at the inner cladding surface.

Solution of the complete system of equations Eqs. (47)-(54) allows to find oxygen boundary concentration at the external oxide surface and then to find oxygen distribution in the cladding according to the Thomas algorithm.

So, the described here implicit coupling of the hydriding and the oxidation modules gives an opportunity to find distribution of the different components in the gas and solid phases simultaneously for one time step.

4.4. Coupling of hydriding/oxidation and channel gas kinetics modules

In the above presented calculations it was assumed that the mass fluxes of the gas components at the channel inlet are much higher than that from the gas phase into the specimen due to the hydriding and oxidation processes. Such an assumption allows consideration of partial pressures of the components in the bulk of the gas phase as independent on time and determined by the mass flow at the channel inlet. Under the experimental conditions [6] this assumption is not anymore valid, and a more accurate consideration of the mass fluxes in the gas channel is necessary.

The mass exchange equations for the gas mixture being averaged over the channel cross-section take the form similar to Eq. (4). In these equations the values of the mass fluxes of the components to the gas volume are connected with that to the solid phase, entering in the system Eqs. (47)-(51), by simple balance relationships:

$$J_{H_2O} = -\frac{\mu_{H_2O}}{\mu_O} J_O^{(Ox)}, \qquad (55)$$

$$J_{H_2} = \left(\frac{\mu_{H_2}}{\mu_O} J_O^{(Ox)} - J_H^{(Ox)}\right) \qquad (56)$$

The numerical method for the solution of Eq. (4) with specified values of the mass flows of the components to the gas volume is described in detail in [10].

The coupling between hydriding/oxidation and channel gas kinetics modules was accomplished in an explicit way as follows. In the first time step the initial distribution of the different components in the bulk of the gas phase is transferred to the hydriding/oxidation modules. In these modules the mass flows of hydrogen and steam to the gas volume are calculated and transferred into the channel gas kinetics module. After the solution of Eq. (4) with fixed values of the mass flows, the new distribution of the different components in the bulk of the gas phase emerges, and so on.

4.5. Test simulations

The complete numerical model was applied to the conditions of experiments [6]. In the experimental work [6] the mass gain due to the oxygen and hydrogen uptake by Zircaloy cladding under LWR accident conditions was investigated. The test specimens of 30 mm length were cut from the tubing of 10.75 mm external diameter and 0.725 mm wall thickness. The samples were exposed to the flowing H_2:H_2O:Ar gas mixture of atmospheric pressure under isothermal or temperature transient conditions. The mass flows at the channel inlet in the considered experiment were: steam – 25 ml/min; hydrogen – 0, 100 ml/min; argon – 1000 ml/min.

The measured specimen mass gain for 1100 and 1300 °C are compared with the calculation results in Figs. 7 and 8. The set of the parameters used in the numerical model was modified as compared with that introduced in [4]. In work [4] the corresponding model parameters were derived by fitting of the calculation results to the experimental data [5] on of hydrogen absorption by Zr1%Nb cladding during oxidation in steam. So, in the course of the present work some fitting of the model parameters (A,λ) for the proper description of the Zyrcaloy cladding (instead of Zr1%Nb cladding) was needed.

Virtually in the whole considered time interval, the steam starvation conditions are valid and the supply rates of oxygen and hydrogen determine their consumption. Both test and calculation results clearly demonstrate that an addition of hydrogen into the H_2O:Ar gas mixture leads to the increase of the specimen mass gain. This mass increase is connected with the additional hydrogen consumption by the specimen from H_2:H_2O:Ar gas environment in the initial period of interactions, when the oxide thickness was small (≤ 1 μm).

Under the experimental conditions [6] the specimen mass gain due to hydrogen uptake is much less than that due to oxygen consumption. For this reason, an accurate determination of hydrogen absorption in the tests [6] is quite difficult. For quantitative validation of the model presented in this report more direct measurements of hydrogen uptake in the oxidising atmosphere is recommended (e.g. by hot extraction analysis).

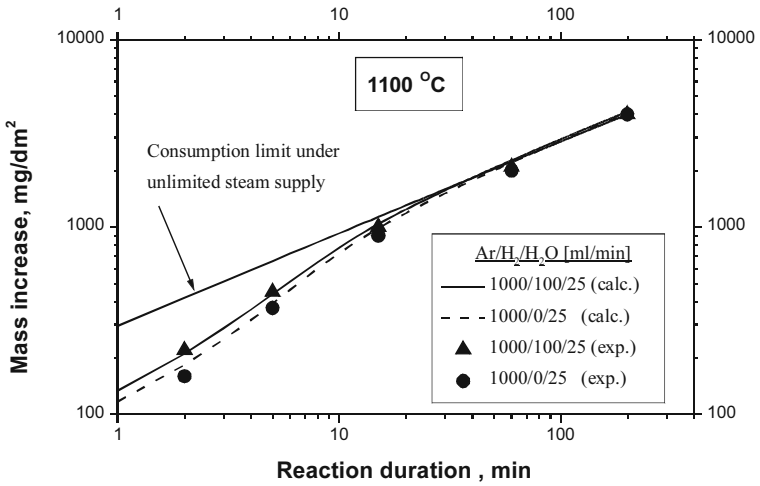

Fig. 7. Reaction kinetics at 1100 °C in hydrogen-containing and hydrogen-free Ar/steam atmospheres.

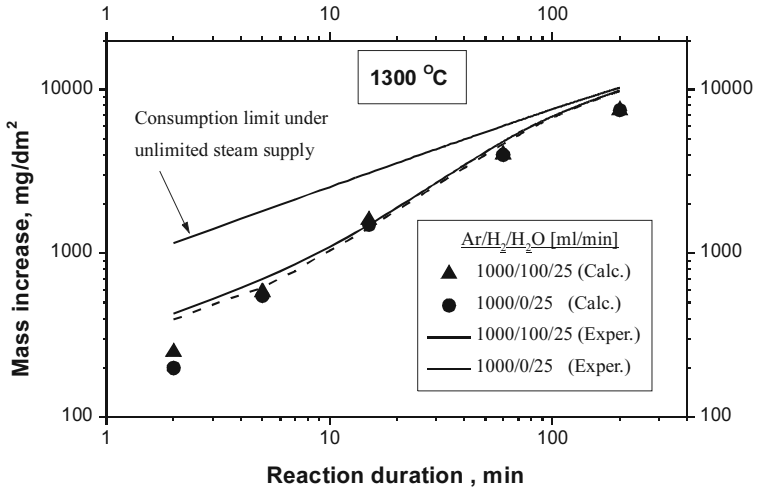

Fig. 8. Reaction kinetics at 1300 °C in hydrogen-containing and hydrogen-free Ar/steam atmospheres.

5. Conclusions

In order to simulate the hydrogen absorption by the Zr cladding, a general model considering the cladding interactions with hydrogen/steam/argon mixtures at high temperatures is developed. This general model comprises the two previously developed models (presented in Sections 2 and 3) as the limiting cases: first, direct reaction with molecular hydrogen (gaseous hydriding), and second, absorption of hydrogen liberated by the decomposition of water or steam during the oxidation process and absorbed as part of the oxidation mechanism. The model was tightly coupled with the cladding oxidation model and the channel gas kinetics model.

The model considers mass transfer in the three layers: gas, oxide and metal, and at the corresponding interfaces: gas/oxide and oxide/metal; the gas phase comprises the hydrogen/steam/argon mixture with some arbitrary molar ratio of the three components: $H_2 : H_2O : Ar = X : Y : 1$

The model is qualitatively and numerically analysed. It is shown that, at first, the dilution of steam by hydrogen leads to the increase of hydrogen absorption by the cladding. At some H_2:H_2O ratio (1:1) hydrogen absorption attains its maximum value and then decreases. For the steam content in the gas mixture lower than 1 mol.%, hydrogen absorption by the cladding

becomes comparable with that in the pure steam atmosphere, and continues to decrease with the further decrease of the steam content in the mixture. However, at low steam contents in the gas mixture (≤ 0.1 mol.%) steam starvation is sustained during a short initial time interval of oxidation. During this period while the oxide scale is rather small (≤ 1 μm), the direct gaseous hydriding from the H_2 reach atmosphere occurs leading to a noticeable increase of the integral value of the absorbed hydrogen.

The model qualitatively reproduces the measurement results of the experimental work [6], in which oxygen and hydrogen uptake by Zircaloy cladding segment exposed to a flowing $H_2 : H_2O$: Ar gas mixture of atmospheric pressure was investigated.

The hydriding module data base previously validated against steam/Zr1%Nb cladding interactions was modified for the description the hydrogen absorption by the Zry cladding in oxidising atmosphere. For the quantitative validation of the model and more accurate extension of the data base to the Zry cladding material, new tests on the Zry cladding/steam interactions with the post-test hydrogen analysis of specimens are recommended.

References

1. *B. Cox*, Advances in Corrosion Science and Technology, 5 (1976) 173.
2. *M. Steinbrück*, J.Nucl.Mater., 334 (2004) 58.
3. *M. Moalem, D.R. Olander*, J.Nucl.Mater., 178 (1991) 161.
4. *M.S. Veshchunov, A.V. Berdyshev*, Modelling of Hydrogen Absorption by Zirconium Alloys during High Temperature Oxidation in Steam. J. Nucl. Mater., 255 (1998) 250.
5. *J. Freska, G. Konczos, L. Maroti, L. Matus*, Oxidation and Hydrating of Zr1%Nb Alloys by Steam. Report KFKI-1995-17/G, 1995.
6. *G. Schanz, S. Leistikow, Ch. Adelhelm*, Zur konkurrierenden Sauerstoff- und Wasserstoff-Aufnahme des Zircaloy-4 bei hohen Temperaturen, in Gase in Metallen, Ed. By D.Hirshfeld, 1984.
7. *D.R. Olander*, Nucl.Engineering and Design, 148 (1994) 253.
8. *K. Park, D.R. Olander*, J.Am.Ceram.Soc., 74 (1991) 72.
9. *M. Moalem, D.R. Olander*, J.Nucl.Mater., 182 (1991) 170.
10. *P. Hofmann, A. Miasoedov, L. Steinbock, M. Steinbruck, A.V. Berdyshev, A.V. Boldyrev, A.V. Palagin, V.E. Shestak, M.S. Veshchunov*, Quench Behavior of Zircaloy Fuel Rod Cladding Tubes. Small-Scale Experiments and Modeling of the Quench Phenomena. FZKA 6208, INV-COBE(98)-D018, 1999.

Deformation Behavior of Oxidized Zr Fuel Cladding under High Temperature Conditions

A.V. Boldyrev

1. Introduction

The results of CORA test with quenching show that the highest temperatures in the bundle were reached during reflooding. At the reflooding stage of the experiments up to 80 % of the generated hydrogen was produced. Temperature and hydrogen release escalation are the result of intensive oxidation of Zircaloy in steam atmosphere.

High temperature can lead to an increase of internal pressure and, hence, to ballooning of fuel cladding. Cladding ballooning influences a heat generation during oxidation by the following way:

- an increase of cladding surface area available for oxidation and heat transfer;
- burst of the cladding allows steam ingression into the gap formed by the fuel pellets and the ballooned cladding and internal oxidation starts;
- oxide cracks and fresh metallic surface becomes available for steam.

After burst of the cladding and equalization of external and internal pressures, the factors that impact the oxide scale rupture are:

- volumetric expansion of Zircaloy due to oxidation;
- difference in the thermal expansion coefficient of the formed phases;
- steep radial and axial temperature gradients near the quench front leading to the spalling of the oxide scale;
- fuel pellets expansion.

Oxide cracking and spalling decrease the protective power of the oxide scale. Steam reacts with metallic component of the newly formed surface, and as a result of the oxidation, local temperature escalation takes place again.

To take into account the influence of the cladding deformation behavior on the capability of the oxidized cladding to withstand the quench loads the next model is presented.

2. The base model description

2.1. Structure of the oxidized cladding

Oxidation of Zircaloy at high temperature (> 1200 K) in steam produces a three-layer structure :

- an outer brittle layer of zirconium dioxide ZrO_2,
- an underlying brittle layer of α phase metal stabilized against transformation into β phase by the presence of dissolved oxygen,
- phase core, containing a smaller amount of dissolved oxygen.

2.2. Effect of oxidation on the cladding deformation behavior

Investigations of deformation behavior of pressurized Zircaloy fuel cladding in steam atmosphere [1-5] show the strengthening effect of oxidation. Oxidation can increase time to rupture due to ballooning in several times or even prevent it.

This can be explained by a decrease of the creep rate of oxygen stabilized α phase. The most strengthening is observed if a layer of oxygen stabilized α phase exists. If the material is heated to produce a duplex structure of α phase dispersed in β phase matrix the creep rate observed

is characteristic of the weaker β phase and little strengthening due to oxygen stabilized α phase takes place. The addition of oxygen in solid solution has no effect on the creep behavior of β phase Zircaloy until the β/α + α phase boundary is reached. Further addition of oxygen produces an outer layer of stronger α phase and the creep rate is decreased [4].

Another effect of oxidation on cladding deformation is an embrittlement of cladding material. Oxide is assumed to be a brittle material up to its melting. Oxygen in α phase decreases its ductility, especially at low temperatures, besides the cooling rate of cladding through the temperature range of β→α phase transformation influences the microstructure and extent of oxygen redistribution. Ductile behavior of heavily oxidized Zircaloy cladding depends on oxygen distribution and thickness of β phase [6, 7] and influences the capability of cladding to withstand thermal shock loads during quenching as well as loads during handling and transport of fuel assemblies.

2.3. Effect of irradiation on deformation behavior of oxidized fuel cladding

Because of the strong irradiation of the fuel claddings it is important to know the burst behavior and embrittlement of irradiated claddings in a hypothetical loss-of-coolant accident (LOCA) of LWR.

Results reported in [8] describe transient-heating tube-burst tests of specimens obtained from spent-fuel rods, results published in [9] describe embrittlement under irradiation. These results show that as the burst-behavior as the embrittlement of fuel cladding do not significantly depend on irradiation. The absence of irradiation influence on these properties is not unexpected for the given temperature. The studies of the annealing of irradiation damage indicate complete annealing of irradiation strengthening at temperatures below 973 K during transient heating at rates up to 28 K/s. Increase in ductility due to recrystalization tend to lag behind the strength changes but are beginning at 973 K, even at the highest heating rate of 28 K/s, and continue to increase as the maximum transient temperature is increased [8]. The elevated temperatures attached to film boiling operation tend to rapidly anneal irradiation defects [9].

2.4. Main assumptions of proposed model of deformation behavior of oxidized fuel cladding

Taking into consideration the above stated features of oxidation and deformation behavior of fuel cladding the next assumptions were used to simulate the cladding behavior under severe accident conditions:

- The fuel rod is divided into meshes along axial direction. Each mesh consists of fuel pellet and Zircaloy cladding.
- For each mesh the cladding is considered as multilayer cylindrical shell consists of an external oxide layer, an underlying alpha layer, beta layer and the most inner layer that includes the rest of clad wall thickness, Fig.1.
- Material of oxide layer is monoclinic, tetragonal or cubic ZrO_2 phase. It is assumed each oxide phase is stoichiometric ZrO_2 with constant oxygen concentration. Oxide material is assumed to have elastic properties up to melting.
- Material of alpha layer can consist of oxygen stabilized α phase, oxygen reached β phase or mixture of these two phases. Alpha layer material is assumed to have visco-elastic properties up to melting.
- Beta layer is thought to contain a small amount of dissolved oxygen. Material of beta layer can consist of β phase, α phase or mixture of these two phases. Beta layer material is assumed to have visco-elastic properties up to melting.
- The innermost layer includes the materials that are the product of internal oxidation, fuel-cladding interaction or downward relocation of molten material. It is assumed that this layer has no deformation strength and its material is considered as incompressible liquid.
- Fuel pellet is assumed to be a rigid body with radial thermal strain.
- All layers' materials are thought to be isotropic.

Material of alpha and beta layers is thought to be subjected only creep deformation. Plastic strain which does not depend on time is not included separately, since creep is the dominant deformation mechanism at high temperatures.

All materials are assumed to be isotropic because at the high temperatures when intensive oxidation occurs the anisotropy of mechanical properties of Zircaloy is not observed.

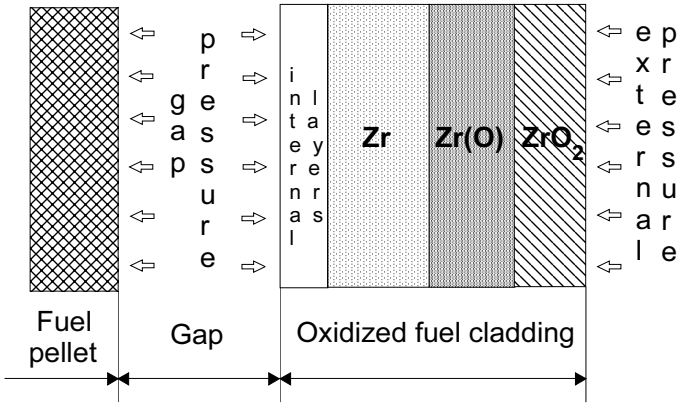

Fig. 1. Structure of the mesh of Zircaloy oxidized fuel cladding.

2.5. Constitutive equations

2.5.1. Stress-strain state of a mesh of oxidized fuel cladding

The factors that impact the mechanical response of the cladding are:

- the internal (in the gap between fuel pellets and cladding wall) and the external (in the channel of the coolant) pressures;
- the volumetric expansion of the material due to oxidation;
- the difference in the thermal expansion coefficient of the formed phases;
- the temperature;
- the expansion of the fuel pellets.

Temperature variation in the radial direction of a mesh is considered, but each layer has an uniform temperature. It is assumed that each layer of a mesh can be described as a thin-walled cylinder. Hence its dimensions can be characterized with the help of a middle radius *R*, thickness *t*, and height *h.*

The three-dimensional stress state of the thin-walled cylinder can be obtained in the following way:

$$\sigma_r = -\frac{1}{2}(P_\mathrm{i} + P_\mathrm{e}),$$
$$\sigma_\theta = P_\mathrm{i}\frac{R_\mathrm{i}}{t} - P_\mathrm{e}\frac{R_\mathrm{e}}{t}, \qquad (1)$$
$$\sigma_z = \frac{N}{t},$$

where $R_\mathrm{i}, R_\mathrm{e}$ — the internal and external layer radii; $t = R_\mathrm{e} - R_\mathrm{i}$ — the layer thickness; $P_\mathrm{i}, P_\mathrm{e}$ — the internal and external layer pressures; N — the layer axial force per circumference unit length; r, θ, z — the directions of cylindrical coordinate system. Because of mesh applied loads do not vary along axial and azimuth directions these stress are principle stresses and shearing stress and strain are equal to zero.

The total strain in a given layer is taken to be the sum of elastic, creep and temperature strains:

$$\varepsilon_\chi = \varepsilon_\chi^e + \varepsilon_\chi^{\mathrm{cr}} + \varepsilon_\chi^T, \qquad (2)$$

where $\varepsilon_\chi^e, \varepsilon_\chi^{\mathrm{cr}}, \varepsilon_\chi^T$ — elastic, creep and temperature layer strains, correspondingly; index $\chi = r, \theta, z$.

According to Hook's law elastic strains are:

$$\varepsilon_r^e = \frac{1}{E}(\sigma_r - \nu(\sigma_\theta + \sigma_z)),$$
$$\varepsilon_\theta^e = \frac{1}{E}(\sigma_\theta - \nu(\sigma_r + \sigma_z)), \qquad (3)$$
$$\varepsilon_z^e = \frac{1}{E}(\sigma_z - \nu(\sigma_r + \sigma_\theta)),$$

where E, ν — Young's modulus and Poisson's ratio of a layer material.

Using assumption that stresses do not change significantly due to dimensions changes during time interval dt, creep strains increments are given by

$$d\varepsilon_\chi^{cr} = \frac{3d\varepsilon_{\mathrm{int}}^{\mathrm{cr}}}{2\sigma_{\mathrm{int}}}(\sigma_\chi - \sigma_0), \qquad (4)$$

where $d\varepsilon_{\mathrm{int}}^{\mathrm{cr}}$ — the creep strain intensity increment; $\sigma_0 = (\sigma_r + \sigma_\theta + \sigma_z)/3$; σ_{int} — the stress intensity. Strain and stress intensities can be written as

$$\varepsilon_{\text{int}} = \frac{\sqrt{2}}{3}\sqrt{(\varepsilon_r - \varepsilon_\theta)^2 + (\varepsilon_\theta - \varepsilon_z)^2 + (\varepsilon_z - \varepsilon_r)^2}$$
$$\sigma_{\text{int}} = \frac{1}{\sqrt{2}}\sqrt{(\sigma_r - \sigma_\theta)^2 + (\sigma_\theta - \sigma_z)^2 + (\sigma_z - \sigma_r)^2}. \quad (6)$$

Zircaloy creep tests data are well described by a function [10]:

$$\frac{d\varepsilon^{cr}}{dt} = A \cdot \sigma^n \cdot e^{-\frac{Q}{T}}, \quad (7)$$

where $d\varepsilon^{\text{cr}}/dt$ — the secondary creep velocity; A, n, Q — the creep constants; σ — the applied stress; T — the absolute temperature. Since layer temperature is assumed to be a constant during time interval dt , creep strain intensity increment for the case of three-dimensional stress state can be determined in the following way:

$$d\varepsilon_{\text{int}}^{\text{cr}} = A \cdot \sigma_{\text{int}}^n \cdot e^{-\frac{Q}{T}} dt \quad (8)$$

Oxygen concentration impacts creep rate of oxygen stabilized α phase and it can be taken into account in the following way [4]:

$$\frac{d\varepsilon^{\text{cr},\alpha}(C)}{dt} = \frac{d\varepsilon^{\text{cr},\alpha}(0)}{dt} \cdot e^{-3.42 \cdot C} \quad (9)$$

where $d\varepsilon^{cr,\alpha}(0)/dt$ — the creep rate of α phase with oxygen concentration of as-received cladding; $d\varepsilon^{\text{cr},\alpha}(C)/dt$ — the creep rate of oxygen stabilized α phase with oxygen concentration C ; C — the weight fraction of excess oxygen in percents.

Thermal strains can be written as:

$$\varepsilon_r^T = \varepsilon_\theta^T = \varepsilon_z^T = \sqrt[3]{\frac{\rho(T_{ref})}{\rho(T)}} - 1 \quad (10)$$

where $\rho(T_{ref}), \rho(T)$ — the layer material densities at temperatures T_{ref} and T ; T_{ref}, T — the initial temperature and the current temperature of the layer, correspondingly.

Finally, if R,t, and h are the layer dimensions before loading, then under applied loads (temperature, internal and external pressures) layer dimensions are given by:

$$\begin{aligned} R_{\text{def}} &= R(1+\varepsilon_\theta), \\ t_{\text{def}} &= t(1+\varepsilon_r), \\ h_{\text{def}} &= h(1+\varepsilon_z), \\ R_{\text{i,def}} &= R(1+\varepsilon_\theta) - \frac{1}{2}t(1+\varepsilon_r), \\ R_{\text{e,def}} &= R(1+\varepsilon_\theta) + \frac{1}{2}t(1+\varepsilon_r), \end{aligned} \quad (11)$$

where R_{def} — the middle layer radius under load; t_{def} — the layer thickness under load; h_{def} — the layer height under load; $R_{\text{i,def}}, R_{\text{e,def}}$ — the internal and external layer radii under load, correspondingly. The strains are considered infinitesimal.

Consideration of the mutual layers displacements under loads (calculation diagram is given in Fig. 2) yields the following system of equations:

$$\begin{aligned} R^\beta(1+\varepsilon_\theta^\beta) + \frac{1}{2}t^\beta(1+\varepsilon_r^\beta) - R^\alpha(1+\varepsilon_\theta^\alpha) + \frac{1}{2}t^\alpha(1+\varepsilon_r^\alpha) &= 0, \\ R^\alpha(1+\varepsilon_\theta^\alpha) + \frac{1}{2}t^\alpha(1+\varepsilon_r^\alpha) - R^{\text{ox}}(1+\varepsilon_\theta^{\text{ox}}) + \frac{1}{2}t^{\text{ox}}(1+\varepsilon_r^{\text{ox}}) &= 0, \\ h^\beta(1+\varepsilon_z^\beta) - h^\alpha(1+\varepsilon_z^\alpha) &= 0, \\ h^\alpha(1+\varepsilon_z^\alpha) - h^{\text{ox}}(1+\varepsilon_z^{\text{ox}}) &= 0, \end{aligned} \quad (12)$$

where indices α, β, ox denote the beta, alpha and oxide layers, rspectively. Upon substitution of (1)–(11) in (12), the system of equations (12) can be written in 5 unknowns: $N^\beta, N^\alpha, N^{\text{ox}}, P^{\beta,\alpha}=P_e^\beta=P_i^\alpha$, *and* $P^{\alpha,\text{ox}}=P_{\text{e}}^\alpha=P_{\text{i}}^{\text{ox}}$.

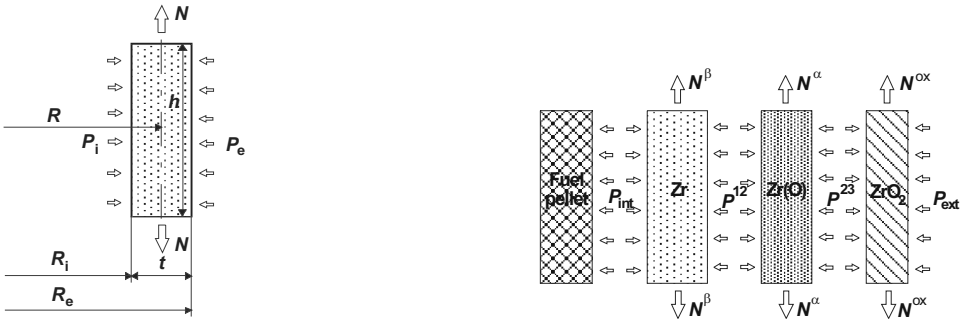

Fig. 2. Layer dimensions and calculation diagram of a mesh of oxidized Zircaloy cladding.

The fifth equation can be obtained from the consideration of the force balance for the plugged cylinder:

$$N^{\beta} + N^{\alpha} + N^{\text{ox}} - N^{\Sigma} = 0, \qquad (13)$$

where N^{Σ} — the total axial force, due to internal and external pressures, per unit length.

The total axial force can be written as:

$$N^{\Sigma} = \frac{P_{\text{int}} \cdot R_{\text{int}}^2 - P_{\text{ext}} \cdot R_{\text{ext}}^2}{R_{\text{int}} + R_{\text{ext}}}, \qquad (14)$$

where $R_{\text{int}}, R_{\text{ext}}$ — the internal and external cladding mesh radii under loads; $P_{\text{int}}, P_{\text{ext}}$ — the internal and external cladding mesh pressures.

The considered approach gives solution for the case when the gap between fuel pellet and mesh wall exists. If the internal radius of the mesh is less than external fuel pellet radius, then the internal pressure calculated for cladding as a function of gap volume and temperature is not valid. In this case the obtained solution is not correct and additional equation should be written to determine unknown internal pressure. If fuel pellet is considered as a rigid body and internal cladding layers (besides beta, alpha and external oxide layer) are considered as incompressible liquid then an additional equation can be written in the following way:

$$R^{\beta}(1+\varepsilon_{\theta}^{\beta}) - \frac{1}{2}t^{\beta}(1+\varepsilon_{r}^{\beta}) - R^{\text{pellet}}\sqrt{1+\frac{V_{\text{tot}}}{\pi h_{\text{def}}(R^{\text{pellet}})^2}} = 0, \qquad (15)$$

where R^{pellet} — the external fuel pellet radius; h_{def} — the deformed mesh height at the end of previous time step; V_{tot} — the total volume of the internal layers. Eq.(15) is assumed to be a slipping between the fuel pellets and the fuel rod cladding.

The system of equations (12), (13) is nonlinear in $N^{\beta}, N^{\alpha}, N^{\text{ox}}, P^{\beta,\alpha}, P^{\alpha,\text{ox}}$ and it is solved numerically. For the solution the layer strains are written for the unknowns explicitly and then the system of equations is linearized, the obtained system is solved and the solution approximation is found. As initial approximation an elastic solution (creep strains are equal to zero) of the system (12), (13) is used. The iterations go on up to the moment when the given simulation accuracy will be achieved.

After solving the system of equations (12), (13) for the unknown $N^{\beta}, N^{\alpha}, N^{\text{ox}}, P^{\beta,\alpha}, P^{\alpha,\text{ox}}$ one can evaluate the stresses and strains for each mesh layer, and then mesh dimensions. Because of the assumption that changes of layers dimensions during time step are negligible, hence, an intensity of creep strain increments should be checked. If the creep strain increment intensity exceeds the given limit value then time step is reduced and calculations start again.

New mesh dimensions are calculated using (11), creep strains accumulated at the time step lead to irreversible changes of the layer dimensions:

$$\begin{aligned} R_{\text{new}} &= R(1+\Delta\varepsilon_{\theta}^{\text{cr}}), \\ t_{\text{new}} &= t(1+\Delta\varepsilon_{r}^{\text{cr}}), \\ h_{\text{new}} &= h(1+\Delta\varepsilon_{z}^{\text{cr}}), \end{aligned} \qquad (16)$$

where $\Delta\varepsilon_{r}^{\text{cr}}, \Delta\varepsilon_{\theta}^{\text{cr}}, \Delta\varepsilon_{z}^{\text{cr}}$ — the creep strain increments of the layer at the end of time step Δt.

2.5.2. Modification of cladding layers dimensions due to oxidation

Oxidation leads to change of each layer thickness and influences the mesh deformation behavior. Mass of each mesh layer at the end of k time step can be obtained in the following way:

$$M_k^{\xi} = V_k^{\xi}\rho(T_{\text{ref}}), \qquad (17)$$

where M_k^{ξ} — the mass of layer ξ (ξ=β,α,ox) at the end of time step k; V_k^{ξ} — the volume of layer ξ for unloaded state (at the initial temperature T_{ref}, without pressures and axial forces) at the end of time step k with account of accumulated creep strains:

$$V_k^{\xi} = \pi((R_{\text{e},k}^{\xi})^2 - (R_{\text{i},k}^{\xi})^2)h_k^{\xi}, \qquad (18)$$

where $R_{\text{e},k}^{\xi}, R_{\text{i},k}^{\xi}$ — the external and internal radii of layer ξ for unload state at the end of time step k; h_k^{ξ} — the height of layer ξ.

After oxidation during the next time step k+1 the masses of the layers changed to M_k^{ξ}, hence the mass increments can be found. For the oxide layer:

$$\Delta M_{\text{i}}^{\text{ox}} = M_{k+1}^{\text{ox}} - M_k^{\text{ox}}. \qquad (19)$$

It is assumed that this mass change is caused by oxygen stabilized alpha to oxide phase transformation and it occurs at the alpha-oxide surface. The corresponding mass increment of alpha layer at the external surface is given by:

$$\Delta M_{\text{e}}^{\alpha} = -\frac{W^{\alpha}}{W^{\text{ox}}}\Delta M_{\text{i}}^{\text{ox}}, \qquad (20)$$

where W^{α}, W^{ox} — the molar mass of alpha layer material and oxide, correspondingly.

The mass increment of alpha layer at the internal surface is given by:

$$\Delta M_{\text{i}}^{\alpha} = M_{k+1}^{\alpha} - M_k^{\alpha} - \Delta M_{\text{e}}^{\alpha}. \qquad (21)$$

In such way the mass increments of beta layer can be found:

$$\begin{aligned} \Delta M_{\text{e}}^{\beta} &= -\frac{W^{\beta}}{W^{\alpha}}\Delta M_{\text{i}}^{\alpha}, \\ \Delta M_{\text{i}}^{\beta} &= M_{k+1}^{\beta} - M_k^{\beta} - \Delta M_{\text{e}}^{\beta}, \end{aligned} \qquad (22)$$

where W^{β} — the molar mass of beta layer material.

Dividing these mass increments by the density at the initial temperature T_{ref} one can obtained the volume increments of the layers Fig.3:

$$\Delta V_{\lambda}^{\xi} = \frac{\Delta M_{\lambda}^{\xi}}{\rho(T_{\text{ref}})}, \qquad (23)$$

where ΔV_{λ}^{ξ} — the volume increment of layer x at l surface, (l = i, e).

Thus, the new layer radii changed due to oxidation during time step k+1 are :

$$R_{\text{i},k+1}^{\xi} = \sqrt{(R_{\text{i},k}^{\xi})^2 - \frac{\Delta V_i^{\xi}}{\pi h_k^{\xi}}}; \quad R_{\text{e},k+1}^{\xi} = \sqrt{(R_{\text{e},k}^{\xi})^2 + \frac{\Delta V_{\text{e}}^{\xi}}{\pi h_k^{\xi}}}. \qquad (24)$$

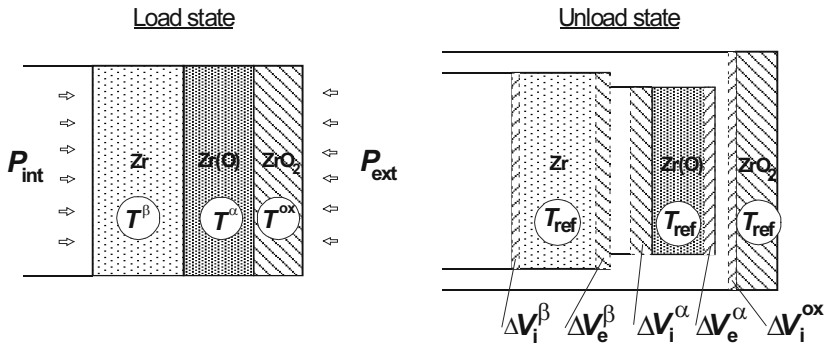

Fig. 3. Change of the layers dimensions due to oxidation.

These dimensions are used in the system of equation (12), (13) to simulate the cladding mesh deformation behavior during time step k+1. At the end of time step, the final dimensions of alpha and beta layers are changed due to creep strain (16).

2.6. Oxide scale microcracking

It is assumed that if the stresses generated in the oxide scale exceed the limit value, then the oxide cracks, i.e. microcracks emerge and lead to the decrease of the oxide carrying capacity. The simplified approach assumes the loss of carrying capacity of the oxide scale after microcracking. If oxidation continues, then a new uncracked oxide layer appears and influences the stress-state of the cladding. This simplified assumption on the loss of the carrying capacity of the cracked oxide works well for the case of the cladding heat-up when an internal overpressure plays a dominant role in the cladding deformation behavior and leads to a rapid cladding rapture due to the ballooning. After the ballooning an influence of a thick oxide layer on a stress-state of the cladding is more important. Consider the phenomenon of the oxide scale microcracking in more detail.

2.6.1. Strength limits of zirconia

The oxide mechanical properties are taken from the MATPRO data base [11]. However, only the Young's modulus and tensile strength of the stabilised zirconia as functions of temperature are available in this data base. The mechanical properties of the oxygen free Zircaloy are presented in more detail.

The lack of reliable oxide data on compressive strength and flexural strength (i.e. the maximum stress in the outer fibre at the moment of crack or breach formation) significantly complicates the modeling of the oxide scale deformation behavior and cracking.

The mechanical properties of the stabilised zirconia are studied in more detail. Small additions of some oxides, such as CaO, MgO, and Y_2O_3, into the zirconia structure form the solid solution with a cubic structure, which has no phase transformation during heating and cooling. This solid solution termed as the stabilised zirconia is a valuable refractory material. Stabilised zirconia is used as engineering ceramics due to its increased hardness and high thermal shock resistivity.

Despite the stabilised zirconia differs from the pure oxide, one can try to evaluate some necessary mechanical properties of the pure oxide material. The strength limits at room temperature of zirconia stabilised by magnesium oxide are described in [12] and presented in Table 1 (strength limit is a positive value for all types of loading).

One can see a typical tendency for the strength limits in the case of a brittle material, i.e. the compressive strength is many times higher than the tensile one, and the flexural strength is slightly higher than the tensile one. It is reasonable to expect that the strength limits of the oxide material conserve the same tendency at any temperature. Hence, the compressive $[\sigma]_c$ and flexural $[\sigma]_f$ strength can be estimated by the following way:

$$\begin{aligned} [\sigma]_c &= 10 \cdot [\sigma]_t, \\ [\sigma]_f &= 1.5 \cdot [\sigma]_t, \end{aligned} \qquad (25)$$

where $[\sigma]_t$ is the tensile strength of the oxide as a function of temperature [11]. It should be noted that the ratio of the compressive strength to the tensile one is evaluated by a factor of 10.

In the lack of fracture properties of the oxygen stabilised alpha layer and taking into consideration the similar fracture nature of the oxide and oxygen-stabilised alpha phases, it is assumed that the strength limits of the oxygen-stabilised alpha phase are roughly the same as for oxide.

Table 1. Strength limits of stabilised zirconia.

Strength limit	**MPa**
Tensile strength	150
Compressive strength	2 100
Flexural strength	230

2.6.2. Criterion of oxide scale fracture under multiaxial stress state

For the case of the uniaxial stress state the fracture criterion for the material with different strength under tension and compression is the following:

$$\sigma = [\sigma]_t \quad \text{or} \quad |\sigma| = [\sigma]_c, \tag{26}$$

where σ is the stress acting in the specimen cross section, this value is positive in the case of tension and negative in the case of compression. Fracture modes depend on the applied load. In the case of tension the fracture of the brittle materials occurs by crack propagation, the plane of crack propagation is normal to the applied force direction. In the case of compressive load fracture occurs due to sliding along the planes with maximum shearing stress. These planes are located under 45 degrees to the applied force direction.

In the multiaxial stress state the criterion proposed by O. Mohr [13] may be used. According to the main assumption the fracture occurs along the plane where the maximum shearing stresses act. The cause of the fracture are the normal and shearing stresses acting in these planes.

The stresses acting in the plane with the maximum shearing stress are:

$$\tau_{13} = \frac{(\sigma_1 - \sigma_3)}{2}, \quad \sigma_{13} = \frac{(\sigma_1 + \sigma_2)}{2}, \tag{27}$$

where τ_{13} is the maximal shearing stress, σ_{13} is the normal stress in the plane with the maximum shearing stress, σ_1, σ_2, σ_3 are the principal stresses in the given point which satisfy the condition $\sigma_1 \geq \sigma_2 \geq \sigma_3$.

In the coordinate system "σ_{13} — τ_{13}" the point A corresponds to the tensile strength $[\sigma]_t$ and the point B corresponds to the compressive strength $[\sigma]_c$. A straight line connecting these two points represents the fracture curve in this approximation:

$$\tau_{13} = b\sigma_{13} + a, \tag{28}$$

where b and a are the coefficients.

Using the expressions (27), (28) for fracture under tension and compression and writing Eq. (28) in terms of the principal stresses σ_1 and σ_3, one can obtain the fracture curve as a function of the first and the third principal stresses:

$$\sigma_1 - \frac{[\sigma]_t}{[\sigma]_c}\sigma_3 = [\sigma]_t. \tag{29}$$

Hence, in the general case the fracture occurs if the equivalent stress attains the tensile strength, i.e.:

$$\sigma_{eqv} = [\sigma]_t, \tag{30}$$

where σ_{eqv} is:

$$\sigma_{eqv} = \sigma_1 - \psi\sigma_3 \tag{31}$$

and ψ is the ratio of the tensile to the compressive strength.

However, in the particular case of interest the absolute value of the radial stress is much lower than the circumferential one. This follows from the consideration of the balance of forces in the thin-wall cylinder under internal pressure.

It was assumed that the fracture properties of the oxygen-stabilised alpha layer are similar to the oxide ones, hence, the above proposed fracture criterion is applicable also for the alpha layer.

2.6.3. Influence of the oxide scale microcracking on the fuel cladding deformation and oxidation kinetics

Since analytical calculation of the residual carrying capacity of the cracked oxide is overcomplicated, the following approach was used: after cracking only a part of the oxide thickness is assumed to have no deformation strength:

$$t_{def}^{ox} = t^{ox}(1 - \lambda_{def}), \tag{32}$$

where t_{def}^{ox} is the thickness of the oxide with the residual carrying capacity after cracking; t^{ox} — the oxide thickness before cracking; λ_{def} — parameter, $0 \leq \lambda_{def} \leq 1$, which denotes the part of the oxide thickness without carrying capacity. It is considered as a tuning parameter and its real value can be adjusted by the comparison of the simulation and experimental results. It is assumed that after oxide scale cracking the stresses in the oxide relax to zero level.

Oxide scale microcracking also influences Zircaloy cladding oxidation because open cracks provide short circuits for oxygen transport through the cracked part of the oxide. Such a

state of open cracks can be attained when the metal cladding layers are exposed to tensile axial and circumferential strains.

Simulation of Zircaloy oxidation is based on the solution of one dimensional diffusion equation in the layered cylindrical rod. Thus, an accurate mechanistic description of oxygen transport through the oxide layer via two-dimensional network of cracks turns to be beyond the accepted one-dimensional approximation. For this reason, a simplified model can be proposed for modification of the oxidation kinetics by microcracking of the oxide layer.

It is assumed within the framework of this model that microcracking renormalizes an effective thickness of the oxide layer in the oxygen diffusion problem, namely, that a certain part of the cracked oxide scale becomes transparent for the oxygen. With the lack of any systematic experimental data on the oxygen diffusion through the cracked oxide, the ratio between the transparent part of the oxide and the cracked part is an undefined parameter λ_{ox}. In order to clarify a physical meaning of this cracked oxide "transparency" parameter, two limiting cases can be considered. If parameter is equal to zero, it means the absence of any transparent part of oxide layer for the oxygen penetration, i.e. usual diffusion transport through the oxide. In the opposite case when parameter is equal to unit, the whole cracked part of the oxide becomes transparent for the oxygen penetration. Therefore, it can be logically proposed that in reality a certain intermediate value ($0 \le \lambda_{ox} \le 1$) of this parameter should be determined.

2.7. Burst criterion

One of the approach to predict burst strain parameters, such as time-to-rapture and burst strain in pressurized fuel cladding subjected to a high temperature transient is the model based on burst stress proposed by Erbacher *et al*. [5]. In this model, the burst occurs when the calculated circumferential stress in the cladding equals the limit burst stress which is assumed to be dependent on temperature and oxygen concentration of the Zircaloy. This limit burst stress is found from the tests and depends on test conditions.

Otherwise, experimental evidence shows that the onset of ballooning occurs a fraction of a second to ~ 2 s before rupture. During this period strains increase rapidly. A "large strain" criterion may be used to predict time-to-rupture [3]. In this case the limit value of circumferential strain is set to a large strain value (in the present deformation module the default value of the limit strain equals to 50 %). This limit strain is compared with the calculated average strain of the cladding mesh. Where either one equals the limit strain, the cladding is considered to burst and the corresponding burst time can be determined.

The prediction of burst strain is more difficult because the proposed approach (as the burst-stress criterion model) model uniform strain only and do not represent the complex condition in the bulge. Hence, an empirical correlation between the burst strain and some other parameter, which can be predicted, such as burst temperature, can be used [3]:

$$\varepsilon_b = (a_1 + a_2 \cos a_3 T + a_4 \cos 8a_3 T + a_5 \cos 0{,}5a_3 T) \cdot \exp[(T - a_6 + a_7 (T - a_6)^3 \cdot (a_8 - a_9 / \sqrt{H})], \quad (33)$$

where ε_b — true (logarithmic) strain; T — absolute temperature, K; H — heating rate, K/s. Angles are in radians.

The parameters found by least-squares routines for the minimum residual sum of squares are:

$$\begin{aligned} &a_1 = 0.826529, && a_2 = 0.118176, && a_3 = 0.00224865, \\ &a_4 = 0.148563, && a_5 = -1.00638, && a_6 = 1130.99, \\ &a_7 = 0.0000506518, && a_8 = 0.000166479, && a_9 = 0.00356813. \end{aligned} \quad (34)$$

The fitted function is limited to simple temperature ramps with heating rates of 5, 25 and 100 K/s in the following temperature ranges; 900 to 1400 K, 900 to 1550 K, and 900 to 1600 K, respectively. Fig. 4 shows the proposed burst strain as a function of temperature and temperature ramp.

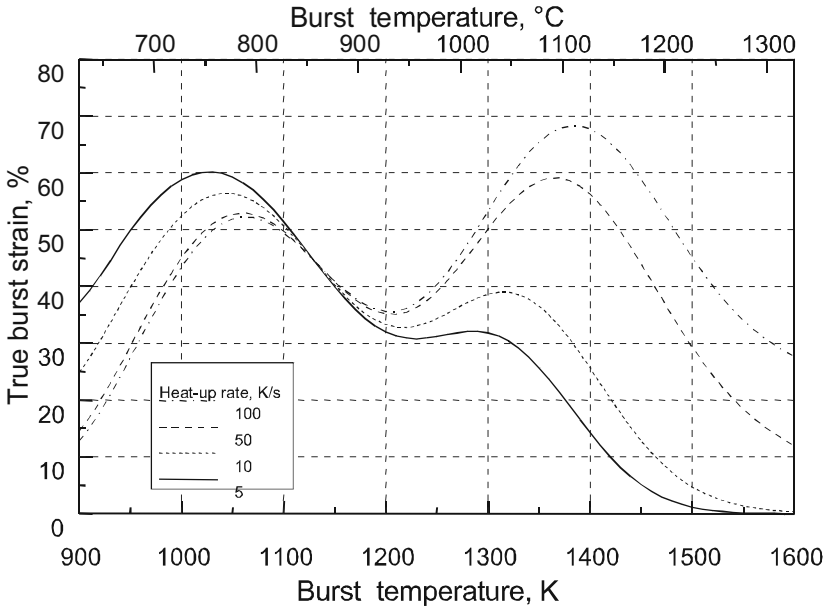

Fig. 4. Burst strain as a function of temperature and temperature ramp.

2.8. Base model testing

On the base of considered approaches the deformation behavior module was worked out. All routines was written in FORTRAN 77. This module and the worked out cladding oxidation module was coupled into the oxidation-deformation stand alone code, which was the prototype of the SVECHA/QUENCH (S/Q) code [14] capable to predict the fuel rod behavior under the severe accident conditions. Some tests simulations were performed to evaluate the predictive capability of this oxidation-deformation code. The results of these simulation are presented below.

2.8.1. Single-rod transient burst test performed within REBEKA project

To verify the prediction of deformation behavior of slightly oxidized fuel cladding the simulations of single-rod burst tests performed within the REBEKA project [5] were carried out. To simulate the oxidation of Zircaloy fuel cladding the mentioned oxidation module was used.

Test preparation: The cladding tubes were made of Zircaloy-4 with 10.75 mm outside diameter and 9.30 mm inside diameter.

Test performance: The internal overpressure and the heating rate were kept constant during the deformation process. A heated shroud surrounded the test rod to minimize temperature differences on cladding circumference. Single-rod transient burst test in steam were performed with the following parameters: internal overpressure — 10 to 140 bar, heating rate — 1 to 30 K/s. Initial temperature — 573 K.

Experimental results: Fig. 5 is a plot of burst temperature versus internal overpressure with heating rate as a parameter. With the same heating rate, a higher internal overpressure results in a lower burst temperature. The diagram reveals a distinct influence of the heating rate on the burst temperature: increasing of heating rate leads to increasing burst temperature.

Simulation results: The burst temperatures predicted by fuel cladding deformation behavior module are presented in Fig. 5. One can see a good agreement between experimental and calculated results.

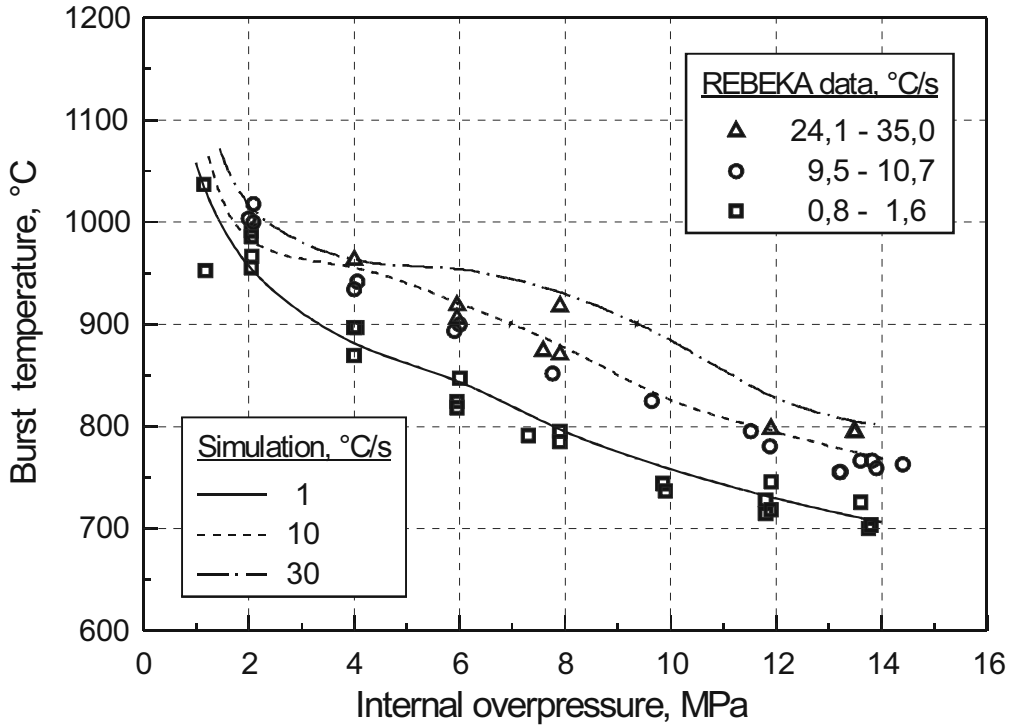

Fig. 5. Module predicted and experimental burst temperature versus internal overpressure.

2.8.2. Sagat experiments

To verify the prediction of oxidation strengthening effect the simulations of single-rod burst tests [2] were carried out. To simulate the oxidation of Zircaloy fuel cladding the carried out oxidation module was used.

Test preparation: The specimens were prepared from Zircaloy-4 cladding 15.25 mm in diameter, 0.45 mm wall thickness, and 489 mm long.

Test performance: Prior to each test, steam was admitted into the test chamber at a flow of about 2 g/s to provide an oxidizing environment on the specimen outside diameter. The apparatus was allowed to stabilize for about 600 s and after then the specimen was internally pressurized with the helium to the test pressure and then the temperature ramped using Joule heating (heating by specimen own resistance) until a predetermined strain was achieved or until the burs occurred. The measured diametral strain was obtained at a heating rate of 5 K/s and at different internal pressures ranging from 0.34 to 1.38 MPa for vacuum and steam environment.

Experimental results: The results showed that at internal pressures greater than or equal to 0.69 MPa (hoop stress of 11.3 MPa) there was little difference between the vacuum and steam data as negligible oxidation occurred during the short test period. The effect of steam oxidation became important at lower pressures where the ramp temperatures exceeded 1300 K, reducing the strain rate of specimens tested in steam. The diametral strains obtained at internal pressures 0.34 and 0.48 MPa in steam are plotted versus temperature in Figs. 6 and 7 together with similar data obtained on specimens tested in vacuum.

Simulation results: The diametral strain data predicted by fuel cladding deformation behavior module are presented in Figs. 6 and 7.

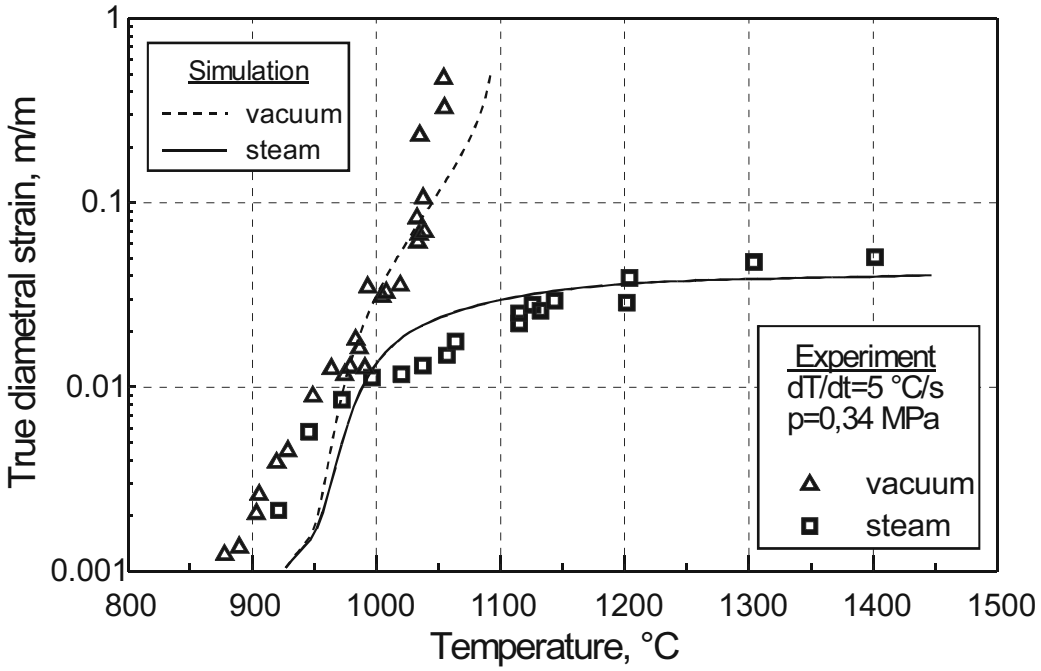

Fig. 6. Module predicted and experimental diametral strain data for internal pressure 0.34 MPa.

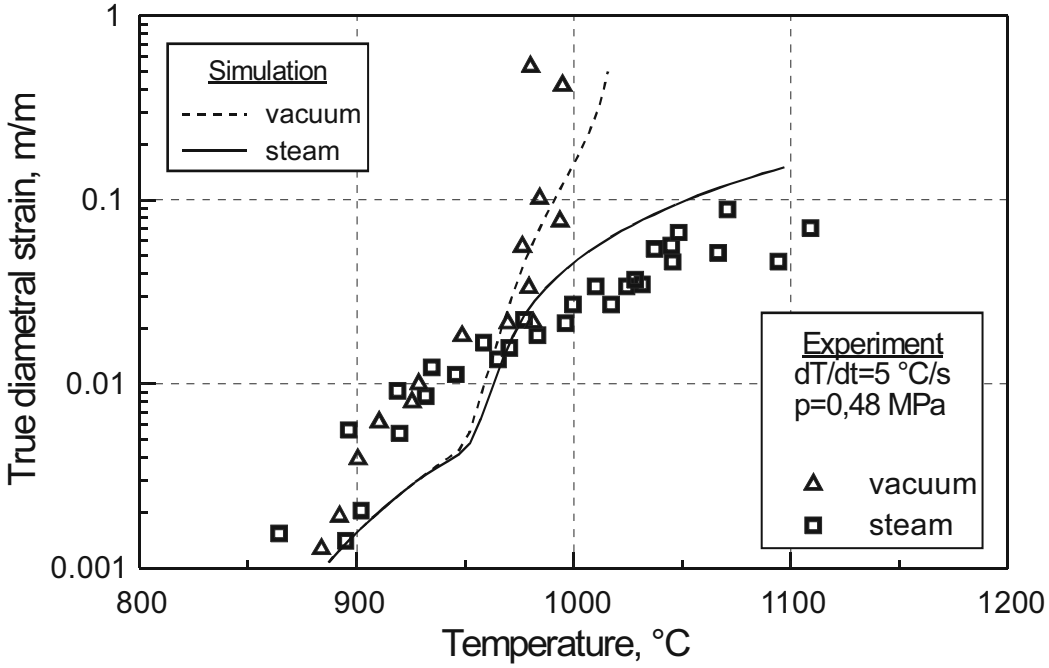

Fig. 7. Module predicted and experimental diametral strain data for internal pressure 0.48 MPa.

3. Development of the base model with reference to quench conditions

The most important accident management measure to terminate a severe accident transient in a Light Water Reactor (LWR) is the injection of water to cool the uncovered degraded core. Analysis of the TMI-2 accident and the results of integral out-of-pile and in-pile experiments have shown that before the water succeeds in cooling the fuel rods there

could be an enhanced oxidation of the Zircaloy cladding that in turn causes a sharp increase in temperature, hydrogen production and fission product release.

The hydrogen generation rate must be known to design appropriately accident mitigation measures because the air-steam-hydrogen mixture is highly explosive. The physical and chemical phenomena of the hydrogen release are, however, not sufficiently well understood. Presently it is assumed that new metallic surfaces are formed by through-wall cracking and fragmentation of the oxygen-embrittled cladding tubes as a result of the thermal shock during flooding leading to enhanced oxidation and hydrogen generation.

The next requirement for the emergency core is maintenance of the coolable geometry. It means that the core geometry shall be such that the core remains amenable to cooling not after successful initial operation of the Emergency Core Cooling Systems (ECCS), but core temperature shall be maintained at an acceptably low value and decay heat shall be removed for the extended period required by the long-lived radioactivity remaining in the core. Fracture and furthermore fragmentation of the fuel rods can have a strong influence on geometry of the emergency core. Hence, formation of the net of the through-wall cracks is the most dangerous because the fuel rods can fragment. If fragmentation of the fuel cladding into small pieces becomes severe, the coolability of the core could be seriously impaired. This is because a large number of cladding fragments and pellet pieces could block the coolant flow channel.

Thus, the formation of the net of the through-wall cracks for the oxidized Zircaloy cladding during quenching is one of the important phenomenon which can have a great influence on an accident progression.

The Forschungszentrum Karlsruhe (FZK, Germany) has started the QUENCH program. One of the objective of this program was the provision of an extensive experimental database for the development of detailed mechanistic fragmentation models and the determination of the oxidized cladding failure criteria.

The experimental part of QUENCH program began with small-scale experiments with short Zircaloy fuel rod segments [15, 16].

3.1. Analysis of the FZK small-scale quench test results

Test preparation: Specimen was a cylindrical sample of the standard Siemens/KWU Zircaloy-4 fuel rod cladding tube with a length of 150 mm, an outside diameter of 10.75 mm and a wall thickness of 0.725 mm filled with high density ZrO_2 pellets with an outside diameter of 9.1 mm.

Test performance: Specimen was heated up to 1400 °C in argon-oxygen atmosphere and then kept at this temperature until the desired oxide scale thickness was attained. Afterwards argon-oxygen was replaced by argon and the specimen was heated up or cooled down to the desired initial temperature, and then bottom-flooded with water or steam. The main test series with specimens without pre-oxidation, with oxide scale thickness of 100 and 300 μm and specimen temperatures of 1200, 1400 and 1600 °C before cooldown were performed. Some additional tests with varied initial pre-oxidation and temperature were also carried out.

Heating during prequench stage was provided by an induction coil around the section of the quartz tube enclosing the specimen, at the start of quench phase of the test the power was switched off. The special designed QUENCH rig allowed quenching by water with a predetermined rate of 3-30 mm/s and initial water temperature of 30 or 90 °C, or rapid cooldown by steam with temperature 140 °C and flow rate about 2 g/s.

The temperature of the outside surface of Zircaloy tube was measured by three thermocouple at 28, 75, and 122 mm elevation from the specimen bottom. Special procedure was used to attach the Pt/Rh thermocouples without eutectic interaction of Zircaloy with thermocouple materials. After passing a condenser the hydrogen content of the outlet gas was determined by two methods. A Caldos device determined the hydrogen concentration of the outlet gas by measurement of the electrical conductivity of the argon-hydrogen mixture. The outlet gas was also sampled at a predetermined rate for mass spectrometer measurements.

Experimental results: Microscopic appearances of specimens tested in the water and steam quenching experiments with the identical initial conditions (pre-oxidation and temperature) are very similar, this indicates that for short cladding segments the thermal condi-

tions during cool-down are very similar in water and steam quenching.

The main features of the post-test examinations can be divided into three groups:

1. Specimens without pre-oxidation and with pre-oxidation 100 μm and the initial quench temperatures not higher than 1400 °C. For these specimens through-wall cracks are not observed and oxidation of newly formed metal surfaces does not take place and, hence, does not influence hydrogen generation.
2. Specimens with pre-oxidation 100 and 300 μm and initial temperature 1600 °C. Observation of a few through-wall cracks without or with partial oxidation of the crack surfaces indicates that cracking has no great influence on the hydrogen release.
3. Specimens with pre-oxidation 300 μm and initial quench temperatures not higher than 1400 °C. Observation of the numerous through-wall cracks and crack surface oxidation indicates that the crack formation takes place at high temperatures and can contribute to the hydrogen production.

Subset of the quench tests were carried out for the case of pre-oxidation and quenching of the specimens by steam with post-test examinations of the geometry and density of the through-wall cracks by stereomicroscope and the liquid penetrants for crack visualization along with standard metallography method [17]. It was found:

- Through-wall crack density is a step function of the oxide thickness with a critical thickness about 200 μm in the case of initial temperature 1200 and 1400 °C and does not depend on steam velocity.
- For the case of oxide thickness greater than 200 μm, axial and circumferential cracks are observed.
- In the interval between 100 and 200 μm of oxide thickness, a few through axial cracks are formed.
- There are no cracks if the oxide thickness is less than 100 μm.
- No inner surface oxidation, only crack surface oxidation is observed.
- Variation of the through-wall crack density along the specimen axis is considerable. It can be explained by variation of oxide thickness from the cold lower part of the rod to the hot upper part, since the crack formation is more pronounced for thicker oxide scales. Difference in oxide layer thickness along axial circumferential directions may attain a magnitude of 50-100 μm.

The total hydrogen generation is very similar for the cases of water and steam quenching, this result may be explained by the similar fracture modes of the specimens:

1. Non-oxidized rods: the hydrogen generation has the maximum values. At higher temperatures the total hydrogen generation is higher.
2. Pre-oxidation 100 μm and quenching temperature 1200 and 1400 °C: low hydrogen generation owing to the formation of the dense oxide scale (without through-wall cracks) which prevents oxygen penetration to the metal phase. Oxide microcracking, due to difference in the thermal strains and temperature gradients, slightly increases oxidation rates and hydrogen generation [3].
3. Pre-oxidation 100 and 300 μm and quenching temperature 1600 °C: relatively high hydrogen production. Possible mechanism of hydrogen release for this case is an intensive oxidation of substoichiometric oxide (formed under steam starved conditions in the pure argon atmosphere during heating from the pre-oxidation temperature to 1600 °C) and the appearance of the oxide cubic phase near the temperature 1500 °C, with the large substoichiometric deviation and high oxygen diffusion coefficient.
4. Pre-oxidation 300 μm and quenching temperature 1200 and 1400 °C: hydrogen release is practically the same as for the non-oxidized rods. The through-wall cracks formed on cool-down at high temperature, and, hence, the crack surface oxidation significantly contributes to the hydrogen production.

3.2. The base deformation model modifications

As stated above experimental observations confirm qualitative conclusions:

- Rupture is absent in the case of the thick ductile beta layer.
- Crack density depends on the oxide layer thickness.

And provide the new features:

- Axial cracks dominate in the interval of oxide thickness between 100 and 200 μm.
- For thicker oxide scales, crack density follows a step-wise distribution function.

In the framework of the above-presented consideration these observations can be interpreted in the following way. Criterion proposed in [6] predicts that a cladding which has a part of the beta layer with ≤0.9 wt. % oxygen content thicker than 100 μm, withstands any thermal shock including quenching. Hence, beta layer has a great influence on the capability of cladding to withstand the thermo-shock loads during quench. It is explained by high ductility of β phase which prevents cracks initiation and arrests the propagation of cracks generated in oxide and alpha layers.

The proposed failure criteria predict conditions when the oxidized cladding never fails due to through-wall cracks formation under quenching. However, the accurate quantitative prediction of the fracture time and reasons of failure is still impossible. One can propose the following factors leading to oxidized cladding failure:

- axial temperatures gradients at the quench front,
- pellet-cladding interaction due to different thermal expansion of pellets and cladding wall,
- oxide phase transformation.

Simulation results of the FZK small-scale quench tests by the next version of S/Q code [14] with implemented heat exchange and heat conduction modules allow to reveal the following important features:

- oxide phase transition from tetragonal to monoclinic phase is the main reason of through-wall crack formation at the high temperature stage of quenching,
- difference in the thermal strain of the oxidized cladding materials and radial temperature gradients are the reasons of oxide cracking,
- radial temperature gradient at the quench front (where the film boiling changes to the nucleate boiling) is the reason of the oxide scale spalling,
- axial temperature gradient at the quench front is the main reason for through-wall crack formation or fragmentation at the low temperature stage of the quenching,
- metal layer with low oxygen content is the main reason which prevents the through-wall crack formation.

In order to describe numerically these peculiarities of the quenching rod behavior, the base mechanical deformation module was modified. The subsequent modifications were implemented in the base model:

- **Phase transition in the metal phase.** In the lack of data on the oxygen stabilized alpha phase density as a function of temperature, the unknown values are generated from the oxygen free Zircaloy data under (generally accepted) assumption that the dissolved oxygen does not change a specific volume of the material and its mass contributes to the density of the oxygen free Zircaloy [10]. In its turn, the specific volume of the oxygen free material is temperature dependent and determined by the thermal strains in accordance with the linear relationship [11]. On this basis the density of the oxygen stabilized α phase at temperatures above the phase transition point ≈1100 K can be calculated. In order to make such a calculation, it is assumed that the thermal strain of the stabilized α phase can be obtained by interpolation of the α phase "branch" of the thermal strain curve for the oxygen free Zircaloy to high temperatures. Then, calculating the specific volume of the Zr matrix and adding the mass of dissolved oxygen to the mass of this matrix, one can obtain the density of the oxygen stabilized α phase. Analogously, the same approach can be applied to obtain the thermal strain of the β phase with dissolved oxygen.
- **Phase transition in the oxide**. The real oxide scale is nonstoichiometric and the average oxygen content can vary with the pre-oxidation history, influencing the deformation behavior under quenching. From the consideration of the FZK quench data one can see that in the tests performed at the initial temperature 1000 °C, the surface of the specimens were free from the visually observed macrocracks.

It is known that the tetragonal to monoclinic phase transformation in the stoichiometric oxide occurs at the temperature ≈1200 °C. Phase transition of the nonstoichiometric oxide is more smooth and, hence, the stresses induced in the metal layers by the phase transformation have enough time to relax by the plastic deformations in the metal layers and/or by the oxide cracking. Significant decrease of the average oxygen concentration may be

erage oxygen concentration may be connected with the test procedure, since the cooling (or heating) of the pre-oxidized specimen from the oxidation temperature 1400 °C to the quench-starting temperature occurred in the argon atmosphere, i. e. under oxygen starved conditions, that leads to the average oxygen concentration decrease. To calculate the thermal strain of the nonstoichiometric oxide, an approach similar to one of the metal phase transformation description, was used.

- **Radial temperature gradient.** It was revealed that under assumption of the linear temperature distribution across the oxide scale thickness the additional stresses do not generated in the metal sub-layers. Hence, the stress state in the oxide scale is a superposition of the oxide stresses due to average temperatures of all the cladding layers (the base model solution) and the stresses due to linear temperature distribution in the separate oxide cylindrical shell.

If the tensile stresses on the oxide external surface exceed the flexural strength or the average tensile stresses exceed the tensile strength, then the microcracks penetrate through the oxide scale up to the alpha layer and then stopped by compressive stress in the alpha layer. Thus, the large radial temperature drop on the oxide scale leads to decrease of the oxide layer carrying capacity and decrease the possibility of through-wall cracks formation.

3.3. Modelling of the net of through-wall cracks formation

In order to determine the conditions of through-wall crack formation, one can consider the balance of forces in a piece of cladding. A part of the cladding cross section is presented in Fig. 8. It is assumed that the beta layer is absent, i.e. the cladding is highly oxidized and thus the through-wall cracks can appear.

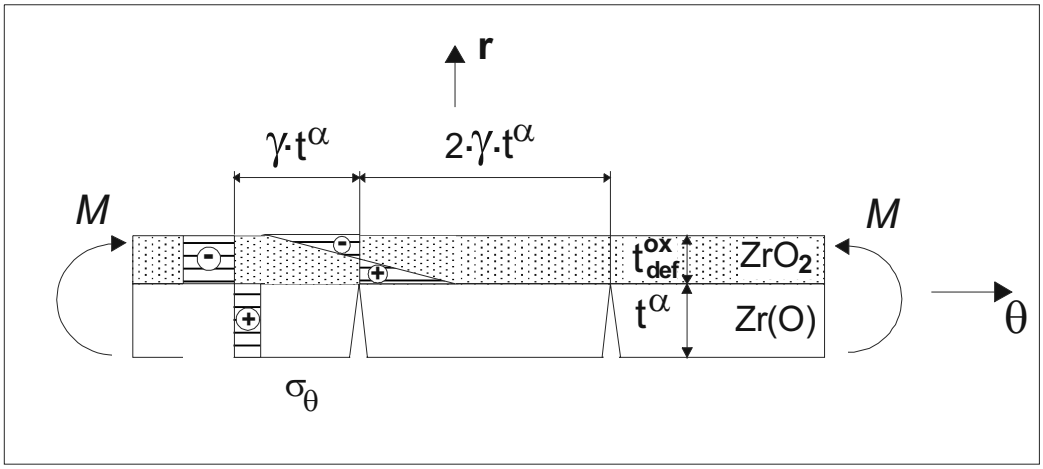

Fig. 8. Scheme of the average circumferential stress distribution in the highly oxidized cladding cooled down below the tetragonal-to-monoclinic phase transition in oxide.

The circumferential stress distribution will be analysed. There are two variants of the stress distribution along radial direction: the first, tensile stress in the oxide and compressive one in the alpha layer, and the second, vice versa. The first case is typical for the oxide cracking due to the difference in thermal strains, the radial temperature gradient or volumetric expansion under oxidation, i.e. for cool down above the temperature of the tetragonal-to-monoclinic phase transition in the oxide. However, the oxide phase transition from the tetragonal to monoclinic phase is apparently the main reason for the through-wall crack formation in the high temperature stage of quenching, and this assumption is confirmed by the S/Q code simulation results. So, the second case is the main interest and will be considered in more detail.

The stress distribution in the cladding layers is shown in Fig. 3. The total circumferential force of this stress distribution is equal to zero, but the axial bending moment acts in any axial cross section of the cladding. It can be expressed as follows:

$$\sigma^{ox} \cdot t_{def}^{ox} = \sigma^{\alpha} \cdot t^{\alpha},$$
$$M = \sigma^{ox} \cdot t_{def}^{ox} \cdot \frac{(t_{def}^{ox} + t^{ox})}{2}, \quad (35)$$

where σ_{ox} , σ_{α} are the absolute values of the average stresses acting in the oxide and alpha layers, correspondingly; t_{def}^{ox} is the thickness of the oxide layer with residual carrying capacity; t^{α} is the thickness of the alpha layer; M is the bending moment per unit length in the axial direction.

If the tensile stress in the alpha layer attains or exceeds the tensile strength, then cracks penetrate through the layer and are stopped by the compressive stress in the oxide scale. Since crack surfaces are free of stress, the relaxation occurs in the alpha layer. The influence of a crack extends within the characteristic distance $\sim \gamma \cdot t^{\alpha}$ (coefficient $\gamma > 1$). In the area outside this range the stress state relaxes and the bending moment has the same value. To provide the force balance this moment should act in any section and, hence, in the section near the crack tip. So, the stress state in the oxide layer changes and, instead of compressive stress, the tensile stress appears in some part. The maximum tensile stress under bending is given by

$$\sigma_{max}^{ox} = \frac{6 \cdot M}{(t_{def}^{ox})^2}. \quad (36)$$

Taking into account that the radial stress is negligibly small and the stress in the alpha layer has attained the tensile limit, the oxide layer cracks and a through-wall crack forms if this maximum stress satisfies the following condition:

$$\sigma_{ox,max} \geq [\sigma]_f = 1.5 \cdot \sigma_a. \quad (37)$$

After substitution of Eqs. (35), (36) into Eq. (37) one can obtain that the through-wall crack forms in the following case:

$$\frac{t^{\alpha}}{t_{def}^{ox}} \geq \frac{\sqrt{3}-1}{2} \approx 0.35. \quad (38)$$

It means that the thickness of the cracked alpha layer should be greater than one-third of the oxide scale thickness to form a through-wall crack. Thus, under the accepted assumption about the strength properties of the material, it follows that the through-wall cracks were formed in the FZK specimens after the alpha layer cracking, since the condition (38) was valid in all the FZK tests. It is important to note that the thickness t_{def}^{ox} is calculated using the loading history and oxide microcracking in the previous stages.

The stress in the alpha layer attains the strength limit under phase transition for the slightly microcracked oxide scale. If the oxide microcracked more intensively before the phase transition, then the oxide thickness with the residual carrying capacity is thinner and the compressive stress in oxide can first attain the strength limit. In this case the oxide failure mode, as mentioned above, is connected with the sliding in the planes with maximum shearing stresses and cracks in the oxide scale do not open in this case. Therefore, the axial bending moment in the alpha layer does not occur and the through-wall cracks do not form. The stresses generated by the oxide phase transition reduce or relax due to further oxide scale microcracking.

The reasons preventing the through-wall cracks penetration during the phase transition are:

- the presence of the ductile beta layer, which arrested the cracks propagation,
- the radial temperature gradient, which leads to the intensive oxide microcracking without average stress generation. The influence of the radial temperature gradient increases during the phase transition in oxide, since the absolute value of the thermal expansion coefficient sharply increases.

Another conclusion which can be drawn from the consideration of the proposed mechanism of the through-wall crack formation, concerns the characteristic distance between the cracks. Since the stress relaxation occurs within a distance $\sim \gamma \cdot t^{\alpha}$ from the crack, or for the presence beta layer $\sim \gamma \cdot (t^{\beta} + t^{\alpha})$, the distance between the neighbouring cracks should be somewhat less than the double distance of the relaxation range.

All above considerations is also valid for the case of the axial stress. If the axial and circumferential through-wall cracks formation during the oxide phase transition occurs at the same moment, then a net of perpendicular cracks forms. Then, the crack density ρ_{cr} can be found using the following expression:

$$\rho_{cr} \sim \frac{1}{2\cdot\gamma\cdot(t^{\beta}+t^{\alpha})}+\frac{1}{2\cdot\gamma\cdot(t^{\beta}+t^{\alpha})}=\frac{1}{\gamma\cdot(t^{\beta}+t^{\alpha})}. \quad (39)$$

Experimentally determined through-wall crack densities of the highly oxidized rod segments are presented in Table 2. If the coefficient γ is the value about 3 then the crack densities calculated in accordance with expression (39) are in a good agreement with experimental ones.

Table 2. Experimentally determined through-wall crack density.

Test	Oxide thickness	Initial temperature	Crack density
	μm	°C	mm/mm^2
0804_1	220	1200	0.15
0904_2	215-250	1200	0.5-1.0
1004_1	225-240	1200	0.5-1.0
2102_1	300-340	1200	2.5
20027_2	259	1400	0.65
21027_1	315	1200	0.55
03037_1	198	1200	0.46
09047_2	207	1200	0.46
10047_1	242	1200	0.5

4. Conclusions

The model of deformation behavior and rapture of the oxidized Zircaloy cladding of the LWR fuel rod is presented. The proposed model allows to predict the cladding deformation and the failure modes as at the initial stage of the loss-of-coolant accident which accompanied by the internal overpressure increase as at the latest stage of cold water ejection into the reactor core (quenching). The possible failure modes of the oxidized cladding are the ballooning due to internal overpressure and the net formation of the through-wall cracks. The following phenomena influencing on the deformation behavior are taken into consideration:

- the phase formation under oxidation,
- the phase transformation in the metal and the oxide layers as a function of the oxygen content and the phase temperature,
- the dependence of the phase mechanical properties on the oxygen content and the temperature,
- the internal and the external pressures,
- the volumetric expansion due to oxidation under the condition of non-planar geometry,
- the difference in the thermal expansion coefficient of the formed phases,
- the radial temperature gradient,
- the expansion of the fuel pellets.

Numerical simulations by S/Q code, included the deformation behavior module worked out on the base on the presented model parallel with the oxidation, the heat exchange and the heat conduction modules, and the analysis of the small-scale quench test results obtained in FZK (Germany) revealed the following peculiarities of the fuel rod cladding deformation behavior under severe accident conditions:

- Oxidation of the cladding increase time to rupture due to ballooning. The main reason is the presence of the alpha layer with low creep rate.

- The reason of the net formation of the through-wall cracks during quenching is the oxide phase transition from tetragonal to monoclinic phase near 1200 °C. The barrier which prevents this failure mode is the sufficiently thick ductile beta layer with the dissolved oxygen content less than the critical value.
- The radial temperature gradient and the difference in the thermal coefficient of the phases lead to oxide microcracking without cladding rupture. These processes accelerate the oxidation by decreasing the protective thickness of the formed oxide scale.
- The axial temperature gradient has no great influence on the net formation of the through-wall cracks at high temperatures. However, it is the main reason for the cladding rupture (some individual through-wall cracks formation or separation of the fuel rod into some parts) at low temperatures. The maximum axial gradient takes place near the quench front when the transition from film to nuclear boiling occurs, i.e. near Leidenfrost temperature. At this temperature oxidation is too slow, hence, the cladding rupture does not lead to the temperature and hydrogen release escalation.

References

1. *S. Leistikow and G. Schanz*, "Oxidation Kinetics and Related Phenomena of Zircaloy-4 Fuel Cladding Exposed to High Temperature Steam and Hydrogen-Steam Mixtures Under PWR Accident Conditions", Nuclear Engineering and Design 103 (1987) 65-84, Noth-Holland Amsterdam, pp. 65-84.
2. *S. Sagat, H.E. Sills and J.A. Wolsworth*, "Deformation and Failure of Zircaloy Fuel Sheaths Under LOCA Condition", Zirconium in the Nuclear Industry: Sixth International Symposium, ASTM STP 824, D. G. Franklin and R. B. Adamson, Eds., American Society for Testing and Materials, 1984, pp. 709-733.
3. *S. Leistikow and R. Kraft*, "Creep-Rupture of Zircaloy Tubing under Superimposed High Temperature Steam Oxidation at 900 C", EUROCOR'77 6th European Congress on Metallic Corrosion, London 12-13 September 1977, Society of Chemical Industry, pp. 577-584.
4. *B. Burton, A.T. Donaldson and G.L. Reynolds*, "Interaction of Oxidation and Creep in Zircaloy-2", Zirconium in the Nuclear Industry (Fourth Conference), ASTM STP 681, American Society for Testing and Materials, 1979, pp. 561-585.
5. *F.J. Erbacher, H.J. Neitzel, H. Rosinger and K. Wiehr*, "Burst Criterion of Zircaloy Fuel Claddings in a Loss-of-Coolant Accident",Zirconium in the Nuclear Industry; Fifth Conference, ASTM STP 754, D.G.Franklin, Ed., American Society for Testing and Materials, 1982, pp. 271-283.
6. *H.M. Chung and T.F. Kassner*, "Embrittlement Criteria for Zircaloy Fuel cladding Applicable to Accident Situations in Light-Water Reactor",Summary Report, Argonne National Laboratory, Materials Science Division, NUREG/CR-1344, ANL-79-48, January 1980.
7. A.Sawatzky, "A Proposed Criterion for the Oxygen Embrittlement of Zircaloy-4 Fuel Cladding", Zirconium in the Nuclear Industry (Fourth Conference), ASTM STP 681, American Society for Testing and Materials, 1979, pp. 479-496.
8. *A.A. Bauer, L.M. Lowry and W.J. Gallagher*, "Tube-Burst Response of Irradiated Zircaloy Spent-Fuel Cladding", Zirconium in the Nuclear Industry (Fourth Conference), ASTM STP 681, American Society for Testing and Materials, 1979, pp. 465-476.
9. *R.R. Hobbins, S.L. Seiffert, S.A. Ploger, A.S. Mehner and P.E. MacDonald*, "Embrittlement of Zircaloy-Clad Fuel Rods Irradiated Under Film Boiling Conditions", Zirconium in the Nuclear Industry (Fourth Conference), ASTM STP 681, American Society for Testing and Materials, 1979, pp. 586-599.
10. NOTE TECHNIQUE DRS/SEMAR 92/24. ICARE2. Version 2.MOD 0 and MOD 0.1. Description of physical models. Institute de Protection et de Surete Nucleaire. CEA-France.
11. SCDAP/RELAP5/MOD2 Code Manual, Volume 4: MATPRO-A Library of Materials Properties for Light-Water-Reactor Accident Analysis. NUREG/CR-5273 EGG-2555. Vol.4., 1990.
12. *Y.M.Lakhtin, V.P.Leont'eva*, "Materials Research", Moscow, 1990 (in Russian).
13. *V.L.Blagonadezjin, Y.A.Okopnyi and V.P.Chirkov*, "Mechanics of materials and constructions", Moscow, 1994 (in Russian).
14. *M.S.Veshchunov A.V.Berdyshev, A.V.Boldyrev, L.V.Matweev, A.V.Palagin, V.E.Shestak*, "Phisico-Chemical Behavior of Zircaloy Fuel Rod Cladding Tubes During LWR Severe Accident Reflooding, Part:II Modelling of quench phenomena", Forschungszentrum Karlsruhe, Technik und Umwelt, FZKA 5846, May 1997.

Modeling of Melt Relocation (Candling Process)

A.V.Palagin

1. Introduction

The process of molten materials flowing down the fuel rod during a severe accident at Nuclear Power Plant is called a candling process. This process is very essential in the development of the accident because it may cause a change of the flow cross section or a blockade of the coolant channel and lead to a decrease of the fuel rod coolability and further heatup of the fuel rod at this elevation. So, the dynamics and distribution of relocated masses along the fuel rod are of great interest.

The modeling of the candling process in the existing system codes is characterized by a variety of approaches [1]. In German KESS code [2] the detailed candling model treats the melt relocation as a falling film. If the film velocity is high enough, creeping flows are neglected. Due to the relevance of the gravity or the friction force the film is accelerated or decelerated. In the model the transient, one-dimensional conservation equations in cylindrical coordinates are solved. The decrease of the melt mass due to refreezing is considered. To describe the relocation of the single rivulets, a wetting factor is used.

Based on the detailed candling model, a simplified model is also available in the framework of the KESS code, as well as in the German ATHLED-CD code [3]. Here, a constant velocity of the film is assumed and the solution is restricted to mass and energy balances. Adequate to the detailed model, the melt refreezes, if the cladding temperature is below the solidus temperature of the melt.

In the SCDAP/RELAP5 code [4] the coupled integral equations of mass, momentum and energy for the relocating materials are solved explicitly to describe the meltdown of components. The code considers the downward movement of the molten materials as the axisymmetrical viscous film flow.

In the ICARE2 code (France), versions up to V2 mod1 [5], the candling model assumed a constant velocity of a flowing film. The model solves the mass transport from the top to the bottom with possible mass freezing in axial direction deduced from the solution of heat transfer equation.

An OECD/CSNI State of the Art report (1991) on in-vessel core degradation concluded that although the experimental data base and models are adequate in some areas, there are still substantial gaps. This was confirmed by the results of two OECD International Standard Problems: ISP 28 (PHEBUS B9+ test, [6]) and ISP 31 (CORA-13 test, [7]).

Model inadequacies are quite common for the majority of existing codes. These inadequacies have been formulated for the SCDAP/RELAP5 code in the Independent Peer Review (1994) and, with reference to the candling process, can be summarized as follows:

«*The Zr-U-O mixture relocation is based on a gravity driven mixture, slug-ring flow. Rivulet, rather than slug, flow has been established experimentally as the dominant relocation process (seen especially clearly [8] in the CORA tests).*

This process is not modeled.»

For the adequate description of the mentioned above phenomena (drop and rivulet flow) the account must be taken of the capillary effects. Generally, mass relocation during candling process is the result of a complex interaction of several factors: capillary effects, viscosity, heat exchange and gravity. In the present paper the **candling model** which accounts for all these effects is described. Some details of this candling model were described before [9-13].

Let us consider a drop on a vertical wall. If its volume is sufficiently small, the drop will rest on the wall (gravity force is balanced by the capillary forces). Now let the volume of the drop V be gradually increasing. The drop will begin to move down when V exceeds some

critical value V_{c1} (*the first critical volume*). This value V_{c1} can be determined from the relation

$$\rho g V_{c1} = F_c, \qquad (1)$$

where ρ is the density of the liquid and F_c is the maximum value of the *capillary drag force*. The presence of this force is connected with the resistance of the contact line (which is formed at the intersection of liquid, solid and gas) to displacement [14]. It can be shown [15, 16] that the value of F_c is proportional to the surface tension coefficient σ:

$$F_c = \sigma\omega\left(\cos\theta_R - \cos\theta_A\right), \qquad (2)$$

where ω is the width of the drop (maximum size in the cross section normal to the direction of gravity force); θ_R and θ_A are so-called receding and advancing contact angles [17]. Substituting F_c from (1) into (2), one has the connection between the first critical volume V_{c1} and the corresponding value of the width (*the first critical width*):

$$\rho V_{c1} g = \sigma\omega_{c1}\left(\cos\theta_R - \cos\theta_A\right). \qquad (3)$$

The values of V_{c1} and ω_{c1} are some complex functions of the surface tension coefficient σ, the advancing and receding contact angles and density, determined by the solution of the capillary surface equation [14-16]. At the same time both V_{c1} and ω_{c1} may be determined experimentally, by direct measurements. Such measurements (for example, by the use of the close-up photographs) seem to be more simple way as compared to the fine measurements of the surface tension and the contact angles with subsequent solution of the capillary problem. In the present model the values of V_{c1} and ω_{c1} are considered as empirical ones.

In order to make an estimation of the values V_{c1} and ω_{c1}, the width ω may be considered approximately as proportional to $V^{1/3}$ over some interval of V. On the basis of this approximation one has from (3) the following relations:

$$V_{c1} \propto \left(\frac{\sigma}{\rho g}\right)^{3/2}, \qquad (4)$$

$$\omega_{c1} \propto \left(\frac{\sigma}{\rho g}\right)^{1/2}. \qquad (5)$$

One can see, that the scale of the problem is determined, as one would expect, by the well-known capillary length [18]

$$a_c = \left(\frac{\sigma}{\rho g}\right)^{1/2}. \qquad (6)$$

As CORA experiments show, when moving the molten materials mixture wets the surface and leaves the track, a thin liquid film. So, the volume of a drop decreases. When it becomes less than V_{c1} the drop will stop. This is the capillary mechanism of the moving drop stopping, which plays an important role in the drops dynamics.

The greater is the volume of a drop, the greater is the velocity of its flowing down. When the volume of the drop exceeds the value of *the second critical volume* V_{c2} the kinetic energy of liquid exceeds the surface energy, and the drop transforms into rivulet. The value of V_{c2} is one more important parameter of the present model, which is on the one hand some function of surface tension, density and viscosity, and on the other hand may be measured directly.

The motion of liquid inside drops and rivulets is governed by Navier-Stokes hydrodynamical equation. On the basis of the solution of this equation with corresponding boundary conditions the *viscous drag force* connected with the dissipation of energy due to viscosity should be calculated.

In the limit of large rivulet volumes (long rivulets) the velocity of quazistationary flowing down is determined in the main by the balance of gravity and viscous drag force and tends to some finite value U_i. This velocity is a further important parameter.

It should be emphasized, that all these parameters: V_{c1}, ω_{c1}, V_{c2}, and U_r have clear physical sense and correspond to well-defined processes: the release of a drop, the transformation from a drop into a rivulet, the establishment of the stationary motion of a long rivulet. At the same time, from the candling model standpoint, they represent the adequate description of the material properties. To be sure, these parameters depend on the chemical composition of the relocating mixture and current temperature. That is why the experimental measurements of these values should be performed in sufficiently wide range of mixture chemical compositions and temperatures.

The paper is organized as follows. In Sec. 2, the general equations of motion of the liquid elements are derived. In Sec. 3, the drops and rivulets motion is investigated. In Sec. 4, the verification of the presented model is discussed and the comparison with the experimental results is presented.

2. General equations

The main processes involved in candling (capillarity, heat exchange and hydrodynamics) are described by complex nonlinear partial differential equations. The numerical or analytical solution of these equations requires sufficient efforts and is not acceptable within the framework of a system code, where corresponding problems appear a lot of times.

On the other hand, the main values of interest here are not the *exact* shape of the drop, the *exact* distribution of velocity inside the drop, and the *exact* temperature distribution. The main values of interest are *average* values: *average* (over the volume) velocity of the drop (i.e. velocity of centre of masses), *average* (over the contact area) rate of heat exchange between drop and fuel rod, and so on. The balance equations for these average values can be obtained by integration of the corresponding exact equations over the volume of a liquid element.

2.1. Momentum balance equation

The distribution of velocity U_r inside the liquid element is determined by Navier-Stokes equation

$$\rho\frac{\partial U_i}{\partial t} = -\frac{\partial \Pi_{ik}}{\partial x_k} + \rho g_i . \qquad (7)$$

Here

$$\Pi_{ik} = \rho U_i U_k + p\delta_{ik} - \eta\left(\frac{\partial U_i}{\partial x_k} - \frac{\partial U_k}{\partial x_i}\right) \qquad (8)$$

is the momentum flow tensor, ρ is the density, g_i is the gravity acceleration, p is the pressure, and η is the viscosity (see, for example, [18]). The integration of the equation (7) over the volume V of the liquid element gives

$$\int_V dV\left(\rho\frac{\partial U_i}{\partial t}\right) = -\int_V dV\left(\frac{\partial \Pi_{ik}}{\partial x_k}\right) + \rho g_i V . \qquad (9)$$

The first term may be rearranged in the following way:

$$\int_V dV\left(\rho\frac{\partial U_i}{\partial t}\right) = \frac{\partial}{\partial t}\int_V \rho U_i dV = \frac{\partial}{\partial t}\rho\bar{U}_i V , \qquad (10)$$

where $\rho\bar{U}_i V$ is the total momentum of the drop and $\bar{U}_i$ is the average velocity. When factoring out the sign of derivative from the integral in the last equation it was assumed, that the region of integration (shape of the liquid element) is not changed.

In reality, the shape of the liquid element may change due to the mass transfer to the surface (wetting). However, as it follows from the CORA experiments, the thickness of the track is sufficiently small, and the contribution of this process to the momentum exchange is also small (proportional to the track thickness) in comparison with the other factors (gravity, viscosity, capillary drag force). This contribution will be neglected below by virtue of the assumption about smallness of the track thickness.

The other example of the shape variations is transformation from a drop into a rivulet. In the present model this process is assumed to be instantaneous one, and is not considered in the momentum balance equation.

The integration over the volume in the second term may be replaced by the integration over the boundary (surface) of the liquid element:

$$\int_V dV\left(\frac{\partial \Pi_{ik}}{\partial x_k}\right) = \int_S \Pi_{ik} ds_k = \\ = \int_S \left(pn_i + \rho U_i U_k n_k - \pi_{ik} n_k\right) ds = \int_S f_i ds. \qquad (11)$$

Here ds_k is the surface element, n_i is the unit vector normal to the surface element and

$$f_i = pn_i + \rho U_i U_k n_k - \pi_{ik} n_k \qquad (12)$$

is the force, applied to the surface element.

So, one has the following momentum balance equation for the liquid element:

$$\rho\frac{d\left(\bar{U}_i V\right)}{dt} = -\int_S f_i ds + \rho g_i V \,. \qquad (13)$$

Taking into account the boundary conditions for the velocity on the liquid-solid interface, the total value of the *viscous drag force* F_v is given by the integration of the value of f_i over the contact area:

$$F_{vi} = \int_{S_{ls}} f_i ds = \int_{S_{ls}} \eta\left(\frac{\partial U_i}{\partial x_k} + \frac{\partial U_k}{\partial x_i}\right) n_k ds \,. \qquad (14)$$

Similarly, the *capillary drag force* F_c is given by the integration of f_i over the liquid-gas contact area [18]:

$$F_{ci} = \int_{S_{lg}} \sigma\left(\frac{1}{R_1} + \frac{1}{R_2}\right) n_i ds. \qquad (15)$$

The final form of the momentum balance equation is

$$\rho\frac{d\left(\bar{U}_i V\right)}{dt} = -F_c - F_v + \rho g_i V. \qquad (16)$$

2.2. Mass and energy balance equations

The integration of the continuity and energy conservation equations with the account of corresponding boundary conditions and possible change of the liquid element shape leads easily to the mass balance equation

$$\frac{dM}{dt} = -J_m \qquad (17)$$

and the energy balance equation

$$\frac{d}{dt}\left(\rho V \varepsilon\right) = -Q_c - Q_r - Q_m + H. \qquad (18)$$

Here

$$\varepsilon = h_s + C\left(T - T_s\right) \qquad (19)$$

is the internal energy of the mixture per unit mass, h_s is the mixture enthalpy at the solidus temperature, C is specific heat; Q_c is the total energy flow into fuel rod due to heat conduction, Q_r is the total energy flow due to radiation, Q_m is the total energy flow from a liquid element to the track due to mass transfer, and H is the internal heat generation.

Substitution of the mass balance equation (17) into (18) leads to the following form of the energy equation:

$$V\frac{d}{dt}\left(\rho\varepsilon\right) = -Q_c - Q_r + H. \qquad (20)$$

3. Drops and rivulets motion

3.1. Drops and rivulets

3.1.1. Drop

Liquid elements with volumes $V < V_{c1}$ are held on the vertical surface by the capillary forces and do not move. Liquid elements with volumes $V > V_{c1}$ flow down as single drops. As the volume of a drop is increased the linear dimensions a_d (width, thickness, length) are also increased. The nonlinearity of the capillary equation leads to a complex dependence of these quantities on the value of drop volume V_d. But in some interval of values of V $\left[V_{c1};\, V_{c2}\right]$ it may be assumed that

$$a_d \propto V_d^{1/3}. \qquad (21)$$

So, a *drop* is determined as liquid formation with volume V within the interval $\left[V_{c1};\, V_{c2}\right]$ and linear dimensions proportional to $V^{1/3}$.

3.1.2. Rivulet

The characteristic velocity of flowing down of the drop increases with the volume increase. When the volume of the drop reaches the value of the second critical volume V_{c2}, the drop becomes unstable because the kinetic energy of liquid exceeds the surface energy and the capillary forces are not able to hold liquid in the shape of a drop any more. That is why a free flowing down liquid element with volume $V > V_{c2}$ after fast transient process transforms into rivulet. The simplest estimation of the value of V_{c2} is based on the inequality

$$E_{kin} \propto \rho V U^2 > E_s \propto \sigma S, \qquad (22)$$

where $S \propto V^{2/3}$ is the square of the drop surface. This relation gives for the value of the second critical volume

$$V_{c2} \propto \left(\frac{\sigma}{\rho U^2} \right)^3. \qquad (23)$$

However, the value of the drop velocity U is also some function of the volume. More accurate estimation of the value of V_{c2} will be given below, after determination of capillary and viscous drag force terms in the momentum balance equation (16).

A rivulet has drop-like front part (due to the presence of the front contact line) and the main part, which is characterised by the width ω_r and the average (over the width) thickness $\bar{h}_r$. The value of $\bar{h}_r$ is assumed to be constant along the main part. Complex transient processes of wavy variations of $\bar{h}_r$ along the main part of the rivulet are assumed to be very quick and are not considered.

Flowing down velocity U_{mp} of the main part of a rivulet depends on the value of $\bar{h}_r$. The value of $\bar{h}_r$ is determined from the condition that the velocity of the drop-like front part of the rivulet U_{fp} must be equal to U_{mp}. This condition corresponds to the assumption of the stable shape of the rivulet. Thus, the average thickness of a rivulet $\bar{h}_r$ in the case of quazistationary flowing down cannot be arbitrary but has some fixed value which depends on the liquid properties.

In the present model it is assumed that the values of ω_r and $\bar{h}_r$ do not depend on the rivulet volume V_r. The only changing value is the length L_r of the rivulet which is proportional to V_r. So, one has by definition

$$V_r = (\text{width}) \times (\text{thickness}) \times (\text{length}) = \\ = \omega_r \cdot \bar{h}_r \cdot L_r. \qquad (24)$$

Thus, in quazistationary approximation a *rivulet* is defined as a liquid element with volume $V > V_{c2}$ and the length proportional to V_r. The width ω_r and the average thickness $\bar{h}_r$ have fixed values, determined by the condition of the stability of the rivulet's shape.

3.2. Momentum equation

3.2.1. Capillary drag force

The value of the capillary drag force F_c must be calculated in accordance with eq. (15) on the basis of capillary equation solution with corresponding boundary conditions. However, it is a rather complex mathematical problem [14, 19]. Furthermore, surface tension σ and especially contact angle θ are very sensitive to the presence of impurities and under real severe fuel damage conditions one may speak only about some efficient averaged values of σ and θ.

At the same time the adequate description of capillary effects may be given in terms of another pair of quantities: the first critical volume V_{c1} and the first critical width ω_{c1} instead of surface tension and contact angle. On the one hand these values represent the solution of the described capillary problem (find V_{c1} and ω_{c1} upon knowing σ and θ), and on the other hand they may be considered as empirical ones: they can be easily measured directly.

Substituting definition (3) into eq. (2), one obtains

$$F_c = \rho g V_{c1} \frac{\omega}{\omega_{c1}}. \qquad (25)$$

Here

$$\omega = \omega_d; \quad \omega_{c1} < \omega_d < \omega_{c2}$$

is the width of a drop, and

$$\omega = \omega_r = \omega_{c2}$$

is the width of a rivulet.

3.2.2. Viscous drag force

The direct analytical calculation of F_v is very difficult, because in order to find the velocity distribution one is to solve hydrodynamical equations for the region with complex boundary (liquid-gas interface). That is why for the case of a drop motion the empirical correlations will be used.

The motion of a liquid element down the vertical wall will be considered in quazistationary approximation: F_v value will depend only on U (but not on time derivatives of U). Then, according to similarity law the velocity distribution inside the drop (and hence, viscous drag

force F_v) is to depend only on Reynolds number. This dependence will be approximated by the power formula:

$$F_v = C_v \frac{\eta^2}{\rho} \mathrm{Re}^{\gamma} = C_v \frac{\eta^2}{\rho} \left(\frac{\rho U a}{\eta} \right)^{\gamma}. \quad (26)$$

Here factor η^2/ρ is chosen from the dimension considerations, and constant C_v is determined by the geometrical shape of the liquid element and does not depend on velocity.

The exponent γ accounts for the dependence of the viscous drag force on the regime of flowing down. In the limit of small velocities laminar flow is realised and $\gamma = 1$. CORA experiments show that the characteristic velocity of melt is of order of several dozens cm per second. The corresponding value of Re is $10^3 \div 10^4$. At such big values of Re, the turbulent flow takes place and one can expect that in such case the exponent γ will satisfy the unequality

$$\frac{3}{2} < \gamma < 2. \quad (27)$$

In the case of a drop motion Reynolds number is to be based on the characteristic thickness of a drop

$$h_d = V_d^{1/3} \quad (28)$$

and the expression for the viscous drag force has the form:

$$F_v = C_{vd} \frac{\eta^2}{\rho} \mathrm{Re}_d^{\gamma} = C_{vd} \frac{\eta^2}{\rho} \left(\frac{\rho U h_d}{\eta} \right)^{\gamma}. \quad (29)$$

The typical rivulet is assumed to be rather long: its length L exceeds sufficiently its width ω_{c2} and average thickness $\bar{h}_r$. In this case one may expect that the rate of energy dissipation inside the rivulet due to viscosity (and, consequently, viscous drag force) is proportional to the length L because of the identical nature of the motion of the liquid inside the different regions of the main part of the rivulet. Neglecting the contribution to the viscous drag force from the front drop-like part and the upper end of the rivulet, one may write

$$F_v = C_{vr} \frac{\eta^2}{\rho} \mathrm{Re}_r^{\gamma} \frac{L\omega_{c2}}{\bar{h}_r^2} = C_{vr} \frac{\eta^2}{\rho} \left(\frac{\rho U \bar{h}_r}{\eta} \right)^{\gamma} \frac{L\omega_{c2}}{\bar{h}_r^2}. \quad (30)$$

The contribution to the drag force due to the friction with the flowing steam is believed to be small as compared with the viscous drag force. That may be concluded from the CORA experiments video records: the falling down drops are moving much faster than the flowing down ones.

3.2.3. Steady-state rivulet velocity and the second critical volume

Taking into account expressions for capillary and drag forces (25), (29) and (30) the momentum equation (16) has the form:

$$\rho \frac{d(UV)}{dt} = -\rho g V_{c1} \frac{\omega}{\omega_{c1}} - C_{vd} \frac{\eta^2}{\rho} \left(\frac{\rho U h_d}{\eta} \right)^{\gamma} + \rho g V \quad (31)$$

in the case of a drop, and

$$\rho \frac{d(UV)}{dt} = -\rho g V_{c1} \frac{\omega_{c2}}{\omega_{c1}} - C_{vr} \frac{\eta^2}{\rho} \left(\frac{\rho U \bar{h}_r}{\eta} \right)^{\gamma} \frac{L\omega_{c2}}{\bar{h}_r^2} + \rho g V \quad (32)$$

in the case of a rivulet.

It should be noted that in the limit of rivulets with big length $L\,(L \to \infty)$ the relative influ-

ence of the capillary force F_c goes to zero. Really, F_c value does not depend on L, but two other forces (gravitational and viscous) are proportional to L. In a stationary situation ($d(UV)/dt = 0$) a balance of these two forces determines the value of steady state rivulet velocity U_r. From (32) it follows

$$\mathrm{Re}_r = C_{vr}^{-1/\gamma}\left(\frac{\bar{h}_r}{\delta_{g\nu}}\right)^{3/\gamma}, \qquad (33)$$

$$U_r = C_{vr}^{-1/\gamma}\cdot\frac{\eta}{\rho\bar{h}_r}\left(\frac{\bar{h}_r}{\delta_{g\nu}}\right)^{3/\gamma}. \qquad (33')$$

Here

$$\delta_{g\nu} = \left(\frac{\eta^2}{\rho^2 g}\right)^{1/3} \qquad (34)$$

is a well-known characteristic length of gravitational-viscous interaction.

Now it is possible to derive the relations for the values of the second critical volume V_{c2} and the second critical width ω_{c2} on the basis of the relation (22) and the momentum equation (31). The maximum velocity of a drop which corresponds to the volume V_{c2} may be estimated from eq.(31) by setting $dU/dt = 0, V = V_{c2}, \omega = \omega_{c2}$:

$$C_{vd}\frac{\eta^2}{\rho}\left(\frac{\rho U_{\max} h_d}{\eta}\right)^{\gamma} = \rho g V_{c1}\left(\frac{V_{c2}}{V_{c1}} - \frac{\omega_{c2}}{\omega_{c1}}\right). \qquad (35)$$

Equation (35), together with the relation (23) represents the implicit estimation of the values of V_{c2} and ω_{c2}.

The value of the second critical volume V_{c2} and the value of rivulet steady-state velocity U_r (33) are expressed in terms of average thickness and width of a rivulet, characteristic length of gravitational-viscous interaction, viscosity, surface tension, etc.

Some of these parameters are unknown; the others have been measured only for few temperatures and *U-Zr-O* mixture chemical compositions.

At the same time the values of V_{c1}, V_{c2} and U_r can be measured directly, by the use of close-up video recording or photographs in some range of temperatures and mixture chemical compositions, and thus may be considered as empirical parameters.

3.2.4 Motion of infinite rivulets

To a first approximation infinite rivulet can be considered as a film with constant thickness $h_f = \bar{h}_{ir}$ (i.e. the profile of the rivulet cross-section is assumed to be rectangular). The influence of the profile real shape [20-23] can be accounted for by the thickness averaging procedure. So, the description of infinite rivulets flowing down can be given using available experimental data of steady-state film flowing down the vertical surface.

The motion of a film is characterized by the value of film Reynolds number

$$\mathrm{Re}_f = \frac{\rho U h_f}{\eta}.$$

Depending on the value of Re, there exist the following types of the film flowing down the vertical surface [24]:

1. The stabilized laminar flowing down takes place for

$$\mathrm{Re}_f < \mathrm{Re}_B = 2.3 Ar^{0.2}, \qquad (36)$$

where

$$Ar = \left(\frac{\sigma^3\rho}{\eta^4 g}\right)^{1/2} \qquad (37)$$

is Archimed number. Estimations show that for the materials and temperatures involved the value of Re_B is of order of 60.

The connection between Re_f and h_f for this film flowing type is given by

$$\mathrm{Re}_f = \frac{1}{3}\left(\frac{h_f}{\delta_{g\nu}}\right)^3, \quad \mathrm{Re}_f < \mathrm{Re}_B \qquad (38)$$

2. Laminar-wavy flowing down:

$$\mathrm{Re}_f = \frac{1}{3}\left(\frac{h_f}{0.9\delta_{g\nu}}\right)^3, \quad \mathrm{Re}_B < \mathrm{Re}_f < 100 \qquad (39)$$

3. Transient laminar-turbulent flowing down:

$$\mathrm{Re}_f = \left(\frac{h_f}{0.3\delta_{g\nu}}\right)^{5/3}, \quad 100 < \mathrm{Re}_f < 400 \qquad (40)$$

4. Turbulent flowing down:

$$\mathrm{Re}_f = \left(\frac{h_f}{0.31\delta_{g\nu}}\right)^{12/7}, \quad \mathrm{Re}_f > 400 \div 500 \qquad (41)$$

The form of the relation (33) between steady-state rivulet velocity U_r and average thickness

$\bar{h}_r$ for the case of finite rivulet is of the same type as (38)-(41). It should be noted, however, that unlike the case of infinite rivulets the thickness $\bar{h}_r$ cannot be arbitrary. As it was mentioned above, the value of $\bar{h}_r$ is determined by the condition of the stability of rivulets shape and is some function of the mixture material properties.

3.3. Mass balance equation

The mass flow term J_m in the mass balance equation (17) in the case of a drop/rivulet flowing down can be represented in the following form:

$$J_m = \rho h \omega U, \qquad (42)$$

where h is a thickness of a track. The estimations based on the available experimental data show that the value of h is much less than the characteristic size of the drop:

$$h << \omega \propto a_c. \qquad (43)$$

This fact makes it possible to reduce the problem of a drop's track to the problem of a plane which is taken out from the liquid perpendicular to its surface. The last problem was considered by Landau and Levich [25]. Their expression for the thickness of a track, remaining on a plane has the following form:

$$h = B \frac{(\eta U)^{2/3}}{\sigma^{1/6} (\rho g)^{1/2}}, \qquad (44)$$

where B is some constant of order of unity.

The difference between three-dimensional situation of a drop and two-dimensional situation of a plane may lead to some deviations from the expression (44). However, one may believe that the dependence of the track thickness h on the velocity of a drop U will be just the same. Really, the expression (44) can be rewritten in terms of characteristic lengths and dimensionless Reynolds number:

3.4. Energy balance equation

The current temperature of the liquid element is given by the energy balance equation (18). For the solution of this equation it is necessary to determine the value of the total heat flow due to heat conduction Q_c (heat flow due to radiation is not considered here).

The comparison of the relations (33) and (38)-(41) gives for the value of the viscous drag force exponent γ:

$$\gamma = 1$$

in the laminar case, and

$$\gamma = 1.75 \div 1.8$$

for different turbulent regimes in line with the assumption (27).

$$h = B \frac{\delta_{gv}^2}{a_c} \mathrm{Re}^{2/3}. \qquad (45)$$

Since the difference between a drop and a plane cases (different shape of the liquid surface) is due to capillary effects, one may expect that it will manifest itself in the dependence of h on the capillary characteristic size a_c, but not in the dependence on Re. Together with the unequality (43) this consideration represents sufficient basis for the relation (44) to be used in the present model.

At the same time for the calculation of a track thickness in accordance with (50) it is necessary to know the value of surface tension and viscosity. For the same reasoning as for critical volumes V_{c1} and V_{c2} and steady-state rivulet velocity U_r, the thickness of the track (more exactly, the dimensionless characteristic thickness β, see below, Subsec.3.5) is considered as empirical quantity. The latter allows, among other aspects, to take into account the above mentioned possible influence of three-dimensional shape of the drop.

Substituting expression (44) in (17) one has the final form of the mass balance equation:

$$\frac{dV}{dt} = -B \frac{\eta^{2/3}}{\sigma^{1/6} (\rho g)^{1/2}} \omega U^{5/3}. \qquad (46)$$

As it was shown in [9], the approximating formula for the heat flow Q_c has the following form:

$$Q_c = \rho_w C_w V \frac{T_d - T_w}{t_h}, \qquad (47)$$

Here

$$t_h = \frac{1}{t_0^{-1} + t_\infty^{-1}} \qquad (48)$$

is effective heat exchange time;

$$t_0 = \frac{\omega^2}{\chi_w} \qquad (49)$$

is the characteristic heat exchange time, which correspond to the limit of non-moving drop

$$t_\infty = \frac{1}{2}\left(\frac{\pi\omega^3}{\chi_w U}\right) \qquad (50)$$

is the characteristic heat exchange time, which correspond to the limit of high velocities of a drop. Here subscript w (wall) instead of r (rod) for the temperatures and the properties of the fuel rod was used to avoid confusion with rivulet.

3.5. Dimensionless system of equations

Equations (18), (31)-(32), (46) with relations (47)-(50) constitute the full system of equations describing the flowing of drops and rivulets down a fuel rod. These equations contain several constants and physical parameters (critical volumes, critical widths, density, viscosity, etc.) which are not known or not determined exactly. However, the introducing of the new dimensionless variables makes it possible to reduce the large number of undefined parameters to a limited set of values, which have been discussed above ($V_{c1}, \omega_{c1}, V_{c2}, U_r$).

The new dimensionless variables are:

$$\begin{aligned}
v &= \frac{V}{V_{c1}} && \text{— volume,}\\
u &= \frac{U}{U_0} && \text{— velocity,}\\
p &= vu && \text{— momentum,}\\
z &= \frac{Z}{U_0^2/g} && \text{— position,}\\
t' &= \frac{t}{U_0/g} && \text{— time.}
\end{aligned} \qquad (51)$$

Here, the value of characteristic velocity U_0 is determined from the condition that the maximum value of rivulet velocity with $L >> \omega_{c2}$ at some characteristic temperature T_{char} is equal to the steady-state rivulet velocity U_r. The value of U_0 is given by

$$U_0 = U_r \cdot \exp\left(\frac{2-\gamma}{\gamma}\frac{\vartheta}{T'}\right)\cdot\left(\frac{V_{c2}}{V_{c1}}\right)^{(\gamma-3)/\gamma}. \qquad (52)$$

Such definition allows taking into account temperature dependence of the mixture viscosity:

$$\eta = \eta_0 \exp\left(\frac{\vartheta}{T}\right). \qquad (53)$$

In (52) γ is the exponent from the viscous drag force (26).

In terms of the introduced dimensionless variables the balance equations (18), (31)-(32), (46) with relations (47)-(50) may be written in the following universal form describing the motion of liquid elements both in drop-like and rivulet cases:

$$\frac{dp}{dz} = -p^{\gamma-1}v^{1-2\gamma/3}A^{\gamma-3}\exp\left(\frac{(2-\gamma)\vartheta}{T}\right) + p^{-1}v^2 - p^{-1}v^{4/3}A, \qquad (54)$$

$$\frac{dv}{dz} = -\beta p^{2/3}v^{-1/3}A\cdot\exp\left(\frac{2\vartheta}{3T}\right), \qquad (55)$$

$$\frac{dT}{dz} = -\frac{\rho_w C_w}{\rho C}\xi\left(T - T_w\right)\cdot\left[p^{-1}v^{1/3}A^{-2} + \frac{2}{\sqrt{\pi}}\lambda^{1/2}p^{-1/2}v\right], \qquad (56)$$

$$\frac{dt'}{dz} = p^{-1}v. \qquad (57)$$

Here the drop/rivulet switch parameter A

$$A = 1 \quad \text{if} \quad 1 \le v \le \frac{V_{c2}}{V_{c1}} \quad \text{(drop)},$$
$$A = \left(\frac{V_{c2}}{v V_{c1}} \right)^{1/3} \quad \text{if} \quad v > \frac{V_{c2}}{V_{c1}} \quad \text{(rivulet)}. \tag{58}$$

is introduced, which takes into account the difference in the linear sizes changing with volume changing for drop and rivulet cases.

The dimensionless position z is taken as an independent variable (this choice is convenient from the point of view of the determination of the liquid element location with respect to the fuel rod). The last equation (57) simply represents the definition of time derivative:

$$\frac{dz}{dt} = u = \frac{p}{v}$$

The other designations are:

$$\beta = h_U \frac{U_0^2}{g} \frac{\omega_{c1}}{V_{c1}}. \tag{59}$$

is the dimensionless track thickness;

$$h_U = B \frac{\left(\eta_0 U_0\right)^{2/3}}{\sigma^{1/6} \left(\rho g\right)^{1/2}}. \tag{60}$$

is the characteristic track thickness (just the same expression as the real track thickness (44), but based on the characteristic values U_0 (52) and η_0 (53));

$$\xi = \frac{U_0 \chi}{\omega_{c1}^2 g} = \frac{\tau_3}{\tau_1} \tag{61}$$

$$\lambda = \frac{U_0 \omega_{c1}}{\chi} = \frac{\tau_1}{\tau_2} \tag{62}$$

are dimensionless ratios. In the last two relations the following characteristic times, analogous to (48)-(49) but based on the characteristic values are used:

$$\tau_1 = \frac{\omega_{c1}^2}{\chi} \tag{63}$$

$$\tau_2 = \frac{\omega_{c1}}{U_0} \tag{64}$$

$$\tau_3 = \frac{U_0}{g} \tag{65}$$

One can see, that as it was stated above, all the parameters of the dimensionless system (54)-(57) are expressed in terms of the critical volumes V_{c1} and V_{c2}, the critical width ω_{c1}, rivulet steady-state velocity U_r and dimensionless track thickness β (59) (with an accuracy of the ratio C_{vd}/C_{vr}). The value of β can be either calculated upon knowing σ, η, V_{c1}, and ω_{c1} or determined by the comparison of the experimentally observed drop motion with the theory predictions. Note that the value of β (59) does not depend on the current volume or velocity of a drop.

So, β may be considered as a function of a given mixture chemical composition, just as the values of $V_{c1}, V_{c2}, \omega_{c1}$, and U_r are.

Therefore, from the present candling model standpoint, these values represent the complete description of the mixture properties.

4. Conclusions

The process of molten materials flowing down the fuel rod during severe accident at Nuclear Power Plant (candling process) was investigated in the present paper. The influence of this process upon the global core behavior during the accident is conditioned by the fact that it results in a change of flow cross sections or a blockage of the cooling channels, further fuel rod heatup and extended core degradation. The model is based on the system of differential equations obtained by the integration of the hydrodynamical equations over the volume of the moving liquid element taking into account boundary conditions on the liquid--solid and liquid-gas interfaces. The model allows to take into account: capillary effects (contact angle hysteresis, contact line resistance to displacement, wetting of the fuel rod surface) and to introduce

capillary scale; viscous effects (viscous drag force, laminar/turbulent regimes); heat exchange influence (temperature dependence of viscosity, surface tension, etc). The model allows to describe: various types of flowing down (drops, rivulets of different, length, films); transient processes (drop-rivulet transitions); non-stationary heat exchange of the liquid mixture with arbitrary temperature distribution along the fuel rod and thus, gives most adequate description of the candling process.

References

1. *T.J. Haste* et al., EUR-16695-In-vessel core degradation in LWR severe accidents, ECSC-EC-EAEC, Brussels-Luxembourg, 1996.
2. *J. Kronenberg, A.Schatz*, Extended Model of the Candling Process During Severe LWR Accidents, Technical Report IKE 2-126, Stuttgart, FRG, 1995.
3. *J. Burwell* et al., The thermal-hydraulics code ATHLET for analysis of PWR and BWR systems, 4th International Meeting on Nuclear Reactor Thermal-Hydraulics, Karlsruhe FRG, October, 1989.
4. *C.M. Allison* et al., SCDAP/RELAP/MOD3.1 Code Manual, NUREG/CR-6150, Volumes 1-5, INEL, Idaho, USA, 1990-1993.
5. *R. Gonzalez, P. Chatelard and F. Jacq*, ICARE2: a computer program for severe core damage analysis in LWRs, Note Technique SEMAR 93/33, IPSN, France, May 1993.
6. *B. Adroguer, S. Bourdon and C.Rongier*, Results of the International Standard Problem 28 on the PHEBUS SFD test B9+, 28th ASME/AIChE/ANS National Heat Transfer Conference, San Diego, August 1992.
7. *S. Hagen, P. Hofmann* et al., Results of SFD experiment CORA-13 (OECD International Standard Problem 31), KfK 5054, February 1993.
8. *W. Hering and R. Meyder*, Evaluation of CORA experiments using the Severe Core Damage Analysis Package (SCDAP), Kerntechnik, 53(1) (1988) 21-25.
9. *A.V. Palagin*, On the flowing down the fuel rod of *Zr-U-O* liquefied mixture during severe accident at nuclear power plant, Preprint NSI-1-93, Nuclear Safety Institute, Moscow, January 1993.
10. *A.V. Palagin*, Relocation of Molten Materials During Core Degradation (Candling). Transactions of SMiRT-13 Conference, Vol.1, 1995, pp. 139-144.
11. *M.S. Veshchunov, A.E. Kisselev, A.V. Palagin* et al., Code Package SVECHA: Modelling of Core Degradation Phenomena at Severe Accidents. Proceedings of the 7th International Meeting on Nuclear Reactor Thermal-Hydraulics NURETH-7, Vol.3, 1995, pp. 1914-1929.
12. *A.V. Palagin* "SVECHA Project Candling Model: Description of Melt Relocation During Core Degradation" Proceedings of the 31th National Heat Transfer Conference, Severe Accidents Fundamentals Session, Houston, USA, Vol.1, 1996.
13. *A.V. Palagin*, Physical model for molten materials relocation at the first stage of core degradation, Izvest. Acad. Nauk, Energetics, 4 (2002) 93 (in Russian).
14. *R. Finn*, Equilibrium Capillary Surfaces, Springer-Verlag, New York, 1986.
15. *E.B. Dussan V and R.Tao-Ping Chow*, On the ability of drops or bubbles to stick to non-horizontal surfaces of solids, J.Fluid Mech. 137 (1983) 1-29.
16. *E.B. Dussan V*, On the ability of drops or bubbles to stick to non-horizontal surfaces of solids. Part 2. Small drops or bubbles having contact angles of arbitrary size, J.Fluid Mech. 151 (1985) 1-20.
17. *E.B. Dussan V*, On the spreading of liquids on solid surfaces: static and dynamic contact lines, Ann. Rev. Fluid. Mech. 11 (1979) 371-400.
18. *L.D. Landau and E.M. Lifshitz*, Fluid Mechanics, Pergamon Press, New York, 1959.
19. *F. Milinazzo and Marvin Shinbrot*, A numerical Study of a drop on a vertical wall, J.Coll.Int.Sci. 121 (1988) 254-264.
20. *G.D. Towell and L.B. Rothfeld*, Hydrodynamics of rivulet flow, A.I.Ch.E.Journal, 12(5) (1966) 972-980.
21. *S. George Bankoff*, Minimum thickness of a draining liquid film, Int.J.Heat Mass Transfer, 14 (1971) 2143-2146.
22. *A. Doniec*, Laminar flow of a liquid down a vertical solid surface. Maximum thickness of liquid rivulet, PCH PhysicoChemical Hydrodynamics, 5 (1984) 143-152.
23. *A. Doniec*, Laminar flow of a liquid down a vertical solid surface, Can.J.Chem.Eng., 69(1) (1991) 198-202.
24. *S.S. Kutateladze*, Handbook of Heat Transfer and Hydrodynamic Resistance, Energoatomizdat, Moscow, 1990 (in Russian).
25. *V.G. Levich*, Physical-Chemical Hydrodynamics, Prentice-Hall, Inc., Englewood Cliffs, NJ, 1962.

Model for UO_2 Dissolution by Molten Zr

M.S. Veshchunov, A.V. Berdyshev

1. Introduction

Dissolution of UO_2 by molten Zircaloy (Zry) at high temperatures ≥1760 °C (melting point of Zry) is an important chemical process influencing core melt progression in nuclear reactor severe accidents. Owing to this process, liquefaction and relocation of UO_2 take place about 1000 degrees below the melting point of the fuel (≈2850 °C). This process has been intensively studied experimentally and theoretically.

1.1. Review of the existing tests

The first molten Zry/UO_2 — crucible experiments up to 2000 °C were reported by Dienst, Hofmann and Kerwin-Peck [1]. From their observations of cooled specimens from dissolution tests at 2000 °C, Dienst et al. postulated that, after the short time interval required from crucible wetting, rapid crucible dissolution occurs to form a homogeneous (U, Zr, O) melt. This melt subsequently decomposes during cooling into α-Zr(O), a (U, Zr) alloy and, with higher oxygen concentrations in the melt, a ceramic (U, Zr)O_2 phase.

In subsequent work [2, 3], Hofmann and coworkers performed a series of crucible dissolution tests at 100 °C intervals within the temperature range 1950-2250 °C, using an argon atmosphere and an outer tungsten crucible as the susceptor. They used large UO_2 crucibles (in comparison with subsequent experiments) with Zry charge, which after rapid cooling in the end of the tests were sectioned and analysed metallographically. The melts were analysed by an indirect method, by correlating the measured area fraction of the (U, Zr)O_2 phase in the melt with (U, Zr)O_2 area fraction in control samples of known chemical composition.

Based on the melt analyses and metallographic observations, Hofmann stated that up to ~ 30 wt.% UO_2 can be dissolved in the melt before the ceramic (U,Zr)O_2 phase is seen in the cooled specimen. He postulated that very rapid crucible dissolution during the first ~100 s at 1950 and 2050°C (the incubation, or saturation period) forms a homogeneous (U,Zr,O) melt that decomposes during cooling into α-Zr(O) and a (U, Zr) alloy. After this time (during the post-incubation, or precipitation period), continuous increase of the ceramic phase (U, Zr)O_2 portion in the refrozen melt was observed which was interpreted as increase of the melt UO_2 content. The dissolution rate at each temperature during this period calculated within the above mentioned methods (by measured correlation between the ceramic phase fraction and the melt UO_2 content), followed a parabolic time law. The most important confirmation of the continuation of the dissolution process during the precipitation stage were visual observations of the UO_2 crucible wall thinning at this stage detected in the post-test photographs of the samples.

Later Kim and Olander published the results of two sets of crucible-based experiments [4, 5]. In the first set, the reaction between UO_2 and molten Zry was investigated at temperatures between 1900 and 2200 °C using yttria-washed thoria crucibles to contain the molten Zry charge, and with a thin disk of either single-crystal or polycrystalline UO_2 covering each crucible floor. Polished sections of the post-test specimens were examined by optical microscopy, scanning electron microscopy, Auger electron spectroscopy and electron microprobe analysis. The complicated structure observed in the quenched specimens contained a two-phase region at the interface between solid and molten phases. Growth of the two-phase layer followed the parabolic rate law, as did the thickness decrease of the UO_2 disk. Average concentration distributions in the direction

normal to the reacting surface revealed diffusion mass transfer in the melt.

Although these experiments provided important insights into many aspects of the UO_2/molten Zry reaction, the melts were essentially quiescent because of the absence of gravity-driven convective stirring. For this reason, Kim and Olander performed a second set of experiments to investigate convection-controlled UO_2 dissolution. These tests were performed in crucible machined from LWR fuel pellets (and for this reason with smaller dimensions in comparison with Hofmann's tests), each containing a charge of either as-received Zry or a prefabricated oxygen containing Zry (6 wt.% O) alloy. Other test details were identical to those for diffusion-controlled dissolution tests of the first series.

Kim and Olander observed that after the termination of the rapid first, saturation stage, a two-phase region appeared in the microstructure. Simultaneously with the appearance of this region, the bulk of the refrozen melt did not show anymore a (U, Zr) alloy, and chunks (precipitates) of (U, Zr)O_{2-x} appeared (qualitatively the same behavior as observed in the experiments of Hofmann et al. [1-3]). The dissolution kinetics were unambiguously characterised in Kim's thesis [5] by the parabolic time dependence of the uranium content in the liquid phase (during the second, precipitation stage) and described by an Arrhenius equation.

Additional confirmations of the continuation of the UO_2 dissolution during the precipitation stage were the direct measurements of the UO_2 crucible wall thinning at this stage. From figures presented in [4, 5] it was clearly seen that the UO_2 wall dissolution rates during the precipitation (post-incubation) stage, being rather small at 2000 °C, significantly increased at higher temperatures (2100 and 2200 °C).

A serious qualitative disagreement exists between the data presented above, of the two groups and the results of Hayward and George [6, 7] who observed none of the above-described phenomena after the termination of the saturation stage: a) increase of the U atom concentration in the molten zone; b) increase of the ceramic phase portion in the refrozen melt; c) reduction of the UO_2 crucible wall thickness. On this basis Hayward and George deduced a logical conclusion about the cessation of the dissolution process after saturation of the liquid phase during the first, saturation stage in their tests.

In order to understand apparent inconsistencies in the literature and reduce uncertainties in the fuel dissolution modeling, new tests were carried out jointly by AECL (P. Hayward) and FZK (P. Hofmann and J. Stuckert) with analytical support of IBRAE within CIT Project (4^{th} Framework programme of EC) [8]:

(i) isothermal UO_2 crucible dissolution tests at 2100 and 2200 °C and reaction times up to 30 min., and (ii) additional tests at 2200 °C where the crucible-cavity bottom was isolated from the reaction by an inert yttria disc.

Main test results were:

- The dissolution of UO_2 takes place in two stages: a first short saturation period with a rapid dissolution and a second period during which there is a slower UO_2 dissolution accompanied by precipitation of a ceramic (U, Zr)O_{2-x} phase in the saturated melt.
- The main cause of the discrepancy amongst the previous results was connected with different UO_2 crucible sizes (wall thickness), UO_2/Zry mass ratios and melt surface to volume ratios (S/V) which influence the oxygen diffusion from crucible walls to the melt.

1.2. Review of the existing models

The original work of Hofmann et al. [2] led to development of the LISI numerical code [9]. This code involved an assumption that oxygen diffusion was the main parameter controlling UO_2/molten Zry interaction and ignored the influence of melt convection on fuel dissolution in the UO_2 crucible tests.

Kim and Olander subsequently demonstrated in [4, 5] that gravity-driven convection in such tests with vertical crucible walls was the controlling parameter for dissolution rates. They used the well-known analogy between heat and mass transfer to derive an expression for the mass transfer coefficient in the melt. However, in their model [4], Kim and Olander did not consider an important influence of the oxygen diffusion from the interior of the UO_2 into the melt and, for this reason, their model predicted very a slow approach of the U content in the melt to the saturation point at a late stage of the disso-

lution process. In order to fit this model prediction to their measurements in the second, precipitation stage (initially interpreted in [5] as continuous UO_2 dissolution obeyed parabolic time law), further in the paper [4] they attempted the description of the U content in the molten phase approaching saturation composition by another function of time, $\propto (1+\alpha t)^{-4}$.

For modeling of the first series of Kim and Olander tests with dissolution of UO_2 disk (without convective stirring of the melt), an O-diffusion-based theoretical model describing mass transport through the two-phase region at the UO_2/molten Zry interface was proposed by Veshchunov and Volchek [10]. Being based on the self-consistent consideration of the oxygen diffusion in the three regions (solid, liquid and two-phase zones) the model allowed description of the two-phase layer growth (as well as the thickness decrease of the UO_2 disk) followed the parabolic rate law, in fair agreement with observations [4, 5].

An attempt of self-consistent consideration of the oxygen diffusion mass transport in the solid phase and convective mass transport in the liquid phase for modeling of fuel dissolution in the UO_2 crucible test series was made in the paper of Olander [11]. However, being qualitatively correct for description of initial stage of the dissolution process, the model predicted very slow approach of the melt bulk composition to the final saturation value (during $\sim 10^4$ s). The onset of the ceramic phase $(U,Z)O_{2-x}$ chunks after initial time period (~ 50-100 s) observed in the tests [4] was assigned to the interface disintegration during continuous approach of the melt to the final saturation composition.

Qualitatively similar behavior (continuous approach to the saturation composition of the melt during all the dissolution process) was proposed by Hayward and George [6] who considered solid/liquid interface kinetics as a rate-controlling step, thus, neglecting mass transfer mechanisms in both the solid and liquid phases.

In the model of Veshchunov and Hofmann [12] it was demonstrated for the first time that in the crucible tests the bulk melt composition attains its saturation value during a short time interval of the first, saturation period. In the subsequent time interval (precipitation period) the continued oxygen supply to the interface by diffusion from fuel interior leads to an oversaturation of the melt, resulting in precipitation of the ceramic $(U, Zr)O_{2-x}$ phase in the melt. Simultaneously, dissolution of solid UO_2 can be continued (and can be accompanied by disintegration of the solid phase boundary with the same composition $(U,Zr)O_{2-x}$ as precipitated particles). Therefore, the oxygen diffusion in the solid UO_2 phase determines the kinetics of both processes of the UO_2 dissolution and the formation of $(U,Zr)O_{2-x}$ precipitates after completion of the saturation stage, and for this reason these kinetics have to obey a parabolic time law ($\propto t^{1/2}$) in the precipitation stage. This allows a natural explanation of the apparent contradictions between observations of various groups since various wall thickness of the crucibles in different tests lead to different diffusion times determining cessation of the dissolution process.

The model further developed by Veshchunov and Hofmann in cooperation with Berdyshev [13] self-consistently describes various saturation melt compositions attained during the saturation stage in all the three test series (Hofmann et al., Kim and Olander, Hayward and George) with various oxygen contents (zero and non-zero) of the initial Zr melt.

For the description of the second, precipitation period a general approach was formulated in [12, 13]. However, in the absence of all necessary data for the solution of the obtained complete system of equations of the general model, a simplified approach for searching for the model solution was proposed in [12]. By this approach an additional assumption about invariable composition of the forming precipitates (satisfactorily corresponding to the independent observations of Hofmann et al. and Kim and Olander) was made. This assumption allowed to avoid a complicated consideration of the mass transfer in the two-phase zone of the melt during precipitation period. As a result, the model self-consistently described (at least, qualitatively) all the observations of the different experiments [2, 4, 6] at different temperatures.

In the subsequent paper [14], for the explanation of the Hayward and George's data [6, 7] Olander searched for another particular solution of the general model formulated in the paper [12], using different additional assumption. Namely, it was postulated that the dissolution rate is equal to zero in the precipitation period at 2000 °C. However, this solution was valid only for the partial description of the particular case of the dissolution process at

2000 °C in the tests [4], being in direct contradiction with observations either of Hofmann or of Kim and Olander at higher temperatures 2100-2200 °C. For this reason, the model was not applied for the description of high temperature tests of Kim and Olander [4].

The new AECL tests [8] performed with the thick wall crucibles originally used in the Hofmann's tests had to resolve the contradiction amongst previous experimental results and/or their interpretations and specify a particular solution of the developed general model in [12, 13] corresponding to the new observations. Among the earlier found solutions for the precipitation stage corresponding to: (i) continuous dissolution of the crucible walls and roughly invariable composition of growing precipitates ([12, 13]), and (ii) zero dissolution rates and varying precipitate composition ([14]); a more general solution of the model [12, 13] corresponding to continuous dissolution and varying precipitate composition was also searched. This last approach was realized in the subsequent papers of the authors on simultaneous dissolution of UO_2 and ZrO_2 by molten Zry (see p. 82 in this issue).

2. Modeling of UO_2 dissolution by molten Zircaloy

The following section gives brief generalized descriptions of the UO_2-dissolution tests modeling.

2.1. Basic model

In accordance with the previously developed model [12, 13], the bulk melt composition in the crucible tests attains its saturation value during the short time interval of the first, saturation period. In the subsequent time interval (precipitation period) the continued oxygen supply to the interface by diffusion from fuel interior leads to an oversaturation of the melt, resulting in precipitation of the ceramic $(U, Zr)O_{2-x}$ phase in the melt. Simultaneously, dissolution of solid UO_2 can be continued (and can be accompanied by disintegration of the solid phase boundary with the same composition $(U, Zr)O_{2-x}$ as precipitated particles). Therefore, the oxygen diffusion in the solid UO_2 phase determines the kinetics of both processes of the UO_2 dissolution and the formation of $(U, Zr)O_{2-x}$ precipitates after completion of the saturation stage, and for this reason these kinetics have to obey a parabolic time law ($\propto t^{1/2}$) in the precipitation stage.

It was demonstrated by Kim and Olander [4] that in the case of a vertical position of the solid/liquid interface a mass transfer in the liquid phase could be produced by natural convection driven by the density differences in the melt (due to the large weight of U atoms in comparison with Zr atoms). A rather high value of the mass transfer coefficient estimated in [4] was re-evaluated and confirmed in the paper [12] by the analysis of the concentration profiles observed in the crucible melts. The values of the convective mass transfer coefficients estimated in [4]: $k_O \approx 10^{-2}$ cm/s, $k_U \approx 0.5 \cdot 10^{-2}$ cm/s, are also used in the present report for modeling of the new crucible tests.

The consideration of the UO_2 crucible interactions with the Zry melt in the previously developed model [12, 13] was performed in the framework of the simplified one-dimensional (1-D) model with the cylindrical geometry and linear dimensions (radii) corresponding to the same *S/V* (surface to melt volume) ratio as in the crucibles at the beginning of interactions.

2.2. Development of a two-dimensional model

In order to account for the observed continuous increase of the melt volume and interactions of the melt with fresh surfaces of the UO_2 crucible, Fig. 1, a two-dimensional (2-d) model was developed. The model generalises the simplified 1-d model, in which linear dimensions of the interaction system in the vertical direction was fixed and invariable with time. Such a consideration apparently does not correspond to the real geometry of the crucible tests in which melt dissolves crucible bottom simultaneously with the walls, on the one hand, and the upper level of the melt continuously increases in the course of dissolution process, on the other hand. As can be concluded from the comparison of calculation results, the 1-d model allows satisfactory predictions of the variation of the uranium weight content in the melt, however, incorrectly describes the depth of the dissolved crucible walls.

The molar density of pure liquid U is ≈ 0.071 mol/cm^3 and of liquid Zr is ≈ 0.064 mol/cm^3, thus it was assumed that the molar density of the melt is independent of the U/Zr ratio:

$$c_U + c_{Zr} + \theta c_O = \text{const} = c_M \approx 0.068 \text{ mol/cm}^3, \quad (1)$$

where $0 \le \theta \le 1$ (see [12, 13]). In the limiting case $\theta = 1$, the molar density of the melt is independent of its composition and is denoted by c_M. In the other limiting case $\theta = 0$, the molar density of the melt is independent of the dissolved oxygen concentration and is denoted by c_M on an oxygen-free basis [11]. In the following calculations $\theta = 1$ is accepted, however, the calculations can be easily generalized to the other values of the parameter θ.

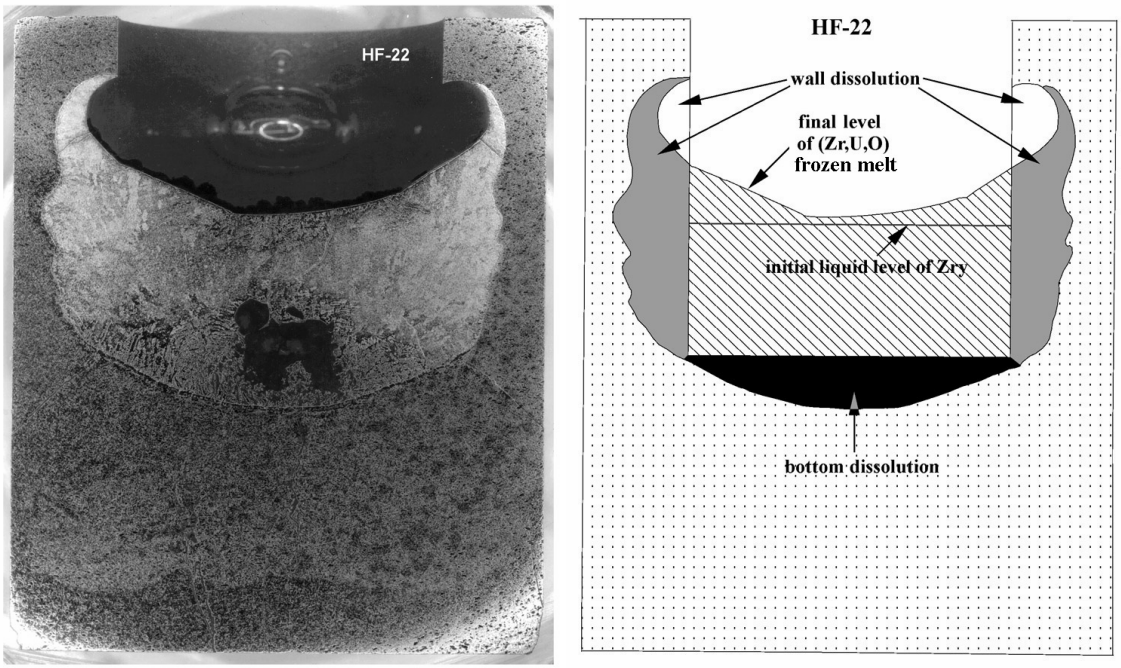

Fig. 1. Cross section of UO_2 crucible: as-polished sample and its image analysis (from [8]).

2.2.1. Saturation stage

During the first, saturation stage, rather a quick dissolution of UO_2 and saturation of molten Zry with U and O atoms up to the limiting value (determined by the liquidus line of the equilibrium ternary U-Zr-O phase diagram) takes place. The description of this process within the 2-D model is based on the self-consistent consideration of the mass balance equations in the melt for each component (O, U, Zr) along with the flux matches at the vertical and horizontal interfaces.

Mass balances of the different components (O, U, Zr):

$$\frac{\partial\left[c_{\mathrm{O}}(B)\pi R^2(h+H)\right]}{\partial t}=\rho_{\mathrm{O}}(I)\left[2\pi R(h+H)\frac{\partial R}{\partial t}+\pi R^2\frac{\partial h}{\partial t}\right]+D_{\mathrm{O}}^{(\mathrm{UO_2})}\left.\frac{\partial\rho_{\mathrm{O}}}{\partial r}\right|_I\left[2\pi R(h+H)+\pi R^2\right], \tag{2}$$

$$\frac{\partial\left[c_{\mathrm{U}}(B)\pi R^2(h+H)\right]}{\partial t}=\rho_{\mathrm{U}}(I)\left[2\pi R(h+H)\frac{\partial R}{\partial t}+\pi R^2\frac{\partial h}{\partial t}\right], \tag{3}$$

$$\frac{\partial\left[c_{\mathrm{Zr}}(B)\pi R^2(h+H)\right]}{\partial t}=0, \tag{4}$$

where $c_i(I)$, $c_i(B)$ are the molar densities (mol/cm^3) of the different components (i = O, U, Zr) at the interface boundary and in the bulk of the liquid phase, respectively; $\rho_i(I)$, $\rho_i(B)$ are the corresponding values in the solid phase; $D_{\mathrm{O}}^{(\mathrm{UO_2})}$ is the oxygen chemical diffusion coefficient in the solid phase; *R, H,* and *h* denote liquid phase linear dimensions, presented in Fig. 2.

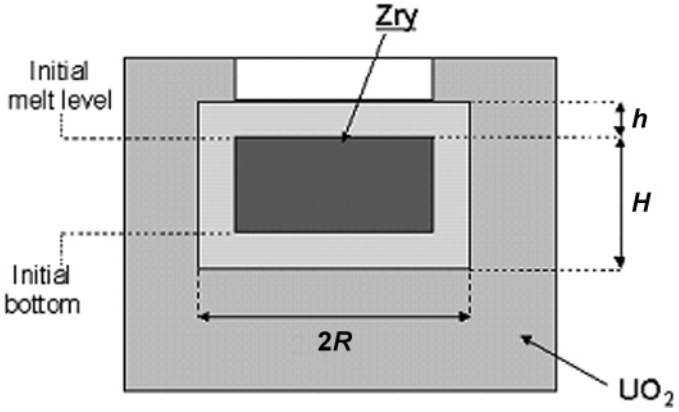

Fig. 2. Linear dimensions of the melt in the UO_2 crucible at different moments (schematic).

Vertical interface flux matches:

oxygen:

$$\left[\rho_{\mathrm{O}}(I_{\mathrm{V}})-c_{\mathrm{O}}(I_{\mathrm{V}})\right]\frac{\partial R}{\partial t}=c_{\mathrm{O}}(B)v_R(I_{\mathrm{V}})+k_{\mathrm{O}}\left[c_{\mathrm{O}}(I_V)-c_{\mathrm{O}}(B)\right]-D_{\mathrm{O}}^{(\mathrm{UO_2})}\left.\frac{\partial\rho_{\mathrm{O}}}{\partial r}\right|_{I_{\mathrm{V}}}. \tag{5}$$

uranium:

$$\left[\rho_{\mathrm{U}}(B)-c_{\mathrm{U}}(\mathrm{I_V})\right]\frac{\partial R}{\partial t}=c_{\mathrm{U}}(B)v_R(I_{\mathrm{V}})+k_{\mathrm{U}}\left[c_{\mathrm{U}}(I_{\mathrm{V}})-c_{\mathrm{U}}(B)\right]. \tag{6}$$

zirconium:

$$\left[-c_{\mathrm{Zr}}(I_{\mathrm{V}})\right]\frac{\partial R}{\partial t}=c_{\mathrm{Zr}}(B)v_R(I_{\mathrm{V}})+k_{\mathrm{Zr}}\left[c_{\mathrm{Zr}}(I_{\mathrm{V}})-c_{\mathrm{Zr}}(B)\right]. \tag{7}$$

where k_i is the convective mass transfer coefficients of different components (i = O, U, Zr) in the melt; I_V designates the vertical interface; v_R is the net velocity of the melt near the vertical interface.

These equations should be completed by the Stefan-Maxwell equation in the transition layer:

$$k_O\left[c_O(I_V)-c_O(B)\right]+k_U\left[c_U(I_V)-c_U(B)\right]+k_{Zr}\left[c_{Zr}(I_V)-c_{Zr}(B)\right]=0. \quad (8)$$

Superposition of Eqs. (5)-(8) yields:

$$\rho_L v_R(I_V)=(\rho_O(I)+\rho_U(B)-\rho_L)\frac{\partial R}{\partial t}+D_O^{(UO_2)}\frac{\partial \rho_O}{\partial r}.\Big|_{I_V}. \quad (9)$$

Horizontal interface flux matches:

oxygen:

$$\left[\rho_O(I)-c_O(I_H)\right]\frac{\partial H}{\partial t}=c_O(B)v_H(I_H)+k_O\left[c_O(I_H)-c_O(B)\right]-D_O^{(UO_2)}\left.\frac{\partial \rho_O}{\partial r}\right|_{I_H}. \quad (10)$$

Uranium:

$$\left[\rho_U(B)-c_U(I_H)\right]\frac{\partial H}{\partial t}=c_U(B)v_H(I_H)+k_U\left[c_U(I_H)-c_U(B)\right], \quad (11)$$

and superposition relationship:

$$\rho_L v_H(I_H)=(\rho_O(I)+\rho_U(B)-\rho_L)\frac{\partial H}{\partial t}+D_O^{(UO_2)}\frac{\partial \rho_O}{\partial r}.\Big|_{I_H}. \quad (12)$$

where I_H designates the bottom (horizontal) interface; v_H is the net velocity of the melt near the horizontal interface.

2.2.2. Precipitation stage

For the theoretical description of the precipitation stage the model self-consistently accounts for three simultaneous processes: (1) dissolution of UO_2 crucible by the liquid phase; (2) formation and growing of ceramic (U, Zr)O_{2-x} precipitates; (3) diffusion transport of oxygen from UO_2 to the liquid. As demonstrated in [12, 13], the last process is especially important since after completion of the saturation stage the oxygen diffusion in the solid UO_2 phase determines the kinetics of both processes of the UO_2 dissolution and the formation of (U, Zr)O_{2-x} precipitates, which for this reason obey a parabolic time law ($\propto t^{1/2}$) in the precipitation stage.

The system of mass balance equations of different elements (O, U, Zr) in the homogeneously mixed liquid phase (containing ceramic precipitates) initially proposed in [12, 13], has the general form:

$$-\frac{\partial}{\partial t}\left(\rho_U \alpha V\right)=\frac{\partial}{\partial t}\left[c_{Zr}\left(W-V+\Phi\right)\right], \quad (13)$$

$$-\frac{\partial}{\partial t}\left[\rho_U\left(1-\alpha\right)V\right]+\frac{\partial}{\partial t}\left[\rho_U W\right]=\frac{\partial}{\partial t}\left[c_U\left(W-V+\Phi\right)\right], \quad (14)$$

$$-\frac{\partial}{\partial t}\left[\rho_O V\right]+\frac{\partial}{\partial t}\left[\rho_O W\right]-D_O^{(UO_2)}=\frac{\partial}{\partial t}\left[c_O\left(W-V+\Phi\right)\right], \quad (15)$$

where the parameter α describes the composition of the ceramic precipitates $(U_{1-\alpha}, Zr_\alpha)O_{2-x}$, V is defined as the integral volume of this precipitated phase, $(W+\Phi)$ is the integral volume occupied by the melt (containing the precipitates), Φ is the fraction of this volume connected with the expansion of the melt (see Fig. 6 in [12]).

The system of Eqs. (13)-(15) should be generally completed by the flux match conditions at the solid/liquid interface for the self-consistent description of the dissolution process. However, the formation of the two-phase zone (liquid + ceramic precipitates) near the interface makes this problem especially complicated. In [12, 13] a general approach for the description of mass transfer through the two-phase zone was formulated. However, lacking additional experimental data necessary for the development of the complete model, the authors used a simplified approach. Instead of the flux match equations, it was proposed to use additional simple assumptions based on the experimental observations which allowed the solution of the incomplete system of mass balance equations (13)-(15). In [12] such an assumption was $\alpha \approx$ const, which corresponded to the invariable composition of the ceramic phase $(U_{1-\alpha}, Zr_\alpha)O_{2-x}$ formed during the precipitation stage. This assumption was in fair agreement with observations either of Hofmann et al. [16] or Kim [5].

As demonstrated in [13], for the description of the crucible tests [4] at 2273 K such a model predicts a rather slow rate of the UO_2 crucible walls dissolution (which was really observed at this temperature in [4]), thus, for this particular test series this additional condition $\alpha \approx$ const can be substituted with a satisfactory accuracy by the condition $\partial W/\partial t \approx 0$. Namely this assumption was made in the paper by Olander [14]. However, this solution was in direct contradiction with observations at higher temperatures 2373–2473 K either of Hofmann [3] or Kim and Olander [4, 5], and for this reason, the model [14] was not applied to the description of high-temperature tests of Kim and Olander [4].

An additional post-test EDX analysis of some of the samples obtained in the new test series at 2273 K revealed that among ceramic particles in the melt formed on cool down, there exist also other particles with a different composition corresponding to $\alpha \approx 0.25$-0.35. It was assumed that namely these particles were formed at temperature and, for this reason, the value of the model parameter α in this test series was searched in the vicinity of the above indicated interval. For the other tests this parameter was searched by fitting of the model calculations to the measured data.

2.2.3. Verification of the model parameters

Specification of the model parameters was performed on the base of the model validation against the previous AECL tests with smaller crucibles at T = 2373 and 2473 K [6, 7]. At temperature 2273 K the model was verified against experiments performed by different groups [5-7] on dissolution of the UO_2 crucibles by molten Zircaloy. The uranium saturation concentration in the melt attained in the end of the saturation stage was different in these tests owing to the different dimensions of the UO_2 crucibles and Zry charges, and the model reproduced these data satisfactory, Fig. 3. Further correlation was made between the numerical model and experimental results [6, 7] at temperatures 2373 and 2473 K, Fig. 4. In the tests [6,7] two sets of experimental data on UO_2/Zry and UO_2/(Zry/25at.%O) interactions under identical conditions were presented. These data give an opportunity, at first to choose the position of the liquidus line at 2373 and 2473 K (from the first set of the experiments, with pure Zry), and then to perform on this basis the validation of the numerical model for the pre-oxydized charge (Zry with 25at.%O) using derived parameters of the liquidus line linearised in a small vicinity of the melt composition. Numerical results obtained in such a way were in a good agreement with the experimental data, Fig. 4.

Subsequent calculations and analyses of the new experimental data were carried out without any additional fitting of the parameters.

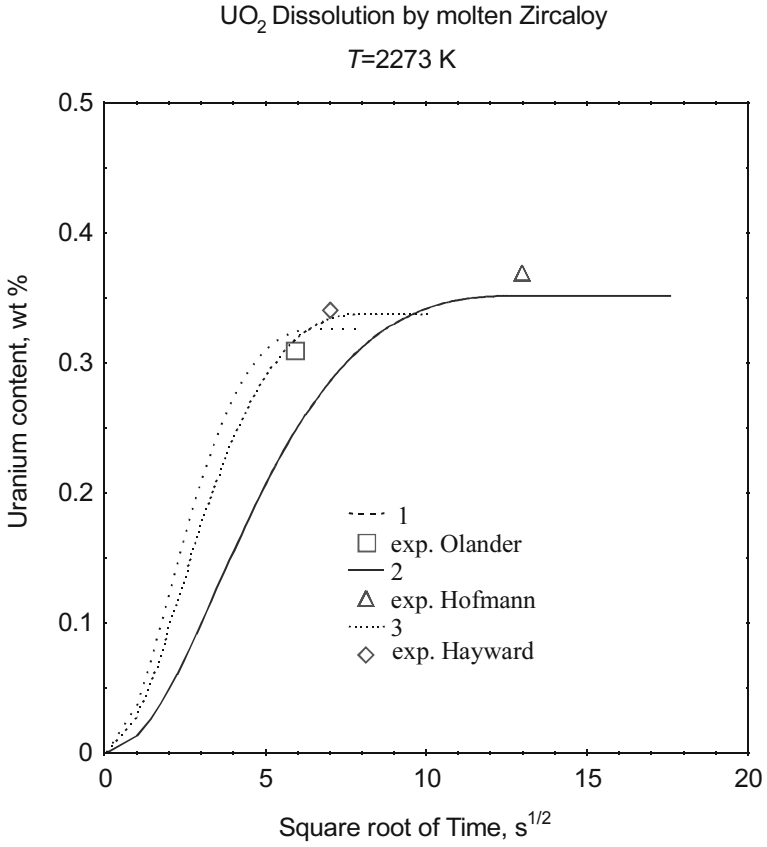

Fig. 3. Uranium weight content in the melt in the first, saturation stage of the dissolution process. Calculated curves 1,2,3 correspond to the experimental data [2, 4, 6].

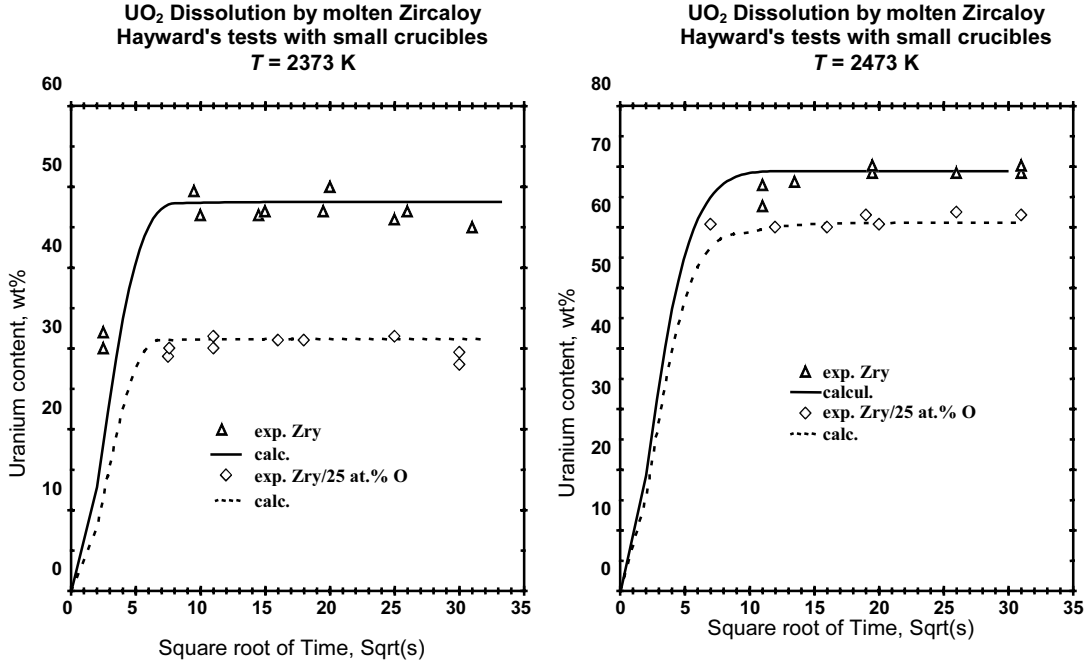

Fig. 4. Comparison of calculated and measured uranium weight content in the melt in the first, saturation stage in two tests [6] at 2373 K and 2473 K with pure and pre-oxydized Zry charges.

2.3. Model predictions

The calculation scheme and numerical algorithms of the simplified model [12,13] were generalised and applied for the solution of the present 2-D model.

Based on the above-described new 2-D model, the new results can be interpreted as follows:

In the tests [8] with large crucibles, the model predicts the same level of melt saturation during the initial 200-300 s (the saturation period) as in the small crucible tests [6]. These saturation levels are ≈ 50 wt.% U at 2373 K and ≈ 71 wt.% U at 2473 K. In the large crucible tests, however, dissolution of the crucible walls is predicted to continue during the subsequent 100–200 s (the precipitation period), until the oxygen diffusion flux from the crucible walls is sustained. In the tests without bottom isolation (i.e., with no yttria discs), the uranium melt concentration will increase during the precipitation period by 6-8 wt.% at 2373 K, Fig. 5, and by 3-4 wt.% at 2473 K, Fig. 6a, giving final concentrations of ≈ 57 wt.% U and ≈ 74 wt.% U, respectively.

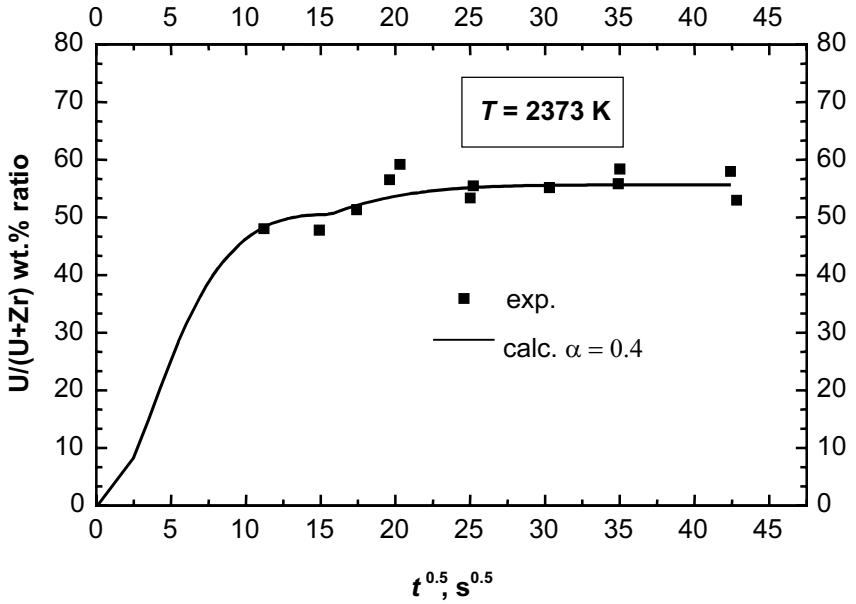

Fig. 5. Time evolution of uranium weight content in the melt at 2373 K (tests [8] without bottom isolation).

In the new 2200 °C test series with bottom isolation [8] (i.e., with yttria discs), the maximum uranium melt concentration of 74 wt.% is predicted to occur after 300–400 s Fig. 6b. However, this time is within the duration of the saturation period, because the time for saturation to occur is extended by the higher melt *S/V* (surface to volume) ratio used in these tests (and practically coincides with the characteristic time of oxygen diffusion from the crucible walls). For the same reason (higher *S/V* ratio), the saturation level reached in the tests with yttria discs would be ≈ 74 wt.% U, i.e., 3-4 wt.% higher than the saturation level reached in the tests without yttria discs (≈ 71 wt.%). This level would be very close to the maximum U content attained in tests without yttria discs at the end of the saturation + precipitation periods, Fig. 6a.

Calculation results for the wall dissolution depth in the various tests, Fig. 7, are in a reasonable agreement with the results of the post-test image analysis of the crucible cross-section photographs performed in the FZK [8].

Since crucibles have rather thick UO_2 bottom (≈ 10 mm), oxygen diffusion from the bottom is continued after ≈ 400 s during the subsequent ≈ 1200 s. Being exhausted with oxygen, the crucible walls will not be dissolved during this time interval. However, owing to continuous oxygen supply from the interior of the bottom into the melt, precipitation process in the melt will be continued during this time interval (in accordance with observations).

After successful verification of the model against the new test data, it was applied to the prediction of the fuel pellet dissolution in the real fuel rod configuration with various melt thickness and melt oxygen concentrations. Results of the calculations are presented in Fig. 8.

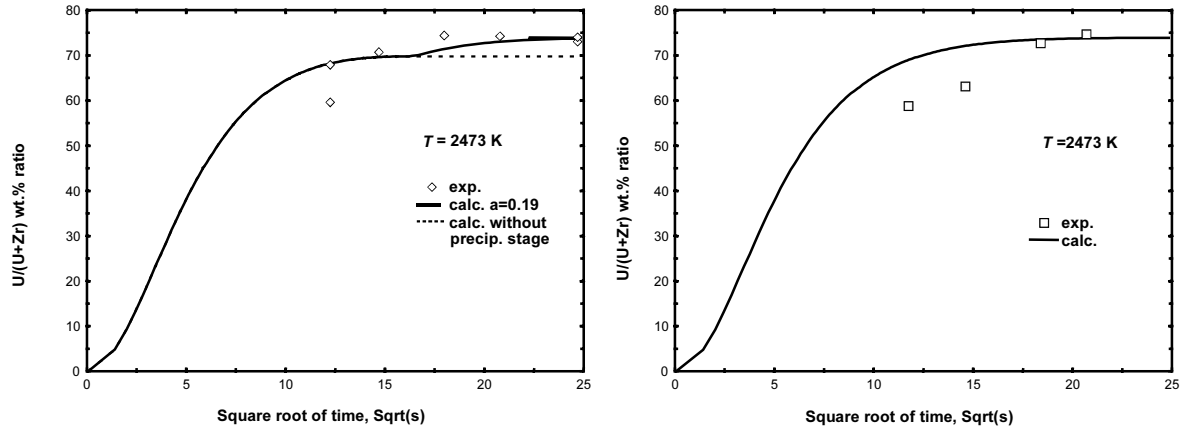

(a) *(b)*

Fig. 6. Time evolution of uranium weight content in the melt at 2473 K (tests [8] without (a) and with (b) bottom isolation).

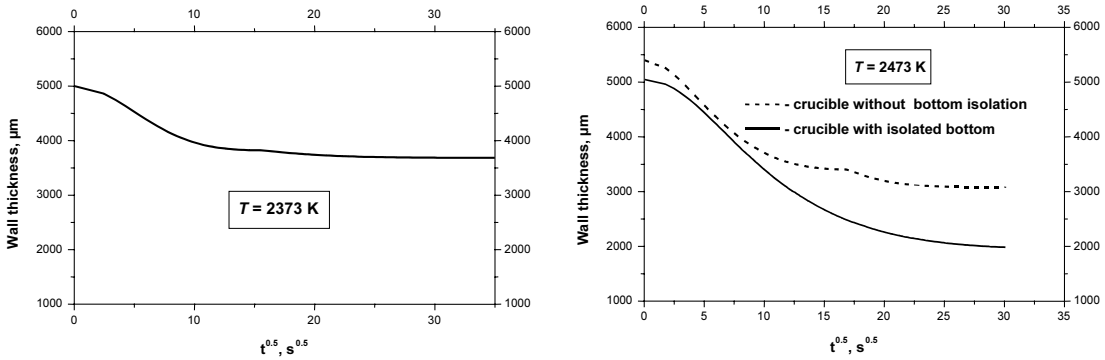

(a) *(b)*

Fig. 7. Time evolution of crucible wall thickness at (a)2373 K and (b) 2473 K (tests [8] with and without bottom isolation).

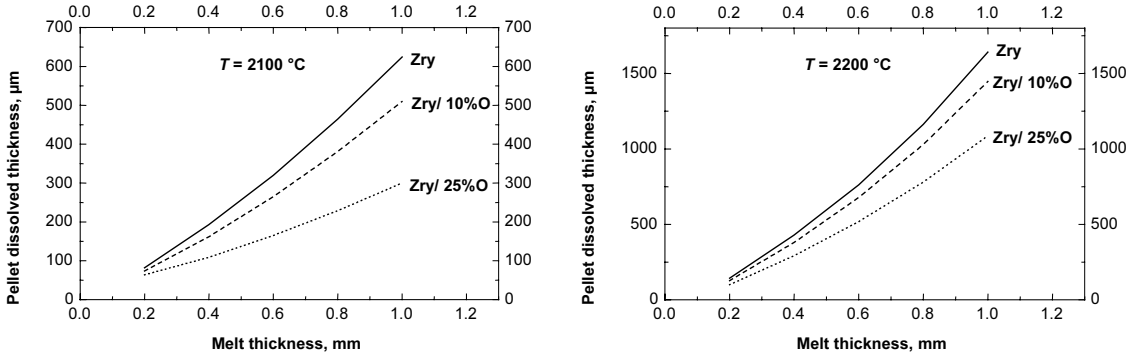

Fig. 8. Application of the model to the fuel rod configuration: dependence of the fuel pellet dissolved thickness on the melt thickness at various oxygen contents in the melt.

3. Conclusions

It can be generally concluded that, depending on the test conditions and the melt/crucible geometry, dissolution of the crucible walls can continue during one or two periods.

Dissolution of the UO_2 crucible by molten Zry in the AECL tests [8] continued during two stages and was satisfactory simulated by the new 2-D model.

The major part of a crucible was dissolved during the first, saturation stage. In this stage dissolution occurred with high rates until melt saturation was reached.

The minor part of a crucible was dissolved during the second, precipitation stage. In this stage dissolution occurred with slow rates and was accompanied with the ceramic phase precipitation. However, the amount of dissolution during the second period was not so significant as assumed in the beginning of the test program.

These conclusions cannot be directly applied to the description of fuel dissolution under real accident conditions, because the influence of dissolved oxygen in the Zircaloy melt on the rate and saturation level of uranium has not been studied experimentally in the tests [8]. Thus, the current model needs to be extended to include this phenomenon, as well as simultaneous dissolution phenomena.

References

1. *W.Dienst*, P.Hofmann and D.Kerwin-Peck, Nucl.Technol.65 (1984) 109.
2. *P.Hofmann, H.Uetsuka, A.N.Wilhelm and E.A.Garcia*, Proc.Int.Symp. on Severe Accidents in Nuclear Power Plants, Sorrento, Italy, March 21-25, 1988, IEAE-SM-296/1, p.3.
3. *P.Hofmann, Ch.Adelhelm, H.Uetsuka, H.Zimmermann, J.Burbach, G.Gausmann, D.Kempf, K.Kurz, H.Metzger, G.Streib*, Jahresbericht 1985, KfK 4000(1986)4200-56.
4. *K.T.Kim and D.R.Olander*, J.Nucl.Mater. 154 (1988) 85, 102.
5. *K.T.Kim*, UO_2 dissolution by molten Zircaloy, Thesis (University of California, Berkeley), 1988
6. *P.J.Hayward and I.M.George*, J.Nucl.Mater. 208 (1994) 35, 43.
7. *P.J.Hayward and I.M.George*, J.Nucl.Mater. 232 (1996) 1, 13.
8. *P.J. Hayward, P. Hofmann, J. Stuckert, M.S. Veshchunov, A.V. Berdyshev*, UO_2 Dissolution by Molten Zircaloy. New Experimental Results and Modelling. Report FZKA 6379, INV-CIT(99)-P029, Karlsruhe, Germany, 1999.
9. *A.Wilhelm and E.Garcia*, J.Nucl.Mater. 158(1988)143.
10. *M.S.Veshchunov and A.M.Volchek*, J.Nucl.Mater., 188 (1992) 177.
11. *D.R.Olander*, Materials-Chemistry and Transport Modeling for Severe Accident Analysis in Light-Water Reactors, Lawrence Berkeley Laboratory Report LBL-32530 (1992).
12. *M.S.Veshchunov and P.Hofmann*, J.Nucl.Mater. 209 (1994) 27.
13. *M.S.Veshchunov, P.Hofmann, A.V.Berdyshev*, J.Nucl.Mater., 231 (1996) 1-19.
14. *D.R.Olander*, J.Nucl.Mater., 224 (1995) 254.

Model for ZrO_2 Dissolution by Molten Zr

M.S. Veshchunov, A.V. Berdyshev

1. Introduction

The dissolution of ZrO_2 by molten Zry (≥ 1760 °C) influences many physico-chemical processes during core collapse: liquefaction of ZrO_2 at about 1000 °C below its melting point, relocation of (U, Zr, O) melts after failure of the outer ZrO_2 layer on cladding tubes and FP release rates.

1.1. Review of existing tests

The first published dissolution rates for ZrO_2 in molten Zry are from the work of Hofmann et al. [1, 2]. Their data (hereafter called as KfK data) were obtained from crucible-based experiments wherein molten Zry charges were held in ZrO_2 crucibles for known time intervals while being isothermally heated at temperatures in the range 2000-2400 °C. The used crucibles were of cubic zirconia stabilised with 2.7 wt.% CaO and were ~ 75% of theoretical density. Melt analysis was performed by an indirect method involving comparison of the melt microstructures and phase contents with those of previously melted ZrO_2 standards. The amount of dissolved ZrO_2 in each crucible melt was determined by correlating the measured area fraction of ZrO_2 in the cooled melt with those in the standards. After an initial brief period of very rapid ZrO_2 dissolution, the dissolution rate followed a parabolic time law.

However, this procedure of post-test analysis neglects additional amounts of oxygen in the melt transported from the oxide by the diffusion mechanism. For this reason, interpretation of the obtained data in terms of dissolved ZrO_2 in [1] might be erroneous. Nevertheless, direct data [1] are rather valuable and can be correctly reinterpreted by a model taking into account the diffusion fluxes in the solid phase (see below).

The experimental data [1] on the ZrO_2 crucible wall dissolution by molten Zry had only preliminary character, however, unambiguously demonstrated that the ZrO_2 dissolution rates at high temperatures ($T \geq 1900$ °C) are significant and comparable with the UO_2 dissolution rates measured in the analogous crucible tests. Besides, it was observed in these tests that the composition of the solidified melt was spatially homogeneous, analogously to the observations in the UO_2 dissolution tests. This implies that convective mixing of the melt occurs also in the course of ZrO_2 dissolution by molten Zry.

Moreover, additional visual analysis of the post-test photographs of the specimens obtained in [1] (see below Section 3) apparently evidences that after cessation in ~ 500 s of the dissolution process the propagation of the solid/liquid interface changes its direction from inward to outward, that is the erosion of the ZrO_2 turns to the corrosion.

A recent AECL study of Hayward and George [3] was designed to overcome deficiencies of indirect analysis of [1] using a more direct chemical analysis method that can distinguish between chemical dissolution and oxygen diffusion reactions. The experiments involved isothermal heating tests at 2000-2300 °C with Zry charges in yttria-stabilised ZrO_2 crucibles that also contained ~1.4 wt.% HfO_2 as a natural impurity. Each post-test melt was then sectioned, dissolved and analysed for Zr, Hf, and Y by ICP spectrometry. Optical and electron-microscopy examinations and analyses were also performed on the post-test samples. The Hf content of each melt was used to calculate the corresponding crucible weight fraction that had dissolved or become dispersed in the melt, based on the assumption that Hf dissolves congruently with Zry.

Chemical analyses of the melts [3] indicates that, in all but the 2000 °C experiments, rapid dissolution had occurred during the first ~ 100-200 s. After this time, a solid ZrO_{2-x}

layer formed at the crucible/melt interface and grew at a rate that was proportional to $t^{1/2}$ but independent of the reaction temperature.

In order to understand apparent inconsistencies in the literature and reduce uncertainties on the clad failure conditions, new isothermal ZrO_2 dissolution tests with ZrO_2 crucibles of different dimensions with and without bottom isolation by yttria disks at 2100, 2200, and 2300 °C and reaction times up to 30 min, were carried out in FZK [4]. Additionally the post-test analysis of the earlier tests on ZrO_2 crucibles dissolution performed in KfK [1, 2] and AECL [3] and comparison with the new FZK test data, were performed in [4].

Main results of the tests [4] are:

The crucible/melt interaction is governed by the oxygen diffusion along grain boundaries and occurs in two stages: erosion (or dissolution) and corrosion. During the corrosion stage the dissolution ceases and an interface oxide layer growth commences. The erosion/corrosion process develops up to melt oxygen saturation and in some tests continues with a slower rate accompanied by the ceramic ZrO_2 phase precipitation in the saturated melt. The kinetics increase with the surface to volume (*S/V*) ratio and strongly depend on the crucible wall thickness.

1.2. Review of existing models

Kinetics of ZrO_2 dissolution by molten Zry was modelled by Veshchunov and Berdyshev [5, 6] within a general approach for modeling of more complicated process of simultaneous dissolution of UO_2 and ZrO_2 by molten Zry, observed in the integral CORA tests as an important mechanism of core degradation. Detailed qualitative and quantitative data on post-tests metallographic examinations of the fuel rods in the bundle CORA tests allowed generalisation of the theoretical UO_2 dissolution model of Veshchunov and Hofmann [7] for modeling simultaneous dissolution kinetics. As a particular case of the general model, separate dissolution of ZrO_2 by molten Zry was specially analysed in [5,6].

In accordance with visual observations of [1], the model qualitatively correctly describes system behavior at early (erosion) and late (corrosion) stages of the interaction process. It was demonstrated that the direction and velocity of the interface propagation is determined by the oxygen flux matching condition at this interface. In the initial stage of solid/liquid interactions the oxygen mass flux in the convectively stirred melt is rather large in comparison with that in the solid phase; for this reason, a high dissolution rate proportional to the difference between the two fluxes prevails. Since the melt approaches the saturation composition as a result of the dissolution process, the convective flux reduces and eventually matches the oxygen flux in the ZrO_2. This moment corresponds to the cessation of the erosion stage. After this moment the flux in the solid phase becomes larger than that in the melt since reduction of the latter with time is much quicker. According to the flux matching equation the velocity of the interface propagation changes its sign and the corrosion stage commences.

The subsequent experiments [3] confirmed the independent model predictions [5, 6] qualitatively (two stages of erosion/corrosion process) and quantitatively (close to the parabolic rate law of oxide layer growth at the second, corrosion stage).

A further development of the model and a more thorough analysis of the new FZK tests [4] on ZrO_2 dissolution by molten Zry in comparison with the previous tests [1-3] are presented in the current report.

The IBRAE developed model explains the disagreement observed in previous dissolution results and reproduces correctly the new FZK tests.

The ZrO_2 dissolution model is able to describe self-consistently the two erosion and corosion stages observed in the previous KfK and AECL tests and the unique erosion stage observed in new FZK tests. Differences between KfK, AECL and FZK results are due to different crucible/melt geometries which induce different characteristic times in dissolution and oxygen diffusion processes.

The new model can be applied for analysis of cladding oxide shell failure presented in the current issue, see p. 100.

2. Model description

The model of ZrO_2 dissolution is essentially based on the theoretical consideration of the ZrO_2/(Zry melt) interactions proposed in the authors' paper [6] for modeling KfK tests [1, 2].

The experimental data [1, 2] on the ZrO_2 crucible wall dissolution by molten Zry had only preliminary character, however, unambiguously demonstrated that the ZrO_2 dissolution rates at high temperatures ($T \geq 1900$ °C) were significant and comparable with the UO_2 dissolution rates measured in the analogous crucible tests. Besides, it was observed in these tests that the composition of the solidified melt was spatially homogeneous, analogously to the observations in the UO_2 dissolution tests. This implies that convective mixing of the melt occurs also in the course of ZrO_2 dissolution by molten Zr. In the UO_2 dissolution tests a mass transfer in the liquid phase could be produced by natural convection driven by the density differences in the melt (due to the large weight of U atoms in comparison with Zr atoms). In the ZrO_2 dissolution tests the convective stirring of the melt apparently occurs only owing to high temperature gradients in the crucible system (the temperature difference between crucible walls and the melt attained 50-100 K in the crucible tests [4]). For this reason, the mass transfer coefficient in the melt was expected to be much smaller in the ZrO_2 dissolution tests in comparison with the UO_2 dissolution tests.

On the other hand, some differences exist between the two dissolution processes. Additional visual analysis of the post-test photographs of the specimens obtained in [1] apparently evidences that after cessation of the dissolution process within ~ 500 s (termed hereafter the erosion stage) the propagation of the solid/liquid interface changes its direction from inward to outward, that is the erosion of the ZrO_2 turns to the corrosion, Fig. 1.

Such a behavior has quite a natural explanation. As it will be shown below, the direction and velocity of the interface propagation is determined by the oxygen flux matching condition at this interface. In the initial stage of solid/liquid interactions the oxygen mass flux in the convectively stirred melt is rather large in comparison with that in the solid phase; for this reason, a high dissolution rate proportional to the difference between the two fluxes prevails. Since the melt approaches the saturation composition as a result of the dissolution process, the convection flux reduces and eventually matches the oxygen flux in the ZrO_2. This moment corresponds to the cessation of the erosion stage. After this moment the flux in the solid phase becomes larger than that in the melt, since reduction of the latter with time is much quicker. In accordance with the flux matching equation the velocity of the interface propagation changes its sign and the corrosion stage commences. For these reasons, in the following calculations the both stages are represented by a single curve for the "dissolved wall thickness" which becomes positive in the erosion stage and negative in the corrosion stage.

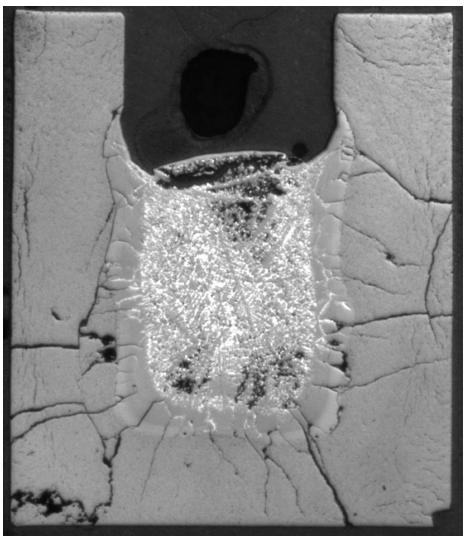

Fig. 1. Post-test appearance of ZrO_2 crucible cross-sections in FZK dissolution tests [4] at ≈ 2200 °C with duration 10 min and sidewall corrosion layer thickness ≈ 1 mm.

Equations, describing (molten Zr)/ZrO_2 dissolution process, express various elements (oxygen, zirconium) mass balances and interface oxygen flux matches [6] in the one-dimensional (1-D) geometry: plane or cylindrical, Fig. 2. In the frames of the convective mixing model after some transformations, these equations take the form

$$\frac{dC_O(B)}{dt} = \frac{(k_O + \partial r_2/\partial t)\left[C_O(I) - C_O(B)\right]}{r_2^L - r_1^L}(2r_2)^{L-1}, \quad (1)$$

$$\frac{dr_2}{dt} = \frac{D_O^{(ZrO_2)}\left.\frac{\partial \varphi_O}{\partial r}\right|_{II} - k_O\left[C_O(I) - C_O(B)\right]}{C_O(I) - \varphi_O(I)\tilde{B}}, \quad (2)$$

$$\frac{dr_3}{dt} = (1-\tilde{B})\left(\frac{r_2}{r_3}\right)^{L-1}\frac{dr_2}{dt}, \quad (3)$$

where r_1 and r_2 are the melt boundaries positions; r_3 is the ZrO_2 outer boundary position; $\tilde{B} = C_{Zr}/\rho_{Zr}$ is the zirconium molar density ratio in the liquid (molten Zr) and solid (ZrO_2) phases; $C_O(B)$, $C_O(I)$ are the bulk and interface values of oxygen concentration in the liquid Zr, respectively; $\varphi_O(r)$ is oxygen concentration in the solid phase and $\varphi_O(I)$ is its interface value at the lower ZrO_{2-x} phase boundary. Eqs. (1)-(3) are written in the general form comprising cylindrical ($L = 2$) and plane geometry ($L = 1$).

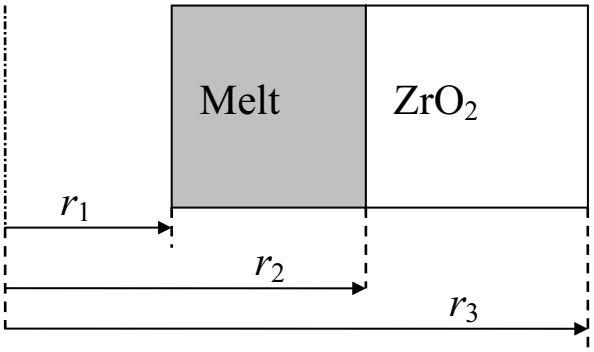

Fig. 2. Schematic representation of the two interaction layers in the ZrO_2/(molten Zry) system.

Oxygen radial distribution in zirconia $\varphi_O(r)$ and relevant boundary gradient $(\partial\varphi_O/\partial r)\big|_{r=r_2}$ at the (molten Zr)/ZrO_2 interface are found by the solution of a moving boundary diffusion problem:

$$\frac{\partial \varphi_O}{\partial t} + V\frac{\partial \varphi_O}{\partial r} = \frac{1}{r}\frac{\partial}{\partial r}\left(rD_i\frac{\partial \varphi_O}{\partial r}\right), \quad (4)$$

with boundary conditions $\varphi_O(r=r_2, t) = \varphi_O(I)$ and $(\partial\varphi_O/\partial r)\big|_{r=r_2} = 0$, corresponding to the conditions of the dissolution experiments in an inert atmosphere.

The model includes parameters such as k_O, $D_O^{(ZrO_2)}$, $C_O(I)$ which are poorly known, especially at temperatures above 2000 °C. These parameters could be derived by fitting experimental and theoretical data.

In order to simulate the crucible tests without bottom isolation (KfK [1], AECL [3] and FZK [4]) in the framework of the 1-D model, a special procedure for calculation of linear dimensions (internal and external radii) of the effective 1-D cylinder was applied. Namely, the internal radius $R_{in} = r_2(t = 0)$ of the cylinder was chosen to provide the same *S/V* ratio as in the real crucible (i.e. $R_{in} = 2S/V$), whereas the external radius $R_e = r_3(t = 0)$ was chosen to provide the same ratio V_{cr}/V_{liq}, where V_{cr} is the total volume of the interacting part of the crucible (bottom + wetted parts of the walls), V_{liq} is the melt volume. These two conditions afforded an appropriate treatment of the mass transfer process in the melt and oxygen diffusion in the crucible in the course of the interactions.

3. Model validation

3.1. Analysis of the KfK tests

In the experiments [1] dissolution of the inner walls of ZrO_2 crucibles by molten Zircaloy was studied at temperatures between 2000 and 2400 °C. The data on weight content of ZrO_2 in the melt were obtained by comparison of a cooled melt microstructure with those of previously prepared (Zry melt)/ZrO_2 standards. This procedure generally neglected additional

amounts of oxygen in the melt transported from the oxide by the diffusion mechanism. For this reason, interpretation of the obtained data in terms of dissolved ZrO_2 in [1] might be inaccurate. However, these data can be correctly re-interpreted by the present model taking into account the oxygen diffusion fluxes in the solid phase. Indeed, the determined in [1] quantity W_{ZrO_2} (recalculated from the observed ceramic phase fraction in the solidified melt) can be uniquely connected with the molar oxygen density $C_O(B)$ in the liquid phase by formula:

$$W_{ZrO_2} = \frac{0.5C_O(B)(\mu_{Zr} + 2\mu_O)}{C_{Zr}\mu_{Zr} + C_O(B)\mu_O}, \qquad (5)$$

where μ_O (μ_{Zr}) is the oxygen (zirconium) molar weight, C_{Zr} is the zirconium molar density in the melt. Hence, experimental results [1] can be treated within the framework of the present model in order to extract necessary parameters. The density of the stabilised zirconia was taken 75%TD in accordance with the crucible material properties; the lower oxygen concentration in zirconia (attained at the interface) was taken ≈ 60 at.% in accordance with the EDX measurements performed in the new FZK test series [4] with a similar crucible material.

Calculated by the numerical model and measured values of weight content of ZrO_2 in the melt are presented in Fig. 3. Fitted parameters are shown in Table 1. Temperature dependence of mass transfer coefficient is well described by the Arrhenius equation:

$$k_O = 1.06 \cdot 10^7 \cdot \exp(-108436/RT) \text{ cm/s},$$

where R = 1.987 cal/mol, T in K, which fairly corresponds to the power dependence $k_O \propto D_{liq}^{3/4}$ (D_{liq} is the oxygen diffusion coefficient in the melt). As expected, the value of k_O in the ZrO_2 dissolution tests occurred to be much smaller than that in the UO_2 dissolution tests (which at 2000 °C was estimated as ~ 10^{-2} cm/s [7], i.e. one order of magnitude larger).

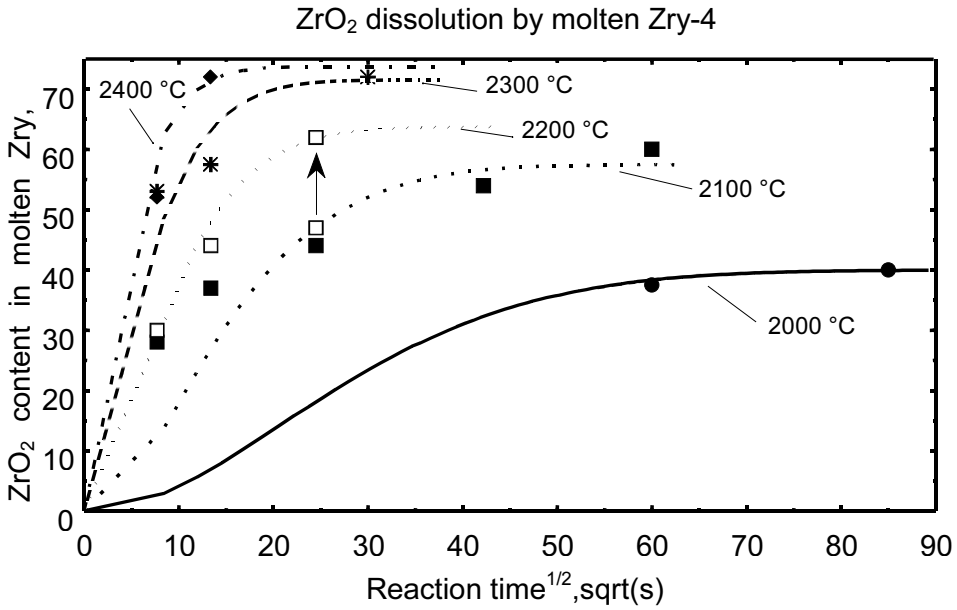

Fig. 3. ZrO_2 weight content in the liquid phase.Validation of the model against KfK test data [1], corrected by the new FZK [4] post-test analysis (arrow at 2200 °C).

Oxygen diffusion coefficient in the stabilised ZrO_2 is described by the Arrhenius correlation:

$$D_O^{(ZrO_2)} = 4 \cdot \exp(-24000/T) \text{ cm}^2/\text{s}.$$

The largest deviation of the calculated kinetic curves from the test data was attained at 2200 °C after 600 s, however, this discrepancy was successfully eliminated (see an arrow in Fig. 3) after additional image analysis of the corresponding KfK test sample microphotograph (see [4]).

Table 1. Oxygen mass transfer coefficient and oxygen terminal solubility in the molten zirconium obtained by fitting of the experimental data [1] and calculated values

T,°C	k_O, cm/s	$C_O(I)$, at.(wt.)% calculated
2000	$3 \cdot 10^{-4}$	40 (10.5)
2100	$1.1 \cdot 10^{-3}$	49 (14.5)
2200	$2 \cdot 10^{-3}$	50 (15)
2300	$6 \cdot 10^{-3}$	56.5 (17.6)
2400	$1.3 \cdot 10^{-2}$	57.4 (19.2)

3.2. Analysis of the AECL tests

The same model was applied without any additional tuning of the model internal parameters (such as mass transfer and diffusion coefficients and the oxygen terminal solubility in the liquid zirconium) for modeling the AECL tests [3] which were performed under identical conditions (2100 and 2200 °C), but in smaller crucibles with larger material density (5.9 g/cm^3). Since the *S/V* ratio and wall thickness in these tests differed considerably from that in the KfK tests, the model predicts quite different behavior in comparison with the previous case.

Indeed, as seen from Figs. 4 and 5, in both temperature cases that model predicts a small erosion (≈ 0.2 mm) during the first ≈ 200 s of the interactions, and then a noticeable growth of the corrosion layer. Being compared with the available experimental data [3], these results demonstrate a very good agreement with the measurements in the first ≈ 1000 s of the interactions, however, at a later stage of the corrosion period the model overpredicts the corrosion layer thickness. Deviations of the calculated kinetic curves from the experimental points in Figs. 4 and 5 occur practically simultaneously with the onset of the melt oversaturation, i.e. when the oxygen melt content exceeds ≈ 14 at.% at 2100°C and ≈ 15 at.% at 2200 °C. This confirms that the ceramic ZrO_2 phase precipitation in the melt bulk at a late stage of corrosion can influence the interaction kinetics. Further development of the model for consideration of the precipataion process was presented in [8].

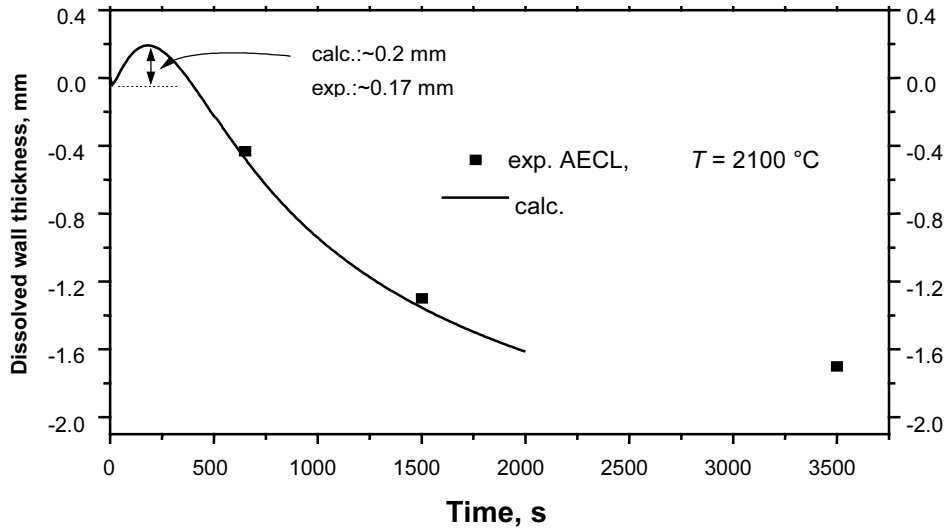

Fig. 4. Simulations of AECL tests [3] on ZrO_2 crucible dissolution by molten Zry: erosion and corrosion at 2100 °C.

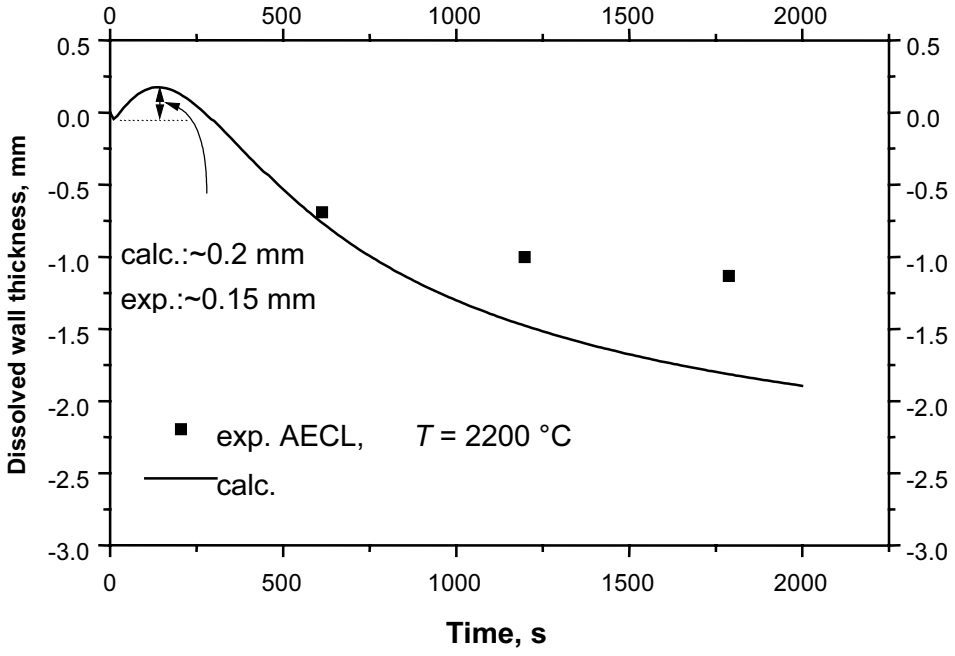

Fig. 5. Simulations of AECL tests [3] on ZrO_2 crucible dissolution by molten Zry: erosion and corrosion at 2200 °C

3.3. Analysis of the FZK tests with small crucibles

The new FZK test series [4] with small crucibles was performed under conditions similar to the previous AECL tests [3] and with the same crucible dimensions, specially to reproduce the main qualitative observations of the previous tests. In order to avoid the melt transfusion from the top of the crucibles at a late stage of the interactions, the initial Zry charge volume was decreased in comparison with the AECL tests, thus, the *S/V* ratio was also decreased, correspondingly.

In this case the model predicts a similar to the previous case erosion behavior during the first 100-200 s and a more rapid growth of the corrosion layer after this time interval, Figs. 6 and 7. As in the previous case, the model well predicts the corrosion layer growth kinetics in the beginning (≈600 s), but overpredicts the layer thickness in the late stage of the corrosion period when melt oversaturation and precipitation of the ceramic ZrO_2 phase in the melt bulk commence.

3.4. Analysis of the FZK tests with large crucibles

The new FZK test series [4] with large crucibles was performed under conditions similar to the previous KfK tests and with the same crucible dimensions (but with the higher crucible density, 93% TD). However, some tests were performed with the crucible cavity bottom isolation by Y_2O_3 discs, in order to reproduce the one-dimensional dissolution process typical for the fuel rod geometry, and to avoid the above described difficulties in modeling simultaneous dissolution of the crucible walls and bottom by the simplified one-dimensional model (see the end of Section 2).

For the tests without crucible bottom isolation performed at 2200 °C, the model predicts a similar to the KfK test behavior, however, with a somewhat smaller dissolution depth in the erosion stage (and a slower growth of the corrosion layer in the subsequent period) owing to the higher crucible material density. The model predictions for the dissolved wall thickness are in a reasonable agreement with the data at the two available time points ≈100 and 600 s, Fig. 8.

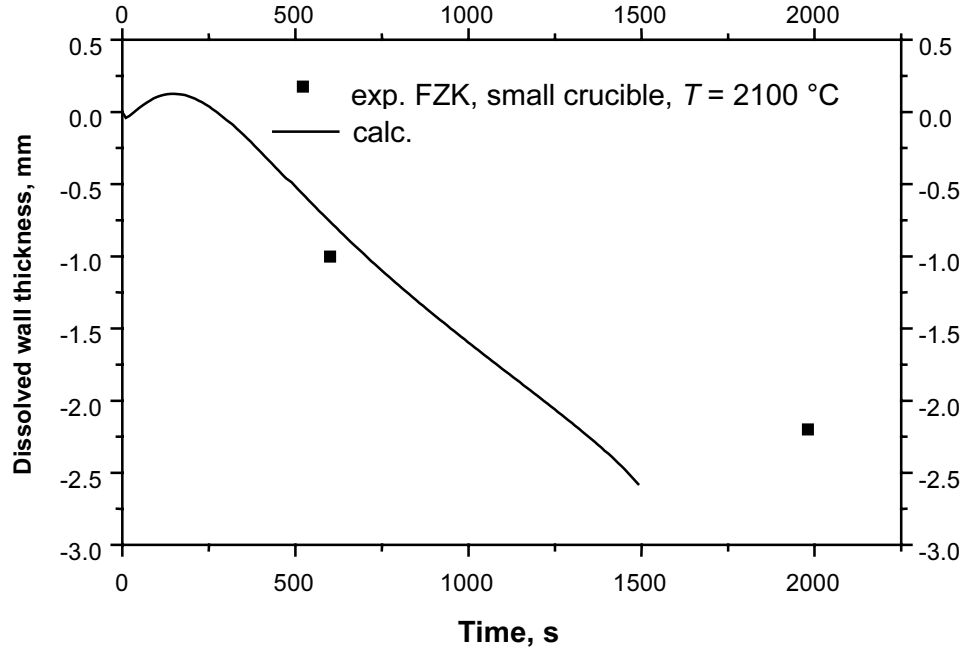

Fig. 6. Simulations of FZK small crucible tests [4] at 2100℃

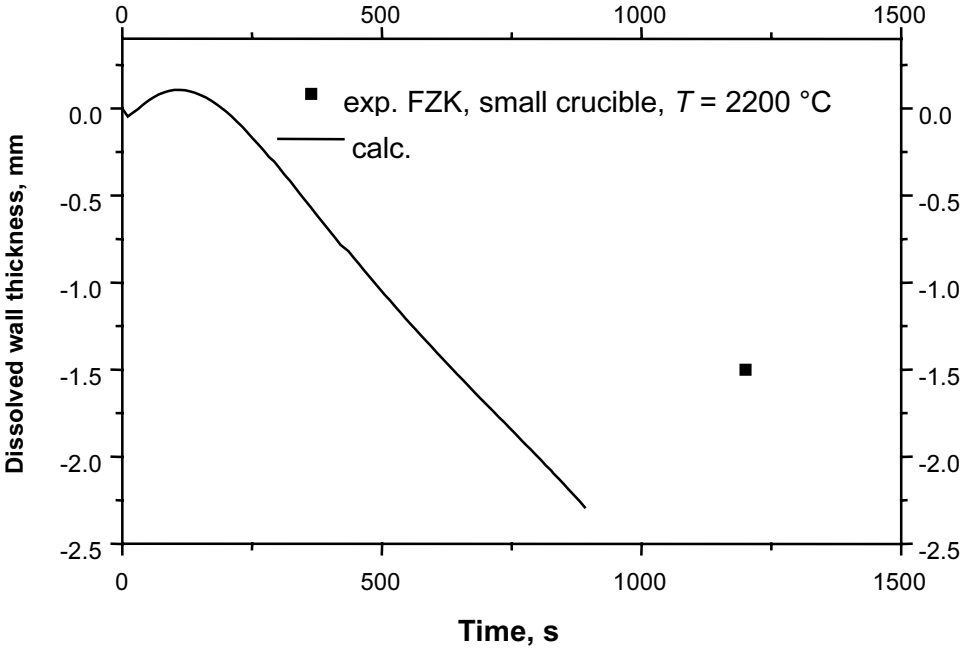

Fig. 7. Simulations of FZK small crucible tests [4] at 2200℃

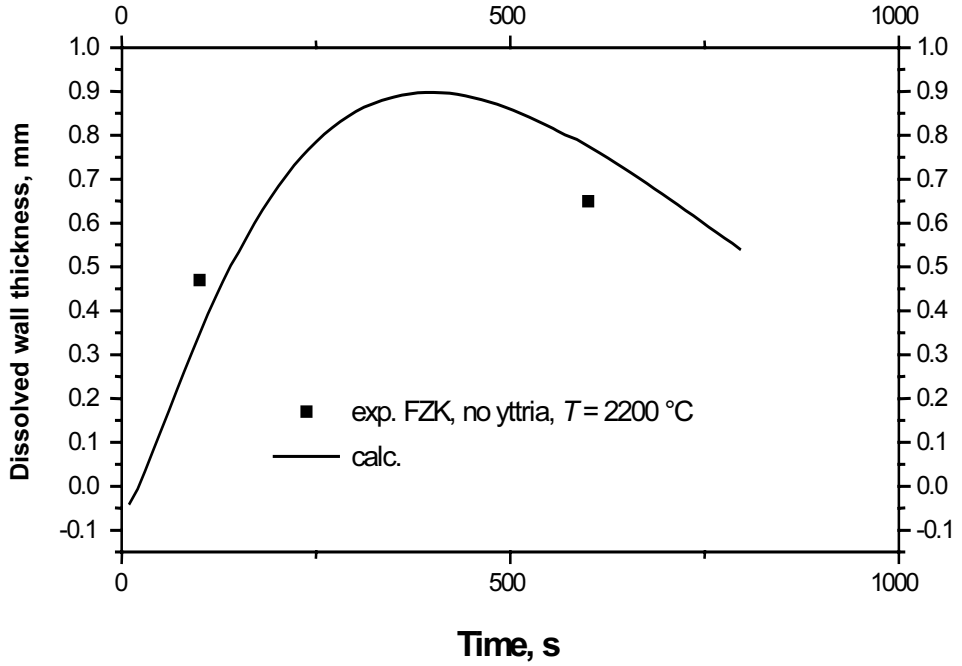

Fig. 8. Simulations of FZK large crucible tests [4] without bottom isolation at 2200 °C

For the tests with yttria discs preventing the crucible bottom from interactions with the melt, calculations were performed in the one-dimensional geometry with the real internal and external radii of the crucible walls. A systematic temperature shift of about 100 K to lower temperatures was accounted for in the calculations in accordance with the analysis of the test procedure presented in Section [4]. Such temperature corrections allowed reasonable coincidence with the test data at two temperatures initially measured as 2100 and 2200 °C but then assigned to 2000 and 2100 °C, respectively (see Fig. 9 and 10).

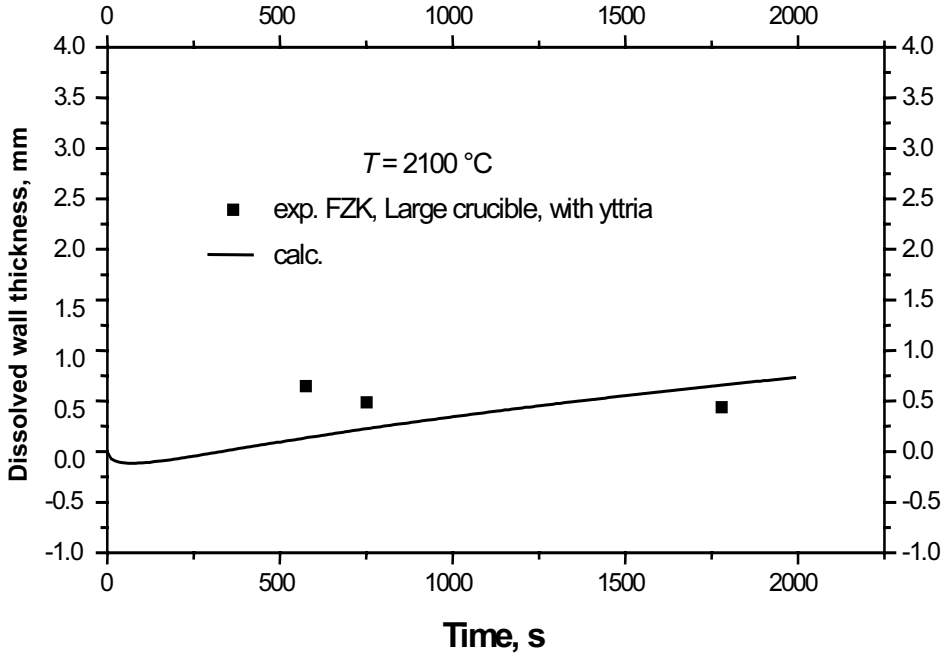

Fig. 9. Simulations of FZK large crucible tests [4] with bottom isolation by yttria disc at 2100 °C.

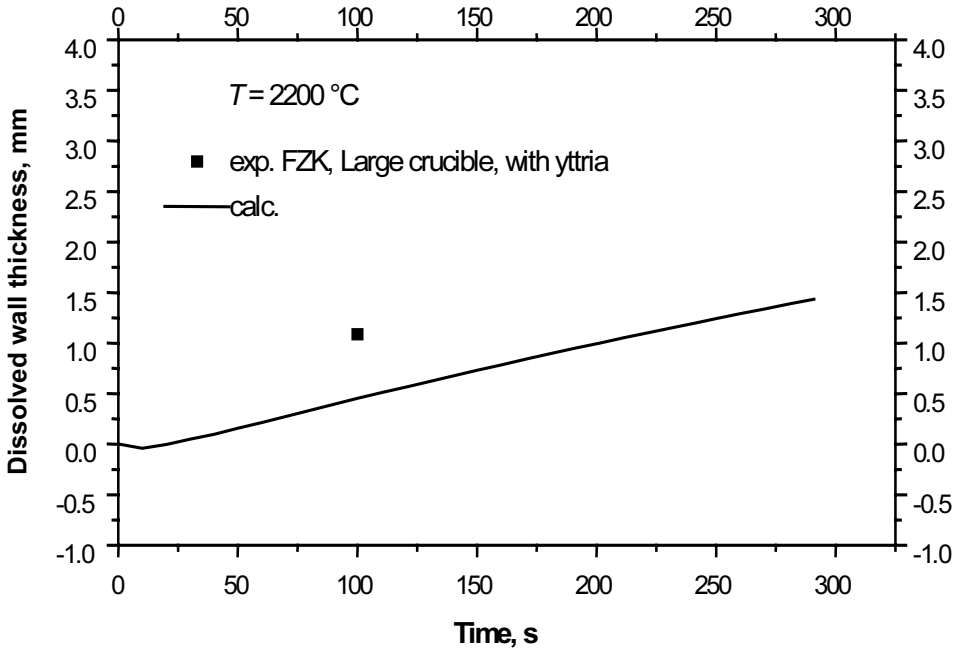

Fig. 10. Simulations of FZK large crucible tests [4] with bottom isolation by yttria disc at 2200°C.

4. Conclusions

The present model for ZrO_2 dissolution by molten Zr qualitatively and quantitatively correctly describes different interaction kinetics observed in the three test series: KfK [1,2], AECL [3] and FZK [4] tests.

Depending on temperature, crucible dimensions (*S/V* ratio and wall thickness) and geometry (with/without bottom isolation), two stages (erosion and corrosion) or only one stage (erosion) of the crucible/melt interactions are correctly predicted by the model.

Being implemented in the single-rod version of the SVECHA code, the model allows simulations of the new FZK tests on cladding oxide shell failure (see p. 100 of the current issue).

References

1. *P. Hofmann, Ch. Adelhelm, E. Garcia, M. Markiewicz, J. Burbach, G. Gussmann, K. Kurz and H. Metzger*, Chemische Auflösung von festem ZrO_2 durch geschmolzenes Zircaloy-Hüllmaterial. Kernforschungszentrum Karlsruhe Report No. KfK-4100. September 1987
2. *P. Hofmann, S. Hagen, G. Schanz, and A. Skokan*, Nuclear Safety, 87 (1989) 146.
3. *P. J. Hayward and I.M. George*, J.Nucl.Mater., 265 (1999) 69.
4. *P. Hofmann, J. Stuckert, A. Miassoedov, M.S. Veshchunov, A.V. Berdyshev, and A.V. Boldyrev*, ZrO_2 Dissolution by Molten Zircaloy and Cladding Oxide Shell Failure. New Experimental Results and Modelling. Report FZKA 6383, INV-CIT(98)-P026, Karlsruhe, Germany, 1999.
5. *M.S. Veshchunov, A.V. Berdyshev, and A.V. Palagin*, Theory of simultaneous dissolution of UO_2 and ZrO_2 by molten Zircaloy in oxidizing atmosphere and its application for description of chemical interactions of relocating melt. Preprint IBRAE-96-10, Moscow 1996.
6. *M.S. Veshchunov and A.V. Berdyshev*, J.Nucl.Mater., 252 (1997) 98.
7. *M.S.Veshchunov and P.Hofmann*, J.Nucl.Mater. 209 (1994) 27.
8. *M.S. Veshchunov, K. Mueller, and A.V. Berdyshev*, Nucl. Eng. Des. 235 (2005) 2431-2450.

Model for Simultaneous Dissolution of UO_2 and ZrO_2 by Molten Zr

M.S. Veshchunov, A.V. Berdyshev

1. Introduction

The results obtained in the crucible tests on the kinetics of UO_2 and ZrO_2 dissolution by molten Zr as separate processes cannot be directly applied to interpretation of the fuel rod dissolution observed in various bundle tests, owing to convective mixing of the molten materials in the course of their interaction with solid UO_2 and ZrO_2 phases observed in those tests.

To resolve this problem and to extend the existing experimental data base, the new experiments on simultaneous dissolution UO_2 and ZrO_2 by molten Zry were performed by RIAR (Dimitrovgrad, Russia) in collaboration with FZK (Karlsruhe) and JRC/IE (Petten) [1]. The analysis of results and the analytical support of the experiments were carried out by IBRAE.

In the current paper development of the mechanistic model for simultaneous dissolution of UO_2 and ZrO_2 by molten Zr based on the previously developed models on separate interactions of UO_2 and ZrO_2 with molten Zr (presented in two preceeding papers in this issue), and its validation against the full set of RIAR experimental data [1], is presented.

2. Model description

In order to consider simultaneous dissolution of UO_2 and ZrO_2 by molten Zr, one should consider a ternary U-Zr-O system at test temperatures. The melt in crucible and bundle tests has rather homogeneous composition due to the convective stirring, and for this reason, concentration changes from the interface to bulk values occur in a thin transition layer δ in the melt at the interface.

The interface concentrations in the melt $c_O(I)$, $c_{Zr}(I)$ and $c_U(I)$ sustain in equilibrium with solid phase and, thus, belong to the liquidus line:

$$\begin{aligned} &F_{\mathrm{liq}}\left(c_{\mathrm{O}}(I), c_{\mathrm{U}}(I), c_{\mathrm{Zr}}(I)\right) = \\ &= F_{\mathrm{liq}}\left(c_{\mathrm{O}}^{*}, c_{\mathrm{U}}^{*}, c_{\mathrm{Zr}}^{*}\right) = 0. \end{aligned} \tag{1}$$

In the simplest approximation this equation can be linearised:

$$c_{\mathrm{O}}(I) = g_1 + g_2 c_{\mathrm{U}}(I), \tag{2}$$

where temperature dependent parameters $g_1(T)$ and $g_2(T)$ determine position of a straight (liquidus) line in the ternary phase diagram, Fig. 1.

The molar density of the melt for simplicity is assumed independent of the dissolved oxygen and is denoted by $c_{\mathrm{M}} \approx 0.068$ mol/cm^3 on an oxygen-free basis [2]:

$$c_{\mathrm{U}} + c_{\mathrm{Zr}} = c_{\mathrm{M}}. \tag{3}$$

The solidus line:

$$F_{\mathrm{sol}}\left(\rho_{\mathrm{O}}^{*}, \rho_{\mathrm{U}}^{*}, \rho_{\mathrm{Zr}}^{*}\right) = 0, \tag{4}$$

can be represented with a good accuracy by a straight line parallel to the U-Zr axis [3, 4] in the ternary phase diagram, Fig. 1, and thus can be described by relationships:

$$\rho_{\mathrm{U}}^{*} + \rho_{\mathrm{Zr}}^{*} = \rho_S = const \quad \rho_{\mathrm{O}}^{*} = const, \tag{5}$$

where ρ_{S} and ρ_{O}^{*} coincide with the corresponding values $\rho_{Zr(U)}$ and $\varphi_{\mathrm{O}}(I_2) \equiv \varphi_{\mathrm{O}}$ ($\rho_{\mathrm{O}}(I_1) \equiv \rho_{\mathrm{O}}$) in pure ZrO_{2-x} (UO_{2-x}).

The equilibrium tie-lines in the phase diagram connect points in the liquidus and solidus lines, therefore, they relate also the interface concentrations in the melt and solid phase. This means that composition of the solid ceramic phase near the interface can be different from pure ZrO_{2-x} (or UO_{2-x}) and contains an admix-

ture of U (or Zr) cations, i.e. corresponds to the mixed ceramic phase $(U,Zr)O_{2-x}$.

It is straightforward to show that in the case of the UO_2 or ZrO_2 layer dissolution, the thickness of the interface boundary layer in the solid phase with the mixed composition $(U,Zr)O_{2-x}$ is extremely small (owing to a rather small diffusivity of cations in the ceramic phase which prevent them from deep penetration in the solid bulk), and therefore can be neglected in the mass balance and flux matching equations. In this case an "effective" boundary concentration $\tilde{\rho}_{U(Zr)}$, which corresponds to the bulk solid layer composition, i.e. pure UO_2 (ZrO_2) phase, should be used: $\tilde{\rho}_U = \tilde{\rho}_{Zr} = \rho_S$.

Conversely, in the case of the oxide (UO_2 or ZrO_2) layer growth this boundary layer is not anymore small, since the oxide layer grows with the mixed composition $(U,Zr)O_{2-x}$ that is in equilibrium with the U-Zr-O melt at the interface. In this case the real boundary concentration which is determined by intersection of the equilibrium tie-lines with the solidus line, should be used in the mass transfer equations: $\tilde{\rho}_U = \rho^*_U$, and $\tilde{\rho}_{Zr} = \rho^*_{Zr}$.

On the other hand, in accordance with numerous observations in the crucible tests, it is additionally assumed for the UO_2 layer that only dissolution of this layer (and no growth) can occur in the course of its interactions with the U-Zr-O melt, whereas either dissolution or growth of the ZrO_2 layer (i.e. "erosion" and "corrosion" stages [5]) were observed in the tests and will be considered in the current model.

The tie-lines that connect equilibrium concentrations at the interface, for simplicity, can be considered as straight lines starting from the O apex in the ternary phase diagram, as shown in Fig. 1 by dotted lines, i.e.

$$\frac{\rho^*_U}{\rho_S} = \frac{c^*_U}{c_m}, \quad \frac{\rho^*_{Zr}}{\rho_S} = \frac{c^*_{Zr}}{c_m}. \tag{6}$$

Such a simplification can be easily avoided if more accurate equations for the tie-lines are available.

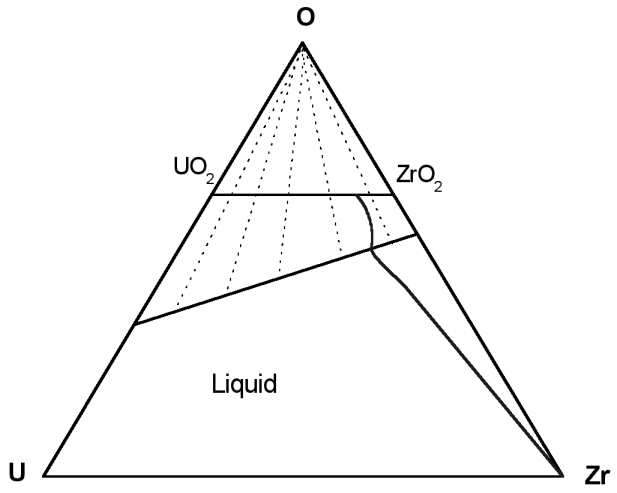

Fig. 1. Schematic representation of the ternary U-Zr-O phase diagram with equilibrium tie-lines (dotted lines).

2.1. Saturation stage

In this approximation for the tie-lines, the system of equations for the mass transfer in the first, saturation stage in a general formulation (applicable either to plane, L =1, or to cylindrical, L =2, geometry) takes the form:

- Mass balances

$$-D_O^{UO_2}\left.\frac{\partial \rho_O}{\partial r}\right|_{I_1} r_1^{L-1} - \rho_O(I_1) r_1^{L-1}\frac{dr_1}{dt} + D_O^{ZrO_2}\left.\frac{\partial \varphi_o}{\partial r}\right|_{I_2} r_2^{L-1} - \varphi_O(I_2)\left[r_3^{L-1}\frac{dr_3}{dt} - r_2^{L-1}\frac{dr_2}{dt}\right] = \frac{1}{L}\frac{d}{dt}\left[c_O(B)(r_2^L - r_1^L)\right] \tag{7}$$

$$-\rho_S r_1^{L-1}\frac{dr_1}{dt} - \tilde{\rho}_U(I_2)\left[r_3^{L-1}\frac{dr_3}{dt} - r_2^{L-1}\frac{dr_2}{dt}\right] = \frac{1}{L}\frac{d}{dt}\left[c_U(B)(r_2^L - r_1^L)\right], \tag{8}$$

$$-\rho_S\left[r_1^{L-1}\frac{dr_1}{dt} + r_3^{L-1}\frac{dr_3}{dt} - r_2^{L-1}\frac{dr_2}{dt}\right] = \frac{c_M}{L}\frac{d}{dt}\left[r_2^L - r_1^L\right], \tag{9}$$

where r_1, r_2, and r_3 are positions of the boundaries of the solid UO_2 and ZrO_2 layers, as schematically shown in Fig. 2.

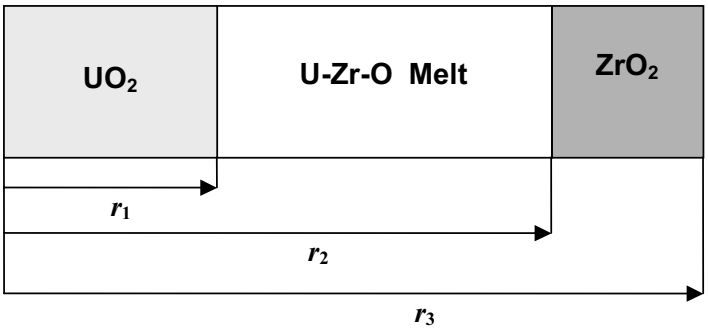

Fig. 2. Schematic representation of the cylindrical model geometry.

In accordance with the above presented explanation, the "effective" interface boundary concentration in the ZrO_2 phase is different for various regimes and can be represented in the form:

$$\tilde{\rho}_{\mathrm{U}}(I_2)=\left[\varphi_{\mathrm{U}}-\left(\varphi_{\mathrm{U}}-\rho_S\frac{c_{\mathrm{U}}(I_2)}{c_M}\right)\theta\left(\frac{d(r_3^L-r_2^L)}{dt}\right)\right], \tag{10}$$

which corresponds to $\tilde{\rho}_{\mathrm{U}}(I_2)=\varphi_{\mathrm{U}}$ (φ_U is uranium molar concentration in zirconia at internal interface, for instance, $\varphi_{\mathrm{U}}=0$ at the beginning of dissolution process) in the cases of the ZrO_2 layer dissolution, and to the mixed composition determined by Eq. (6), $\tilde{\rho}_{\mathrm{U}}(I_2)=\rho_S\frac{c_{\mathrm{U}}(I_2)}{c_M}$, in the case of the ZrO_2 layer growth.

- Flux matches

$$-D_{\mathrm{O}}^{\mathrm{UO_2}}\left.\frac{\partial\rho_{\mathrm{O}}}{\partial r}\right|_{I_1}-\rho_{\mathrm{O}}(I_1)\frac{dr_1}{dt}=k_{\mathrm{O}}(I_1)\left[c_{\mathrm{O}}(I_1)-c_{\mathrm{O}}(B)\right]+c_{\mathrm{O}}(I_1)\left[v_1(I_1)-\frac{dr_1}{dt}\right], \tag{11}$$

$$-\rho_S\frac{dr_1}{dt}=k_U(I_1)\left[c_U(I_1)-c_U(B)\right]+c_U(I_1)\left[v_1(I_1)-\frac{dr_1}{dt}\right], \tag{12}$$

$$-\rho_S\frac{dr_1}{dt}=c_{\mathrm{M}}\left[v_1(I_1)-\frac{dr_1}{dt}\right], \tag{13}$$

$$c_{\mathrm{O}}(I_1)=g_1(T)+g_2(T)c_{\mathrm{U}}(I_1), \tag{14}$$

and

$$\begin{aligned}k_{\mathrm{O}}(I_2)\left[c_{\mathrm{O}}(B)-c_{\mathrm{O}}(I_2)\right]+c_{\mathrm{O}}(I_2)\left[v_1(I_1)\left(\frac{r_1}{r_2}\right)^{L-1}-\frac{dr_2}{dt}\right]=\\ =-D_{\mathrm{O}}^{\mathrm{ZrO_2}}\left.\frac{\partial\varphi_{\mathrm{O}}}{\partial r}\right|_{I_2}+\varphi_{\mathrm{O}}(I_2)\left[\frac{dr_3}{dt}\left(\frac{r_3}{r_2}\right)^{L-1}-\frac{dr_2}{dt}\right],\end{aligned} \tag{15}$$

$$k_{\mathrm{U}}(I_2)\left[c_{\mathrm{U}}(B)-c_{\mathrm{U}}(I_2)\right]+c_{\mathrm{U}}(I_2)\left[v_1(I_1)\left(\frac{r_1}{r_2}\right)^{L-1}-\frac{dr_2}{dt}\right]=\tilde{\rho}_{\mathrm{U}}(I_2)\left[\frac{dr_3}{dt}\left(\frac{r_3}{r_2}\right)^{L-1}-\frac{dr_2}{dt}\right], \tag{16}$$

$$c_M\left[v_1(I_1)\left(\frac{r_1}{r_2}\right)^{L-1}-\frac{dr_2}{dt}\right]=\rho_S\left[\frac{dr_3}{dt}\left(\frac{r_3}{r_2}\right)^{L-1}-\frac{dr_2}{dt}\right], \quad (17)$$

$$c_O(I_2)=g_1(T)+g_2(T)c_U(I_2), \quad (18)$$

where

ρ_O (φ_O) – oxygen molar density in the UO_2 (ZrO_2) layer,

$c_{O(U,Zr)}$ – oxygen (uranium, zirconium) molar density in the melt,

$D_O^{UO_2(ZrO_2)}$ oxygen diffusion coefficient in the UO_2 (ZrO_2) layer,

v_1 – net velocity of the melt, due to density difference between liquid and solid phases,

$k_O(I_i)$ – oxygen mass transfer coefficient in the melt at *i*-th interface, i =1,2;

$k_{U(Zr)}(I_i)$ – uranium (zirconium) mass transfer coefficients in the melt that, due to Eq. (3) obey an additional relationship:

$$k_{Zr}\left(c_{Zr}(I)-c_{Zr}(B)\right)=-k_U\left(c_U(I)-c_U(B)\right)$$

In the melt stirred by natural convection, mass transfer coefficients are calculated as

$$k_O=\frac{D_O^{liq}}{\delta}\quad k_U=\frac{D_U^{liq}}{\delta}\approx k_O/2, \quad (19)$$

where δ is the thickness of the transition boundary layer,

$$\delta\approx d/Sh^{1/4}=d/\left(0.54Gr^{1/4}Sc^{1/4}\right)\quad \text{if } Gr\cdot Sc>10^3, \quad (19a)$$

$Gr=g(\Delta\rho/\rho)d^3/\nu^2$ is the Grashoff number, $Sc=\nu/D_U^{liq}$ is the Schmidt number, d is characteristic dimension of the melt (i.e. in the considered cylindrical geometry $d=r_2-r_1$).

Similarly to [6], this can be written in the form:

$$k_O(I_i)=k_O^*(I_i)\left(c_U(I_i)-c_U(B)\right)^{1/4},$$

where

$$k_O^*(I_i)\approx 0.54\left(\frac{g(D_U^{liq})^3}{\nu dc_M}\right)^{1/4}\left[\frac{(M_U-M_{Zr})\left(c_U(I_i)-c_U(B)\right)+M_O\left(c_O(I_i)-c_O(B)\right)}{M_{Zr}}\right]^{1/4}, \quad (20)$$

D_U^{liq} – uranium diffusion coefficient in the melt,

v – viscosity of the melt,

$M_{U(Zr)}$ – atomic weight of U (Zr).

In the diffusion regime when $Gr\cdot Sc<10^3$, mass transfer by molecular diffusion in the melt should be considered. For simplicity of numerical calculations, the convection equations will be applied to the diffusion regime by formal extension of Eq. (19a) to the limit $Sh\to 1$, i.e. $\delta\approx d$ (also in the following consideration of the precipitation stage).

An additional assumption $k_O=k_U$ (instead of Eq. (19)) can significantly simplify calculations. Sensitivity of calculation results to this simplification is demonstrated in Fig. 3 for UO_2/melt interaction and in Fig. 4 for the UO_2/melt/ZrO_2 simultaneous dissolution. Analytical transformation of Eqs. (11)-(18) under such a simplification allows explicit representation of the interface velocities, taking into account the above-mentioned prevention of the UO_2 layer growth and, according to Eq. (20), weak dependence of mass transfer coefficients on melt composition:

$$\left.\frac{dr_1}{dt}\right|_{T=T_{UO_2},I_1} = \begin{cases} \dfrac{-D_O^{UO_2}\left.\dfrac{\partial \rho_O}{\partial r}\right|_{I_1} - k_O(I_1)\left[c_O^{max} - c_O(B)\right]}{\rho_O - (g_1 + c_m g_2)\dfrac{\rho_S}{c_M}}, & \dfrac{dr_1}{dt} \le 0, \\ 0 & \dfrac{dr_1}{dt} > 0, \end{cases} \tag{21}$$

$$\left.\left(r_3^{L-1}\frac{dr_3}{dt} - r_2^{L-1}\frac{dr_2}{dt}\right)\right|_{T=T_{ZrO_2},I_2} =$$

$$= \begin{cases} r_2^{L-1}\dfrac{D_O^{ZrO_2}\left.\dfrac{\partial \varphi_O}{\partial r}\right|_{I_2} - k_O(I_2)\left[c_O^{max} - c_O(B)\right]}{\varphi_O - g_1\dfrac{\rho_S}{c_M}}, & r_3^{L-1}\dfrac{dr_3}{dt} - r_2^{L-1}\dfrac{dr_2}{dt} \le 0 \\ r_2^{L-1}\dfrac{D_O^{ZrO_2}\left.\dfrac{\partial \varphi_O}{\partial r}\right|_{I_2} - k_O(I_2)\left[c_O^{max} - c_O(B)\right]}{\varphi_O - c_O^{max}\dfrac{\rho_S}{c_M}}, & r_3^{L-1}\dfrac{dr_3}{dt} - r_2^{L-1}\dfrac{dr_2}{dt} > 0 \end{cases}, \tag{22}$$

where

$$c_O^{max} = \left[g_1(T) + c_U(B)g_2(T)\right]. \tag{23}$$

Therefore, Eqs. (21)-(23) can be directly used instead of Eqs. (15)-(17) in the following calculations.

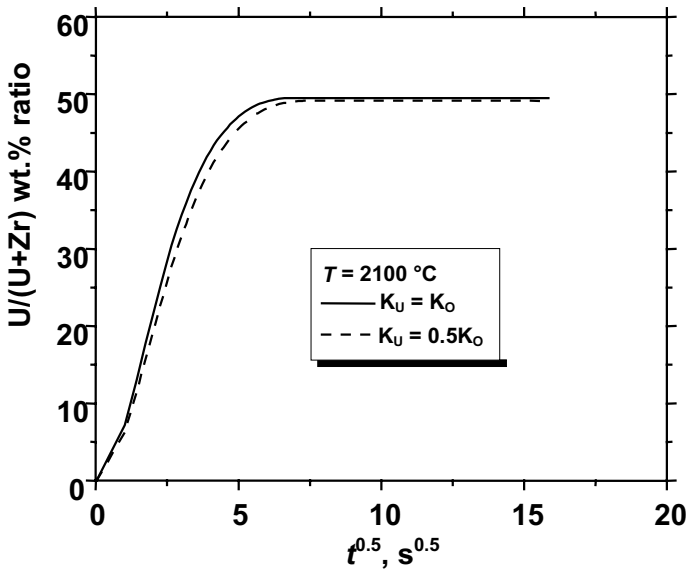

Fig. 3. Comparison of models with different mass transfer coefficients in the melt for the case of UO_2/melt interaction.

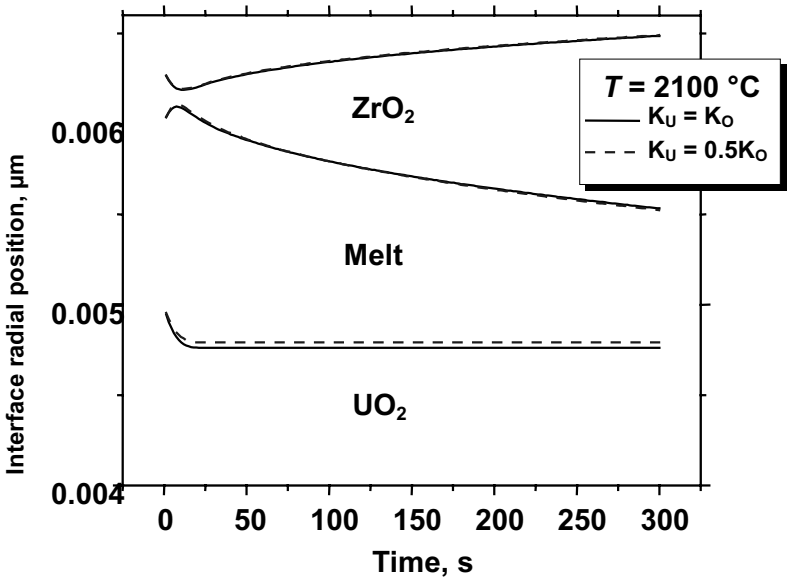

Fig. 4. Comparison of models with different mass transfer coefficients in the melt for the case of UO_2/melt/ZrO_2 interaction.

2.2. Precipitation stage

The saturation stage of the interactions proceeds until saturation of the melt is reached. In the precipitation stage the oxygen flux to the melt continues, this leads to oversaturation of the melt and onset of precipitation.

The $(U,Zr)O_2$ precipitates are in a local thermodynamic equilibrium with the surrounding melt, therefore, their composition belongs to the solidus line, Eqs. (5), and relates to the bulk composition of the melt by the equilibrium tie-line equation, Eq. (6).

In this case the system of governing equations takes the form:

- Mass balances

$$-D_{\mathrm{O}}^{\mathrm{UO_2}}\left.\frac{\partial\rho_{\mathrm{O}}}{\partial r}\right|_{I_1} r_1^{L-1}-\rho_{\mathrm{O}}r_1^{L-1}\frac{dr_1}{dt}+D_{\mathrm{O}}^{\mathrm{ZrO_2}}\left.\frac{\partial\varphi_o}{\partial r}\right|_{I_2} r_2^{L-1}-\varphi_{\mathrm{O}}\left[r_3^{L-1}\frac{dr_3}{dt}-r_2^{L-1}\frac{dr_2}{dt}\right]= \\ =\frac{1}{L}\frac{d}{dt}\left[\left(c_{\mathrm{O}}^{*}(1-f)+f\rho_{\mathrm{O}}^{*}\right)\left(r_2^L-r_1^L\right)\right], \tag{24}$$

$$-\rho_S r_1^{L-1}\frac{dr_1}{dt}-\tilde{\rho}_{\mathrm{U}}(I_2)\left[r_3^{L-1}\frac{dr_3}{dt}-r_2^{L-1}\frac{dr_2}{dt}\right]=\frac{1}{L}\frac{d}{dt}\left[c_{\mathrm{U}}^{*}\left(1-f\cdot\left(1-\frac{\rho_S}{c_M}\right)\right)\left(r_2^L-r_1^L\right)\right], \tag{25}$$

$$-\rho_S\left[r_1^{L-1}\frac{dr_1}{dt}+r_3^{L-1}\frac{dr_3}{dt}-r_2^{L-1}\frac{dr_2}{dt}\right]=\frac{1}{L}\frac{d}{dt}\left[\left(c_M(1-f)+f\rho_S\right)\left(r_2^L-r_1^L\right)\right], \tag{26}$$

where f is the volume fraction of the ceramic precipitates in the uniformly stirred melt in the bulk region. In the mass balances a thin transition layer is neglected due to its small thickness, $\delta << L, M$.

It can be shown that considering flux matching equations one can neglect formation of precipitates in the transition boundary layer in the melt, i.e. $f = 0$ in this layer. In such an approximation one obtains:

- Flux matches

$$-D_{\mathrm{O}}^{\mathrm{UO_2}}\left.\frac{\partial \rho_{\mathrm{O}}}{\partial r}\right|_{I_1}-\rho_{\mathrm{O}}(I_1)\frac{dr_1}{dt}=\tilde{k}_{\mathrm{O}}(I_1)\left[c_{\mathrm{O}}(I_1)-c_{\mathrm{O}}^{*}\right]+c_{\mathrm{O}}(I_1)\left[v_1(I_1)-\frac{dr_1}{dt}\right], \tag{27}$$

$$0=\tilde{k}_{\mathrm{U}}(I_1)\left[c_{\mathrm{U}}(I_1)-c_{\mathrm{U}}^{*}\right]+c_{\mathrm{U}}(I_1)\left[v_1(I_1)-\frac{dr_1}{dt}\right], \tag{28}$$

$$-\rho_S\frac{dr_1}{dt}=c_M\left[v_1(I_1)-\frac{dr_1}{dt}\right], \tag{29}$$

$$c_{\mathrm{O}}(I_1)=g_1(T)+g_2(T)c_{\mathrm{U}}(I_1), \tag{30}$$

$$\tilde{k}_{\mathrm{O}}(I_2)\left[c_{\mathrm{O}}^{*}-c_{\mathrm{O}}(I_2)\right]+c_{\mathrm{O}}(I_2)\left[v_1(I_2)-\frac{dr_2}{dt}\right]=-D_{\mathrm{O}}^{\mathrm{ZrO_2}}\left.\frac{\partial \varphi_{\mathrm{O}}}{\partial r}\right|_{I_2}+\varphi_{\mathrm{O}}(I_2)\left[\left(\frac{r_3}{r_2}\right)^{L-1}\frac{dr_3}{dt}-\frac{dr_2}{dt}\right], \tag{31}$$

$$\tilde{k}_{\mathrm{U}}(I_2)\left[c_{\mathrm{U}}^{*}-c_{\mathrm{U}}(I_2)\right]+c_{\mathrm{U}}(I_2)\left[v_1(I_1)\left(\frac{r_1}{r_2}\right)^{L-1}-\frac{dr_2}{dt}\right]=\tilde{\rho}_{\mathrm{U}}\left[\frac{dr_3}{dt}\left(\frac{r_3}{r_2}\right)^{L-1}-\frac{dr_2}{dt}\right], \tag{32}$$

$$c_M\left[v_1(I_2)-\frac{dr_2}{dt}\right]=\rho_S\left[\left(\frac{r_3}{r_2}\right)^{L-1}\frac{dr_3}{dt}-\frac{dr_2}{dt}\right], \tag{33}$$

$$c_{\mathrm{O}}(I_2)=g_1(T)+g_2(T)c_{\mathrm{U}}(I_2), \tag{34}$$

where the bulk values c_{O}^{*}, c_{U}^{*}, c_{Zr}^{*} and ρ_{O}^{*}, ρ_{U}^{*}, ρ_{Zr}^{*} obey Eqs. (2), (5), and (6).

The value of mass transfer coefficient $k_{\mathrm{O(U)}}$ slowly decreases with growth of precipitates in the melt, $k_{\mathrm{O(U)}}\propto Sh\propto \nu^{-1/4}$, due to increase of the apparent viscosity ν of the solid-liquid mixture with the increase of the volume fraction *f* of solid precipitates. In accordance with a recommendation of [7] for corium in the solidification range, the Arrhenius law can be used for the apparent viscosity: $\nu=\nu_{liq}\exp(2.5Cf)$, where ν_{liq} is the liquid phase viscosity, *C* is an adjustable coefficient in the range 4–4.8. Therefore, a new value

$$\tilde{k}_{\mathrm{O(U)}}(I_i)=k_{\mathrm{O(U)}}(I_i)\cdot\exp(-2.5Cf/4)\approx \approx k_{\mathrm{O(U)}}(I_i)\cdot\exp(-2.5f), \tag{35}$$

with $k_{O(U)}$ determined in Eq. (20), is introduced in Eq. (27)-(34) to consider increase of viscosity due to precipitation of the ceramic phase in the melt.

Correspondingly, equations similar to Eqs. (21)-(23) with c_O^{*} and c_U^{*} standing for $c_{\mathrm{O}}(B)$ and $c_{\mathrm{U}}(B)$, respectively, and $k_{\mathrm{O(U)}}\to\tilde{k}_{\mathrm{O(U)}}$, can be derived from the flux matching equations, Eqs. (27)-(34).

2.3. General system of equations (for both stages)

As a result, the systems of equations for both stages can be finally represented in the unified form:

- Mass balances

$$-D_{\mathrm{O}}^{\mathrm{UO_2}}\left.\frac{\partial \rho_{\mathrm{O}}}{\partial r}\right|_{I_1}r_1^{L-1}-\rho_{\mathrm{O}}(I_1)r_1^{L-1}\frac{dr_1}{dt}+D_{\mathrm{O}}^{\mathrm{ZrO_2}}\left.\frac{\partial \varphi_o}{\partial r}\right|_{I_2}r_2^{L-1}-\varphi_{\mathrm{O}}(I_2)\left[r_3^{L-1}\frac{dr_3}{dt}-r_2^{L-1}\frac{dr_2}{dt}\right]==\frac{1}{L}\frac{d}{dt}\left[Y_{\mathrm{O}}\right], \tag{36}$$

$$-\rho_S r_1^{L-1}\frac{dr_1}{dt}-\tilde{\rho}_{\mathrm{U}}(I_2)\left[r_3^{L-1}\frac{dr_3}{dt}-r_2^{L-1}\frac{dr_2}{dt}\right]=\frac{1}{L}\frac{d}{dt}\left[Y_{\mathrm{U}}\right], \tag{37}$$

$$-\rho_S\left[r_1^{L-1}\frac{dr_1}{dt}+r_3^{L-1}\frac{dr_3}{dt}-r_2^{L-1}\frac{dr_2}{dt}\right]=\frac{1}{L}\frac{d}{dt}\left[Y_{\mathrm{UZr}}\right], \tag{38}$$

where

$$Y_{\mathrm{O}} = c_{\mathrm{O}}(B)(r_2^L - r_1^L), \quad Y_{\mathrm{U}} = c_{\mathrm{U}}(B)(r_2^L - r_1^L), \quad Y_{\mathrm{U\,Zr}} = c_M(r_2^L - r_1^L) \tag{39}$$

during saturation stage, and

$$\begin{gathered} Y_{\mathrm{O}} = \left(c_{\mathrm{O}}^*(1-f) + f\rho_{\mathrm{O}}^*\right)(r_2^L - r_1^L),\ Y_{\mathrm{U}} = c_{\mathrm{U}}^*\left(1 - f\cdot\left(1 - \frac{\rho_S}{c_M}\right)\right)(r_2^L - r_1^L), \\ Y_{\mathrm{U}Z} = \left(c_M(1-f) + f\rho_S\right)(r_2^L - r_1^L),\ c_{\mathrm{O}}^* = \left(g_1 + c_{\mathrm{U}}^* g_2\right) \end{gathered}, \tag{40}$$

during the precipitation stage.

- Flux matches:

$$-D_{\mathrm{O}}^{\mathrm{UO_2}}\left.\frac{\partial\rho_{\mathrm{O}}}{\partial r}\right|_{I_1} - \rho_{\mathrm{O}}(I_1)\frac{dr_1}{dt} = \tilde{k}_{\mathrm{O}}(I_1)\left[c_{\mathrm{O}}(I_1) - \tilde{c}_{\mathrm{O}}\right] + c_{\mathrm{O}}(I_1)\left[v_1(I_1) - \frac{dr_1}{dt}\right], \tag{41}$$

$$-\rho_S\frac{dr_1}{dt} = \tilde{k}_{\mathrm{U}}(I_1)\left[c_{\mathrm{U}}(I_1) - \tilde{c}_{\mathrm{U}}\right] + c_{\mathrm{U}}(I_1)\left[v_1(I_1) - \frac{dr_1}{dt}\right], \tag{42}$$

$$-\rho_S\frac{dr_1}{dt} = c_M\left[v_1(I_1) - \frac{dr_1}{dt}\right], \tag{43}$$

$$c_{\mathrm{O}}(I_1) = g_1(T) + g_2(T)c_{\mathrm{U}}(I_1), \tag{44}$$

$$\tilde{k}_{\mathrm{O}}(I_2)\left[\tilde{c}_{\mathrm{O}} - c_{\mathrm{O}}(I_2)\right] + c_{\mathrm{O}}(I_2)\left[v_1(I_2) - \frac{dr_2}{dt}\right] = -D_{\mathrm{O}}^{\mathrm{ZrO_2}}\left.\frac{\partial\varphi_{\mathrm{O}}}{\partial r}\right|_{I_2} + \varphi_{\mathrm{O}}(I_2)\left[\left(\frac{r_3}{r_2}\right)^{L-1}\frac{dr_3}{dt} - \frac{dr_2}{dt}\right], \tag{45}$$

$$\tilde{k}_{\mathrm{U}}(I_2)\left[\tilde{c}_{\mathrm{U}} - c_{\mathrm{U}}(I_2)\right] + c_{\mathrm{U}}(I_2)\left[v_1(I_1)\left(\frac{r_1}{r_2}\right)^{L-1} - \frac{dr_2}{dt}\right] = \tilde{\rho}_{\mathrm{U}}\left[\frac{dr_3}{dt}\left(\frac{r_3}{r_2}\right)^{L-1} - \frac{dr_2}{dt}\right], \tag{46}$$

$$c_M\left[v_1(I_2) - \frac{dr_2}{dt}\right] = \rho_S\left[\left(\frac{r_3}{r_2}\right)^{L-1}\frac{dr_3}{dt} - \frac{dr_2}{dt}\right], \tag{47}$$

$$c_{\mathrm{O}}(I_2) = g_1(T) + g_2(T)c_{\mathrm{U}}(I_2), \tag{48}$$

where

$$\tilde{c}_{\mathrm{O(U)}} = c_{\mathrm{O(U)}}(B) \text{ during saturation stage,} \tag{49}$$

and

$$\tilde{c}_{\mathrm{O(U)}} = c_{\mathrm{O(U)}}^* \text{ during precipitation stage.} \tag{50}$$

From flux matches one can derive:

$$\left.\frac{dr_1}{dt}\right|_{T=T_{\mathrm{UO_2}},I_1}=\begin{cases}\dfrac{-D_{\mathrm{O}}^{\mathrm{UO_2}}\left.\dfrac{\partial\rho_{\mathrm{O}}}{\partial r}\right|_{I_1}-\tilde{k}_{\mathrm{O}}(I_1)\left[c_{\mathrm{O}}^{\max}-\tilde{c}_{\mathrm{O}}\right]}{\rho_{\mathrm{O}}-(g_1+c_m g_2)\dfrac{\rho_{\mathrm{U}}}{c_M}}, & \dfrac{dr_1}{dt}\le 0,\\ 0\ , & \dfrac{dr_1}{dt}>0,\end{cases} \tag{51}$$

$$\left(r_3^{L-1}\frac{dr_3}{dt}-r_2^{L-1}\frac{dr_2}{dt}\right)\Bigg|_{T=T_{\mathrm{ZrO_2}},I_2}=\begin{cases}r_2^{L-1}\dfrac{D_{\mathrm{O}}^{\mathrm{ZrO_2}}\left.\dfrac{\partial\varphi_{\mathrm{O}}}{\partial r}\right|_{I_2}-\tilde{k}_{\mathrm{O}}(I_2)\left[c_{\mathrm{O}}^{\max}-\tilde{c}_{\mathrm{O}}\right]}{\varphi_{\mathrm{O}}-g_1\dfrac{\rho_S}{c_M}}, & r_3^{L-1}\dfrac{dr_3}{dt}-r_2^{L-1}\dfrac{dr_2}{dt}\le 0\\ r_2^{L-1}\dfrac{D_{\mathrm{O}}^{\mathrm{ZrO_2}}\left.\dfrac{\partial\varphi_{\mathrm{O}}}{\partial r}\right|_{I_2}-\tilde{k}_{\mathrm{O}}(I_2)\left[c_{\mathrm{O}}^{\max}-\tilde{c}_{\mathrm{O}}\right]}{\varphi_{\mathrm{O}}-c_{\mathrm{O}}^{\max}\dfrac{\rho_S}{c_M}}, & r_3^{L-1}\dfrac{dr_3}{dt}-r_2^{L-1}\dfrac{dr_2}{dt}>0\end{cases}, \tag{52}$$

where

$$c_{\mathrm{O}}^{\max}=\left[g_1(T)+c_{\mathrm{U}}(B)g_2(T)\right]. \tag{53}$$

The two stages can be separated by parameter

$$\begin{gathered}S_{\mathrm{dir}}=(P_y^2-P_y^1)(P_x-P_x^1)-(P_x^2-P_x^1)(P_y-P_y^1),\\ P=(P_x,P_y)=(1-x_{\mathrm{U}}-\frac{1}{2}x_{\mathrm{O}},\frac{\sqrt{3}}{2}x_{\mathrm{O}}),\quad P^1:x_{\mathrm{O}}=\frac{g_1/c_M+g_2}{1+g_1/c_M+g_2},\quad x_{\mathrm{U}}=\frac{1}{1+g_1/c_M+g_2}\\ P^2:x_{\mathrm{O}}=\frac{g_1/c_M}{1+g_1/c_M},\ x_{\mathrm{U}}=0\quad P:x_{\mathrm{O}}=\frac{Y_{\mathrm{O}}}{Y_{\mathrm{O}}+Y_{\mathrm{UZ}}},\quad x_{\mathrm{U}}=\frac{Y_{\mathrm{U}}}{Y_{\mathrm{O}}+Y_{\mathrm{UZr}}},\end{gathered} \tag{54}$$

which determines a normal distance in the ternary phase diagram, Fig. 1, from the current point determining composition of the melt bulk, to the liquidus line (or more exactly, is equal to the square of a triangle formed by connection of the current point with terminal points of the liquidus line).

In the saturation stage when composition of melt is in the one-phase (liquid) region of the phase diagram, this value is positive, $S_{\mathrm{dir}} > 0$, and Eq. (39) should be used for $Y_{\mathrm{O}}, Y_{\mathrm{U}}, Y_{\mathrm{UZr}}$ and Eq. (49) for $\tilde{c}_{\mathrm{O(U)}}$. In the precipitation stage when composition of melt is in the two-phase (liquid + solid) region of the phase diagram, $S_{\mathrm{dir}} < 0$, and Eqs. (40) and (50) should be used.

The system of Eqs. (36)–(50) completely determines interactions behavior in both stages and can be analyzed numerically.

2.4. Discussion

During the precipitation stage

$$c_{\mathrm{O}}^{\max}=\left(g_1+\tilde{c}_{\mathrm{U}}g_2\right)=\left(g_1+c_{\mathrm{U}}^{*}g_2\right)=c_{\mathrm{O}}^{*}=\tilde{c}_{\mathrm{O}}, \tag{55}$$

and Eqs. (51)-(52) are significantly simplified due to disappearance of the term $\tilde{k}_O\left(c_O^{\max}-\tilde{c}_O\right)$ in these equations.

It is worthwhile to note that such a simplification concerns only explicit Eqs. (51)-(52), whereas flux matching equations Eqs. (36)-(38) (from which Eqs. (51)-(52) are derived) still contain non-vanishing

term $\tilde{k}_O\left[c_O(I_1)-\tilde{c}_O\right]=\tilde{k}_O\left[c_O(I_1)-c_O^*\right]$ that describes oxygen flux in the melt. Indeed, it is straightforward to show that

$$c_O(I_1)=\frac{\left[g_1+c_U^* g_2\right]c_M\rho_O(I_1)-\left[g_1+c_M g_2\right]c_O^*\rho_U+\left[g_1+c_M g_2\right]\rho_U\left.\frac{D_O^{UO_2}}{k_O}\frac{\partial\rho_O}{\partial r}\right|_{I_1}}{c_M\rho_O(I_1)-(c_O^*+\left[c_M-c_U^*\right]g_2)\rho_U+\rho_U\left.\frac{D_O^{UO_2}}{k_O}\frac{\partial\rho_O}{\partial r}\right|_{I_1}}, \qquad (56)$$

which is generally not equal to $\tilde{c}_O=c_O^*=\left(g_1+c_U^* g_2\right)$ during precipitation stage. Therefore, the non-zero oxygen flux from UO_2 into the melt is sustained also during precipitation stage that results in precipitation of the ceramic $(U,Zr)O_{2-x}$ phase in the oversaturated melt, in correspondence with simplified consideration of the dissolution process in [8,9].

Composition of the melt at the interface with the oxide layer is also not equal to $\tilde{c}_O=c_O^*=\left(g_1+c_U^* g_2\right)$, if dissolution of this layer takes place:

$$c_O(I_2)=\frac{\left[g_1+c_U(B)g_2\right]c_M\rho_O(I)-g_1c_O(B)\rho_U-\rho_U g_1\left.\frac{D_O^{ZrO_2}}{k_O}\frac{\partial\varphi_O}{\partial r}\right|_{I_2}}{c_M\rho_O(I)-(c_O(B)-c_U(B)g_2)\rho_U-\rho_U\left.\frac{D_O^{ZrO_2}}{k_O}\frac{\partial\varphi_O}{\partial r}\right|_{I_2}}, \quad r_3^{L-1}\frac{dr_3}{dt}-r_2^{L-1}\frac{dr_2}{dt}\le 0$$

however, coincides with the melt bulk concentration in the case of oxide layer growth during precipitation stage:

$$c_O(I_2)=\left[g_1+c_U(B)g_2\right], r_3^{L-1}\frac{dr_3}{dt}-r_2^{L-1}\frac{dr_2}{dt}>0.$$

Correspondingly, U composition of growing oxide layer smoothly varies in the course of this layer growth.

2.5. Numerical model

As explained above, the model can be formulated using mass balances, Eqs. (36)-(38), and explicit equations for geometrical variations of solid layers, Eqs. (51)-(53), instead of flux matches. Finally, the complete system of equations for the case of cylindrical geometry to be numerically solved takes the form:

$$\frac{1}{2}\frac{d}{dt}\left[Y_O\right]=-D_O^{UO_2}\left.\frac{\partial\rho_O}{\partial r}\right|_{I_1} r_1-\rho_O(I_1)r_1\frac{dr_1}{dt}+D_O^{ZrO_2}\left.\frac{\partial\varphi_O}{\partial r}\right|_{I_2} r_2-\varphi_O\frac{dS}{dt}, \qquad (57)$$

$$\frac{1}{2}\frac{d}{dt}\left[Y_U\right]=-\rho_S r_1\frac{dr_1}{dt}-\tilde{\rho}_U(I_2)\frac{dS}{dt}, \qquad (58)$$

$$\frac{d}{dt}\left[Y_{UZr}\right]=-2\rho_S\left[r_1\frac{dr_1}{dt}+\frac{dS}{dt}\right], \qquad (59)$$

$$\frac{d}{dt}\left[Y_F\right]=-2\tilde{\rho}_U(I_2)\frac{dS}{dt}, \qquad (60)$$

$$\frac{dr_1}{dt} = \frac{-D_{\mathrm{O}}^{\mathrm{UO_2}} \left.\frac{\partial \rho_{\mathrm{O}}}{\partial r}\right|_{I_1} - \tilde{k}_{\mathrm{O}}(I_1)\left[c_{\mathrm{O}}^{\max} - \tilde{c}_{\mathrm{O}}\right]}{\rho_{\mathrm{O}} - (g_1 + c_m g_2)\frac{\rho_{\mathrm{U}}}{c_M}}, \tag{61}$$

$$\frac{dS}{dt} = r_2 \frac{D_{\mathrm{O}}^{\mathrm{ZrO_2}} \left.\frac{\partial \varphi_{\mathrm{O}}}{\partial r}\right|_{I_2} - \tilde{k}_{\mathrm{O}}(I_2)\left[c_{\mathrm{O}}^{\max} - \tilde{c}_{\mathrm{O}}\right]}{\varphi_{\mathrm{O}} - G_S \frac{\rho_S}{c_M}}, \tag{62}$$

where $S = r_3^2 - r_2^2$; $G_S = \begin{cases} g_1, & dS/dt \geq 0 \\ c_{\mathrm{O}}^{\max}, & dS/dt < 0 \end{cases}$;

$Y_F = \varphi_{\mathrm{U}} S$ and fuel layer growth is forbidden in the equation system, i.e. $dr_1/dt = 0$, if $dr_1/dt > 0$. Variable Y_F in Eq. (60) represents an average molar content of uranium in initially pure zirconia layer. In reality uranium is confined within adjacent to the melt intermediate layer with variable mixed composition (U, Zr)O_{2-x}, as explained in section 2.1 of the report. The averaging procedure applied in the model allows avoiding introduction of such an intermediate layer and simplifies handling of the layer structure for the cases of complicated temperature transients.

Diffusion fluxes entering Eqs. (57), (61), and (62) have to be determined by the solution of partial derivative oxygen diffusion equations in relative solid layers with moving boundaries (detailed description see, e.g., in [4]).

The system of differential equations, Eqs. (57)-(62), is effectively solved by the explicit Euler method with variable time step providing required accuracy.

3. Results of new RIAR experiments

Main conclusions from temperature measurements in the second series of RIAR tests on simultaneous dissolution of UO_2 crucible and ZrO_2 cylinder [1] can be briefly formulated as follows:

- temperature gradient in crucible walls was not really large (as assumed in the first test series) and practically disappeared within first ~100 s of annealing stage (either in the tests with isolating coverplate or without);
- pyrometer data are not reliable and should be removed from consideration;
- surface thermocouple data fairly determine temperature conditions of melt in both (1st and 2nd) test series;
- therefore, results of the first test series should be reconsidered as conducted at higher temperatures than ascribed before (by pyrometer).

These conclusions can be derived from comparison of temperature measurements by two thermocouples (surface and "deep") and pyrometer in tests with and without insulating coverplates (over the crucible) presented in Figs. 5 and 6, respectively.

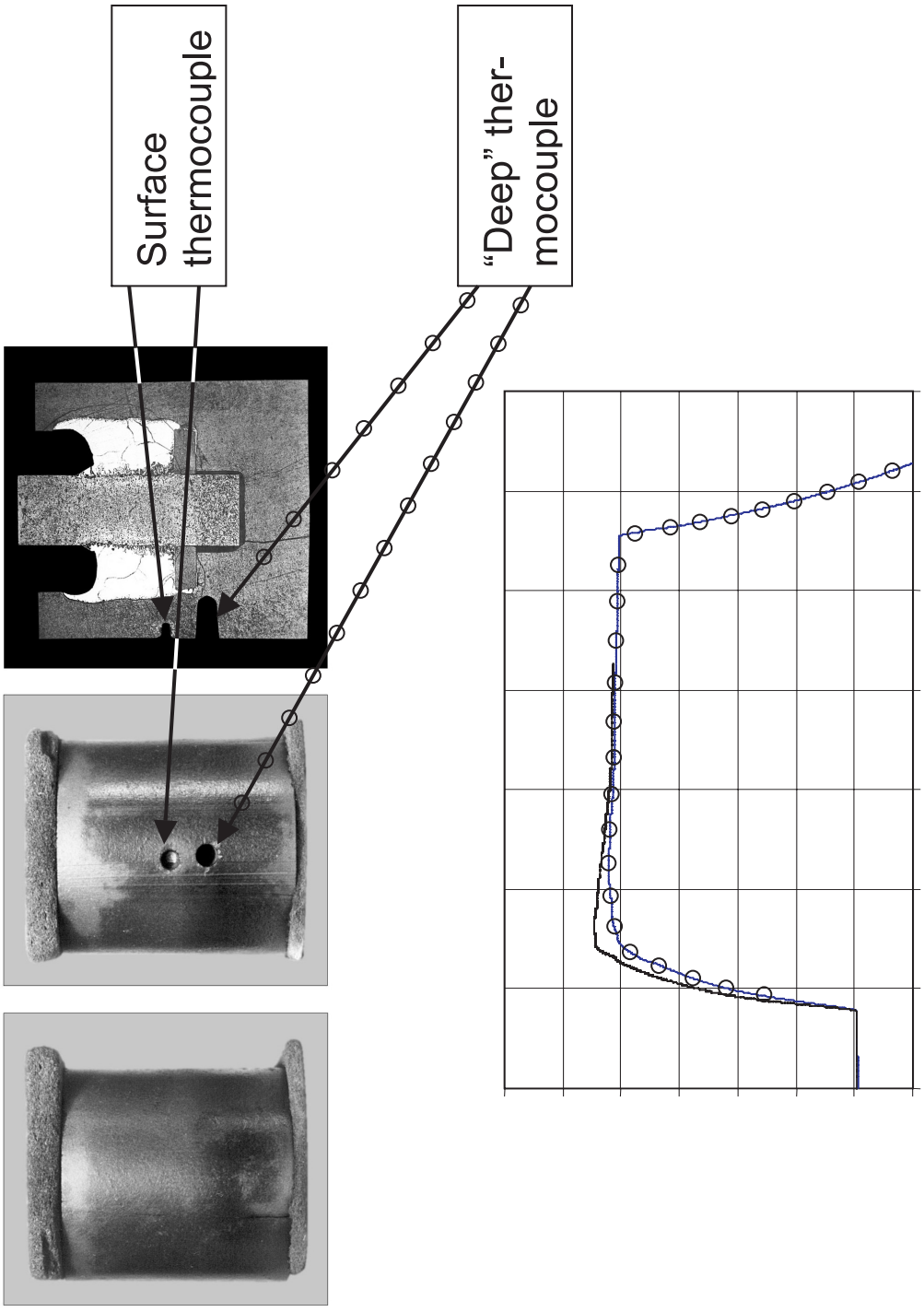

Fig. 5. Results of RIAR tests with "deep" thermocouple and with coverplate (2nd test series, T = 2100 °C, t = 400 s).

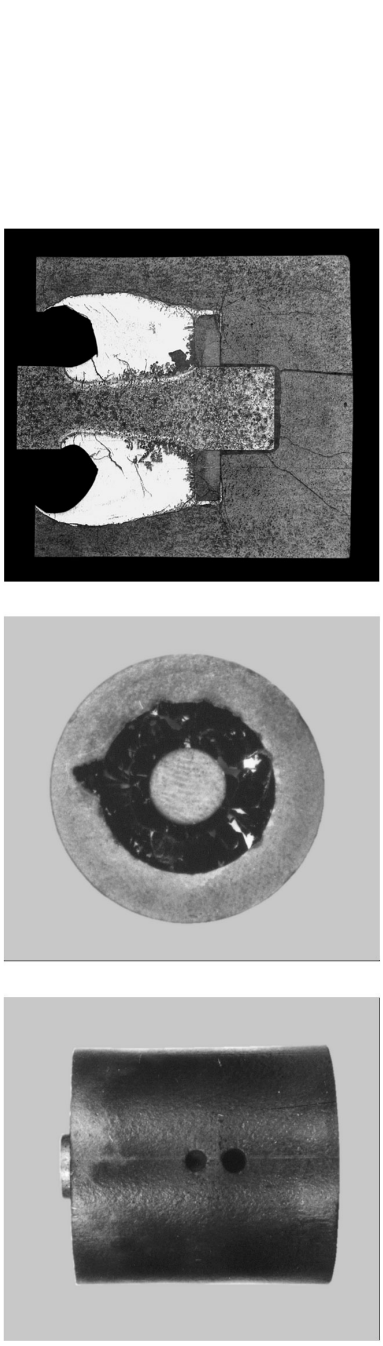

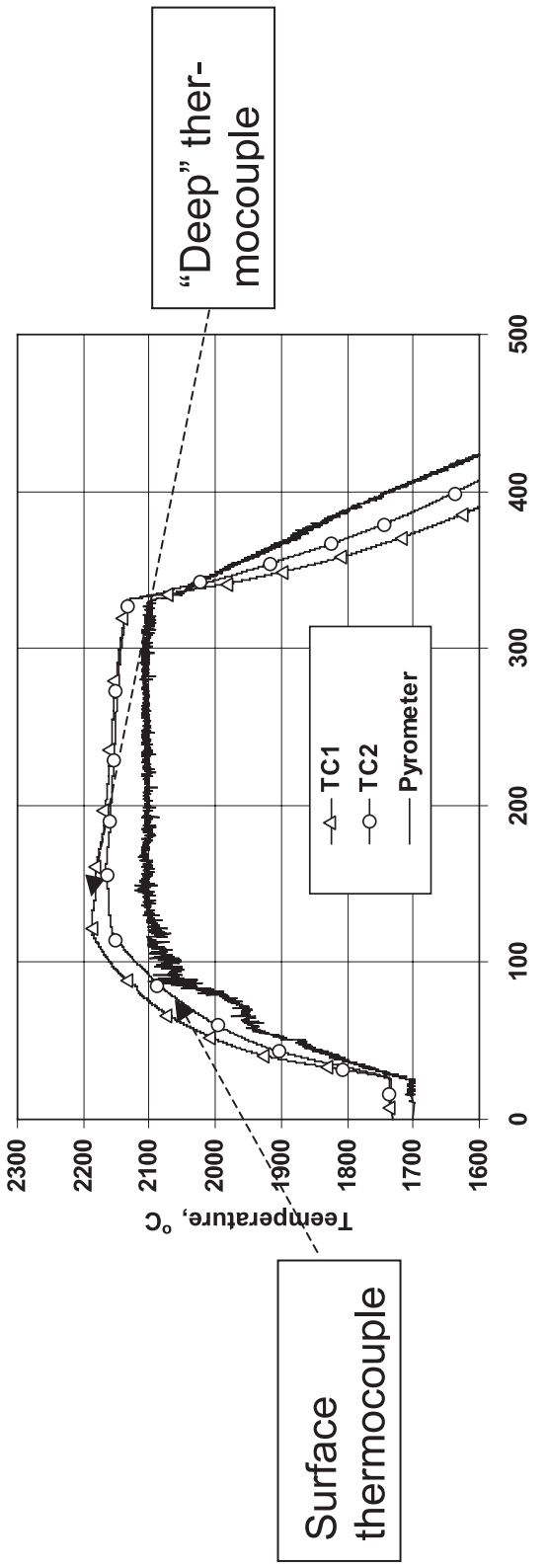

Fig. 6. Results of RIAR test [1] with "deep" thermocouple and without coverplate (2,[nd] test series, T = 2100 °C, t=200 s).

4. Simulation of RIAR tests

4.1. Adjustment of model parameters

Before starting simulation of RIAR tests, a preliminary procedure of the main model parameters tuning was performed. For this purpose, the model was validated against previous AECL test series on UO_2 crucible wall dissolution by molten Zry [11]. In this test series either pure or pre-oxydized (with 25 at.% of oxygen) Zry charge were used at the same test temperatures 2100 and 2200°C. This allows to fix unambiguously model parameters g_1 and g_2 determining position of the liquidus line at the test temperatures. Results of such fitting are presented in Fig. 7. In all subsequent calculations of the RIAR tests these fitted parameters will be fixed and invariable.

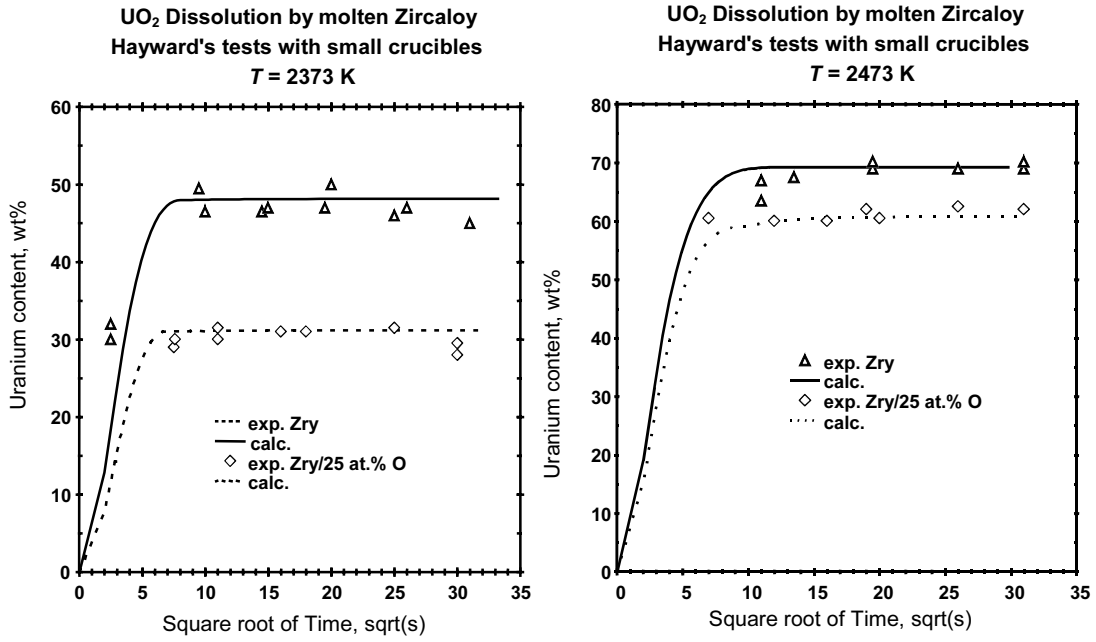

Fig. 7: Uranium weight content in the melt in the two tests at 2373 and 2473K with pure and pre-oxydized Zry charges [10].

4.2. Simulation of the 2nd test series (crucibles with isolating coverplates)

The second series of RIAR tests performed with isolating coverplates, consists of three tests: two tests at 2100 °C with duration 200 and 400 s, and one test at 2200 °C with duration 180 s. The uranium weight content in the melt was measured along with image analysis of dissolved volumes of UO_2 and ZrO_2 materials. As demonstrated by RIAR experimentalists [10], these results are in a fair consistence with each other, i.e. uranium weight content recalculated from dissolved UO_2 and ZrO_2 volumes satisfactory fits to the directly measured value. This allows an advanced validation of the model by comparison of calculated dissolution rates with measured ones independently for each solid material.

Results of simulation of the 2nd series of RIAR tests are presented in Figs. 8 and 9.

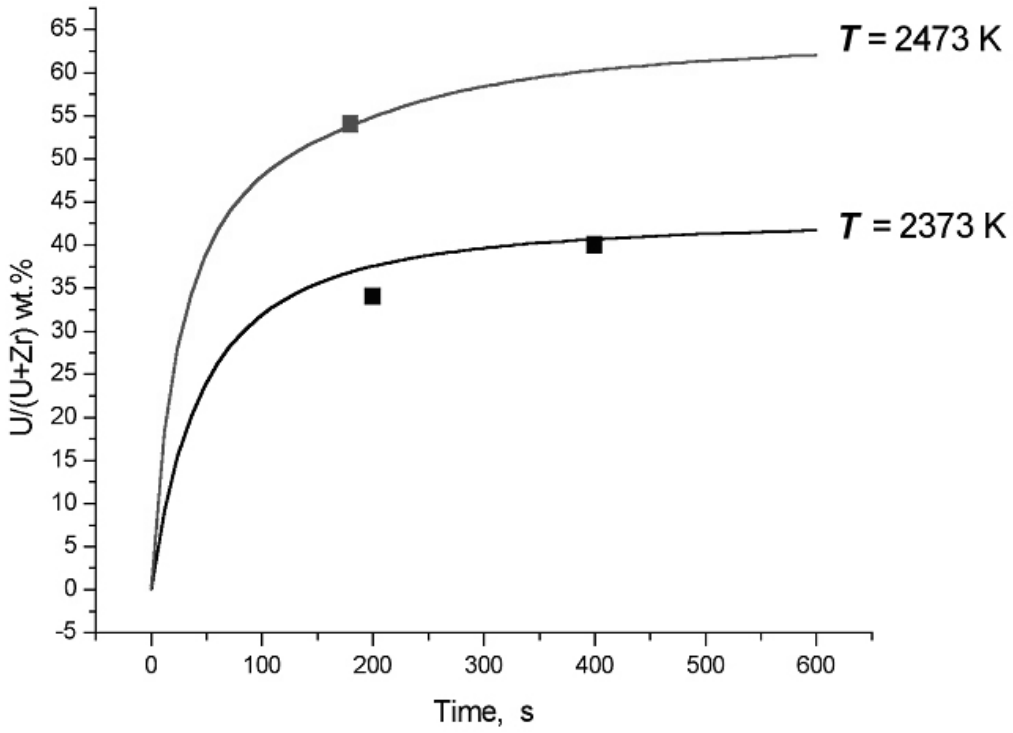

Fig. 8. Comparison of calculated and measured uranium weight content in the melt in the 2nd series of RIAR tests performed at 2100 and 2200 °C.

4.3. Simulation of the 1st test series (crucibles without isolating coverplates)

On the base of above presented (in Section 3) conclusions from the new test observations, re-interpretation of test conditions in the 1st test series has been done. Namely, it was assumed that the surface thermocouple data rather than pyrometer ones determine temperature of the melt during annealing. This results in a significant shift for the test temperature in the range 50-100 K (from test to test) in comparison with the temperatures initially ascribed from pyrometer data. Therefore, simulation of the 1st series of RIAR tests (conducted without coverplates) was carried out for temperature conditions determined by surface thermocouples. Results of these calculations performed with the same set of model parameters as in simulation of the 2nd test series, are in a reasonable agreement with measurements, Fig. 10.

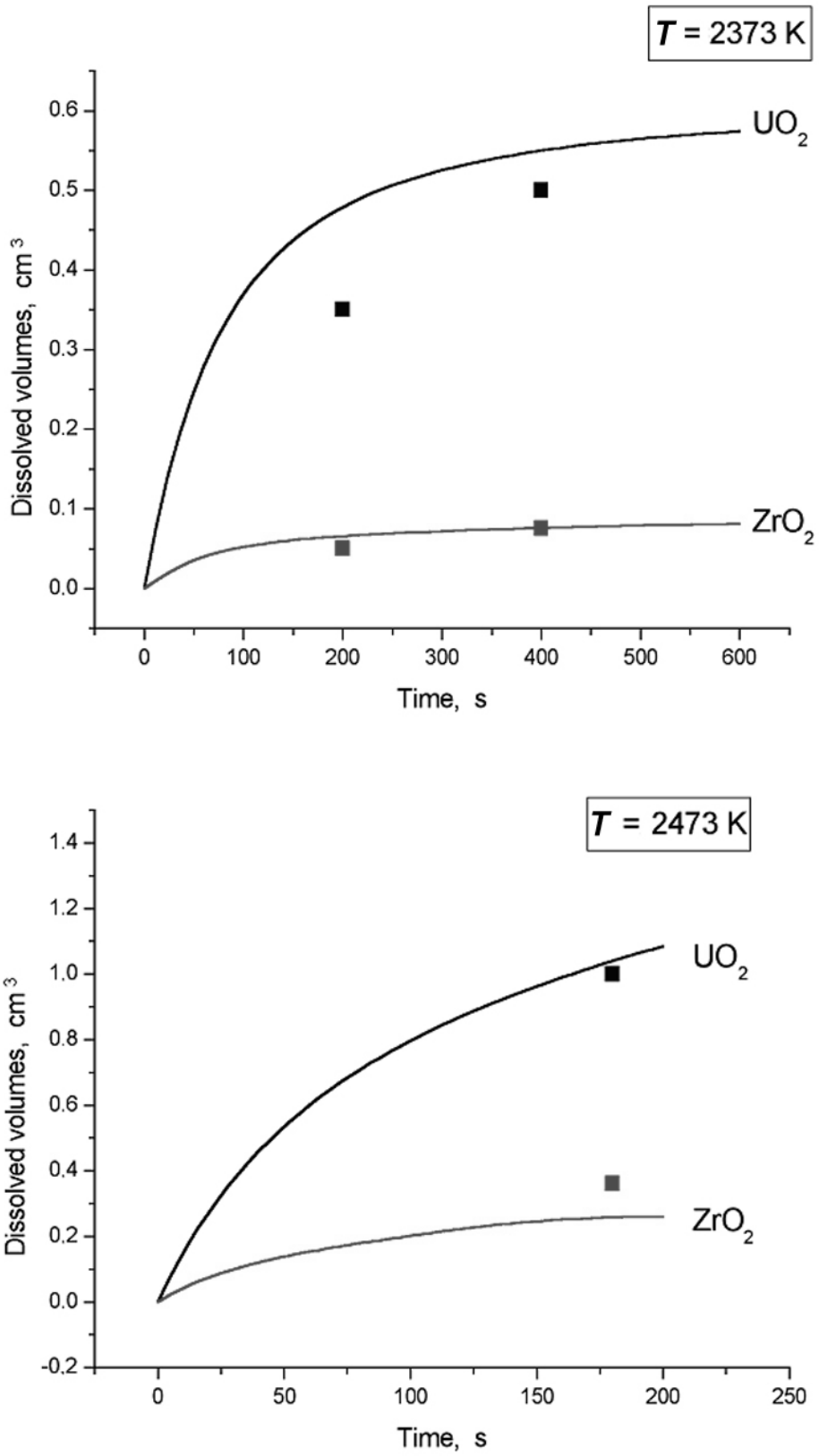

Fig. 9. Comparison of calculated and measured dissolved volumes of UO_2 and ZrO_2 in the melt in the 2nd series of RIAR tests performed at 2100 and 2200 °C.

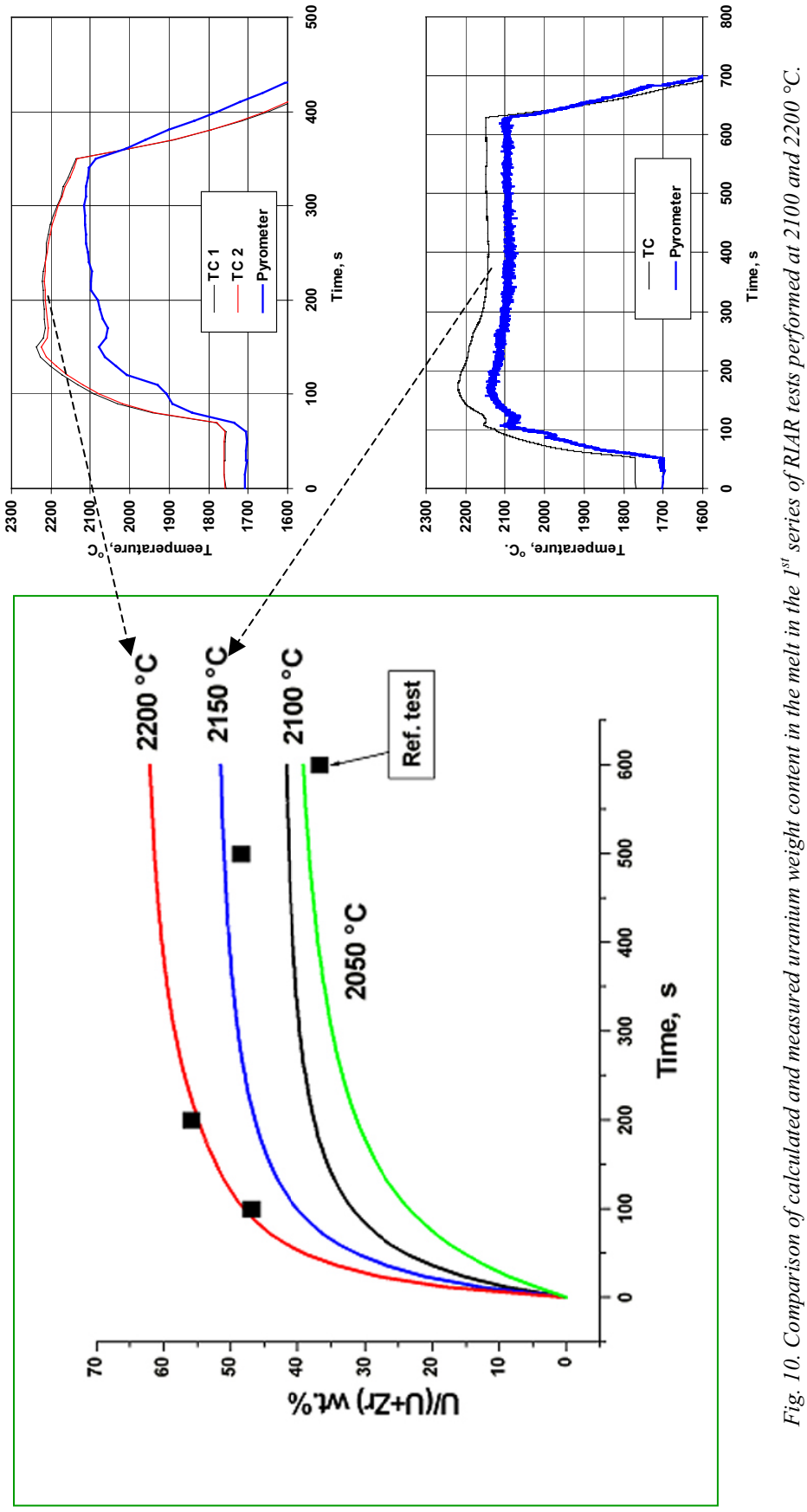

Fig. 10. Comparison of calculated and measured uranium weight content in the melt in the 1st series of RIAR tests performed at 2100 and 2200 °C.

5. Conclusions

On the base of the previously developed models for separate dissolution of UO_2 and ZrO_2 by molten Zr, a new model for simultaneous dissolution of these materials was developed. The model considers interactions of solid materials with convectively stirred melt during the two stages: saturation and precipitation. The system of equations includes mass balances for three components (U,Zr,O) and flux matches at two solid/melt interfaces.

The model was used for pre-test calculations and analytical support of the RIAR tests. A set of modellers' recommendations for test design and conduction (e.g. additional tests with insulating coverplate and "deep" thermocouples) was realised by RIAR experimentalists in the second test series.

Results of the second test series (either uranium melt content or dissolved volumes of solid UO_2 and ZrO_2 materials) were self-consistently simulated by the new model without tuning of model parameters.

Analysis of temperature measurements by "deep" thermocouples allowed re-interpretation of test conditions in the first test series. Recalculation of the first test series with corrected melt temperatures resulted in a satisfactory agreement with measured dissolution kinetics.

References

1. *K. Müller, A.V. Goryachev, V.P. Smirnov, A.M. Svyatkin, J. Stuckert, M.S. Veshchunov, A.V. Berdyshev*, Simultaneous Dissolution of UO_2 and ZrO_2 by Molten Zircaloy. New Experiments and Modelling. Report FZKA 6947, SAM-COLOSS-P074, Karlsruhe, Germany, January 2004.
2. *D.R. Olander*, Nucl. Eng. Des. 148 (1994) 253.
3. *P.J. Hayward, P. Hofmann, J. Stuckert, M.S. Veshchunov, A.V. Berdyshev*, UO_2 Dissolution by Molten Zircaloy. New Experimental Results and Modelling. Report FZKA 6379, INV-CIT(99)-P029, Karlsruhe, Germany, 1999.
4. *M.S. Veshchunov, A.V. Berdyshev*, J. Nucl. Mater. 252 (1997) 98-109.
5. *P. Hofmann, J. Stuckert, A. Miassoedov, M.S. Veshchunov, A.V. Berdyshev, A.V. Boldyrev*, ZrO_2 Dissolution by Molten Zircaloy and Cladding Oxide Shell Failure. New Experimental Results and Modelling. Report FZKA 6383, INV-CIT(98)-P026, Karlsruhe, Germany, 1999.
6. *K.T.Kim and D.R.Olander*, J.Nucl.Mater. 154 (1988) 85, 102.
7. *M. Ramacciotti, F. Sudreau, C. Journeau, G. Cognet,* Nucl. Eng. Des., 204 (2001) 377-389.
8. *M.S. Veshchunov and P. Hofmann*, J. Nucl. Mater. 209 (1994) 27.
9. *M.S. Veshchunov, P. Hofmann, A.V. Berdyshev*, "Critical evaluation of UO_2 dissolution by molten Zircaloy in different crucible tests", J. Nucl. Mater. 231 (1996) 1-19.
10. *P.J. Hayward and I.M. George*, "Dissolution of ZrO_2 in Molten Zry-4", J. Nucl. Mater. 265 (1999) 69.

Criteria of the Oxide Scale Failure at High Temperature

A.V. Boldyrev

1. Introduction

When the melting temperature of the metal Zircaloy is reached, the failure of the cladding and the mechanisms of chemical interaction, which take place between the metallic melts and the solid UO_2 pellet and ZrO_2 layer on the external cladding surface, have great relevance to core degradation, giving the possibility for low-temperature (U, Zr, O) mixture relocation and giving rise to an increased release of fission products from the liquefied fuel. If a sufficiently thick oxide layer has formed on the outside surface of the cladding tube, the relocation of any molten Zircaloy will be prevented, or limited inside the gap between cladding and fuel pellets, because of a "crucible" effect due to the high melting point of ZrO_2. The oxide layer will remain in place until its melting point is reached, or until it is dissolved by molten Zircaloy, or until it fails mechanically. Depending on the mode of failure and the melting capability of the solid rod by the liquid mixture, the molten material may relocate as rivulets (heat transfer process).

Analyses of the results of the integral tests on the severe accident behavior of the fuel bundles under the loss of coolant conditions show that the oxide scale failure strongly influences the accident progression. The cladding failure usually occurs after the burst or local melting of the cladding which lead to the internal overpressure disappearance and the onset of the inner cladding surface oxidation. Under the further temperature escalation the metal phases of Zircaloy melt and the oxide scale prevents the molten Zircaloy from relocation. After the oxide scale failure an intensive oxidation of the melt occurs at a high temperature region of a bundle and a blockage forms at lower and more cold parts of the bundle. These can lead to the further sharp temperature increase due to reduction of the bypass flow and heat release due to the melt oxidation.

The oxide scale failure at high temperatures occurs as a wall breach formation and is termed "flowering" due to increase of a distance between breach edges which allows melt relocation.

Knowledge of cladding failure mechanisms above the Zircaloy melting temperature is currently lacking. Only simple parametric models using user-defined parameters are currently available in the code systems. In the assumption currently made, the ZrO_2 layer fails when a certain temperature limit is exceeded (typically 2300-2500 K) and the ZrO_2 layer is less than a limiting thickness (the oxide shell is assumed not to break if typically 60 % of the original wall has been completely oxidized); the uncertainty in the break temperature is more significant. The large scatter in the cladding failure parameters used in the code applications is evidence for the lack of understanding in this area, and for the need to develop physically-based models. The development of such models requires an experimental data base.

The objective of the present paper is to study and clarify the possible reasons and criteria of the oxide scale failure ("flowering") at high temperatures, and to develop a model for its prediction.

2. Experimental data analysis

In the present investigation the available experimental data on the oxide scale failure at high temperatures obtained at the FZKA (Germany) tests [1] are analysed.

2.1. Experimental procedure

Different experimental approaches have been applied to obtain the required data, however, only the experiments in the small-scale QUENCH test apparatus have been successful. The design of the test section for ZrO_2 shell-failure-criteria experiments and specimen are presented in Fig. 1. The tube specimen of a length of 50 mm, filled with ZrO_2 pellets, is suspended inside a quartz tube which is surrounded by an induction heating coil. The specimens were inductively heated up to 1400 °C in an argon-oxygen mixture and were held at this temperature from 2 to 9 min. Then the specimens were further inductively heated up with heating rate from 2 to 10 K/s (Fig. 2) up to the onset of cladding failure and release of the molten material. After the detection of the molten material on the outer specimen surface the power supply was shut down and the specimens cooled down. The cladding surface temperature is measured by a pyrometer in the center of the specimen in all tests, in some tests a centerline thermocouple was used additionally.

After the tests the tube specimen was cut at the location where cladding failure occurred and metallographically prepared to determine the thickness of the remaining layers. In Figs. 3-4, the most typical views of the specimen surfaces and the cross sections near the molten material appearance are presented for the low and the high heating rates.

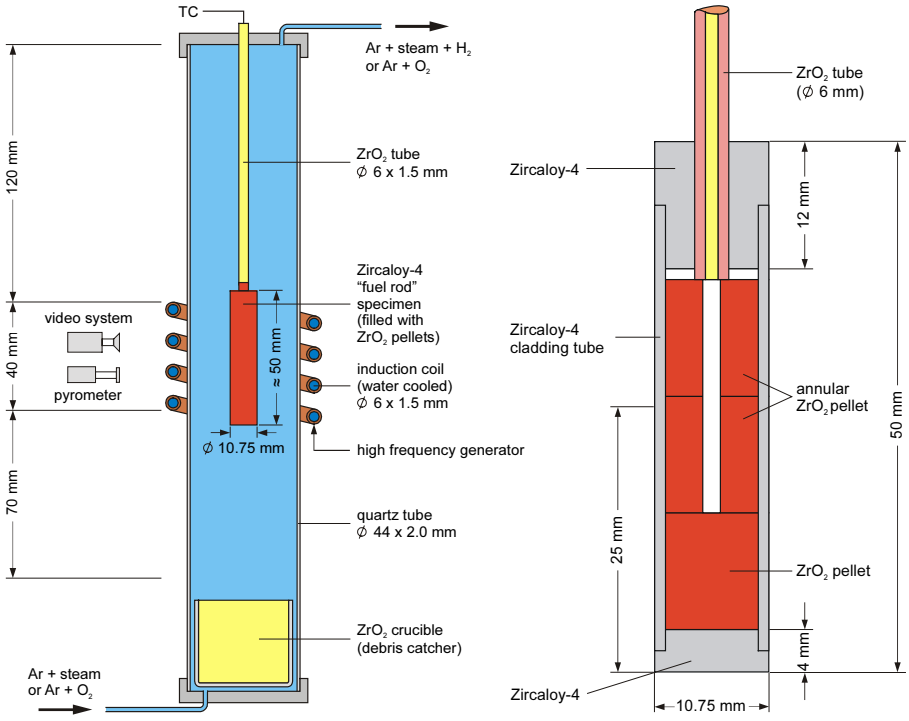

Fig. 1. Test section design and specimen for ZrO_2 shell-failure-criteria experiments.

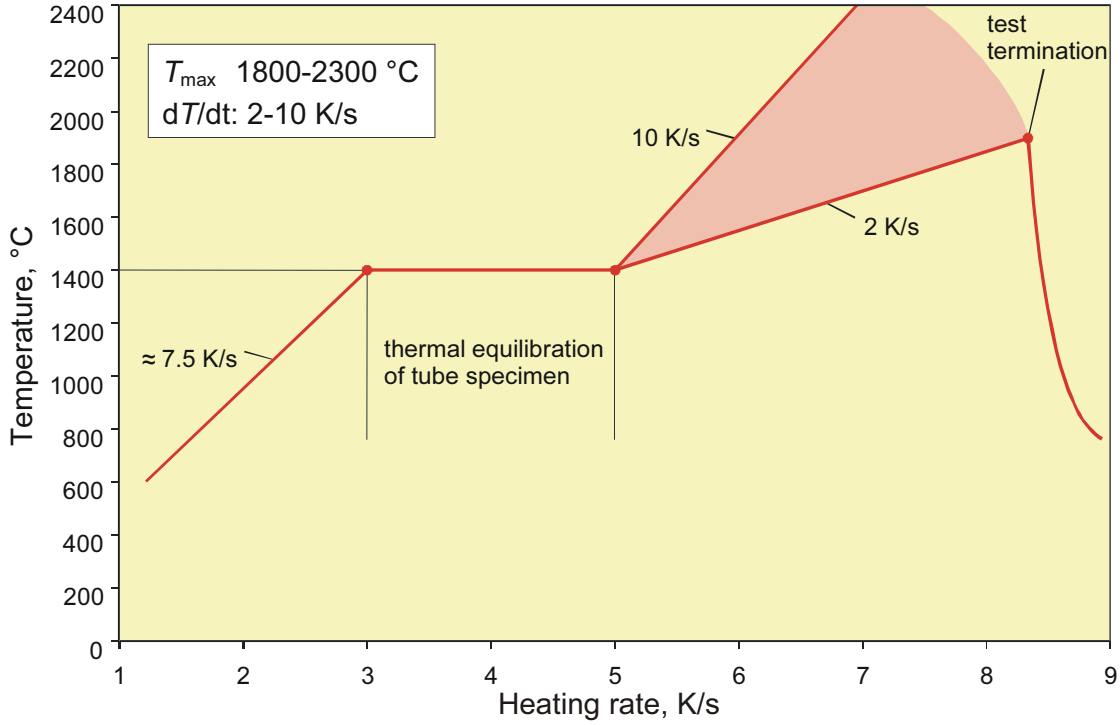

Fig. 2. Test conduct of the ZrO_2 shell-failure-criteria experiments.

2.2. Experimental observations and their interpretation

The essential results of the FZKA experiments with a time of pre-oxidation of 2 min at 1400 °C and different heating rates are presented in Table 1.

For each tests the following data are available:

- The heating rate value.
- The temperature of the specimen outer surface at onset of failure measured by the pyrometer and/or the pellet centre temperature measured by the thermocouple.
- The failure location, i.e., elevation (distance from the sample bottom) where the failure occurred.
- The thickness of the external oxide scale at various elevations. If only the oxide scale was observed at the elevation it was assumed that complete wall oxidation occurred.

In Fig. 5 the temperatures of oxide scale failure and in Fig. 6 the outer oxide scale thicknesses near the failure location are plotted as a function of heating rate. At the same graphs the results of the statistical treatment are presented as the means and the standard deviations.

The following main features of the oxide failure at the given heating rate can be derived from the analysis of the presented experimental results.

- One can see that the pyrometer measured temperature of oxide scale failure varies between 1950 and 2130 °C in the case of heating rate 4 K/s, and between 1980 and 2030 °C in the case of higher heating rates 8 and 10 K/s. The scatter of the "flowering" temperatures is wider for lower heating rate.
- The thickness of the outer oxide layer near the location of the molten material appearance is many times greater in the case of low heating rate, see Fig. 3. In the case of high heating rate the oxide thickness strongly varies in the azimuth and axial directions: the minimum thickness of the oxide scale is observed near the oxide failure location Fig. 4. In the case of low heating rate the oxide thickness variation occurs in the azimuth direction, but this variation is less than for high heating rate.
- A thick inner oxide scale (near the pellets) is observed in all tests with low heating rate, Fig. 3. Oxide thickness varied between 50 and 190 μm. In the case of the high heating rate the inner oxide is absent or very thin (20-30 μm), Fig. 4.
- Cavities in the pellets due to local dissolution by molten Zircaloy are observed only in the test with high temperature rate.

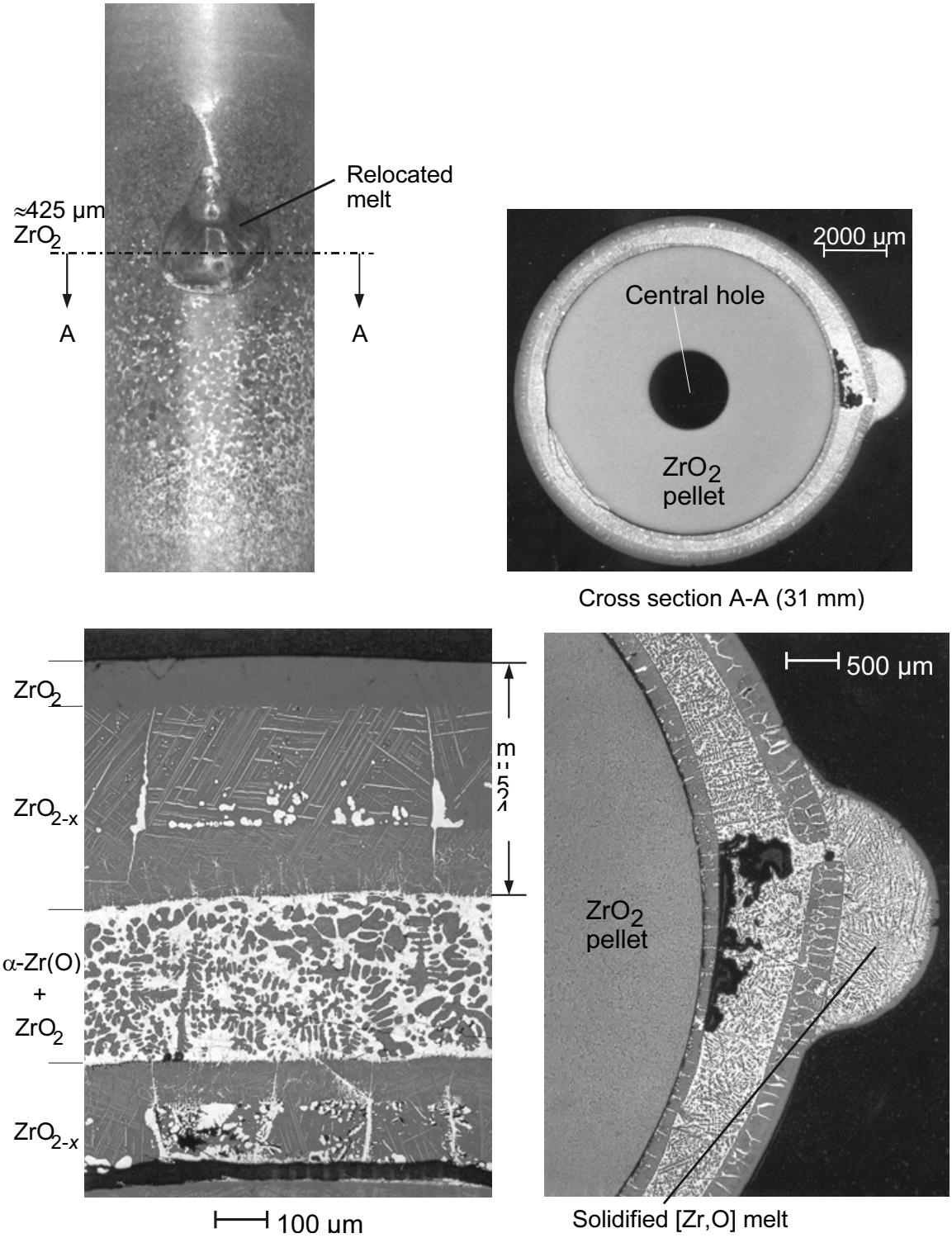

Fig. 3. Test 36SK, Two minutes pre-oxidation at 1400 °C, 4 °C/s heatup rate, melt-through at 2100 °C (pyrometer)/2185 °C (centerline TC). Two upper pictures: outer surface and cross section of the specimen. Two lower pictures: structure of the layers and breach formed in the oxide layer.

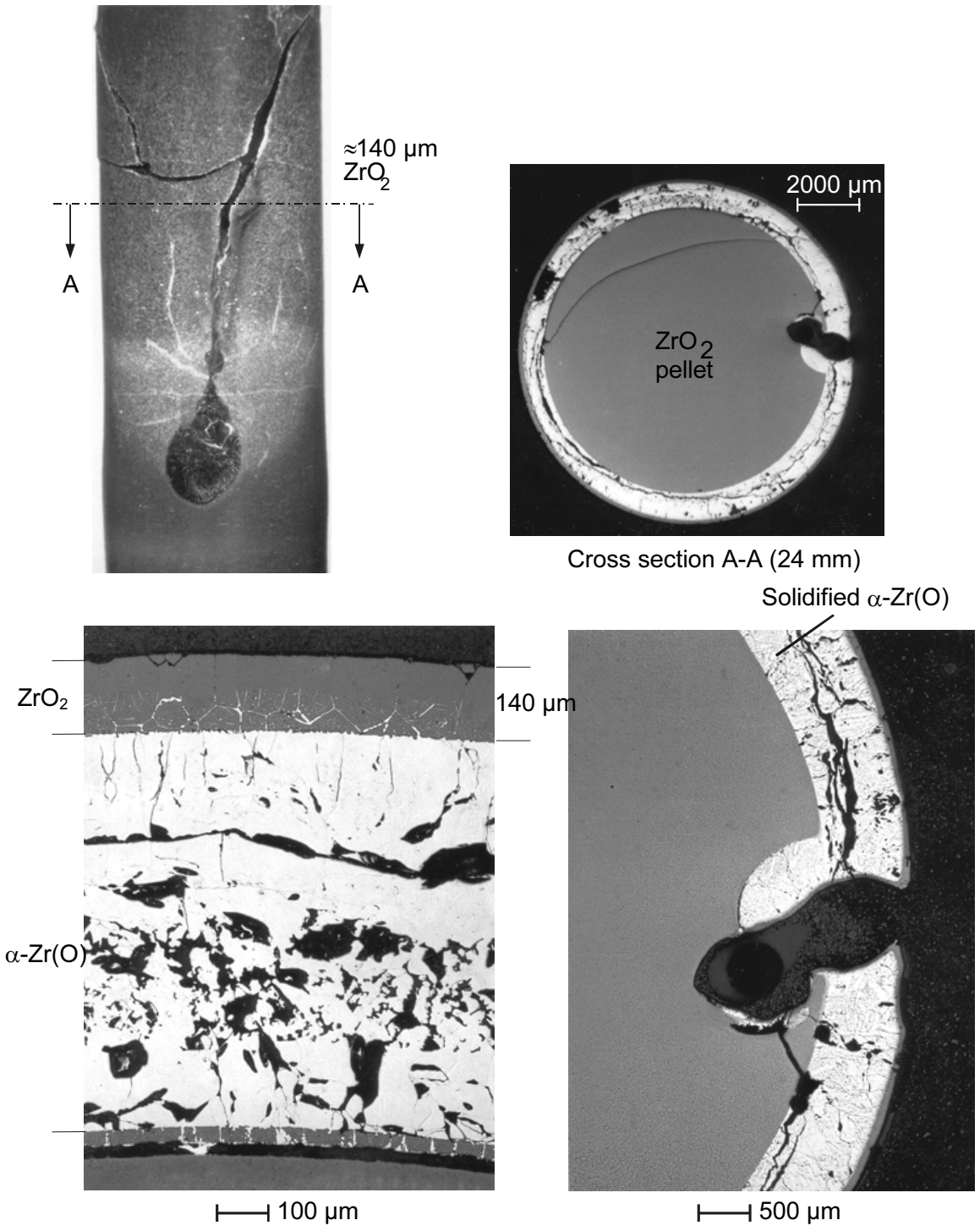

Fig. 4. Test 28SK, Two minutes pre-oxidation at 1400 °C, 10 K/s heatup rate, melt-through at 1960 °C (pyrometer). Two upper pictures: outer surface and cross section of the specimen. Two lower pictures: structure of the layers and breach formed in the oxide layer

- Views of the formed breaches in the oxide shell differ for the various heating rates. In the case of low heating rate the formed breach is covered, as a rule, by the molten material which looks like a drop on the surface, Fig. 3. The cross-section of the formed breach looks like a narrow split in the oxide scale. In the case of high heating rate the formed breach looks like a spot and in some cases the cladding materials are absent due to relocation. Breach formation can be accompanied by the local dissolution of the pellets by molten Zircaloy, Fig. 4. The cross-section of the tube near the failure location shows that the oxide scale is absent along a segment of the circle in the azimuth direction.

Table 1. ZrO_2 shell failure-criteria experiments with Zircaloy-4 tube specimens filled with ZrO_2 pellets.

Heating rate	Temperature at onset of failure		Failure elevation	Outer oxide thickness		Test ID
	Pyrometer	TC		Elevation	ZrO_2	
°C/c	°C	°C	mm	mm	μm	
2	2010	–	10	35 25 9,5	530 compl. 455	22SK
2	1930	–	9	–	–	25SK
2	2020	> 2300	5	36 25 14	compl. compl. compl.	40SK
3	1800	–	25	35 25 13	230 390 270	23SK
3	2170	–	10	35 25 10	compl. compl. 435	24SK
4	1950	–	17	35 25 16,5	180 300 345	19SK
4	2130	1870	30–36	31,5 25 12	395 510 580	35SK
4	2100	2185	27–36	31 25 13	425 550 560	36SK
4	2130	2180	30–33	31,5 26 14	425 530 570	39SK
5	2000	–	26–35	30 25 13	425 380 435	27SK
5	2020	–	13, 25	–	–	29SK
5	2100	1990	23–41	34 24 10	320 340 345	33SK
6	1860	–	25	35 25 13	120 200 215	25SK
6	1930	1859	–	–	–	31SK
6	1975	1815	20–37	35 26 14	140 210 250	34SK
6	1880	2010	27–35	33 25 13	175 230 230	38SK
8	2010	–	26	35 26 13	85 110 175	20SK
8	1980	–	20–28, 32–40	35 24 13	90 125 180	21SK
8	2030	1820	25–39	35 25 12	120 170 210	32SK
8	1970	1855	26–36	–	–	37SK
10	1960	–	10–37	32 24 12,5	110 140 150	28SK

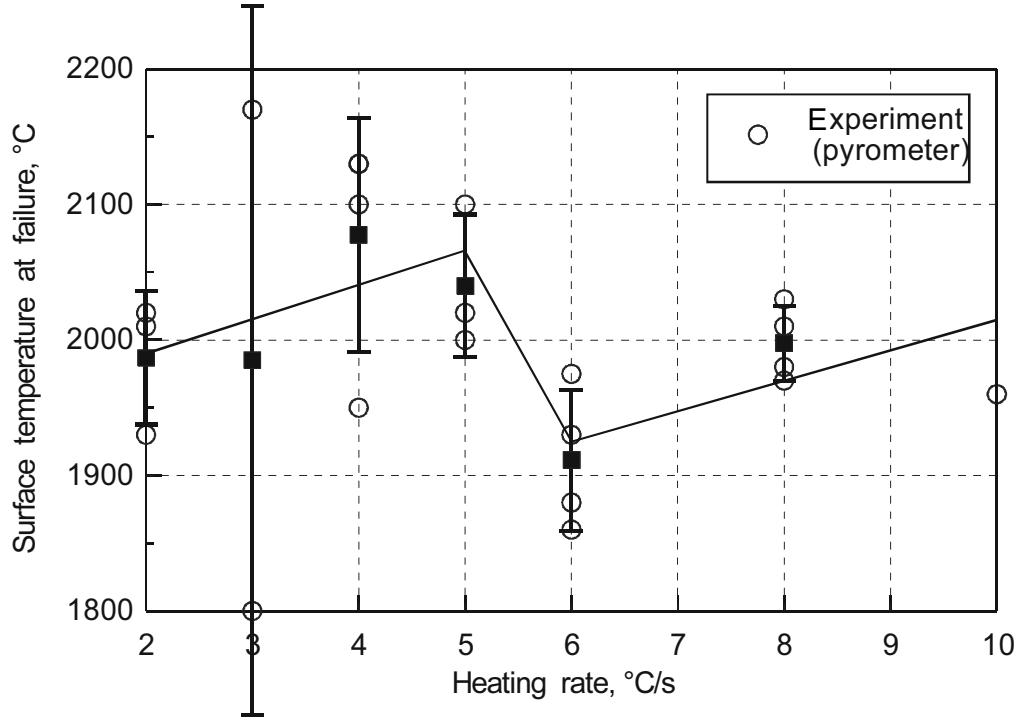

Fig. 5. The measured surface temperature at failure as a function of heating rate and the results of statistical treatment.

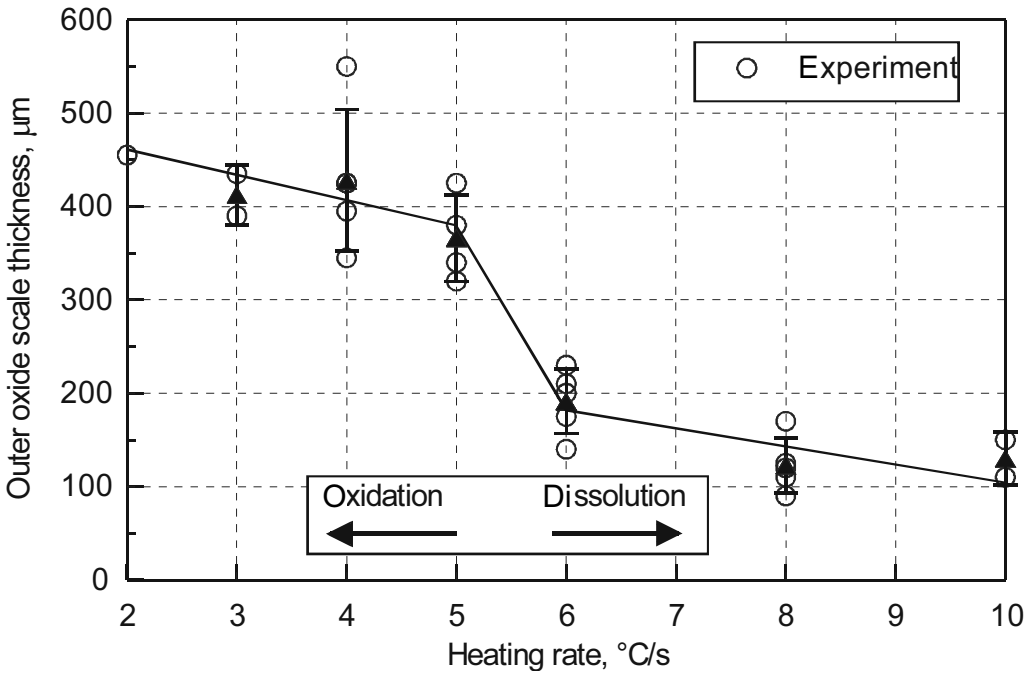

Fig. 6. The measured thickness of the outer oxide scale near the failure location as a function of heating rate and the results of statistical treatment.

These experimental observations lead to the following hypotheses on the modes of the oxide scale failure at high temperatures under various heating rates, Fig. 7:

- At high heating rates the outer oxide scale which was formed in the pre-oxidation stage, is partially dissolved by molten Zircaloy during heating, and the thinned oxide layer is broken by the hydrostatic pressure of molten Zircaloy. The local vigorous dissolution of the oxide scale can occur near the formed breach.
- At low heating rates the outer oxide scale which was formed in the pre-oxidation stage, continues to grow during heating, and the inner oxide layer appears on the

pellet surface. Owing to the volumetric expansion of oxide, the free (gap) volume unoccupied by the melt decreases and finally disappears, leading to the oxide scale failure induced by the incompressible molten Zircaloy pressure.

- Behavior of the oxide scale under loading by molten Zircaloy depends on the oxide scale and metal phase thickness, oxygen concentration in molten Zircaloy and oxygen flux at the cladding surface.

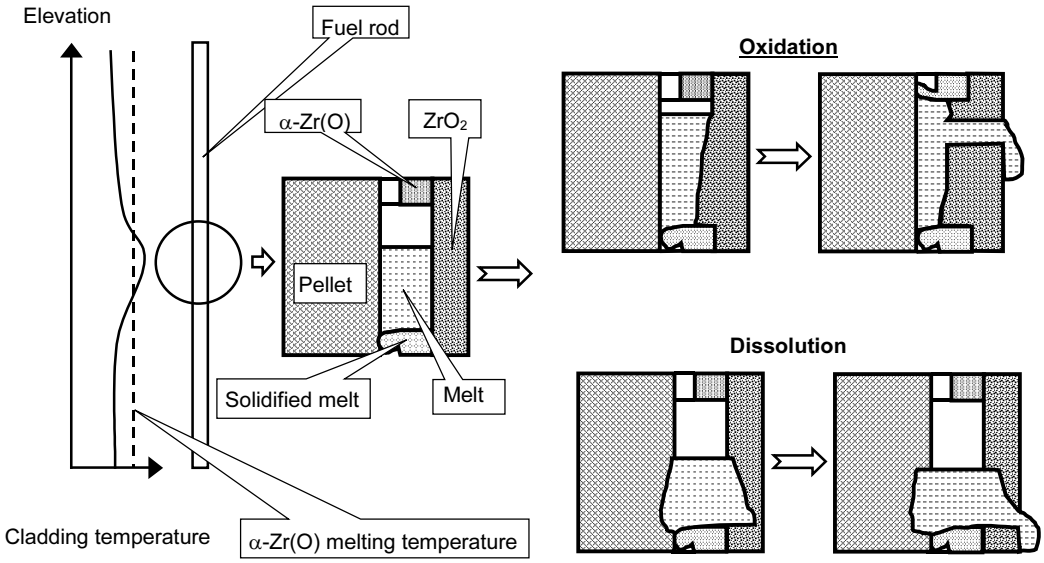

Fig. 7. Scheme of the proposed approach of the oxide shell failure at high temperature.

At high heating rates, the thinner oxide scale grows during transient up to melting of the metal Zircaloy phases. The volume of the molten materials is higher and the oxygen concentration is lower than in the case of low heating (note that a higher amount of grey ceramic phase particles in the post-test view photographs corresponds to a higher oxygen concentration in the melt). This leads to the intensive convective stirring of the melt and dissolution (erosion) of the outer oxide layer and, possibly, of the pellets fabricated from the stabilised zirconia.

At low heating rates, the thick outer oxide scale, smaller volume of the molten materials and higher oxygen content inhibit the dissolution rate and lead to the oxide scale growth. The outer oxide grows due to the outer oxygen flux and the inner oxide grows due to oxygen flux from the pellets. Any factor decreased the gap volume leads to decrease time to oxide scale failure, for example, the increased fuel pellets diameter as a results of inaccuracy during production or due to swelling.

The competitive processes of the oxide scale dissolution (erosion) and oxidation (corrosion) were described by the model [2] developed on the base of the zirconia crucible dissolution tests.

The model CROX of the SVECHA/QUENCH code [3, 4] for the oxide scale deformation and failure at high temperatures was further developed to examine the deformation behavior of the oxydized cladding under conditions of the tests [1] and to verify the proposed hypotheses on the reasons of the oxide scale failure.

3. Oxide scale stress state under the "flowering" conditions

An approach for the stress state evaluation of the oxydized cladding in the stages before Zircaloy melting is described in [3]. In the present section the specific features of the oxide scale deformation under "flowering" conditions are considered.

In the latest stages of an accident when the cladding burst or local melting occurred and

external and internal pressures equalised, the factors of the stress generation in the oxide scale are the following:

- temperature gradient along the oxide scale thickness,
- hydrostatic pressure induced by molten Zircaloy column,
- volumetric expansion under oxidation which leads to disappearance of the gap volume and, then, to generation of the high level pressure in the incompressible Zircaloy melt.

Basing on the assumption that oxide deforms elastically up to its melting, the final stress state is considered as a superposition of the stresses generated by all these factors. For this reason, each of these factors will be considered in more detail.

3.1. Stress in the oxide scale due to temperature gradient in the radial direction

From simulations of the radial temperature distribution by the heat-exchange module of the SVECHA/QUENCH code [3-5], it was found that radial temperature gradients in the metal layers are negligible and the radial temperature distribution in the outer oxide layer may be significant and approximated by a linear function, Fig. 8. It is assumed that the oxide scale can be considered as a thin wall cylindrical shell. Hence, due to a small ratio of oxide thickness to the average oxide radius, the influence of the cylindrical geometry becomes negligible and the average oxide temperature T^{ox} can be determined as a half of the sum of the external T^{ox}_{ext} and internal T^{ox}_{int} surface temperatures:

$$T^{ox} = \frac{T^{ox}_{ext} + T^{ox}_{int}}{2}. \quad (1)$$

The temperature drop in the oxide scale can be calculated as:

$$\Delta T^{ox} = T^{ox}_{int} - T^{ox}_{ext}. \quad (2)$$

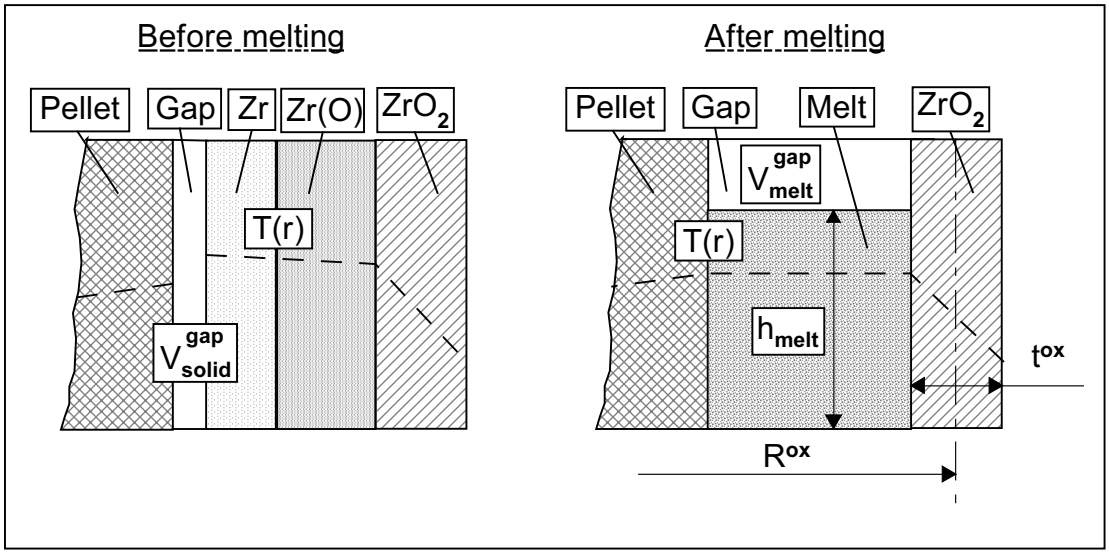

Fig. 8 Structure of layers of the oxidized cladding before and after melting of Zircaloy

Under an assumption of a thin oxide layer the following expression of the linear elasticity theory for the surface circumferential, axial and radial stresses caused by the radial temperature drop can be applied [6]:

$$\sigma^{ox}_{\theta}(r^{ox}_e) = \sigma^{ox}_{z}(r^{ox}_e) = \frac{E^{ox}}{2(1-\nu^{ox})} \cdot \alpha^{ox} \cdot \Delta T^{ox},$$
$$\sigma^{ox}_{\theta}(r^{ox}_i) = \sigma^{ox}_{z}(r^{ox}_i) = -\frac{E^{ox}}{2(1-\nu^{ox})} \cdot \alpha^{ox} \cdot \Delta T^{ox},$$
$$\sigma^{ox}_{r}(r^{ox}_i) = \sigma^{ox}_{r}(r^{ox}_e) = 0, \quad (3)$$

where $\sigma^{ox}_r, \sigma^{ox}_\theta, \sigma^{ox}_z$ are the radial, circumferential and axial stresses in the cylindrical coordi-

nate system, respectively; r_i^{ox}, r_e^{ox} are the internal and external oxide scale radii, respectively; E^{ox}, ν^{ox} are the Young's modulus and Poisson's ratio of the oxide at the average temperature T^{ox}, respectively.

The average stress (across the oxide thickness) is equal to zero, hence, the oxide cracks if the tensile circumferential or axial stress on the surface exceeds the flexural strength. It is assumed that cracks propagate through the oxide scale. If the metal layers did not melt before the oxide cracking, then as a rule the cracks propagation is arrested by the ductile metal layer. In the case of molten Zircaloy the through-wall breach can form.

3.2. Stress in the oxide scale due to pressure of molten Zircaloy

The stress in the oxide scale after melting of Zircaloy depends on the gap volume between the pellets and the cladding. If the gap volume is greater than the volume increment of the metal layers during melting (the volume of Zircaloy increases due to melting), as shown in Fig. 8, then an additional stress is generated by the hydrostatic pressure of molten Zircaloy column:

$$p = \rho \cdot g \cdot h_{melt}, \qquad (4)$$

where p is the pressure of molten Zircaloy on the bottom of the melt, g is the gravity acceleration and h_{melt} is the height of the molten Zircaloy layer after the relocation into the gap between pellets and the oxide scale.

This pressure leads to the circumferential stress in the oxide scale, the axial and radial stresses are negligible. In the case of a thin wall cylinder this average tensile circumferential stress can be found in the following way:

$$\sigma_\theta^{ox} = \frac{R^{ox}}{t^{ox}} \cdot p, \qquad (5)$$

where σ_θ^{ox} is the circumferential stress in the oxide scale, R^{ox} is the average oxide scale radius and t^{ox} is the oxide scale thickness, Fig. 8. If after Zircaloy melting the oxide scale is intensively dissolved, this stress can break the thin oxide scale. The average axial stress is equal to zero.

If the volume increment of the metal layers during melting is greater than the gap volume then the tensile circumferential stress in the oxide scale increases very steeply (the axial stress is much less) owing to the incompressibility of molten Zircaloy. Hence, the oxide scale may crack practically at the moment of Zircaloy melting.

If the volume increment of the metal layers during melting is less than the gap volume, but a further melt oxidation (corrosion) occurs, a similar reason of the oxide scale failure may take place, Fig. 8. In this case the gap volume further reduces owing to the volumetric expansion under oxidation. When the gap disappears, then the oxide scale cracks as described above.

4. Oxide scale cracking

4.1. Criteria of the oxide scale failure under "flowering" conditions

It is assumed that the oxide scale cracks if the following conditions are satisfied:

- The superposition of the average (through the oxide scale thickness) stresses exceeds the limit value.
- The maximum axial or circumferential stress on the oxide scale surfaces exceeds the flexural strength.

In the first case, an approach proposed by Mohr [7] may be used. According to this approach, the fracture occurs along the plane where the maximum shearing stresses act. The fracture is caused by normal and shearing stresses acting in these planes. For the multiaxial stress state the fracture criterion for the material with different strength under tension and compression is the following:

$$\sigma_{eqv} = [\sigma]_t, \qquad (6)$$

where σ_{eqv} is:

$$\sigma_{eqv} = \sigma_1 - \psi\sigma_3, \qquad (7)$$

where σ_1, σ_2, σ_3 are the principal stresses in the given point which satisfy the condition $\sigma_1 \geq \sigma_2 \geq \sigma_3$, and ψ is the tensile to compressive strength ratio.

Taking into consideration that under the "flowering" conditions the average circumferential

and axial stresses are tensile and the radial stress is negligible, the condition of the oxide scale failure may be written as:

$$\sigma_{\theta}^{ox} = [\sigma]_t, \qquad (8)$$

where σ_{θ}^{ox} is the average circumferential stresses induced by the molten Zircaloy pressure.

In the case of the oxide scale failure due to the surface stresses, the criterion can be defined in the following way:

$$\sigma_{\theta,surf}^{ox} = [\sigma]_f \quad \text{or} \quad \sigma_{z,surf}^{ox} = [\sigma]_f \qquad (9)$$

where $\sigma_{\theta,surf}^{ox}, \sigma_{z,surf}^{ox}$ are the surface circumferential and axial stresses, respectively. These stresses are induced by superposition of the stresses due to radial temperature gradient, Eq. (3) and the average stresses due to the pressure of the molten Zircaloy.

4.2. The residual carrying capacity of the oxide layer after cracking

At the heating stages before Zircaloy melting the stresses in the oxide scale can satisfy the criteria of the oxide cracking, Eq. (8) or (11). In the last case the surface stresses are the sum of the stresses due to radial temperature gradient, Eq. (3) and the average stresses obtained from the solution of the stress state problem for the multilayer oxydized cladding [3,4]. The average stresses are the result of the following factors:

- the internal (in the gap between fuel pellets and cladding wall) and the external (in the channel of the coolant) pressures;
- the volumetric expansion of the cladding material due to oxidation under condition of non-planar geometry;
- different thermal expansion of the oxydized cladding materials;
- expansion of fuel pellets in the case of the gap collapse.

If the stresses in the oxide scale satisfy the failure criteria, Eq. (8) or (11) it is assumed that oxide cracks, i.e. microcracks which are arrested by the ductile metal layer and do not penetrate through this layer, emerge and lead to the loss of the oxide carrying capacity to zero value. If oxidation continues, then a new uncracked oxide layer appears and influences the stress-state of the cladding. This assumption of the loss of carrying capacity of the cracked oxide to zero level works well at the first stage of the cladding heat up when an internal overpressure plays a dominant role in the cladding deformation behavior and leads to a rapid cladding rapture due to the ballooning.

At a later stage of an accident, when the internal overpressure is absent, the influence of a thick oxide layer on a stress-state of the cladding is more important and, hence, the residual carrying capacity of the oxide after microcracking should be taken into consideration. Since analytical calculation of the residual carrying capacity of the cracked oxide is overcomplicated, the simplified approach is used. After the oxide scale cracking only a part of the oxide thickness is assumed to have the carrying capacity:

$$t_{def}^{ox} = t^{ox}(1 - \lambda_{def}), \qquad (10)$$

where t_{def}^{ox} is the residual thickness of the oxide with carrying capacity after cracking; t^{ox} — the oxide thickness before cracking; λ_{def} — parameter, $0 < \lambda_{def} < 1$, which denotes the part of the oxide thickness without the carrying capacity. It is considered as a tuning parameter and its real value can be adjusted by the comparison of the simulation and experimental results. It is assumed that after oxide scale cracking the stresses in the oxide relax to zero level and then only the oxide layer with thickness t_{def}^{ox} deforms. The remained oxide layer thickness is considered as incompressible material without carrying capacity, Fig. 9. In the case of further oxidation new uncracked oxide thickness is added to t_{def}^{ox}.

Consideration of the reduced effective thickness of the cracked oxide is an alternative method of the modeling of the carrying capacity decrease due to cracking. Another one is the reduction of Young's modulus of the cracked oxide, however, in this case two oxide layers with different elastic properties should be considered: a new uncracked layer formed as a result of further oxidation, and the cracked one. After the subsequent cracking three layers should be considered, etc. Thus, the reduction of the effective thickness is a convenient method to overcome these difficulties.

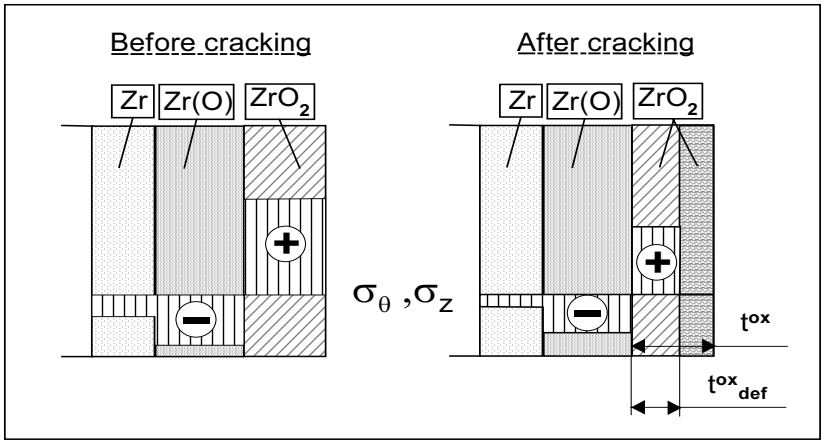

Fig. 9. Reduction of the oxide scale carrying capacity due to cracking.

The effective thickness t_{def}^{ox} corresponds to the residual carrying capacity of the whole cracked oxide layer. Hence, in the real situation this residual carrying capacity is uniformly distributed along the cracked oxide thickness. This should be taken into account during the «chemical thinning» of a cracked oxide under steam starvation or during its dissolution by molten Zircaloy. It is assumed that if the total cracked oxide thickness is t^{ox} and the effective thickness with the residual carrying capacity is t_{def}^{ox}, then the reduction of t^{ox} leads to the proportional reduction of t_{def}^{ox}. For example, if t^{ox} = 100 μm and t_{def}^{ox} = 10 μm, then the reduction of t_{def}^{ox} to the value of 5 μm is caused by dissolution of the half of the total cracked oxide thickness t^{ox}.

5. Simulation of the FZK "flowering" tests

The presented below results were obtained with the help of the SVECHA/QUENCH (S/Q) code [3-5] designed for modeling of the single-rod quenching tests at the FZK facility. The code was modified to take into consideration the specific features of the new FZK tests [1] on failure criteria:

- The deformation behavior module CROX was supplemented with the above described models of the oxide cracking and breaching under the "flowering" conditions.
- The new module LIQF for simulation of the molten Zircaloy oxidation (corrosion) and the oxide scale dissolution (erosion) by the molten Zircaloy, was implemented into the code.

Heating history was simulated by the heat exchange module, the inductive heating was modelled by consideration of the (time dependent) volume heat source in metal layers. Under conditions of a large temperature variation in the oxide scale, the real temperature distribution is very important for oxidation, dissolution and deformation behavior and for correct modeling of the pellets thermal expansion and the oxide scale cracking.

Oxidation kinetics was modelled by the oxidation module of the S/Q code for the solid state and by the dissolution module (LIQF) in the case of Zircaloy melting. It should be noted that the material constants of the dissolution and the oxidation were found from the FZK experimental data on the dissolution of the stabilised zirconia [2], hence, they can differ from the real oxide properties. The channel gas module of the S/Q code was used for an effective treatment of the steam starvation conditions. The material properties were used from the MATPRO data base [8].

The measured and the calculated values of the outer oxide thickness at the failure location are presented in Fig. 10. One can see that simulations reproduced not only the tendency of the thickness decrease with the heating rate increase, but the values of the oxide scale thickness, especially for the case of high heating

rate. Because the dissolution module was worked out for the uranium dioxide pellet, hence, in the case of the pellets prepared from stabilised zirconia interaction between the pellets and melt was not modelled. Thus, in the calculation the inner oxide scale did not form and the volume of the gap was decreased only due to the outer oxide growth. If the experimental values of the inner oxide scale thickness add to the outer ones in Fig. 10 the agreement between the experiment and the calculation will be better.

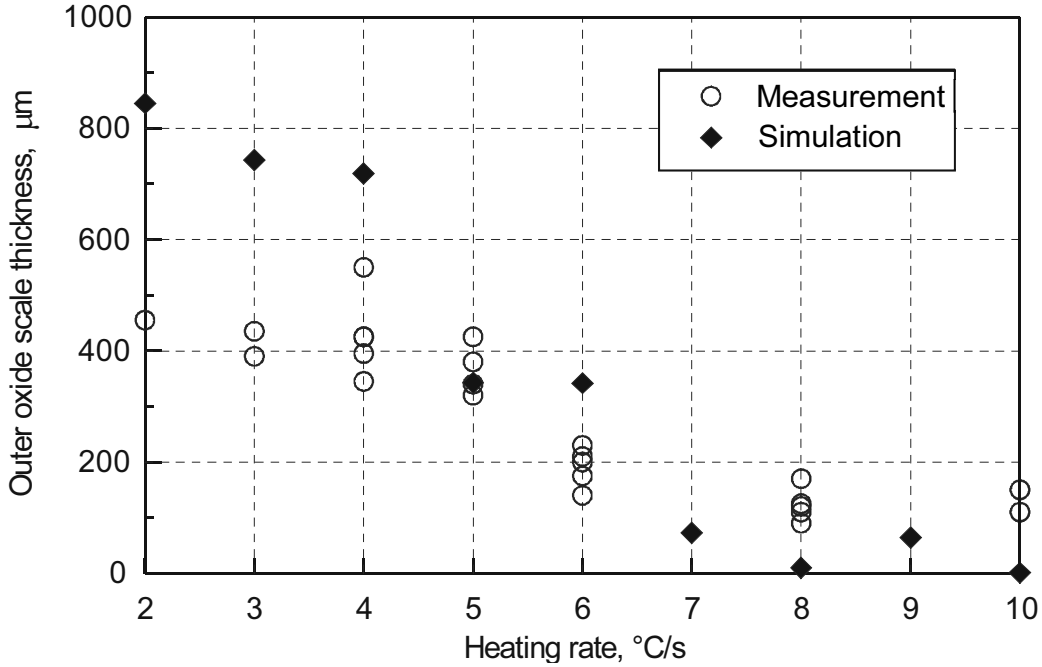

Fig. 10. Comparison of the measured and the simulated thickness of the outer oxide scale near the failure location as a function of heating rate.

So, the measured and the calculated oxide scale thickness are in good agreement, whereas the comparison of the experimental and the calculated failure temperature showed that the agreement is not so good, Fig. 11. In the case of low heating rates (< 5 °C/s), this agreement is not bad but for the case of the high heating rate (6 °C/s) the disagreement increased (see the calculation results with the normal mass-transfer coefficient). Nevertheless, the trend was predicted for the both regimes: the failure temperature increased with the heating rate increase. The possible influence on the obtained results was the inductive heating. It could lead to intensive melt stirring and, hence, to acceleration of the oxide dissolution (this effect is used in induction melting furnace).

Exactly specify the effect of the induction stirring was too hard, therefore the estimation calculation was performed with the mass-transfer coefficient increased by a factor of one hundred, see Fig. 11. One can see a good agreement between the experimental and the calculated failure temperatures in the case of high heating rate. At low heating rate (< 4 °C/c) the results were practically the same and only for the case of heating rate of 5 °C/c the agreement between the measured and the calculated failure temperatures became slightly worse. Thus, one can conclude that the reason of the discrepancy was found and that the heating method can influence on the results in the given conditions.

Let us consider the discussed modes of the oxide scale failure in more detail. In Figs. 12 and 13, the simulation results of the FZK tests with heating rates of 4 and 10 °C/s are presented, these calculations were performed with the normal mass-transfer coefficient. One should keep in mind that after melting one-dimensional figures represent the real system configuration (shown in Fig. 8) conditionally, however, correctly determine the free volume unoccupied by the melt.

In the case of low heating rate (Fig. 12), cladding is heavily oxydized before melting (in accordance with observations). After melting oxidation continues up to the gap disappearance (due to volumetric expansion of oxide) and subsequent oxide failure at ~ 2020 °C due to a high pressure induced by incompressible melt.

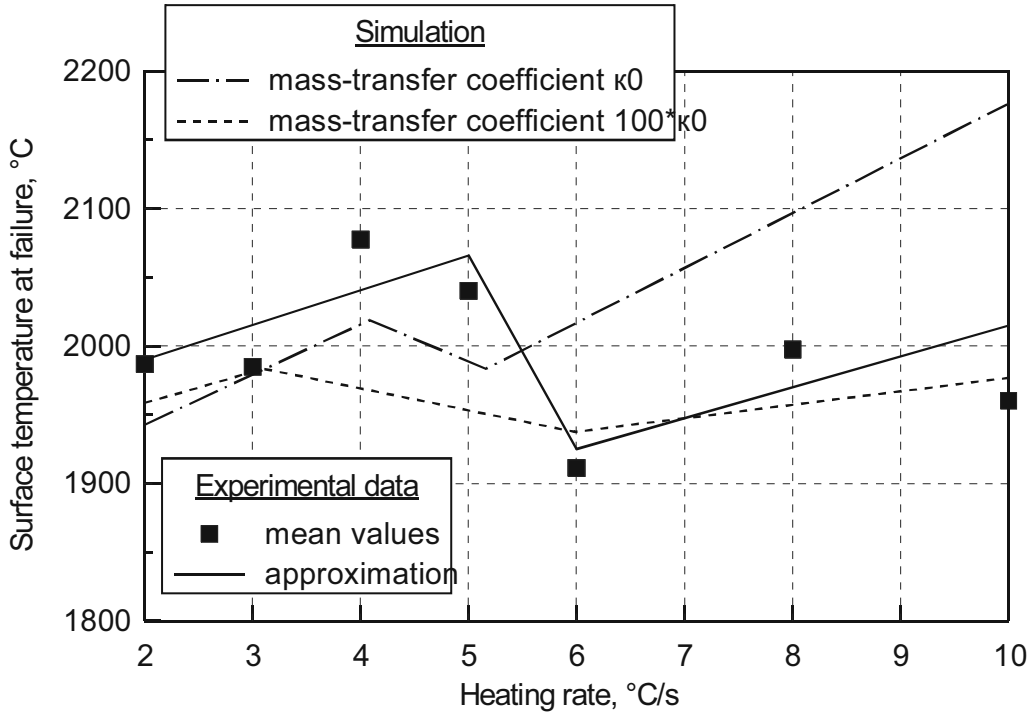

Fig. 11. Comparison of experimental and simulated surface temperature at failure as a function of heating rate.

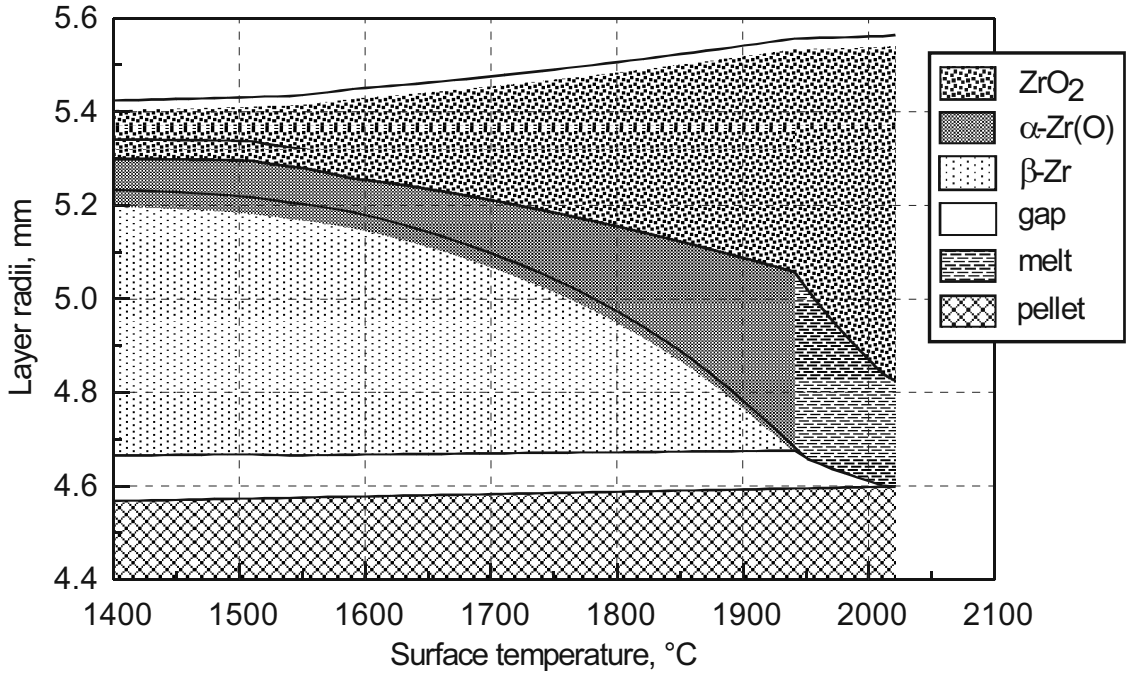

Fig. 12. Calculated evolution of the cladding layers thickness under heating rate of 4 °C/s. Elevation 10-15 mm.

In the case of heating rate 10 °C/c (Fig. 13), the "flowering" occurs at the surface temperature ~ 2180 °C as a result of the oxide scale dissolution and failure of the thinned layer under the hydrostatic pressure of the molten Zircaloy column. One can see that the steam starvation occurred at the upper part of the specimen despite of its short length and could accelerate the oxide scale failure due to additional decrease of the scale thickness. Furthermore, S/Q code simulations shown that the oxygen flux should strongly influence the oxidation kinetics: the decrease of the steam flow in the gas mixture can lead to the transformation of the oxidation kinetics from oxidation to dissolution and vice versa. Hence, time to the oxide scale failure depends on oxidation/dissolution kinetics and the mechanical damages of the oxide scale accumulated in the previous stages of an accident.

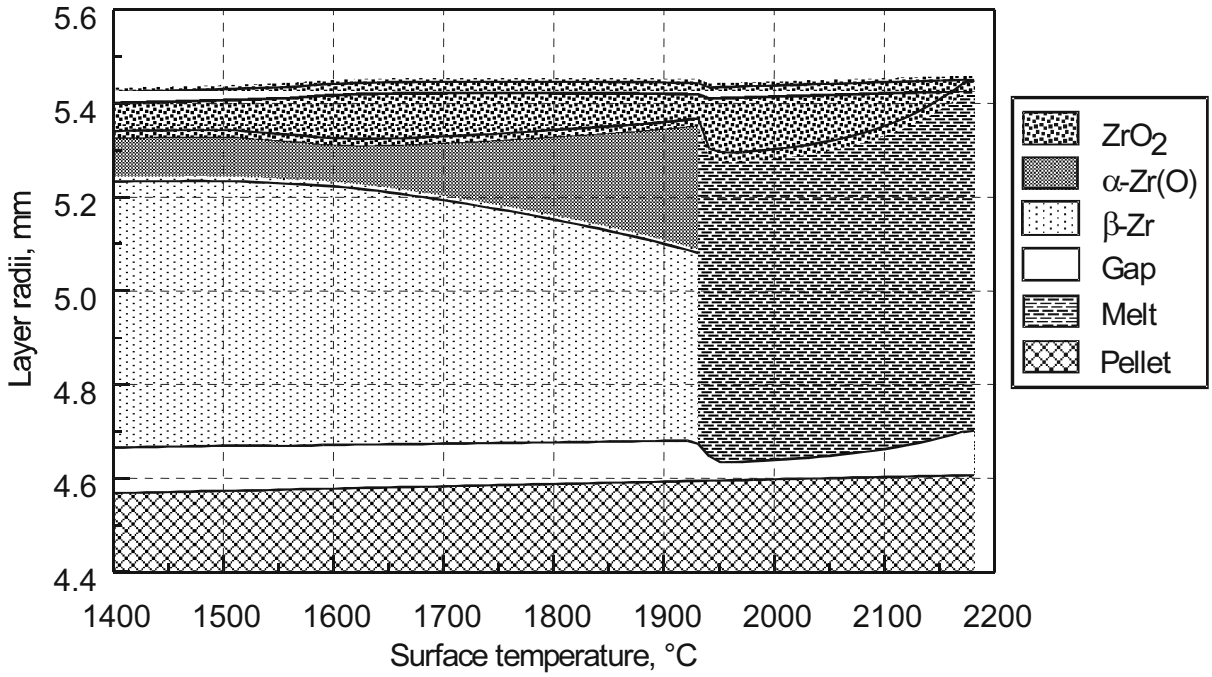

Fig. 13. Calculated evolution of the cladding layers thickness under heating rate of 10 °C/s. Elevation 35-40 mm

From consideration of Fig. 12 it is clear that under slow heating rates the moment of the clad failure is rather sensitive to the gap volume and thus may be rather strongly influenced by a possible deviation (scatter) of the initial pellet radius. In order to simulate such a behavior, an additional calculation with the initial pellet diameter 9.1 mm (instead of the standard value of 9.0 mm) was performed. In this case the "flowering" occurs at a much lower temperature of the surface 2030 °C. Hence, the possible reason of a wide scatter of the "flowering" temperatures observed at low heating rates can be associated with an uncertainty in the initial pellet diameter.

The obtained results allowed to conclude that despite the failure mechanism is the result of mutual interaction of oxidation/dissolution and deformation phenomena, in the first order approximation a simplified approach can be accepted. As revealed in the S/Q analyses breaching due to dissolution mechanism occurs when oxide shell becomes very thin in comparison with the initial thickness, whereas breaching of the oxide shell in the second case (volumetric expansion mechanism) occurs very soon after closure of the pellet-cladding gap. This allows significant simplification of the failure criterion by the following assumptions: the outer oxide scale fails, if:

- either the oxide scale thickness equals to zero (in the first case),
- or the free gap volume equals to zero (in the second case).

Therefore, only simulation of the oxidation/dissolution kinetics may be used to predict the oxide failure under interaction with molten Zircaloy within the simplified approach of the system codes.

6. Conclusions

Analysis of the results of the FZK oxide shell-failure-criteria tests allowed to reveal two modes of the oxide shell failure:

- Oxidation after metal Zircaloy melting: at low heating rates the outer oxide scale which was formed in the pre-oxidation stage, continues to grow during heating, and the inner oxide layer appears on the pellet surface. Owing to the volumetric expansion of oxide, the free (gap) volume unoccupied by the melt decreases and finally disappears, leading to the oxide scale fail-

ure induced by the incompressibility of molten Zircaloy.

- Erosion after metal Zircaloy melting: at high heating rates the outer oxide scale which was formed in the pre-oxidation stage, is partially dissolved by molten Zircaloy during heating, and the thinned oxide layer is broken by the hydrostatic pressure of molten Zircaloy. The local vigorous dissolution of the oxide scale can occur near the formed breach.

The detailed mechanical model of the oxide scale failure was developed on the base of experimental observations. The numerical module of oxide shell failure along with the dissolution module as the components of the mechanistic single rod SVECHA/QUENCH code were used for simulation of the FZK tests. These simulations demonstrated the possibility to predict the reasons and the modes of the shell failure and allowed to approve that:

- Oxygen flux at the outer cladding surface has a dominant influence on the time to the oxide shell failure and the failure mode.
- In the system codes the simplified criteria of the oxide shell failure by molten Zircaloy based only on the oxidation/dissolution kinetics can be applied.

References

1. *P.Hofmann, J.Stukert, A.Miassoedov, M.S.Veshchunov, A.V.Berdyshev, A.V.Boldyrev,* ZrO_2 Dissolution by Molten Zircaloy and Cladding Oxide Shell Failure. New Experimental Results and Modelling. Forschungszentrum Karlsruhe, Technik und Umwelt, FZKA 6383. December 1999.
2. *A.V.Berdyshev and M.S.Veshchunov*, J.Nucl.Mater., 252 (1997) 98.
3. *P.Hofmann, V.Noack, M.S.Veshchunov A.V.Berdyshev, A.V.Boldyrev, L.V.Matweev, A.V.Palagin, V.E.Shestak,* Phisico-Chemical Behavior of Zircaloy Fuel Rod Cladding Tubes During LWR Severe Accident Reflooding, Forschungszentrum Karlsruhe, Technik und Umwelt, FZKA 5846, May 1997.
4. *P. Hofmann, A. Miassoedov, L. Steinbock, M. Steinbrueck, A.V.Berdyshev, A.V.Boldyrev, A.V.Palagin, V.E.Shestak, M.S.Veshchunov,* Quench Behavior of Zircaloy Fuel Rod Cladding Tubes. Small-Scale Experiments and Modeling of the Quench Phenomena. Report FZKA 6208, INV-COBE(98)-D018, Karlsruhe, Germany, 1999.
5. *A.V. Berdyshev, A.V. Boldyrev, A.V. Palagin, V.E. Shestak, M.S. Veshchunov*, Svecha/Quench Code for The Modeling of Reflooding Phenomena in Severe Accidents Conditions. Proceedings of the Ninth International Topical Meeting on Nuclear Reactor Thermal Hydraulics (NURETH-9), paper Log_19 (CD-ROM edition), San Francisco, California, USA 1999.
6. *A.M. Katz,* Theory of elasticity, Moscow, 1956 (in Russian).
7. *V.L.Blagonadezjin, Y.A.Okopnyi and V.P.Chirkov,* "Mechanics of materials and constructions", Moscow, 1994 (in Russian).
8. SCDAP/RELAP5/MOD2 Code Manual, MATPRO-A Library of Materials Properties for Light-Water-Reactor Accident Analysis. NUREG/CR-5273 EGG-2555, 1990.

SVECHA/QUENCH Code for the Modeling of Reflooding Phenomena in Severe Accidents Conditions

A.V. Palagin, A.V. Boldyrev, V.E. Shestak, M.S. Veshchunov

1. Introduction

The reflooding of the reactor core is an important measure for controlling severe accident development in LWRs. As it follows from the analysis of the TMI-2 accident and results of the large-scale experiments, quenching of the degrading core by water injection may lead either to cooling down and cessation of an accident, or to the temperature escalation, intensification of cladding oxidation, steep increase in hydrogen production and even further development of the accident. That will depend on several important parameters characterizing the core state and the way of reflooding. Appropriate understanding of the complex core reflooding processes is necessary for the adequate prediction of the LWR system evolution.

The computer code SVECHA/QUENCH (S/Q) was developed in the Nuclear Safety Institute (IBRAE) of the Russian Academy of Sciences for the detailed modeling of single-rod reflooding phenomena on the basis of the FZK (Forschungszentrum, Karlsruhe, Germany) single rod quenching tests in close cooperation with experimentalists [1, 2]. Within the framework of the S/Q code the main physical phenomena occurring during quenching of fuel rods are considered.

Zirconium oxidation leads to the heat release and hydrogen generation and affects the mechanical properties of the cladding. High cooling rates in the course of quenching sustain non-equilibrium conditions at the interface boundaries of the cladding layers and lead to the appearance of a temperature gradient across the cladding. For the adequate description of the oxidation kinetics under these conditions the Oxidation model based on the partial derivative equations for the multi-layer oxygen diffusion problem was developed zirconium and Zircaloy, respectively, can dissolve large amounts of hydrogen even at high temperatures. Therefore, Zircaloy can act as a sink or source of hydrogen, depending on the environmental conditions. In this way the hydrogen solubility of the cladding material can alter the hydrogen source term. In order to simulate the hydrogen absorption by the Zircaloy cladding observed in the FZK quench tests, the Hydrogen Absorption model considering the cladding interactions with hydrogen/steam mixtures, was developed. The model was tightly coupled with the Oxidation model, and the two models were implemented in the SVECHA/QUENCH code as a combined module.

Cold water injection in the hot core gives rise to the high temperature gradients in the oxidized Zircaloy cladding and initiates oxide layer cracking. The axial temperature gradient at the quench front elevation as well as phase transitions in the cladding materials on cooldown, can lead to the through-wall crack formation and possible fragmentation of the oxidized Zircaloy cladding. The Mechanical Deformation model accounts for the effect of the temperature gradients, $\beta \rightarrow \alpha$ (Zry) and tetragonal-to-monoclinic (ZrO_2) phase transformations on the stress state of the oxidized cladding under quenching conditions and correctly predicts the rod specimen failure modes (cracking, spalling, breaching) observed in the quench tests.

The description of the heat exchange process requires simultaneous solution of two problems: (i) heat conduction problem inside the solid body (fuel rod) and (ii) heat convection problem in the surrounding two-phase water-steam media. For the solution of the first problem in the axially non-uniform multi-layer cylindrical structure (fuel pellets/gap/cladding) the Heat Conduction module was developed. This module is based on the 2-D finite differences numerical scheme with adaptive grid. Thermal-Hydraulic module elaborated for the description of the heat convection process accounts for the heat exchange and non-stationary motion of different water-steam re-

gions. In addition to commonly considered boiling regimes the new "Churn Boiling" regime specific to high overheat (up to 1500-1600°C) is described by the code. This boiling regime is characterized by rather high heat exchange rate and was originally identified by the authors of the present paper on the basis of the analysis of the quench experiments carried out at the FZK (Forschungszentrum, Karlsruhe, Germany) [3]

The heat exchange in the core determines the temperature of the rod surface and thus the oxidation kinetics, hydrogen generation and mechanical deformations of the cladding. The heat released due to Zr oxidation considerably affects the heat exchange, especially at high temperatures. The mechanical behavior of the cladding determines the cladding rupture that provides direct access of oxygen to fresh (non-oxidized) metal surfaces and thus intensification of oxidation and hydrogen production rates.

Therefore, the profound mutual influence of the studied phenomena determines complex behavior of the cladding system during rod quenching. For the adequate description of this process the self-consistent coupling of the Oxidation, Hydrogen Absorption, Fuel and Oxide Scale Dissolution, Mechanical Deformation, Heat Conduction and Thermal-Hydraulic modules into the S/Q code was performed.

The Oxidation, Hydrogen Absorption, Fuel and Oxide Scale Dissolution and Mechanical Deformation modules have been already presented in the preceeding papers, for this reason, only the Heat Conduction and Thermal-Hydraulic modules will be presented here in some details.

The S/Q code was intensively verified against of the FZK single rod quenching tests. The comparison of the calculation results with the experimental data (25 tests with water quenching and 12 tests with cooling by steam) shows satisfactory agreement.

2. Heat conduction module

The oxidized fuel rods have several layers (fuel pellets, gap between the pellets and the cladding, internal oxide layer, metal layer, external oxide layer of the cladding). The Heat Conduction model describes the heat conduction process in such a multi-layered rod (Fig. 1a) with accounting for the different thermal properties of the different layers. The order of layers may be arbitrary; the number of layers is not limited.

The temperature distribution is assumed to be axially symmetrical, so the 2-D finite differences numerical scheme is used. The adaptive grid accounts for the sharp axial temperature gradients in the quench region. The application of the axial meshing refinement in the region of high temperature gradients allows more accurate calculation of the temperature distribution in comparison with the uniform meshing (Fig. 1b). The adaptive grid also accounts for the axial variation of the different layer thickness due to thermal expansion and Zr oxidation.

The spatial distribution of the heat sources due to Zr oxidation is included in the model. The density of the heat sources is calculated by the Oxidation model. The boundary conditions for the heat conduction problem are provided by the Thermal-Hydraulic model.

Figs. 2 and 3 present the results of the Heat Conduction module calculation within the framework of the S/Q code. The FZK test T0507_1 [3] with initial rod temperature 1400°C and 100 μm Zr cladding pre-oxidation was simulated (the conditions of these tests are described below, in the Section 3.2). Fig. 2 presents the temperature distribution in the radial direction at the central TC elevation (75 *mm* from the bottom) at different time instants. Sharp change of the temperature gradient is due to the difference of the heat conduction properties of different layers: pellet (ZrO_2), Zr cladding and external oxide layer. Fig. 3 presents the temperature distribution in the axial direction on the rod surface at different time instants.

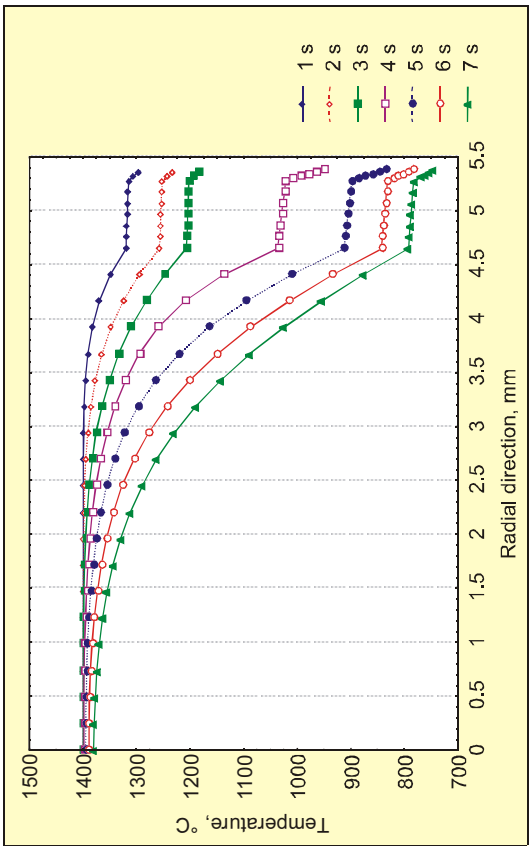

Fig. 2. Temperature distribution in the radial direction at the central TC elevation (75mm from the bottom) at different time instants. FZK T0507_1 experiment simulation (100 μm Zr cladding pre-oxidation, initial rod temperature 1400 °C).

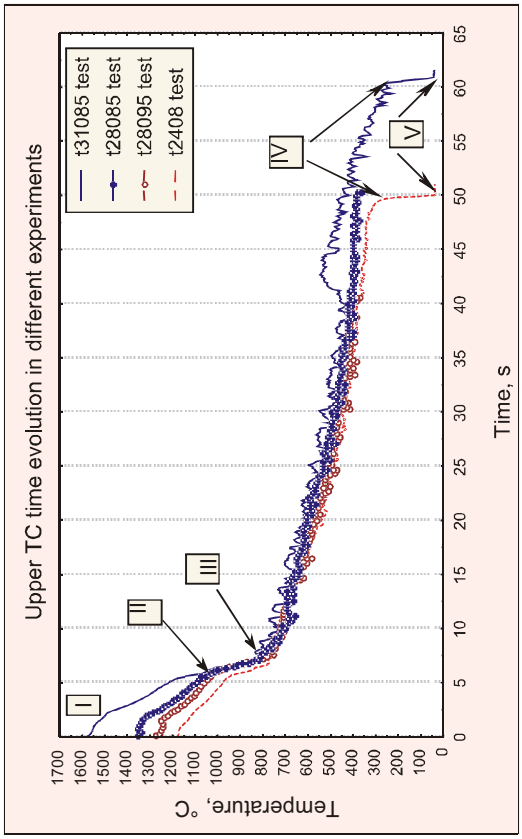

Fig. 4. Temperature evolution of the upper TC in the FZK experiments [3] with different initial temperatures. I-II curves portion: cooling in steam/hydrogen flow (GM region); II-III portion corresponds to CB region; III-IV curves portion: film boiling (IAFB region); IV-V portion: transition from film boiling to nucleate boiling.

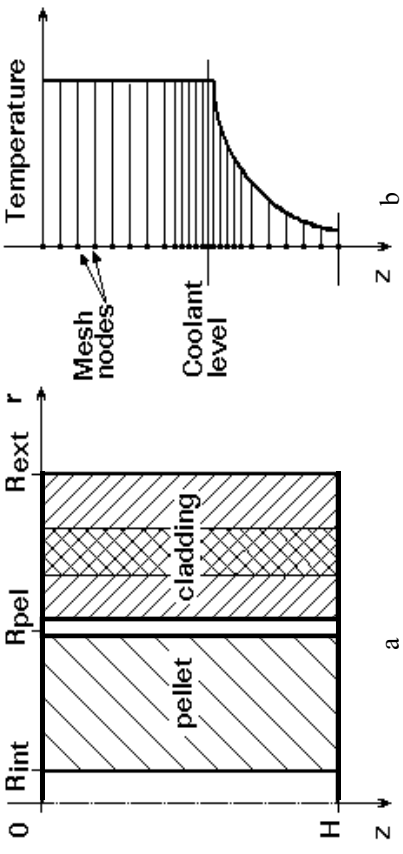

Fig. 1. a). Structure of the many-layered rod element. b). Axial meshing refinement in the region of high temperature gradients.

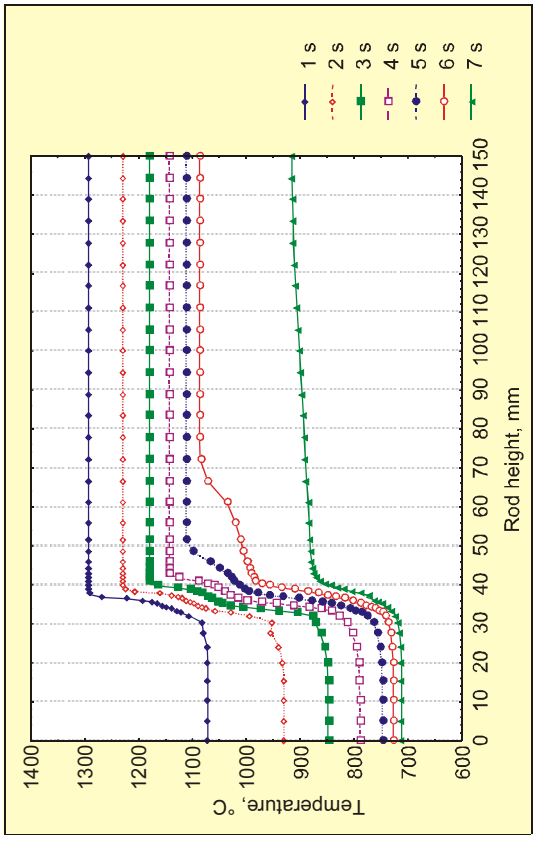

Fig. 3. Temperature distribution in the axial direction on the rod surface at different time instants. FZK T0507_1 experiment simulation (100 μm Zr cladding pre-oxidation, initial rod temperature 1400 °C).

3. Thermal-hydraulic module

3.1. Previous investigations of reflooding phenomena

Numerous theoretical and experimental studies on the heat and mass transfer mechanisms during quenching have been reviewed by Yadigaroglu [4], E. Elias and G. Yadigaroglu [5], Carbajo and Siegel [6], R.A. Nelson [7]. Depending on the surface temperature, different boiling regimes may occur. At the temperatures slightly exceeding the saturation one the nucleate boiling takes place. The nucleate boiling was investigated by Rohsenow [8], Forster and Zuber [9], Chang and Snyder [10], Kutateladze [11] and in many other works.

As the surface temperature grows, the transition from the nucleate boiling to the film boiling begins. In the conditions, typical for the post-dryout core reflooding situation (at relatively low flooding rates and pressures) the film boiling is taking new features. The liquid column is formed downstream the axially progressing quench front (QF, a point at which the rewetting of the hot surface occurs), separated from the hot wall by a thin steam film. This flow regime is often called an Inverted Annular Film Boiling (IAFB). The details of the heat transfer process during stationary film boiling as well as the quazi-stationary IAFB motion and flow regime transitions were studied in different theoretical and experimental works [12-20].

The two-fluid hydrodynamic "6-equation" approach for the quazi-stationary description of the IAFB motion was formulated by Chan and Yadigaroglu [21] and then developed in a number of works [22, 23]. Six equations represent the mass, momentum and energy conservation laws for water and steam, averaged over the radial coordinate.

In several works briefly reviewed in [24] the transitions from the IAFB to so-called Dispersed Flow (DF) and Inverted Slug Flow (ISF) were observed and investigated. In these works mainly the cryogenic fluids: liquid hydrogen [25], liquid nitrogen [26] or freon R-113 [24, 27-30] were used. In the works [31] and [32] the transition from IAFB to ISF and DF for water at relatively low stainless-steel tube surface temperatures (560-770°C) was observed.

The reflooding parameters in the majority of the mentioned above experimental works (subcooling 0-70 °C, flooding rate 0.1-10 cm/s, pressure 1-10 bar, hydraulic diameter ~1 cm) were typical for a LOCA post-dryout reflooding situation. The only but very important exception is the overheat value: in the above experiments the overheat was 200-700 °C, whereas during severe accident the core temperature may exceed the Zr melting point (1750-1800 °C). The description of the reflooding in this situation with high overheats is very important for the prediction of the accident development: cooling down or the further temperature escalation, hydrogen generation and core melting.

3.2 FZK quench experiments

The high overheat values (up to 1550°C) is one of the important features of the current FZK small-scale quench experiments [3]. In these experiments the test specimen was a cylindrical sample of standard Siemens/KWU Zircaloy-4 fuel rod cladding tube with a length of 150 mm, an outer diameter of 10.75 mm and a wall thickness of 0.725 mm filled with ZrO_2 pellets with an outer diameter of 9.1 mm. The specimen was inserted in a quartz tube, which was surrounded by an induction heating coil. The specimens without pre-oxidation and with oxide scales of 100 and 300μm with the initial temperature 1000-1600 °C were quenched from the bottom by water (initial temperature 35 or 90 °C), the flooding rate was 1.5 cm/s. The temperature of the specimen surface at three elevations (28, 75, and 122 mm from the bottom of the specimen) were continuously recorded during the quench test.

The experimental data (in the electronic format) and experiment video records were provided by the FZK experimentalists within the framework of the FZK-IBRAE cooperation. The analysis of the experimental data show, that the large overheats change qualitatively the flow pattern and affect sufficiently the heat exchange rate. The temperature evolution of the cladding surface temperature at the upper TC elevation (122 mm from the bottom) in the

different experiments with the initial temperatures 1200-1600 °C is shown in Fig. 4.

The water inlet temperature in these experiments was close to the saturation value (90 °C). One can recognize four different portions of the temperature evolution curves with different characteristic heat exchange rates: I-II, II-III, III-IV and IV-V. Since the temperature measurements were performed at a fixed elevation, the changing of the heat exchange rates corresponds to the motion of different alternating water-steam regions by this elevation.

The curve portion I-II corresponds to the cooling down of the cladding in the steam/hydrogen flow generated at the lower elevations (the Gas Mixture (GM) region). Here, at high cladding temperatures and relatively low gas flow rates the main contribution to the heat exchange gives the heat flow due to radiation.

The next curve portion, II-III, corresponds to the specific to high overheat water-steam region. This water-steam region is characterized by rather high heat exchange rate and plays an important role in the rod cooling down process. As it can be seen in the experiment video records, the upper part of this region is formed by the water droplets and splashes ejected from below. This droplets and splashes upper part is grade into the vigorously mixing churn water-steam media located below. The motion and mixing of water and steam in this part is similar to the pool boiling. As it will be shown below, this similarity has a certain sense. However, instead of the pool boiling, there is no direct contact between the water and the wall. The steam film adjacent to the wall experiences sharp oscillations with the amplitude comparable with the channel width. This Churn Boiling (CB) region will be discussed in more details in the next subsection.

The curve portion III-IV corresponds to the discussed above Inverted Annular Film Boiling region. It should be noted that the heat exchange rate in this region is distinctly lower as compared with the previous CB region. Noteworthy also is the long duration of the film boiling period (50 s in the case of 1600°C initial rod temperature) typical for high overheats.

Finally, the curve portion IV-V corresponds to the rewetting of the cladding surface and transition from the IAFB to the Nucleate Boiling (NB) region. The Quench Front (QF) position separates the IAFB and NB regions. It should be noted that usually the works on the quench phenomena are concentrated on the investigation of the transition from the IAFB to the NB region and the QF motion. In the case of high overheats, this transition takes place after rather long period of time from the beginning of reflooding and thus, may be not so important for the modeling of the heat exchange process.

In the general case, there may exist four different water-steam regions at a time: Nucleate Boiling region (NB) upstream from the QF, IAFB, CB and, finally GM regions downstream from the QF, at increasing elevations.

The similar picture is usually presented in different works concerning reflooding in low overheats conditions. In doing so, the region between the Gas Mixture and Inverted Annular Film Boiling regions is referred to as Dispersed Flow (DF) or Slug Flow (SF) region. It should be emphasized, however, that in the high overheats conditions the region between the PS and IAFB shows specific properties (the most important is the high heat exchange rate) and differs from the usually described DF and SF regions. The specific features of the CB region are considered in the next subsection.

3.3. Churn Boiling region

The IAFB flow regime and the transition to the Dispersed Flow or Slug Flow regimes in the case of relatively low overheats have been described in several works [24-32]. For a subcooled flow, a part of the heat transferred from the wall is used for evaporation, and the other part is used for the heating of the liquid. In the case of saturated liquid, the heat is used exclusively for evaporation leading to considerable increase of the steam film thickness. The termination of the IAFB regime at a certain distance above the QF and transition to the DF or SF regime is usually explained by the development of large amplitude interfacial waves which break up the liquid column [33]. This occurs when the difference between the steam and the water velocities exceeds a certain limit. In the work [22] the value of the steam velocity in the film is estimated as being 7.5-8.5 m/s and the distance between the collapsed liquid level and the QF position as being 0.15-0.5 m.

- Meanwhile, as it follows from the FZK experiments video records and the temperature evolution data, the breakdown of the IAFB region and the development of the CB region takes place within 2-3 s after the beginning of reflooding, when the steam velocity in the film does not exceed 1-2 m/s and the liquid level is only 3-4 cm from the bottom. Thus, the transition from the IAFB to the CB regime cannot be caused here by the high values of the steam velocity. In these experiments the inlet water temperature was close to the saturation one (90-95 °C).
- The other important observation concerns the FZK experiments with the large subcooling values (inlet water temperature 35°C). In these experiments, the upper liquid level remained practically undisturbed throughout the whole reflooding time interval (with flooding rate 1.5 cm/s it takes 10 *s* to cover the 15 cm rod), and there was clear separation line between IAFB and GM regions.
- The next point is the estimation of the heat flow from the rod due to radiation. Due to Zirconium-steam reaction the ZrO_2 layer (with the emissivity coefficient $\varepsilon = 0.8$ [34]) practically immediately appears on the outer cladding surface. The values of the radiation heat flow calculated as $W_r = \varepsilon\sigma T_r^4$ for the rod surface temperatures in the interval 1650-1300 °C are collected in the following table:

Table 1. Heat flow from the rod surface.

T_r, °C	1650	1600	1550	1500	1450	1400	1350	1300
$W_r, 10^5 W/m^2$	6.21	5.58	5.01	4.48	4.00	3.56	3.15	2.78

Such big values of the heat flows from the solid surface take place during the pool boiling on a vertical plate. The radiation heat flows at high surface temperatures are comparable with the pool boiling maximum heat flow ($8.8 \cdot 10^5$ W/m^2) at normal pressure (1 *bar*).

- In the experiments with different initial rod temperatures, the vertical size of the CB region was noticeably lower in the case of lower initial temperatures.

Based on the above considerations, the following explanation of the initiation and development of the Churn Boiling region may be proposed.

High values of the heat flow from the rod surface lead to the intensive evaporation on the water-steam interface. For the saturated water, the evaporation rate is comparable with the pool boiling on a horizontal plate. However, due to the differences in the geometry between the pool boiling on a horizontal plate and reflooding of a vertical tube, the full-bodied steam bubbles are not formed in the second case. But the component of the generated steam velocity normal to the water-steam interface is high enough to give rise to the large-scale water-steam interface oscillations instead of a simple steam film thickness increase as in the case of low overheats mentioned above.

As a result, the violent and chaotic (churn) motion and mixing of water and steam is established. The thickness of the steam film frequently decreases and some amount of water appears very closely to the rod surface. This leads to the noticeable enhancement of the heat exchange rate, evident at the temperature evolution curves, and further evaporation increase. Fast water-steam oscillations also lead to the ejection of the water droplets and splashes observed at the upper part of this region.

In the case of the subcooled water the intensive bulk boiling cannot take place, and the formation of the CB region is not possible until the water is heated up to the saturation temperature.

Thus, the following criteria for the formation of the CB region deduced from the experimental observation may be formulated:

- The water temperature is close to the saturation oneю
- The total heat flow from the rod exceeds some critical value. This critical value is of order of the pool boiling heat flows.

3.4. Thermal-Hydraulic model description

The Thermal-Hydraulic model of the S/Q code provides the description of the heat- and mass-exchange processes in the coolant channel [1,2]. The model considers the simultaneous existence of several coolant-gas regions: Nucleate Boiling (NB), Inverted Annular Film Boiling (IAFB), Churn Boiling (CB) and Gas Mixture (GM) with different properties at increasing elevations. The model calculates the heat transfer rates for the different regions and determines the non-stationary motion of inter-region boundaries.

In the NB region the dependence of the heat flow on the rod surface temperature (*boiling curve*) is considered. The main parameters of the boiling curve (max. and min. heat flows and corresponding temperatures) depend on the flooding parameters: pressure, subcooling temperature and flooding rate. The model includes consideration of the rewetting phenomena and quench front motion.

For the description of the heat exchange in the IAFB and CB regions two models were developed. The more general one gives the detailed thermal-hydraulic description similar to so-called two-fluid hydrodynamic "6-equation" approach [21-23]. Six equations represent the mass, momentum and energy conservation laws for water and steam, averaged over the radial coordinate. The peculiarities of the heat and momentum exchange in the CB region are accounted for by the introduction of enhancement factors in the corresponding closure relations. The work on the general thermal-hydraulic model is now in progress.

Simplified thermal-hydraulic model [1] was derived from the general system of equations by neglecting several terms of secondary importance: interfacial friction, steam heating and some others. The development of the simplified model is now completed.

In addition to existing approaches [21-23] the presented model considers the non-stationary motion of IAFB/CB and CB/GM boundaries. The region boundary evolution is described on the basis of the calculation of the coolant temperature axial distribution and the mass balance considerations. Consideration of the region motion allows an adequate analysis of the FZK non-stationary quench experiments [3] and prediction of the rod temperature evolution.

The model of the GM region describes mass exchange in the gas mixture located above the CB region. The model is based on the averaged over the channel cross-section conservation equations (analogous to the thermal-hydraulic «6-equations» approach). The model considers steam/hydrogen/argon mixtures and provides the boundary conditions for the Oxidation and Hydrogen Absorption models. Gas mixture model makes it possible to describe correctly the oxidation kinetics in a wide range of the steam concentration values and predict the steam starvation.

4. S/Q code verification

The S/Q code has been verified against the FZK experiments [3] with steam and water quenching. The set of water quenching experiments includes 25 tests collected in the Table 2.

All the water quenching verification calculations have been performed with the identical set of S/Q code FORTRAN modules with all the code parameters being fixed (there were no any tuning or adjusting of the code parameters).

S/Q code showed satisfactory agreement with the experimentally measured temperature evolutions of the rod surface in the course of reflooding. Due to certain technical problems with the thermocouples [3], the temperature measurements in the low temperature range (below 800°C) are not reliable for the experiments with pre-oxidation. That is why the main attention was paid to the high temperature region. Some results of these calculations are presented below.

In Figs. 5 and 6 the results of the T2408_1 experiment simulation, and in Figs. 7 and 8 the results of the T28095_1 experiment simulation are presented. Temperature evolution of upper, central and lower TCs for the time intervals 0-40 s and 0-10 s is shown. In Fig. 9 the results of the T0507_1 experiment simulation are presented. Temperature evolution of upper, central and lower TCs for the time interval 0-10 s is shown.

In these figures one can see the simulation of rather sharp change of the heat exchange rate due to the motion of different water-steam regions (Gas Mixture, Churn Boiling, Inverted Annular Film Boiling) past the thermocouples.

In Fig. 10, the effect of steam starvation on the temperature evolution of the rod surface can be seen. The results of the simulation of T24066_1 and T31085_1 FZK tests are presented in this figure. The first calculation (solid line) was performed with the assumption of the unlimited steam supply. In the second calculation (dashed line) the steam starvation is accounted for by the Gas Mixture model. This simulation presents the tight interaction of the Oxidation, Heat Conduction and Thermal-Hydraulic modules of the S/Q code.

Table 2. The set of water quenching experiments used for the S/Q code verification.

Test	Initial rod temperature, °C	Pre-oxidation, μm	Initial water temperature, °C
t24066_1	1600	0	90
t31085_1	1600	0	90
t1056_1	1600	100	90
t25066_2	1600	100	35
t1007_1	1600	100	90
t19066_1	1600	300	90
t1107_1	1600	300	90
t27095_1	1600	300	90
t26066_1	1400	0	35
t21066_1	1400	0	90
t28085_1	1400	0	90
t29056_1	1400	100	90
t25066_1	1400	100	35
t0507_1	1400	100	90
t05066_1	1400	300	90
t1207_1	1400	300	90
t10096_1	1400	300	90
t2408_1	1200	0	90
t28095_1	1200	0	90
t04066_1	1200	100	90
t0607_1	1200	100	90
t29085_1	1200	300	90
t25095_1	1200	300	90
t30056_1	1200	300	90
t11096_1	1200	300	90

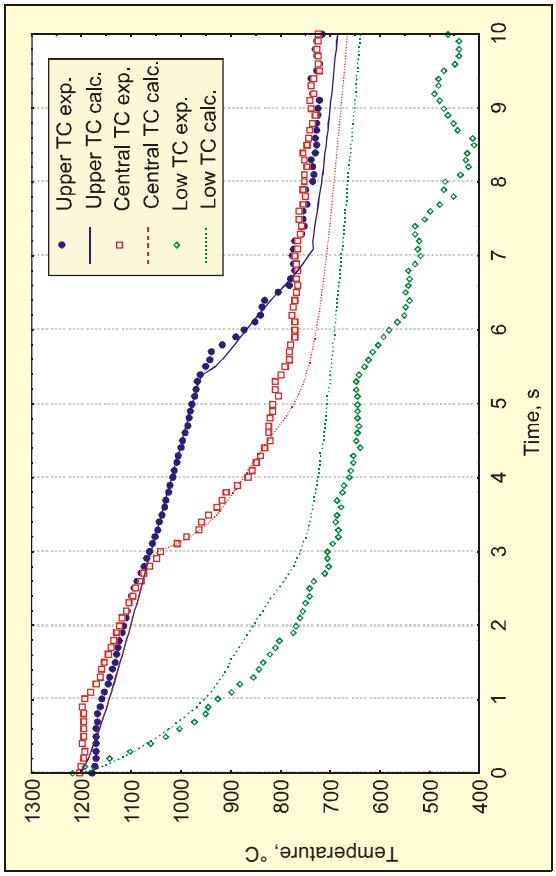

Fig. 6. T2408_1 experiment data and simulation. Temperature evolution of upper, central and lower TCs for the time interval 0-10 s.

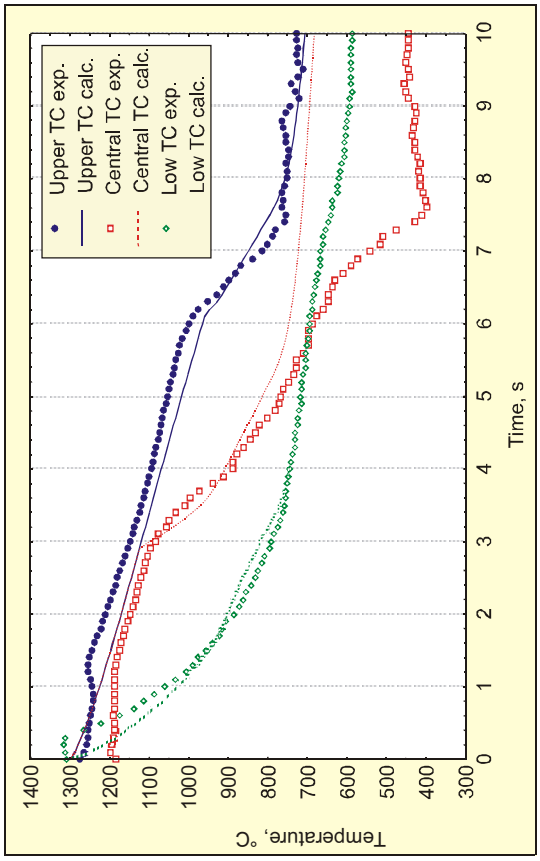

Fig. 8. T28095_1 experiment data and simulation. Temperature evolution of upper, central and lower TCs for the time interval 0-10 s.

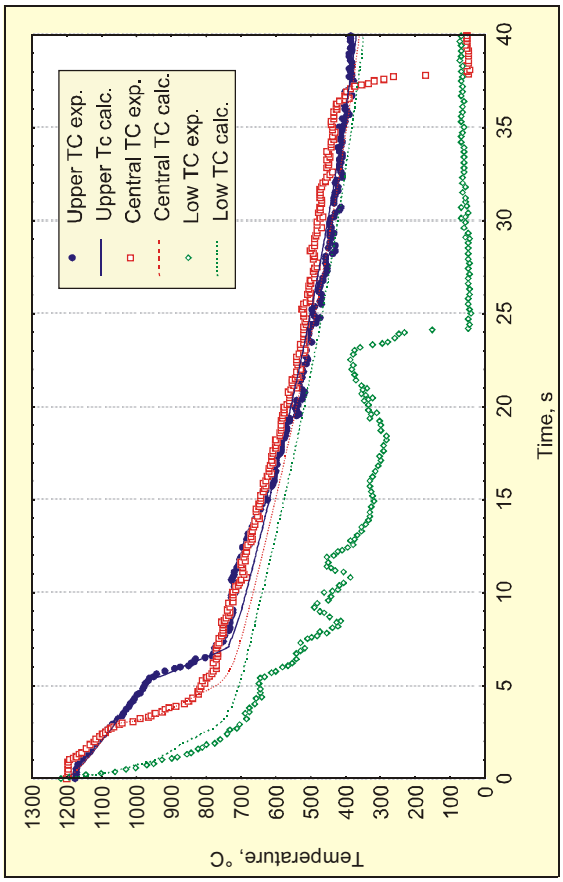

Fig. 5. T2408_1 experiment data and simulation. Temperature evolution of upper, central and lower TCs for the time interval 0-40 s.

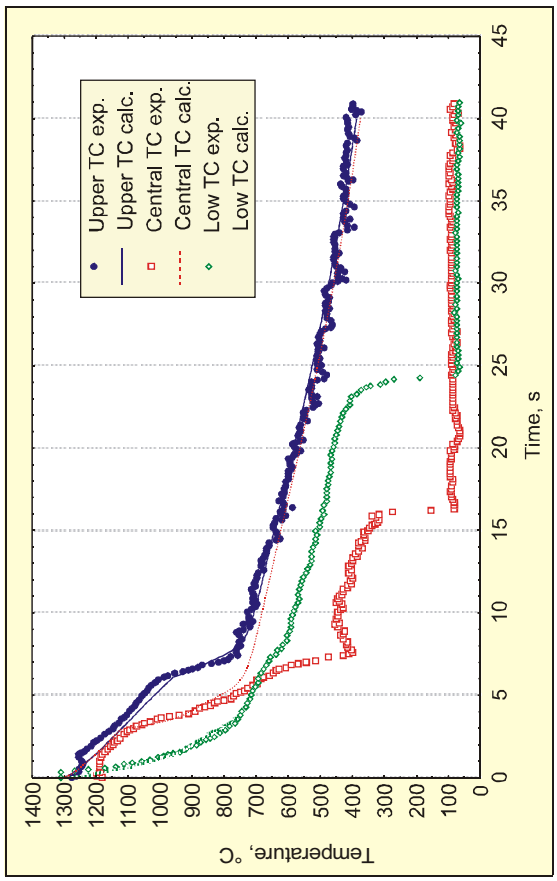

Fig. 7. T28095_1 experiment data and simulation. Temperature evolution of upper, central and lower TCs for the time interval 0-40 s.

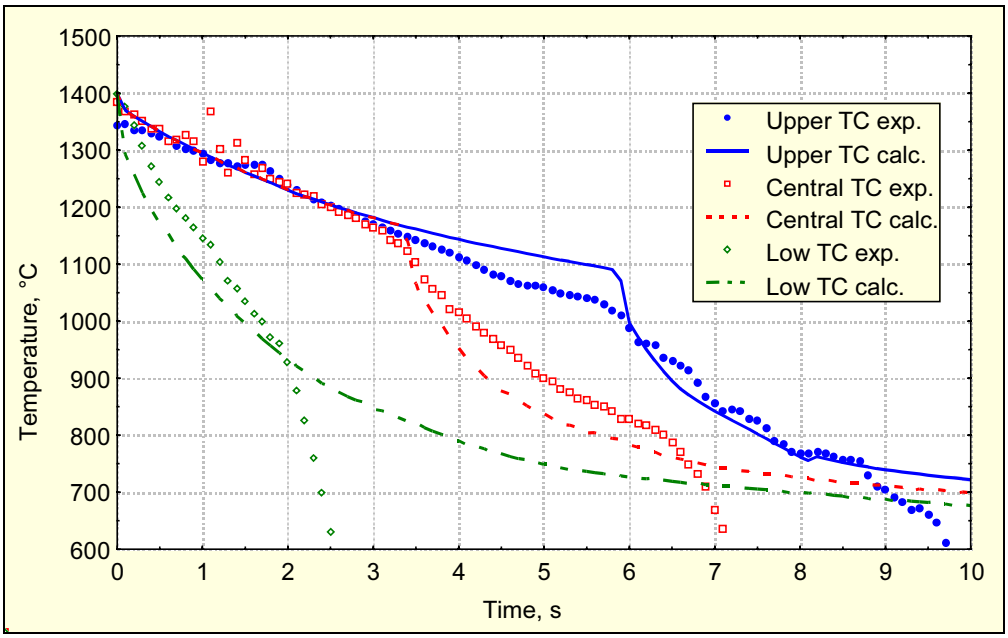

Fig. 9. T0507 experiment data and simulation. Temperature evolution of upper, central and low TCs for the time interval 0-10 s.

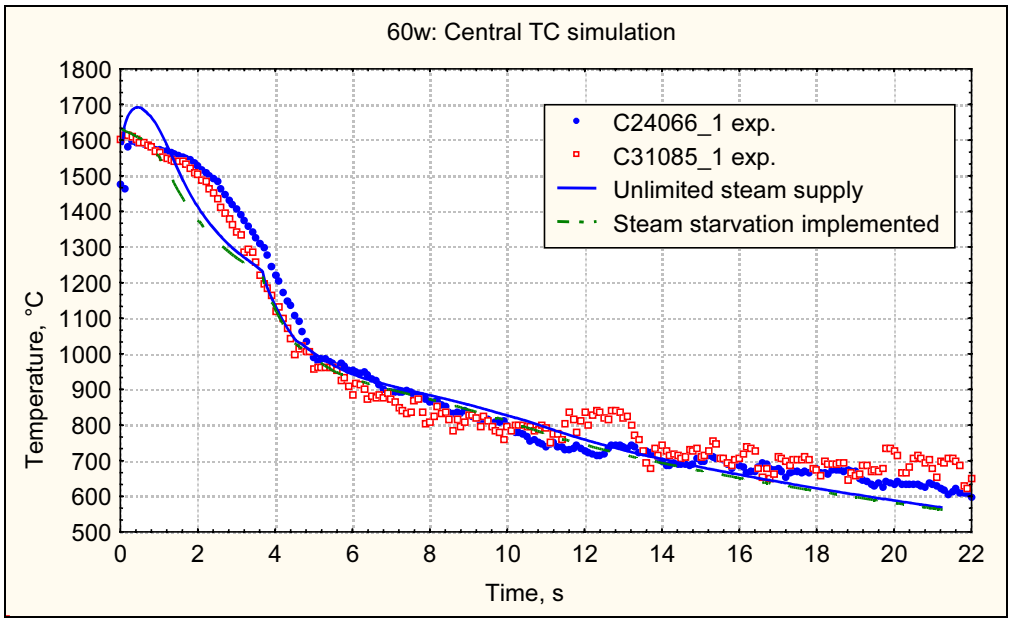

Fig. 10. Effect of steam starvation on the temperature evolution of the rod surface in the FZK experiments. Simulation of T24066_1 and T31085_1 tests (1600 °C initial temperature, 0 μm pre-oxidation, water quenching). Central TC. Solid line - steam starvation is not accounted for (unlimited steam supply), dashed line - steam starvation is accounted for by the Gas Mixture model.

5. Conclusions

In the present paper, the computer code SVECHA/QUENCH (S/Q) developed in the Nuclear Safety Institute (IBRAE) of the Russian Academy of Sciences for the modeling of reflooding phenomena is described. The S/Q code gives the detailed description of the processes taking place during LWR core reflooding under severe accident conditions (intensive heat exchange, oxidation and mechanical deformation of

Zr cladding, hydrogen generation and absorption) and accounts for their mutual influence.

The S/Q code consists of self-consistently coupled Oxidation, Hydrogen Absorption, Mechanical Deformation, Heat Conduction and Thermal-Hydraulic models. Each model was originally developed for the S/Q code and verified against numerous separate-effect tests.

The SVECHA/QUENCH code was intensively verified against the FZK (Forschungszentrum, Karlsruhe, Germany) single rod quenching tests in close cooperation with experimentalists. The comparison of the calculation results with the experimental data (25 tests with water quenching and 12 tests with cooling by steam) shows satisfactory agreement.

References

1. *P. Hofmann, V. Noack, M.S. Veshchunov, A.V. Berdyshev, A.V. Boldyrev, L.V. Matweev, A.V. Palagin, V.E. Shestak*, Physico-Chemical Behavior of Zircaloy Fuel Rod Cladding Tubes During LWR Severe Accident Reflood. Report FZKA 5846, Karlsruhe, Germany, 1997.
2. *P. Hofmann, A. Miassoedov, L. Steinbock, M. Steinbrueck, A.V. Berdyshev, A.V. Boldyrev, A.V. Palagin, V.E. Shestak, M.S. Veshchunov*, Quench Behavior of Zircaloy Fuel Rod Cladding Tubes. Small-Scale Experiments and Modeling of the Quench Phenomena. Report FZKA 6208, INV-COBE(98)-D018, Karlsruhe, Germany, 1999.
3. *P. Hofmann, V. Noack*, Physico-Chemical Behavior of Zircaloy Fuel Rod Cladding Tubes During LWR Severe Accident Reflood. Part I: experimental results of single rod quench experiments. FZKA 5846, 1997.
4. *G. Yadigaroglu*, The Reflooding Phase of the LOCA in the PWRs. Part I: Core Heat Transfer and Fluid Flow. Nuclear Safety, 19 (1978) 20.
5. *E. Elias, G. Yadigaroglu*, The Reflooding Phase of the LOCA in the PWRs. Part II: Rewetting and Liquid Entrainment. Nuclear Safety, 19 (1978) 160.
6. *J.J. Carbajo, A.D. Siegel*, Review and comparison among different models for rewetting in LWR's. Nucl.Eng.Des. 58 (1980) 33-44.
7. *R.A. Nelson*, Mechanisms of Quenching Surfaces, in: *Handbook of Heat and Mass Transfer*, Vol.1, Heat Transfer Operations, pp. 1103-1153; Gulf Publishing Company, Houston, London, Paris, Tokyo, 1986.
8. *W.M. Rohsenow*, A method of correlating heat transfer data for surface boiling on liquids. Trans. ASME, 74 **(**1952) 969.
9. *H.K. Forster, N. Zuber*, Dynamics of vapour bubbles and boiling heat transfer. J.AIChE, 1 (1955) 531.
10. *Y.P. Chang, N.W. Snyder*, Heat transfer in saturated boiling. Chemical Engineering Progress Symposium Series, AIChE, 56 (1960) 25.
11. *S.S. Kutateladze*, Fundamentals of the Heat Transfer Theory, 5th Edn., Atomizdat, Moscow, 1979.
12. *L.A. Bromley*, Heat transfer in stable film boiling. Chem.Engrg.Progr. 46 (1950) 221.
13. *Y.Y. Hsu, J.W. Westwater*, Approximate theory for film boiling on vertical surfaces. Chem. Engrg. 30 (1961) 15.
14. *R. Seban, R. Greif, G. Yadigarodlu, E. Elias, K. Yu,D. Abdollahian, W. Peake*, UC-B Reflood Program; Experimental Data Report, EPRI Report NP-743, 1978.
15. *Y. Sudo*, Film boiling heat transfer during the reflooding phase in a postulated PWR loss-of-coolant accident. J.Nucl.Sci.Technol. 17 (1980) 526.
16. *J.C. Stewart, D.C. Groeneveld*, Low-quality and subcooled film boiling of water at elevated pressures. Nucl.Eng.Des. 67 (1981) 259-272.
17. *M.K. Denham*, Inverted annular flow boiling and the Bromley model. Trans. Instn. Chem. Engrg. 86 (1984) 13.
18. *A. Ohnuki, H. Akimoto, Y. Murao*, Effect of liquid flow rate on film boiling heat transfer during reflood of rod bundle. J. Nucl. Sci. Technol. 27 (1990) 535.
19. *Y. Koizumi, Y. Anoda, H. Kumamaru, T. Yonomoto, K. Tasaka*, High-pressure reflooding experiments of multi-rod bundle at ROSA-IV TPTF, Nucl. Eng. Des. 120 (1990) 301-310.
20. *Y. Barnea, E. Elias, I. Shai*, Flow and heat transfer regimes during quenching of hot surfaces. Int.J.Heat Mass Transfer 37 (1994) 1441.
21. *K.C. Chan, G. Yadigaroglu*, Calculations of film thickness heat transfer above the quench front during reflooding, 19th ASME Heat Transfer Conf. Experimental and Analytical Modeling of LWR Safety Experiments, p.65. 1980.

22. *G.Th. Analytis and G.Yadigaroglu*, Analytical modeling of inverted annular film boiling. Nucl. Eng. Des. 99 (1987) 201.
23. *F. de Cachard*, Development, implementation and assessment of specific, two-fluid closure laws for inverted-annular film boiling. Proceedings of the 7th International Meeting on Nuclear Reactor Thermal-Hydraulics NURETH-7, Vol.1, p.166, 1995.
24. *N. Takenaka, T. Fujii, K. Akagawa, K. Nishida*, Flow pattern transitions and heat transfer of inverted annular flow. Int. J. Multiphase Flow 15 (1989) 767.
25. *J.W.H. Chi, A.M. Vetere*, Two-phase flow during transient boiling of hydrogen and determination of nonequilibrium vapor fractions. Adv. Cryogen. Engng. 9 (1964) 243.
26. *P. Ottosen*, Experimental and theoretical investigation of inverse annular flow, important under LOCA conditions. Riso National Lab. Report No. R-424, Denmark, 1980.
27. *M. Aritomi, A. Inoue, S. Aoki, K. Hanawa*, Thermal and hydraulic behavior of inverted annular flow. In Proc. 2nd Int. Topical Meeting on Nuclear Plant Thermal Hydraulics, 1986.
28. *M. Aritomi, A. Inoue, S. Aoki, K. Hanawa*, Thermohydraulic behavior of inverted annular flow. Nucl.Eng.Des. 120 (1990) 281-291.
29. *G. de Jarlais, M. Ishii*, Inverted annular flow experimental study, Report NUREG/CR-4277, ANL-85-31, 1985.
30. *N.T. Obot, M. Ishii*, Two-phase flow transition criteria post-dryout region based on flow visualization experiments. Int.J.Heat Mass Transfer 31 (1988) 2559.
31. *J. Goodman, E. Elias*, Heat transfer in the inverted annular flow regime during reflooding. Trans. ANS 28 (1978) 397-399.
32. *Z. Edelman, E. Elias, D. Naot*, Inverted annular boiling in a stainless-steel tube with steady heat sources. Int.J.Heat Mass Transfer, 28 (1985) 1281-1292.
33. *M. Kawaji, S. Banerjee*, A two-fluid model for reflooding of a vertical wall: Structure and stability of the inverted annular flow model. Paper presented at the 21th ASME-AIChE National Heat Transfer Conference, 1983.
34. *M. Moalem, D.A. Olander*, Oxidation of Zircaloy by Steam, J. Nucl. Materials 182 **(**1991) 170-194.

Труды ИБРАЭ РАН

Под общей редакцией чл.-кор. РАН Л.А. Большова

Выпуск 1

Модели взаимодействия материалов топливных элементов в процессах разрушения активной зоны реактора при тяжелых авариях на атомных станциях (на английском языке)

Под научной редакцией д.ф.-м.н. В.Ф.Стрижова
Рецензенты: д.ф.-м. н. О.И. Мелихов, д. т. н. А.Е. Киселёв

Издательство «Наука»
117997, Москва, Профсоюзная ул., 90

Сдано в набор 15 октября 2007 г. Подписано в печать 12 ноября 2007 г.
Формат $60 \times 90\,1/8$. Бумага офсетная 80 г/м^2. Печать офсетная. Гарнитура «Таймс».
Усл. печ. л. 12,0. Уч.-изд. л. 12,0. Тираж 500. Заказ 16731.

Отпечатано с готовых диапозитивов типографией ООО «Инфолио-принт»